Identification of Spinal Reflexes

Proefschrift

ter verkrijging van de graad van doctor
aan de Technische Universiteit Delft,
op gezag van de Rector Magnificus prof. dr ir J.T. Fokkema,
voorzitter van het College voor Promoties,
in het openbaar te verdedigen op dinsdag 25 mei 2004 om 13:00 uur
door

Erwin DE VLUGT

werktuigkundig ingenieur
geboren te Heemskerk, Nederland.

Dit proefschrift is goedgekeurd door de promotor:
Prof. dr F.C.T. van der Helm

Samenstelling promotiecommissie:

Rector Magnificus,	Technische Universiteit Delft, voorzitter
Prof. dr F.C.T. van der Helm,	Technische Universiteit Delft, promotor
Prof. dr ir H.G. Stassen,	Technische Universiteit Delft
Prof. dr ir P.M.J. van den Hof,	Technische Universiteit Delft
Prof. dr T. Sinkjær,	Aalborg University Denmark
Prof. dr J.H. van Dieën,	Vrije Universiteit Amsterdam
Prof. dr J. Duysens,	Katholieke Universiteit Nijmegen
Prof. dr J.G. van Dijk,	Universiteit Leiden
Prof. dr ir P.A. Wieringa,	Technische Universiteit Delft, reservelid

ISBN 90-77595-42-2
Keywords: reflexive control, human arm, stability, posture maintenance, system identification

Cover design by Tasso en Erwin

Contents in brief

Contents

Abbreviations

ARMANDA	arm movement and disturbance analysis
ARX	auto regressive and exogenous
CNS	central nervous system
DOF	degrees-of-freedom
DSP	digital signal processor
EMG	electromyography
FFT	fast fourier transform
FP	force perturbation
FRF	frequency response function
FT	force task
GTO	Golgi tendon organ
IEMG	integrated rectified emg
IFFT	inverse fast fourier transform
MBK	mass-damper-spring
MFRF	multivariable frequency response function
MTF	multivariable transfer function
MVC	maximum voluntary contraction
NB	narrow bandwidth
NMS	neuromusculoskeletal
RMS	root-mean-square
RSD	Reflexive Sympathetic Dystrophy
RSI	Repetitive Strain Injury
PD	Parkinson's disease
PP	position perturbation
PT	position task
SD	standard deviation
SNR	signal-to-noise ratio
VAF	variance accounted for
WB	wide bandwidth

Chapter 1

Introduction

Erwin de Vlugt

This thesis comprises experimental and model studies that aim to reveal the neuromuscular properties involved in the maintenance of arm postures. In this chapter, a brief introduction is provided to the components of the neuromusculoskeletal system that are relevant to the study of human arm posture control. With this, a basis is laid and a framework is given for the subsequent chapters. Anatomical properties of muscles and proprioceptive feedback pathways are briefly described and basic system functioning is explained from a control engineering point of view. Theories of posture control are discussed and existing experimental approaches to identify components of the neuromuscular machinery are briefly reviewed. A new experimental paradigm is introduced that is based on the usage of continuous force disturbances facilitating natural position tasks. A novel two degree-of-freedom force controlled manipulator has been developed that is used to explore the arm admittance in the horizontal plane. Experimental findings were synthesized using descriptive models that represent underlying dynamical processes. Derivation of the models from known physiological functioning is explained and their applications for both parametrization and optimization purposes are founded. The last part of this chapter describes the goal and the lay-out of the thesis.

1.1 Introduction

Movement generation and posture maintenance are common everyday life performances of the human body that are learned by trial and error in our early years. What has been gained by learning is the appropriate activation of our muscles and to apply the right corrections based on sensory information of the state of our body. To understand how movement is controlled, the human movement system has to be analyzed in its complete constellation of bones, sensors, muscles and the central nervous system (CNS) that controls and supervises movement. How flexible is the CNS in performing movement under different conditions? What are the constraints imposed by the biological properties of the neuromusculoskeletal (NMS) system? What signals are important to the CNS and how does it make usage of all information sensed? An integral approach to reveal the functioning of the human movement system is not only important to fundamental research but also highly valuable for understanding the pathophysiology of movement disorders. Yet there is still no convincing evidence of how muscles are controlled to perform a movement or maintain a posture.

In this thesis the control properties of the CNS during posture maintenance of the human arm are quantified and analyzed. During posture control, we like to keep an object at a specific place in space, like holding the steering wheel during car driving, holding a cup of coffee, positioning a drilling machine etc. Very often, external disturbances are present that tend to displace the arm from the desired posture. In most cases, the exact properties of the disturbances are not fully known, as they appear at random time instants such that one cannot anticipate on them. To maintain position is to increase the mechanical resistance against such perturbations. Posture control is therefore characterized by disturbance rejection to keep displacements within acceptable bounds or make them as small as possible. The intrinsic stiffness and viscosity of muscles are highly beneficial to disturbance rejection. The reflexive feedback system can further enhance disturbance rejection based on sensory information of the mechanical state of the muscles. Most feedback control mechanisms are fast and, compared to the intrinsic properties, are energy efficient as the muscles are only activated when displacements occur.

Ultimately, full knowledge of the NMS system is obtained if the properties of each subsystem (bones, sensors, muscles, CNS) can be measured directly. In general, system properties are derived from input-output measurements of the particular subsystem. As an example, muscle stiffness can be derived from measurements of the muscle's length (input) and force (output). It is obvious that to obtain the properties of all subsystems, invasive measurement techniques are required. Besides, appropriate measurements of the input-output behavior of the sensory part and in particular of the CNS is technically not possible yet. Since ethical laws prevent the application of invasive experiments on humans, invasive experiments have been undertaken numerously on animals. A lot of these studies have been directed to reveal the mechanical properties of skeletal muscles from controlled stretching one muscle and measuring the responding muscle force. Voluntary and

reflexive forces were mostly excluded by dissection or anesthesia. Explaining natural control functioning from these studies is hardly possible.

For a functional understanding of human motion control, experiments need to be carried out on the intact functioning system. Consequently, one is restricted to those measurements than can be obtained non-invasively such as reaction forces of the whole limb with some sort of environment, hand positions, joint angles from kinematic data and lumped muscle activation from electro-myography (EMG). System properties can be obtained by perturbing the intact system and analyzing the response.

Because the properties of the underlying systems can not be measured directly, a-priori knowledge must be used in the form of descriptive models. These models must include descriptions of the relevant subsystems such that they can be evaluated at the global level at which the measurements were taken. In fact, the absence of detailed measurements is to be compensated for by models. Depending on the application, these models vary by size, i.e. the number of joints included, and by level of detail, i.e. global or detailed mathematical descriptions from basic physics.

A major part of this thesis comprises the development of identification techniques to quantify the intrinsic and reflexive properties of the intact human arm in vivo during posture control. From such an approach, the role of these properties to the overall performance of the arm can be explained functionally. An appropriate measurement technique requires the application of force perturbations that appeal as natural during posture maintenance. Consequently, the usage of intrinsic and reflexive properties have direct effect on the displacements that result from the force perturbations.

The human reflex system is adaptive and it might as well be the case that the measured behavior is particular for a certain condition. Therefore, the experiments should be designed as to cover a wide range of natural conditions. The formulation of the task instruction has major impact to the control of posture. Furthermore, it does make a difference if someone is only told to keep his or her hand on a target instead of asking to minimize the amplitude of the displacement (Burleigh and Horak, 1996). Accompanying learning effects with either task instruction presumably differ as well. The latter, more demanding task formulation was chosen.

Experiments were conducted on healthy subjects and the mechanical admittance at the hand level was estimated. From the mechanical admittance, the underlying joint dynamics were quantified with the aid of descriptive models. To apply force disturbances, an advanced force controlled manipulator is required which act as an external dynamical load to the human arm. As a consequence, the human is embedded in a closed loop configuration with that load. To separate the human response from that of the load, closed loop identification techniques are required.

Experimental and model studies were entangled throughout the thesis exhibiting a continuous interchange of knowledge about the physiology of the human movement apparatus and about theories of posture control.

1.2 The neuromusculoskeletal system

1.2.1 Basic functioning

To understand NMS system functioning, it is necessary to know of which parts it exists and how these parts are mutually related. In this subsection, the general functioning of each part and the coupling between the parts of the NMS are described. The functioning of each subsystem will be explained in the context of posture control. The architecture of each subsystem is described in detail in the subsequent sections.

Basically, the NMS system is build up of four parts, being the skeleton, sensors, CNS and the muscles as schematically shown in Figure 1.1. The skeleton is a constellation of bony segments which are interconnected by joints. The mass of the segments determines the mechanical behavior at fast movements. Also the resonance frequency is directly determined by the inertia of the NMS system.

The state of the skeleton is measured by different type of sensors. For posture control of the human arm, the relevant sensors are the propriocepsis and the visual system. Propriocepsis is a system that provides information about the displacement and velocity of the segments and the forces applied to them. This information is generated by mechanoreceptors in the skin, the joint capsules and the muscles. Most important to the control of arm posture are the mechanoreceptors in the muscles, called the muscle spindles, providing length and velocity feedback. Another important mechanoreceptor is located in the muscle tendon junction that measures muscle force, the so called Golgi tendon organs. The visual system also provides information of the position and velocity of the segments.

The CNS comprises the signal processing in the brain and the spinal cord. Neural signals that originate from inside the CNS (voluntary actions) are integrated with neural signals that enter the CNS from the sensors, and processed into motor commands. These motor commands activate the muscles. The skeleton has to be kept into a position by muscle forces. The muscles behave like mechanical spring-dampers of which the elasticity and viscosity increases with activation level.

Clearly, the human posture control system is characterized by a closed loop system of sensing, integrating and processing of control signals and actuating. Therefore, the dynamics of all subsystems in the loop are of direct importance to the overall performance of the movement task. Another important aspect is the neural delay involved in the transport of sensory signals to the CNS and in the transport of motor commands to the muscles. These time delays substantially limits the performance of the closed loop control system. The NMS system behaves like a hierarchical control system where the spinal cord acts as a subconscious fast controller based on proprioceptive information. Visual information is processed by higher brain centra and is less effective due to the larger time delays involved.

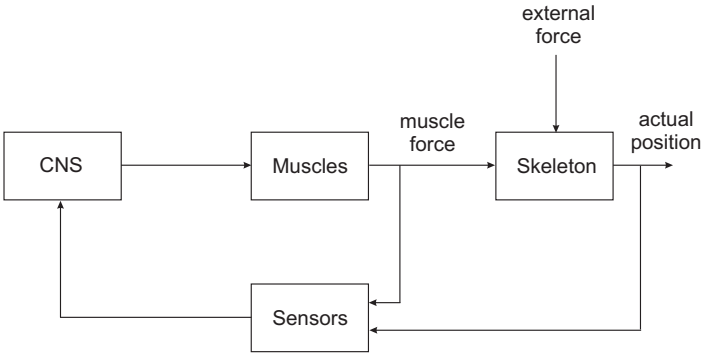

Figure 1.1: *Basic components and functioning of the NMS system. The system exists of a closed loop where sensory information about the state of the skeleton (position, velocity, force) is monitored and send to the CNS (the afferent pathways). Sensory information is integrated and processed by the CNS into control signals to activate the muscles (the efferent pathways). Muscles produce force that acellerate the skeleton (the controlled system). Undesired displacements that result from external forces are to be suppressed by the CNS.*

1.2.2 Nervous system

Information processing and transport in the central nervous system (CNS) is established by nervous cells or neurons. There are three types of neurons that are important to movement control: sensory neurons, motor neurons and interneurons. Sensory or afferent neurons transmit information from the musculoskeletal system to the CNS. Motor or efferent neurons transmit information from the CNS to the muscles. The interneurons are located in the CNS and form complex networks that process sensory information and generate motor control signals. Signal transfer between neurons is the result from electro-chemical processes. If the electrical potential of a neuron is raised to above a critical threshold, a chain reaction takes places which rapidly increases the potential to a positive level and then back to the negative rest potential again. The resulting electrical pulse is called the action potential (spikes) and can be transferred to neighboring neurons via neurotransmitter substances. Signal transfer can be inhibitory causing the potential of the receiving neuron to decrease and consequently lowering the chance to cause an action potential. Alternatively, an excitatory transmission causes the potential of the receiving neuron to increase and therewith increasing the chance to start a new action potential. Since many neurons project on many others (1000 connections per neuron on average), the final determination of an action potential is the result of a lumped weighting of all inhibitory and excitatory connections. The nervous system acts as a regulator of signal strength and can modify the total gain of the signal pathways from the sensors to the muscles which is crucial to the control of movement and posture.

1.2.3 Muscle anatomy and physiology

The main function of the skeletal muscle is force generation and energy transfer in order to rotate the joints and move the limbs for a variety of tasks or for posture maintenance. When a muscle generates force and shortens, it transfers chemical energy into mechanical energy which moves the skeleton. It absorbs mechanical energy while it stretches, transferring energy into heat. To generate a force, contractile machinery in the muscle must be activated by motor commands from the motor neurons.

Active muscle tissue

Active tissue of muscles consists of elements able to shorten when activated. The construction of the skeletal muscle is depicted in Figure 1.2. Skeletal muscles consist of bundles of muscle fibers. Each fiber consists of thick and thin filaments into functional units called the sarcomeres (Fig. 1.2B and Fig. 1.2C). On both sides of the sarcomere boundary the thin filaments of subsequent sarcomeres are attached. The filaments are aligned in parallel and are able to generate force by means of bending proteins called the cross bridges in between the filaments. The globular head of the cross-bridge has two components, one for binding to the active site of the thin filament, and the other contains the enzyme myosin ATPase, which splits ATP and releases its energy for contraction.

Activation dynamics

Important to the control of muscles is their responsiveness to motor commands. How fast does force build-up? Because of the closed loop configuration of the movement system, activation dynamics directly affects overall control behavior and must be taken into account when identifying the NMS as a whole.

Muscle contraction is initiated by action potentials along the muscle fibers which on their turn are caused by action potentials from the motoneurons. The cell bodies of these motoneurons lie in the spinal cord and its branches or axons innervates a group of muscle fibers called a motor unit. Stimulation of the motoneuron causes all muscle fibers of the motor unit to be activated and to contract simultaneously. An action potential that is propagated down the axon causes an action potential that will propagate along the sarcolemma (muscle cell membrane). Action potentials that are generated along the sarcolemma propagate into the transverse tubule system (Fig. 1.2A) and increase the permeability of the sarcoplasmic reticulum membrane. Ca^{2+} ions are released from the sarcoplasmic reticulum, raising the cytoplasmic concentration of Ca^{2+} in the muscle cell about 100 to 1000-fold. Due to the catalyzing effect of Ca^{2+}, cross-bridges are formed and the myofilaments generate force. During the excitatory state brought on by each action potential, Ca^{2+} continually cycles from the sarcoplasmic reticulum to the myofilaments and back to the sarcoplasmic reticulum.

The time constant for activation, i.e. from action potential along the sarcolemma to force build-up, is smaller than for de-activation. The intracellular processes of

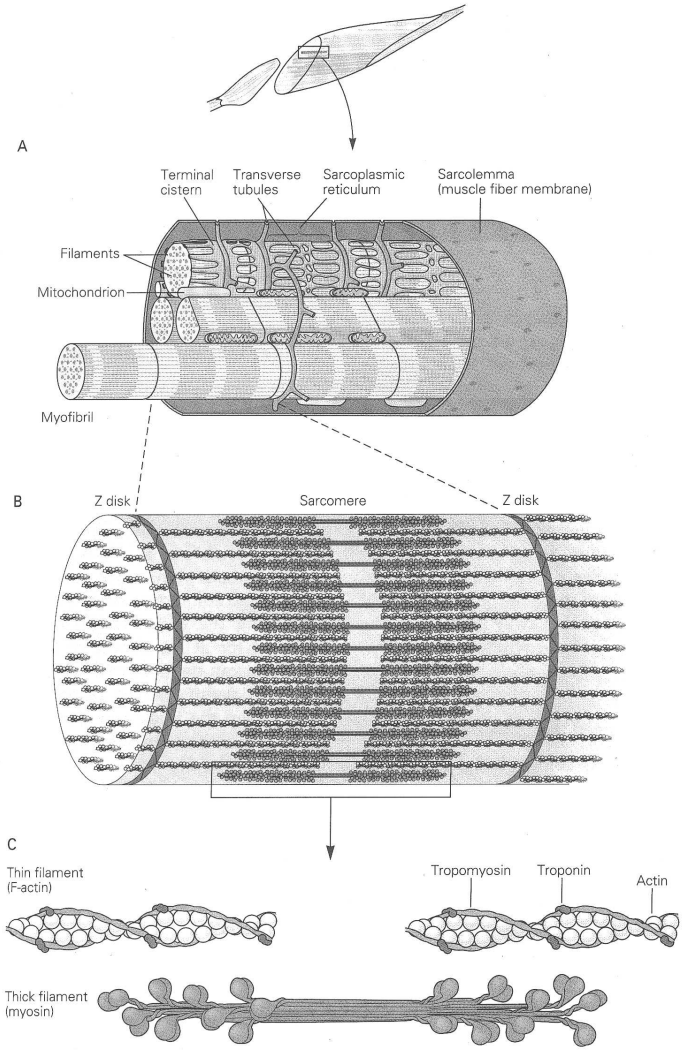

Figure 1.2: *Structure of the skeletal muscle (from Kandel et al., 2000). A. Section of a muscle fiber showing the relationship of the myofibrils to the membrane, transverse tubule system and the sarcoplasmic reticulum. B. The sarcomere as the functional unit of a muscle. It contains the contractile proteins. C. Detail of the contractile proteins or thin and thick filaments.*

calcium activation and de-activation are therefore nonlinear. For continuous variations around a mean force level, the activation process can be accurately approximated by a linear first-order model (Chapter 2 and Van der Helm et al. (2002)). Further improvements resulted in an extension to a second order model that more accurately described the experimental findings (Chapter 3).

1.2.4 Mechanics of muscles

Force-length characteristic

Active muscles have a spring-like characteristic which is useful for the maintenance of posture. When operating in antagonistic pairs, muscles provide the joint the appropriate stiffness depending on their individual lengths and activation level.

The length of a muscle determines how much force can be developed. Muscles develop lower force at lengths shorter than, as well as longer than the optimal length L_0^M, i.e. muscle length where force is at a maximum. For static isometric situations this results in the force-length relationship as depicted in Figure 1.3A. This relation is obtained by high stimulation rates of the muscle for a relatively long period of time so that a fused tetanic contraction arises. The difference in force during the active and passive state of a muscle is called active muscle force (Fig. 1.3A, solid lines). The region were the active muscle force is generated is approximately $0.5L_0^M < L^M < 1.75L_0^M$ for most skeletal muscles. The length at which passive muscle generates force is nominally at L_0^M and longer. The passive force of muscle (Fig. 1.3A, dotted lines) results from binding structures of the fibers (endomysium) and surrounding tissues of whole muscle (perimysium).

The isometric force-length relation can be explained from the sliding filament theory (Huxley, 1957) and is schematically represented in Figure 1.3B. For simplicity, it is assumed here that all sarcomere lengths along the muscle fibers are equal, each contributing the same force to the total active force. Taking the length from small to larger values, the ascending limb of the force-length relation is because of increasing filament overlap. At optimal muscle length L_0^M, the overlap is maximal and all cross-bridges can be formed. Stretching the muscle further from this point, the filament overlap decreases and less force can be generated. At very small lengths the thick filaments bump into the sarcomere boundaries and little external force can develop. The sliding filament theory is a rationale for the force-length property of the isometric contracting muscle. Mainly due to sarcomere length inhomogenity and different fiber types (slow and fast), the actual isometric force-length curve has a shape comparable to Figure 1.3A rather that that of the simplified curve shown in Figure 1.3B.

Muscle stiffness is important for the maintenance of a posture and can be derived by taking the slope of the spatial derivative of the force-length curve at a certain muscle length: $\frac{\Delta F}{\Delta L}$. However, the force-length curve is determined isometrically while muscle stiffness plays a role during small movements around an equilibrium postural position. It is known that derivation of the stiffness from the force-length relationship results in an underestimation of the apparent stiffness during

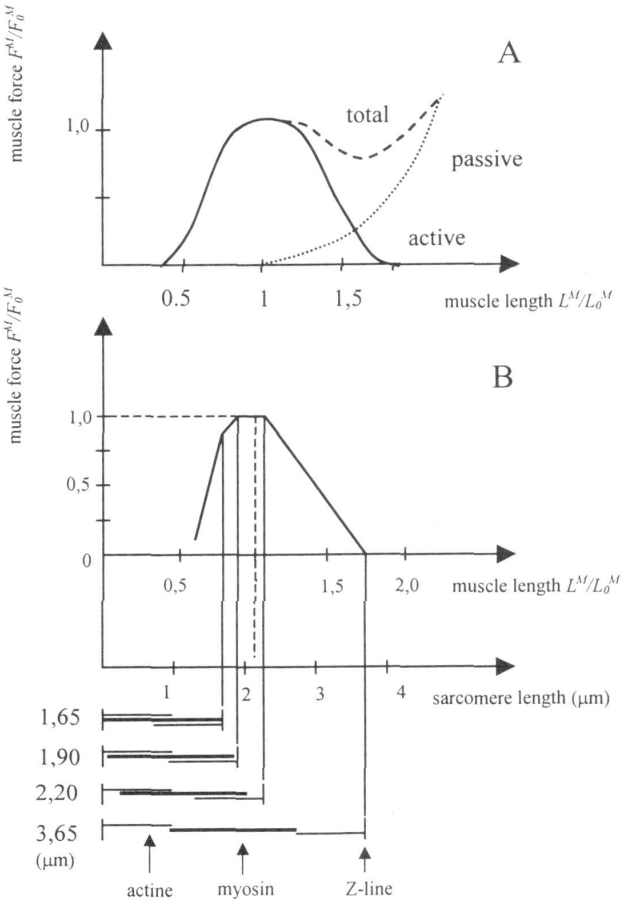

Figure 1.3: *A. Force-length relationship of muscle when passive (dotted curve) and active (dashed curve). The difference between the total force and the passive force is the active force (solid line).* L^M *is the length of the muscle,* F^M *is the muscle force,* L_0^M *is the optimum muscle length at maximum muscle force* F_0^M *and maximum stimulation. B. Schematic force-length diagram of muscle related to sarcomere length and the amount of actin-myosin overlap (reproduced from De Vlugt (1998a), p. 28).*

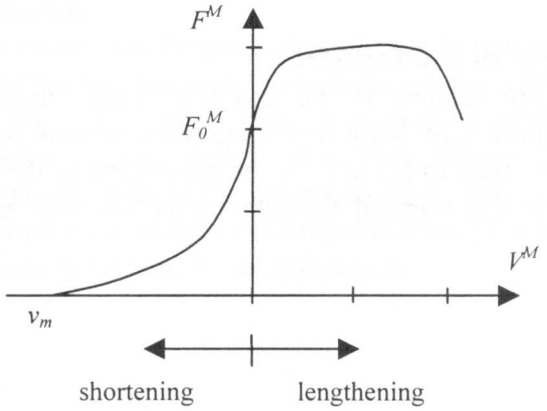

Figure 1.4: *Force-velocity relationship of fully activated muscle, v_m is the maximum shortening velocity (reproduced from De Vlugt (1998a), p. 29).*

movement. Dynamic properties like the short range stiffness from attached cross-bridges and the dependency on contraction history of the contractile machinery also enhance whole muscle stiffness (De Vlugt, 1998b). The models used in this thesis description the net muscle stiffness and so implicitly comprise these additional contributions to stiffness.

Force-velocity characteristic

The velocity at which a muscle shortens or lengthens also determines the force than can be produced, as described by the characteristic force-velocity relation. Hill (1938) measured initial shortening velocities under various isotonic afterloads and demonstrated that the force-velocity relation can be described by two parabolic curves (Figure 1.4). In case of zero velocity a certain number of cross-bridges are in an attached state, others are unattached, even at maximal activation. When the muscle is stimulated constantly the cross-bridges are in cyclic transfer from the attached state to the unattached state and vice versa. If the muscle shortens cross-bridges will bend and detach. After detachment a new bonding place is sought and re-attachment will take place and so on. If shortening velocity increases less cross-bridges are in attached state and total force decreases. Indeed some cross-bridges can not detach in time generating a contracting force and will be forcibly detached by the action of other cross-bridges at the expense of total force. At maximum shortening velocity v_m, all force of force-generating cross-bridges will be consumed for detaching other cross-bridges and zero net force results. At stretching velocities there is an extra net force needed for breaking the cross-bridges. The muscle force therefore increases as can be seen from Figure 1.4. At high stretching velocities less

cross-bridges are able to attach in time and force decreases: muscle yielding.

Muscle viscosity determines the amount of damping of the joints. Well damped systems show little overshoot in the response to steplike force disturbances. Underdamped systems on the contrary show oscillatory behavior that slowly decays in time. Therefore, muscle viscosity plays an important role to the performance of the NMS system during posture maintenance. Muscle viscosity for small displacements around a mean muscle length can be derived from the force-velocity characteristic as the derivative at zero mean velocity where the viscosity is expected to be largest (Fig. 1.4). Net muscle viscosity is described by one parameter in all models used in this thesis.

1.2.5 Passive tissues

Passive structures having the greatest effect on muscle force reside in the tendons and the fascicle that surrounds the muscle. Tendons are located on both sides of the muscle and function as stiff force transfer elements in series with the contractile tissue. The contribution of tendon stretch to the total lengthening of the muscle-tendon complex is very small. Tendon stiffness is at least 10 times higher than the stiffness of the active contractile tissue and is therefore neglected in all subsequent analyses in this thesis. The fascicle is involved in force transfer as well, acting in parallel to active muscle tissues. Other contributions from passive parallel structures are those from binding tissues inside the sarcomeres and the fibers membranes. At optimal muscle length, the parallel stiffness of these passive structures have a modest contribution to the overall muscle stiffness.

1.2.6 Muscle sensory receptors

Muscles contain two important mechanoreceptors that transduce mechanical stimuli into neural activity. The muscle spindle senses changes in muscle length and lengthening velocity while the Golgi tendon organ senses changes in muscle force. The process of sensory transduction occurs in several successive stages. First, the mechanical stimulus causes deformation of the terminal membranes of the receptor, producing conductance changes which give rise to the receptor potential. The receptor potential (or current) is then encoded into nerve impulse activity at a nearby impulse-initiating site.

Muscle Spindles

Muscle spindles are mechanoreceptors which respond to stretch and stretch rate. They consist of intrafusal muscle fibers and sensory nerve endings encapsulated in spindle-shaped structures that are distributed throughout a muscle in parallel with the extrafusal fibers (Figure 1.5). There are two types of sensory innervation to intrafusal muscle fibers, primary endings (group Ia), which are large, fast-conducting nerve fibers, and secondary endings (group II) which are smaller slower-conducting nerve fibers. Group Ia afferents respond to stretch and stretch rate. Group II afferents respond mainly to stretch.

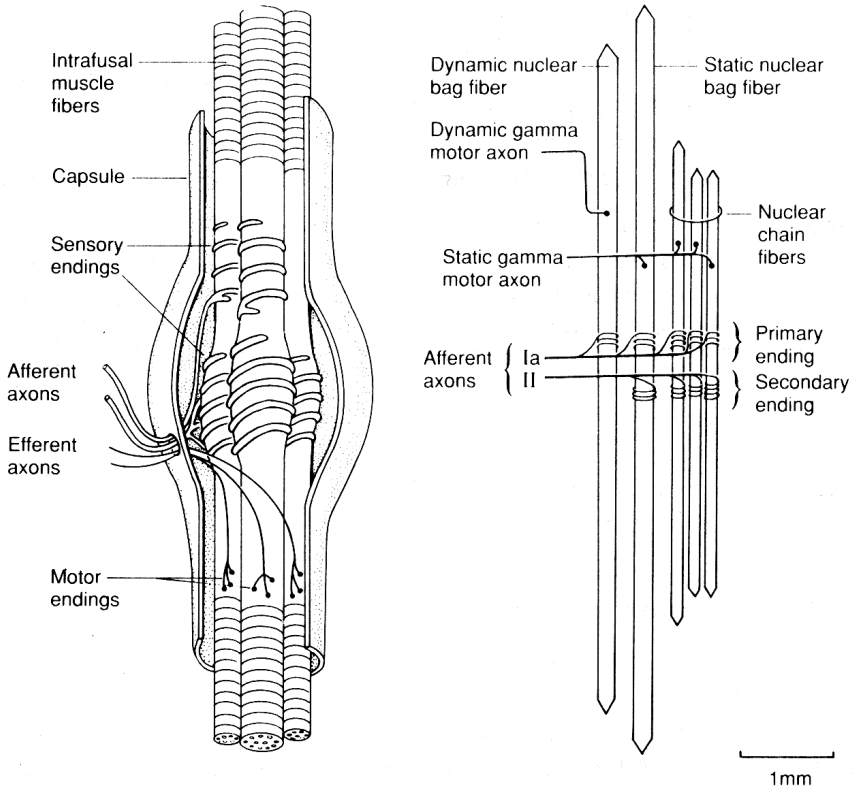

Figure 1.5: *Simplified diagram of the central region of the muscle spindle. Inside the spindles, two types of intrafusal muscle fibre exists: nuclear bag (static and dynamic) and nuclear chain fibres. The middle portion of the fibres contain sensitive celbodies that evoke action potentials in two nerve types: the Ia (primary endings) and II (secondary endings) afferent nerve endings. Stretch of the intrafusal fibres evokes action potentials in both nerve endings. Group Ia afferents are sensitive to stretch and stretch rate. Group II afferents are mainly sensititive to stretch. Fibres endings exist of contractile tissue that are innnervated by γ motoneurons. By intrafusal contraction the sensitivity of the muscle spindles can be changed (from Kandel et al., 2000).*

Intrafusal fibers are innervated by γ-motoneurons, which are divided into static and dynamic groups. Static refers to the stretch-sensitive part and dynamic refers to the stretch rate-sensitive part.

When an intrafusal fiber is stretched, the sensory endings undergo a mechanical deformation that results in a receptor potential. Under the driving force of the receptor potential, the impulse-initiating region of the nerve membrane produces a sequence of nerve impulses (action potentials) that are conducted along the sensory nerve fiber to the spinal cord (afferent transmission). The mechanical properties of

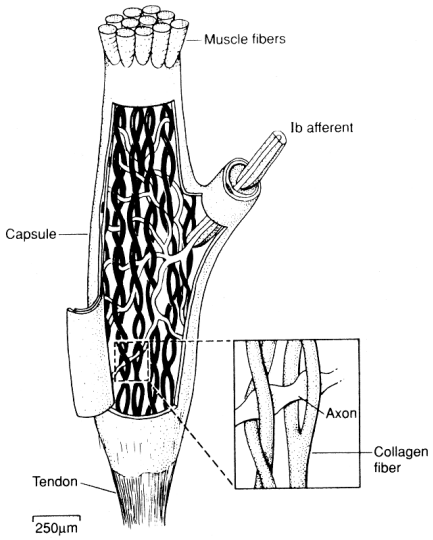

Figure 1.6: *Morphology of the Golgi tendon organ (from Kandel et al., 2000). Muscle force causes the Ib nerve endings to squeeze between the collagen fibers resulting in axon action potentials. Golgi organs lie in series with the muscle fibers and in parallel with the surrounding connective tissues (perimysium).*

intrafusal fibers determine the proportion of an applied stretch that will act on the sensory endings and consequently how the stretch will be transduced into nerve impulses. The sensitivity of primary and secondary sensory endings can be altered by changes in intrafusal fiber stiffness. The polar zones (regions near the ends) of an intrafusal fiber are considerably stiffer than the sensory zones, which are located near the center of the fiber. Therefore, when a muscle spindle is stretched most of the change in length takes place in the sensory zone. Stimulation of the γ-motoneuron produces localized contraction of an intrafusal fiber. The contraction stretches the sensory zone, which is more compliant, and also enhances its sensitivity to stretch since the polar zones become relatively stiffer and hence more resistant to stretch (Chen and Poppele, 1978).

Tendon organs

Tendon organs are mechanoreceptors which respond to force. They consist of bundles of collagen strands and sensory nerve endings enclosed in connective tissue capsules located at junctions between muscle fibers and tendon or aponeurosis (Fig. 1.6). The collagen breaks up into fine strands which are woven around sensory nerve endings. Force is transmitted from the tendon and muscle ends of the organ to its sensory endings through the collagen bundles and capsule cells in which they are embedded. The resulting mechanical deformation of the terminal endings of the sensory nerve fibers gives rise to the receptor potential, which is then encoded

as nerve impulses. The sensory nerve fibers that innervate the tendon organs are known as group Ib afferents. Tendon organ afferents begin to discharge at the onset of contraction of in-series muscle fibers. If the in-series force applied to the tendon organ is sustained afferent discharge will be maintained (Houk and Henneman, 1966). Tendon organs have relatively low sensitivity to tension generated by passive stretching of the tendon, but are highly sensitive to forces generated by active contraction of in-series muscle fibers. In a passive muscle most of the stretch will be taken up by the muscle fibers rather than the tendon. Tendon organs require higher levels of passive tension to produce sustained discharge than do muscle spindles.

1.2.7 Spinal reflexes

Spinal reflexes result from activity in sensory afferent fibers, originating in the periphery, that project either directly or indirectly to motoneurons. Reflex actions are the direct result of synaptic connections between afferent fibers and motoneurons (monosynaptic) or from indirect pathways via of one or more interneurons. The inputs to a single neuron may include sensory inputs from the periphery, descending inputs from supraspinal regions and inputs from other interneurons.

Inputs from descending commands from higher centra of the nervous system onto interneurons can enhance (amplify) or depress (attenuate) the effects of sensory input to the motoneurons. In particular, some interneurons act as gates that control whether a peripheral input reaches motoneurons. Gating can be achieved directly also by descending fibers acting presynaptically on the terminals of afferent fibers to produce presynaptic inhibition (Rudomin, 1999). The excitatory and inhibitory inputs onto motoneurons also allows for the possibility of a change in the sign of reflex action from excitatory to inhibitory or vice versa (Jankowska, 1992). An inhibitory stretch reflex of a tensed muscle will decrease its stiffness since its activation decreases when the muscle is stretched. Reflexive stiffness reduction also occurs in the case an antagonistic muscle is excited when the agonist stretches. This is called reciprocal excitation.

The fastest reflex pathway is the monosynaptic excitation of alpha-motoneurons by Ia afferent fibers. This excitation is distributed to motoneuron pools which are close synergists at the same joint, as well as synergistic motoneurons at neighboring joints (Kandel et al., 2000). In parallel with the monosynaptic excitation of alpha-motoneurons, activity of Ia afferents also causes reciprocal inhibition of alpha-motoneurons of antagonist motoneuron pools. This inhibition is mediated by a class of interneurons known as Ia inhibitory interneurons (Rudomin, 1999). In the stretch reflex, Ia inhibitory interneurons mediate the reciprocal inhibition that coordinates the actions of opposing muscles. As one muscle contracts, the other relaxes. This mode of coordination is also useful in voluntary movements where relaxation of antagonist muscles enhances speed and efficiency by allowing the agonists (or prime movers) to contract without having to work against contraction of opposing muscles.

Activation of tendon organ Ib afferents can lead to the inhibition of alpha motoneurons of the muscle of origin since there is one inhibitory interneuron in the

path. However, an excitatory effect has also been reported to enhance muscle force for leg extensor muscles that act against gravitational forces during gait. See Duysens et al. (2000) for a qualitative overview of force feedback functionality.

There are other reflex pathways, originating from cutaneous sensory afferents, that are known to play important roles in motor control. However, because cutaneous mechanoreceptors provide less accurate sensory information about position and force (along with a larger the time delay) compared to muscle spindles and Golgi tendon organs only reflex pathways involving the latter will be considered in the context of feedback control.

1.3 Posture control

Human posture control is the maintenance of a specific desired position of the body in 3D-space. From a control theoretical point of view, the CNS acts as a regulator to suppress disturbing forces that displace the body segments from the intended position. The CNS regulator requires information about the actual state of the neuromusculoskeletal system for comparison with the desired reference states for subsequent determination of the appropriate corrective muscle forces. It depends on the amount of degrees of freedom which sensors are effective. For whole body stance control many different sensory information channels are useful like visual, vestibular and muscle spindle feedback (Van der Kooij et al., 1999). For arm posture tasks, visual and muscle spindle feedback sensory signals are effective to suppress exogenous disturbing forces. Experimental studies on muscle spindle responsiveness to different local stimuli and whole body functioning support this property (Brouwn, 2000; De Vlugt et al., 2001; Schouten et al., 2001). The role of golgi tendon organs has not been studied still. A possible function proposed by Rozendaal (1997) is that feedback of muscle force increases the bandwidth of the activation dynamics, i.e. making the muscle respond faster to motoneuron excitation. On its own, this is an elegant theory albeit that there is a secondary effect to it, namely that force feedback drastically decreases the mechanical resistance (i.e. the effect of muscle stiffness and viscosity) which is not beneficial for the maintenance of posture.

Characteristic to feedback control loops in general is the existence of a circular information flow from sensors to effectors (muscles) to payload (skeleton) to sensors and so on. The benefit of feedback systems is their self-regulatory property. If not properly adjusted, these feedback systems might become instable by showing a progressive increase or oscillation of the signals inside the loop. Instability occurs when the loop gain (traveling once around) is larger than one and the loop phase shift is smaller (more negative) than -180 degrees. Figure 1.7 shows a blockscheme that illustrates the feedback configuration of human arm posture control. Derivatives of this basic scheme are used throughout this thesis.

Time delays from neural transportation to, from and through the spinal cord are the major threats to stability since they introduce an increasing phase lag with frequency. Consequently, at higher frequencies fast control using spinal feedback pathways ($\pm$ 30-40 ms for arm muscles) is more effective than control via slower

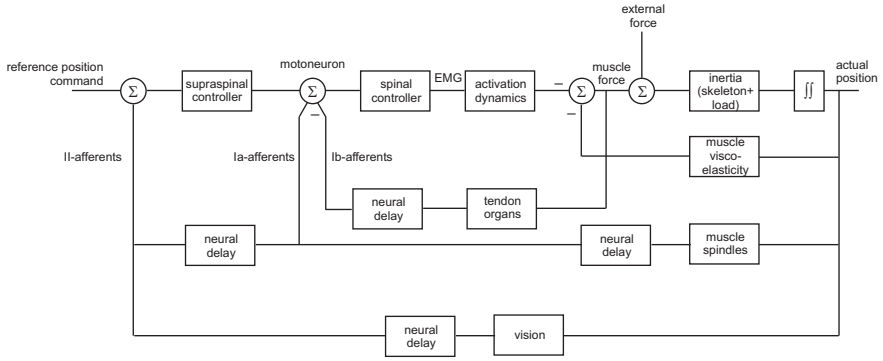

Figure 1.7: *Human arm posture control scheme. The reference position is an encoded neural representation in the higher nervous centra that provides a setpoint to the outer feedback loop. In the outer feedback loop sensory information of the actual arm position is provided by the muscle spindles (ascending pathways, e.g. from slow II afferents) and the visual system. Difference between the actual and reference position are amplified (or attenuated) by supraspinal control and send downwards to command the spinal motoneurons. A subsequent similar comparison is performed at motoneuron level based on force feedback from golgi tendon organs (Ib spinal afferents) and position feedback from muscle spindles (Ia spinal afferents). The spinal controller produces the excitation signals (EMG) that activate the muscles such that the displacements resulting from the external force disturbance are counteracted.*

supraspinal pathways ($\pm$ 60-120 ms). Other contributions to phase lagging come from the activation dynamics, intrinsic muscle viscosity and inertias of the skeleton and possible external attached loads. The effective frequency range for stable control is called the bandwidth of the closed loop. Typically, the spinal feedback loops of the shoulder joints have an average bandwidth of 2.5 Hz, depending on intrinsic and reflexive properties and the configuration of the joints (Rozendaal, 1997). For comparison, the bandwidth of the supraspinal visual feedback loop is $\pm$ 1.0 Hz (McRuer and Jex, 1967). For posture control, high feedback gains are desired for disturbance suppression which at the same time can lead to instable behavior. Stability is the constraint for successful control which the CNS has to preserve. This leads to the concept of optimal control where the control facilities of the CNS (feedback settings, muscle contraction, joint angles) are utilized to obtain a desired and sufficiently stable system behavior.

1.3.1 Optimal control

A functional approach towards understanding the concept of human movement control is the idea of optimal control. Optimal in the broadest sense means the best performance (goal) at the lowest effort (costs). A frequently used explicit function of performance is the minimum average jerk (third power) of the hand position

over time (Hogan et al., 1987). Stroeve (1999) implemented minimum jerk weighted against a cost function with muscular activation terms to learn a neural network during continuous external force disturbances. It was found that the arm stiffness was primarily determined by reflexive feedback from muscle spindles whereas the arm viscosity was to a large extent due to intrinsic muscle contraction. The drawback of the minimum jerk function is that it puts relatively large emphasis on fast movements which can only be controlled stably by intrinsic muscle visco-elasticity.

Another performance measure is related directly to the dynamical properties of the whole arm, i.e. the relationship from external force disturbance (input) to the hand position (output), and is called the endpoint admittance. The lower the admittance the more the effect of external disturbing forces is suppressed. The endpoint admittance is the only appropriate description of the arm during posture maintenance as it represents the arm as a position controller. More or less, each subsystem in the position control loop effects the endpoint admittance. Apart from a good performance measure, admittance is therefore the key entrance to obtain the underlying properties of the NMS system. Rozendaal (1997) optimized a two degree-of-freedom (DOF) arm model on the assumption that the endpoint admittance is always critically damped. A general variant of the endpoint admittance is used in recent 1-DOF and 2-DOF model studies based on the minimization of the variance (related to the second power) of the hand position (De Vlugt et al., 2001; Schouten et al., 2001). Minimization of the variance was shown to be similar to the minimization of the admittance equally at all frequencies. Instead of a cost function, stability was taken as the constraint. It was predicted that reflexive length and velocity feedback from muscle spindles were substantial and always resulted in boundary stable behavior. These results were comparable to those obtained by Stroeve (1999) and to a similar experimental study by (Van der Helm et al., 2002), suggesting that the CNS optimizes the endpoint admittance only over the frequencies included in the force disturbance.

1.4 Experimental approach

In the last three decades many different in vivo experimental studies have been performed to retrieve the control properties of the human arm subserving the maintenance of posture. All studies used some kind of mechanical perturbation signal (transient or continuous) that was applied at the hand and derived neuromuscular properties from the analysis of the response. Most of the time these studies concerned the control of singles joints (wrist, elbow, ankle, knee) and less frequently multiple joints were studied. All studies can be divided roughly into two categories (see Table 1.1 and Abbink (2001) for a complete literature overview).

The first category comprises studies that imposed continuous position perturbations (noise-like signals) while subjects were requested to maintain a mean constant force amplitude (Kirsch et al., 1993; Cathers et al., 1999; Kearney et al., 1997; Zhang and Rymer, 1997; Mirbagheri et al., 2000, 2001; Perreault et al., 2001; Perreault, 2002). These studies can be divided into two categories. The ones that mea-

Table 1.1: *Combinations of task and type of mechanical perturbations used in previous studies to identify the control properties of the human arm. For each combination, the effectiveness of the human controller parts for posture maintenance is given.*

	Perturbation type	
Task	Position	Force
Position	Unfeasible, endpoint admittance has no influence on imposed position	Small endpoint admittance (high resistance) is desired. Beneficial usage of: - intrinsic muscle visco-elasticity - feedback from muscle spindles
Force	High endpoint admittance (low resistance) is desired. Beneficial usage of: - minimal intrinsic visco-elasticity - possibly force feedback from Golgi tendon organs	Unfeasible, endpoint admittance has no influence on imposed (pure) force

sured the global admittance at endpoint without further analysis of the underlying control system. The others that used quantification methods that basically rely on neuromuscular models (i.e. a-priori knowledge) and optimization algorithms to minimize the difference between measured and predicted variables. From these latter studies, quantitative measures of the reflexive system were obtained. However, the main argument against the usage of position perturbations is that any corrective control actions by the CNS has no effect on the hand position since movement is imposed by a manipulator rather than being the result of the human controller. The estimated properties of the muscle spindle reflexive system are therefore hard to interpret with respect to functional motor tasks (bottom left in Table 1.1). Therefore, position perturbations are not appropriate to study the stabilizing properties of intrinsic and reflexive mechanisms that are essential for posture maintenance.

Alternative to continuous position perturbations, transient (step, pulse) displacements were often used (Mussa-Ivaldi et al., 1985; McIntyre et al., 1996; Stein and Kearney, 1995; Tsuji et al., 1995). In contrast to the reaction to the perturbation in the case of continuous perturbations, transients reveal the state of the NMS system just before the onset of the perturbation. In most of these studies, subjects were asked 'not to intervene voluntarily' with the perturbation. From the responses of the reaction forces or EMG recordings, qualitative measures about the timing of reflexive activity was derived. Some studies derived the static stiffness was the ratio of the change in force and position after transient effects were vanished. In another study, even the damping and inertia of the whole arm were derived from the transient position and force signals (Dolan et al., 1993). The drawback of using transients is that voluntary actions can not be fully excluded. Right from the onset of the perturbation humans will more or less react which might induce changes in the

reflexive system. Reactions to the perturbation and voluntary interventions coexist which lead to ambiguous results.

The only proper condition required to analyze posture control is the usage of continuous force disturbances in combination with position tasks, which are most natural for the study of posture maintenance (top right in Table 1.1). Force disturbances allow the position to be controlled by the human. By increasing the mechanical resistance of the arm, the displacements that result from the force disturbances can be reduced. Intrinsic muscle visco-elasticity and reflexive feedback from muscle spindles are perfectly suited for this task.

It is difficult to distinguish between the intrinsic and reflexive components of human arm dynamics during postural control. Many disturbance experiments have been reported that hypothesized the role of stretch reflexes. Whereas the intrinsic mechanics of muscles are reasonably known, reflex dynamics are not. A well-known variability of the stretch reflex is the increase in reflex activity with muscle activation level (Matthews, 1986; Kirsch et al., 1993). Other experiments with isolated cat hindlimb muscles demonstrate that reflexive muscles have different force-length (stiffness) characteristics compared to de-afferented muscles (Feldman and Orlovsky, 1972; Nichols and Houk, 1976; Hoffer and Andreassen, 1981; Shadmehr and Arbib, 1992). The reflexive contribution to postural control has been quantified by the reflexive EMG activity as a response to disturbances, by H-reflexes and by the mechanical behavior, i.e. the change of stiffness and viscosity.

EMG is the most often used source of information about reflex activity. Significant EMG activity has been measured during step-like disturbances, which is attributed to stretch reflex mechanisms (Crago et al., 1976; Lacquaniti et al., 1982; Carter et al., 1990, 1993). Agarwal and Gottlieb (1977a) perturbed the ankle joint and suggested that the stretch reflex mechanism plays an important role for sinusoidal torque disturbances within the 5-8 Hz region, where ankle rotation becomes strongly resonant. However, EMG is a combination of reflex activity and other influences, like voluntary actions (Crago et al., 1976). Moreover, the EMG to force relation is also affected by the muscle length and contraction velocity. It is difficult to estimate the contribution of reflex activity to the mechanical behavior using EMG only.

A second technique to quantify the amount of reflex activity is the use of H-reflexes (Toft and Sinkjær, 1993). A nerve is stimulated, and the relative magnitudes of the direct EMG response and indirect, reflexive EMG response are assumed to show the loop gain of the reflexive pathways. However, many afferent pathways from skin sensors, Golgi tendon organs and muscle spindles are likely to project on the α-motoneurons, some with excitatory and some with inhibitory connections. Stimulating the nerve results in stimulation of many of these pathways, and the resultant EMG response will be a summation of the strength of the combined afferent pathways. The specific mechanical stimulus for each of the pathways (e.g. force, position, velocity) is not taken into account, and therefore the mechanical meaning of the H-reflex response is not clear.

1.4.1 Force controlled manipulators

The generation of force disturbances requires devices that must be strong enough to transmit sufficient mechanical power to the human on the one hand and lightweight to add the least payload to the human arm on the other hand. The payload or the dynamical properties that are apparent to the human at the point of contact are referred to as the virtual dynamics of the manipulator. If the virtual dynamics would be substantial (i.e. large virtual mass, damping or stiffness) it had large disturbance suppressing effect. Consequently it would (partly) take over the posture task that was meant to be performed by the human. The contradicting requirements (strong and virtually compliant) oblige the usage of lightweight stiff materials and fast powerful actuators. A haptic device, called the ARMANDA manipulator, that satisfies these principle design specifications has been build for the purpose of posture control analyses in the horizontal plane of movement (Chapter 6). Haptic refers to the sense of touch providing the subject the experience as if they were moving real physical objects. The virtual dynamics it represents at endpoint was realized by using force control. This means that a virtual trajectory was determined on-line from the force applied by the subject to the manipulator, as being measured by force transducers at the point of contact. Then, the actuators of the manipulator were controlled in such a way that the reference trajectory was followed. These force controlled haptic devices can be used perfectly to impose force disturbances for identification purposes by simply superimposing a self generated signal to the measured force generated by the subject. Force controlled manipulators are therefore highly valuable for the identification of the movement system during natural tasks in realistic environments.

Over the last ten years, haptic control gained an increased attention for many different fields of application such as virtual surgical training (needles in biological tissues), movement rehabilitation (gentle movement assistance) and master-slave application (manual control of a remote plant). In contrast to the purpose of identification, these latter applications are all based on human induced motions that do not require high power transmission from the device to the human. This difference made the ARMANDA manipulator the first force controlled device build for studying the human movement system.

1.4.2 System identification

Nonparametric identification

In the case of posture control where the position deviations are small, linear signal decomposition and system identification techniques can be applied. The main advantage of linear techniques is that analytical descriptions of system behavior can be obtained from the measured signals, like frequency and impulse response functions. Linear techniques are widely developed in the broad field of system identification. Basically, system identification can be divided into two different approaches. The first is to obtain explicit descriptions of the global input-output behavior and is often a first step of identifying a system. This approach is referred to

as non-parametric identification, as it obtains descriptive transferfunctions without requiring apriori physical knowledge.

Frequency based techniques that obtain frequency response functions (FRFs) from measured spectral densities are fast and easy to implement. Complementary time domain methods computing the impulse response functions can also be used. However, time signals do not directly give insight into the dynamical aspects of the system (e.g. oscillation frequency, relative damping, time delays etc.) which can directly be visualized from FRFs. Another method to identify FRFs is by using subspace techniques. In this case the global structure in which underlying mechanisms contribute to the overall (measurable) input-output behavior has to be determined and approximated by a model of sufficient order (the subspace) from which the empirical data is to be explained. Subspace methods are available in many different forms, basically distinguished by the algorithms used to determine the order of the subspace from the measured signals. These methods are generally referred to as parametric identification techniques.

A determining factor to the usage of any identification technique is the presence of feedback loops in the system of concern. If feedback loops exist, as generally is the case in NMS systems, a measured signal from inside the feedback loop acts as both an input and an output simultaneously. It then depends on the amount of noise and the location at which the noise enters the closed loop if the right subsystem is identified (Kearney and Hunter, 1990). Special closed loop identification methods solve this problem by making use of relationships between measurements from inside the loop and an independent perturbation signal from outside the loop.

Parameter estimation

The second approach to identify a system is the estimation of certain properties of the system that are known to be present, based on apriori knowledge of the system. Properties that are relevant to know in this context are joint stiffness and viscosity, feedback gains, time delays etc.

There are two ways to quantify system properties. The first is a rather trivial and that is to include additional measurements of signals that are closer related to the mechanism of interest. Nonparametric (or parametric) identification onto these additional measurements results in more detailed input-output descriptions. The other way is to include a-priori knowledge from physics in order to develop a parametric descriptive model that includes the properties aimed for, comparable to the model as shown in Figure 1.7. Such a model can be fitted onto the identified input-output (non)parametric models to gain the parameters. This step is referred to as physical parameter estimation.

1.5 Goal of the thesis

The prime goal of the thesis is to provide insight into the functionality of reflexive mechanisms subserving human arm posture control. To reach this goal, experimen-

tal and analytical techniques are developed to identify the role of the intrinsic and reflexive mechanisms separately in vivo, based on their contributions to the mechanical behavior of the human arm. In addition, the nature of the reflex system is to be quantified in terms of position, velocity, acceleration and force feedback.

Different experimental conditions were to be designed in order to provoke variation of the reflexive system. These were a) the properties of the disturbance signal, b) the properties of the environment and c) the configuration of the arm joints. The results will be explained from basic control theory using model simulations and optimizations.

1.6 Lay-out of the thesis

With the exception of Chapter 1 (Introduction) and Chapter 8 (General discussion), the chapters are written as autonomous papers and thus can be read independently.

In **Chapter 2**, The goal if this study was to examine if the reflex system of the shoulder adapts to the properties of the environment. In the experiment subjects were asked to maintain their hand at a predefined position while continuous forces were applied to the hand. For this purpose a 1-DOF force controlled haptic manipulator was used of which the apparent damping and mass were varied. As a consequence, the stability margins varied and it was investigated if the CNS takes advantage of these changes. The forthcoming results are important to understand the flexibility of the CNS in modifying the combined mechanical properties of the arm and environment.

Nonparametric frequency response functions (FRFs) were estimated from the measured hand position and hand reaction force describing the mechanical endpoint admittance. Onto the admittance a model of the NMS system was fitted to obtain intrinsic and reflexive parameters. Model optimizations were performed to find out if the estimated reflexive feedback could be explained from a trade-off of performance against feedback control effort.

In **Chapter 3**, To improve the parameter estimation, the reflexive impedance was incorporated in the estimation procedure in addition to the mechanical admittance. Reflexive impedance is the dynamic input-output relationship between hand position and muscle activation. The latter was measured by electromyography (EMG). The NMS model used for parameter estimation was improved by inclusion of a second order model for the activation dynamics and an additional acceleration term in the muscle spindle feedback model. The merits of the reflexive impedance is that it facilitates the estimation of the time delay involved in the short latency reflex pathway and that no assumptions regarding intrinsic and reflexive properties had to be made, which had to be included a-priori in the previous experiment.

In **Chapter 4**, the effect of different disturbance signals and task instructions on the settings of the reflexive feedback properties were investigated. Based on their sensing abilities it was hypothesized that muscle spindles are dominant during position tasks while golgi tendon organs (GTOs) are dominant during force tasks. Subjects performed two types of tasks that were randomly ordered. The first was

to minimize their hand displacements (position task) and the second was to maintain a mean pushing force level (force task). Force perturbations were used in the case of the position task and position perturbations were used in the case of the force task. Additionally, while remaining the task the same the type of perturbation was changed (from positing to force or vice versa) to investigate if the NMS reacts to type conflicts between task and perturbation signal.

Chapter 5 marks the breakpoint from the previous one degree-of-freedom (1-DOF) to multi-DOF studies. The previous single joint studies have contributed to the fundamental understanding of neuromuscular functioning. However, single joint motions are rare under normal physiological conditions and do not provide the opportunity to study the complex interactions between joints that are typical of normal motor functioning. Multiple DOF movements are more natural and provide a richer field of study. In the case of posture control, multiple DOF facilitates the modification of the endpoint admittance in different directions. This directional property of multijoint control is beneficial when resistance in one specific direction is required. In this chapter, a nonparametric identification technique is developed to estimate the multivariable endpoint admittance. Its application and performance are described in the case study of estimating a two-by-two endpoint admittance.

In **Chapter 6**, the utilization and performance of the newly developed 2-DOF ARMANDA manipulator is described. This highly accurate force controlled manipulator uses an admittance based controller that requires a fast inner position servo controller. Difficulties that raised from this control scheme are explained and a systematic approach was taken to optimally adjust the control gains. The final performance was validated using different technical loads and its application was demonstrated by identification of the planar (2-DOF) endpoint admittance FRF of the human arm.

In **Chapter 7**, it was investigated how the reflexive system in the multiple DOF case adapts to different external conditions. Therefore, parameters of the human arm in 3-DOF joint space (shoulder, elbow, wrist) were quantified, using the ARMANDA manipulator, a parametric closed loop identification technique and a large scale NMS model. Movements of the arm were constrained to horizontal plane of movement while perturbations were applied in two orthogonal directions. Despite the kinematic mapping from endpoint position to joint angles is not unambiguous, consistent (dynamical) parameter values were found between subjects. Apart from intrinsic muscle properties and reflex gains (muscle spindles and GTOs), important additional properties were quantified such as the cut-off frequencies of the activation dynamics and neural time delays from feedback pathways of different muscles groups.

Chapter 8 discusses the experimental and analytical techniques and the main experimental findings. Research topics for future directions are indicated.

Chapter 2

Adaptation of reflexive feedback to different environments

Erwin de Vlugt, Frans C. T. van der Helm, Alfred C. Schouten
Biological Cybernetics 2002; 87: 10-26

In this study we have examined the ability of the central nervous system (CNS) to use spinal reflexes to minimize displacements during postural control while continuous force perturbations were applied at the hand. The subjects were instructed to minimize the displacements of the hand from a reference position that resulted from the force perturbations. The perturbations were imposed in one direction by means of a hydraulic manipulator of which the virtual mass and damping were varied. Resistance to the perturbations comprised intrinsic and reflexive stiffness and by the virtual environment. It is hypothesized that reflexive feedback during posture maintenance is optimally adjusted such that position deviations are minimal for a given virtual environment.

Frequency response functions were estimated, capturing all mechanical properties of the arm at endpoint (hand) level. Intrinsic and reflexive parameters were quantified by fitting a linear neuromuscular model to the frequency responses. The reflexive length feedback gain increased strongly with damping and little with the eigenfrequency of the total combined system (i.e. arm plus environment). The reflexive velocity feedback gain decreased slightly with relative damping at the largest eigenfrequency and more markedly at smaller eigenfrequencies. In case of highest reflex gains, the total system remained stable and sufficiently damped while the responses of only the arm were severely underdamped and sometimes even unstable.

To further analyze these results, a model optimization was performed. Intrinsic and reflexive parameters were optimized such that two criterion functions were minimized. The first concerns performance and penalized hand displacements from a reference point. The second one weights afferent control effort to avoid inefficient feedback. The simulations showed good similarities with the estimated values. Length feedback was adequately predicted by the model for all conditions. The

predicted velocity feedback gains were larger in all cases probably indicating a mutual gain limiting relation between length and velocity afferent signals. The results suggest that both reflex gains seemed to be adjusted by the CNS where in particular the length feedback gain was optimal as to maximize performance at minimum control effort.

2.1 Introduction

Human posture control is basically characterized by minimization of position deviations from a reference position. In most cases, these deviations result from external force perturbations acting upon the body. Formalizing the body as a system excited by forces and reacting with corresponding movements, it is appropriately described as a mechanical admittance (dynamic relation between an input force and an output position). Low admittance (large stiffness and damping) results in high resistance to perturbations. Admittance reduction during posture maintenance can be realized by two mechanisms: (1) co-contraction and (2) afferent feedback. Co-contraction increases intrinsic muscle stiffness and damping at the expense of metabolic energy. Afferent length and velocity feedback from muscle spindles can further increase stiffness and damping. Since reflexive feedback introduces phase lags due to inherent neural time delays, its effectiveness is limited in avoiding oscillations.

The ability of the central nervous system (CNS) to specifically adjust length and velocity reflex gains to correct for displacements has been demonstrated in previous studies for the whole arm or segments of it (Bennett et al. 1993; Doemges and Rack 1992a,b; Dufresne et al. 1978; Hogan 1985; Lacquaniti and Soechting 1986).

Compared to constant contraction, the usage of reflexive feedback is energy efficient because muscles are only activated when stretched. Therefore it is hypothesized that under conditions where force perturbations are present or expected, reflex gains are modulated such that the arm admittance is decreased and the resulting position deviations are minimized.

In Van der Helm et al. (2002) the human arm was disturbed with stochastic force perturbations having different frequency content. For small bandwidth perturbation that did not excite the eigenfrequency of the arm ($\pm$ 3 Hz), the reflex gains were substantial. With increasing bandwidth of the perturbation the gains decreased to avoid oscillations around the eigenfrequency. This is because oscillations worsen performance. In nearly all cases, the estimated gains led to boundary stable solutions of the model indicating that performance was always close to optimal.

A model study by De Vlugt et al. (2001) demonstrated that the experimental feedback gains were nearly optimal. Schouten et al. (2001) used a two degree-of-freedom (2-DOF) musculoskeletal model with six muscles, including non-linear actuator and sensor dynamics, to simulate the experiments. It was demonstrated that under these particular experimental conditions (small position deviations) linearization of the neuromuscular system was appropriate. Again, reflex gains were

found to be substantial and directly determined by the task requirements and stability constraint indicating that control effort weighting played a minor role under the experimental conditions.

When the arm is physically attached to an environment (manipulator) the total combined admittance is the parallel connection of arm admittance $H_{arm}(s)$ and admittance of the environment $H_e(s)$ (called the environmental admittance), Fig. 2.1. All system descriptions will be expressed in the frequency domain with $s = \lambda + j2\pi f$ ($\lambda = 0$ because the initial transient response is not of interest). The relation between force and position is:

$$D(s) = \left(H_{arm}^{-1}(s) + H_e^{-1}(s)\right) X(s) \tag{2.1}$$

with $D(s)$ the force disturbance and $X(s)$ the common position of hand and environment, such that the combined admittance $H_{DX}(s)$ with force as the input (causal form) becomes:

$$H_{DX}(s) = \frac{X(s)}{D(s)} = \frac{H_{arm}(s)H_e(s)}{H_{arm}(s) + H_e(s)} \tag{2.2}$$

The performance and stability are now determined by the mechanical properties of the combined system. Changing the properties of the environment evidently changes the effect of the arm admittance on the combined (total) behavior. The combined admittance is dominated by the system having the lowest admittance (Eq. 2.2). Milner et al. (1993) demonstrated the influence of an unstable environment on reflex feedback from wrist muscles. They attached the wrist to a manipulator of which the damping was negatively increased causing the relative damping of the combined system to decrease. It was demonstrated that reflexive feedback was reduced when external damping became more negative. These reflex gain adjustments are in accordance with the role of the CNS as being an optimal controller: decreasing the relative damping of the combined system reduces the stability margins such that reflexive feedback must be tempered to prevent oscillations. In the afore mentioned studies, stability was always a constraint to the adjustments of reflexes. When the admittance of the environment decreases, thereby increasing the stability margins, the question arises whether the CNS makes use of these favourable conditions? More specifically: does an increase in damping of the environment result in higher reflexive feedback? And, if so, is there still a constraint (when stability is not anymore) like a control effort weighting to reflex gain adjustment for these conditions?

The goal of this study is to demonstrate the modulation of reflexes of the arm when external admittance decreases. For this purpose, experiments were performed using a number of relative damping ratios and eigenfrequencies of the combined system in order to investigate the effect on reflex gains. The experimental results are compared with optimizations of a lumped linear model including control effort weighting.

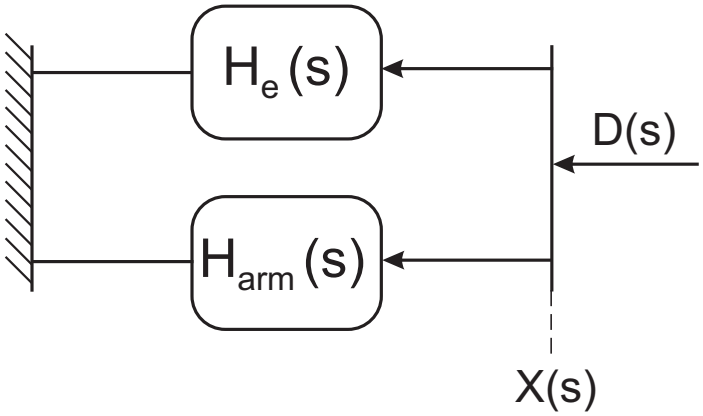

Figure 2.1: *Schematic configuration of parallel coupling of arm admittance $H_{arm}(s)$ and environmental admittance $H_e(s)$ (m/N). The combined admittance is the dynamic relation between the force disturbance $D(s)$ and endpoint (common position of hand and environment) $X(s)$, where $X(s)$ represents the displacements between the endpoint and the fixed world.*

2.2 Materials and Methods

2.2.1 Subjects

Five normal healthy subjects (three men, two women, ranging in age from 20-26 years) participated voluntarily in this study. They had no history of musculoskeletal or neurological disease. The experiments were carried out with the right arm. All the subjects gave their informed consent to the experimental procedure.

2.2.2 Apparatus

A linear hydraulically driven manipulator was used to generate force perturbations on the hand in horizontal directions. Between the handle and the piston of the manipulator a load cell is mounted to measure the hand force applied by the subject to the manipulator. This force is electronically translated into a movement corresponding to a (virtual) environmental admittance consisting of a linear second order mass-damper-spring combination. Its values can vary between $0.6-20$ kg for the mass m_e, $0.6-400$ Ns/m for the damping b_e and $0.1-250$ N/m for the stiffness k_e. The position of the hand results from the force input and the environmental admittance. This position is imposed on the subject by the position control loop of the manipulator. Force perturbations are imposed by adding an external input signal to the measured hand force.

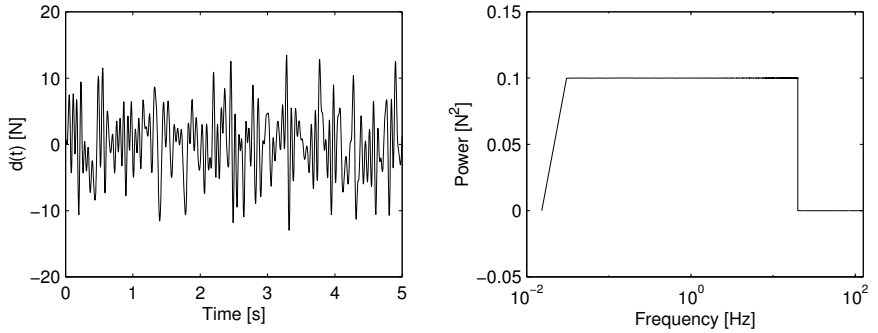

Figure 2.2: *Left: 5 s. sample of the force perturbation $d(t)$. Right: power spectrum of $d(t)$.*

2.2.3 Force perturbation

The force perturbation was the same throughout all the experiments containing frequencies between 0.05-20 Hz. The perturbation signal was generated off-line in the frequency domain, such that within the bandwidth the power has a constant value, whereas the phase is chosen as a random value with a uniform distribution between 0 and 2π rad. The result is transformed to the time domain by Inverse Fourier Transformation. The duration of each perturbation was limited to 40 seconds, a sufficient observation time without causing significant fatigue. Figure 2.2 shows a 5 second sample of the time course of the force perturbation together with its power spectrum. As a result of the random distribution of the phases, the signal was stochastic and unpredictable for the subjects. The signal was passed through a D/A converter with a reconstruction frequency of 125 Hz and applied as input to the manipulator. By adjusting the power of the force perturbation, the hand displacements were kept sufficiently small ($\pm$ 1 cm amplitude in all cases) to justify linear model approximation.

2.2.4 Recording

The following signals were measured via A/D conversion with 12-bit resolution at 500 Hz sample frequency and digitally stored: hand position $x_h(t)$, interaction force $f_h(t)$, external force perturbation $d(t)$ and four EMG signals. EMG was measured using differential electrodes, pre-amplified, highpass filtered (20 Hz, third order Butterworth), amplified, rectified and smoothed at 200 Hz (lowpass, third order Butterworth).

Surface EMG was used to validate the estimated cocontraction level. Activation of four relevant muscles around the shoulder were measured, being for the anteflexors: m. pectoralis major (pars clavicularis) and m. deltoideus anterior; and, for the retroflexors: m. deltoideus posterior and m. latissimus dorsi.

Since only stationary behavior was of interest, initial transient effects were elim-

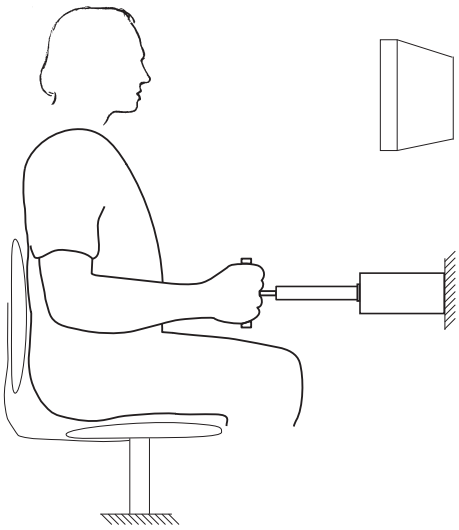

Figure 2.3: *Experimental setup showing the subject sitting upright on a chair with back support, holding the handle mounted on the piston of a hydraulic actuator. The interaction force generated by the subject on to the handle was measured by a force transducer in between the handle and the piston. The actual and reference handle position were displayed on a monitor in front of the subject.*

inated by rejecting the first 3616 samples ($\approx$ 7 sec.) from each time record, leaving 16384 ($= 2^{14}$) samples for further analysis.

2.2.5 Experimental procedures

The subject was seated in a chair (Fig. 2.3) and asked to take a firm grip on the handle in order to minimize movements of the handle with respect to the hand. The motion of the hand was constrained by the manipulator to move only in anterior-posterior direction (shoulder and elbow rotations were dependent). The forearm was horizontally aligned with the piston and the elbow was 90 degrees flexed such that the upper arm was vertically aligned. This is referred to as the reference position. In order to minimize movement of the shoulder rotation center, the subjects were asked not to move their trunk. The task given to the subjects was 'minimize displacements' resulting from the the applied force perturbation. To prevent drifting, the actual hand position was presented to the subject on a display together with the reference position. The subjects were also motivated by the display, since increased effort resulted in visibly smaller displacements.

Afferent feedback from muscle spindle activity was most likely to be inhibited when wide bandwidth (0.05-20 Hz) force perturbations were applied in the case

of a high admittant environment, with $m_e = 0.6$ kg, $b_e = 0.6$ Ns/m, $k_e = 0.1$ N/m (Van der Helm et al. 2002). This result can be explained from the optimal control perspective: high feedback gains result in severe underdamped responses that would violate performance. This experimental procedure is repeated in this study to determine the intrinsic properties of the subject's arm (lumped endpoint mass, damping and stiffness) by fitting an intrinsic model to the estimated arm admittance (Sect. 2.2.7) using a straight forward least squares method in the frequency domain.

Based on the intrinsic properties of the arm, the damping of the environment (manipulator) was adjusted such that the relative damping, β, of the combined intrinsic system, i.e. intrinsic arm plus environment, was assigned fixed values of 0.7 (critical), 1.0, 1.3, 1.6, and 1.9 (all overdamped).

Furthermore, three different values for the external mass m_e were taken, being 0.6, 5 and 10 kg. These values were the same for all subjects. The external stiffness was not changed and remained always at a minimum ($k_e = 0.1$ N/m). The eigenfrequency of the combined (intrinsic) system, f_{0_i}, then follows from the combined mass and stiffness.

For each eigenfrequency all values for relative damping were applied, resulting in fifteen different environmental mass-damping (MB) combinations. Three additional conditions were employed for each eigenfrequency in combination with minimal external damping ($b_e = 0.6$ Ns/m). These conditions represent the lowest attainable relative damping possible with the present equipment and will elicit human control behavior under highly underdamped conditions. For each subject, this makes a total of eighteen MB-combinations of relative damping and eigenfrequency applied. The order in which the combinations were applied to the subjects was randomly distributed to avoid any anticipation. Each condition was repeated four times to improve the estimates by time averaging. This made a total of 72 trials. In between trials, subjects were free to rest as long as they liked. The complete experiment lasted approximately three hours for each subject.

For each MB-combination reflexive length and velocity feedback gains were estimated according to a comparable procedure as used to obtain the intrinsic parameters. For this purpose, the intrinsic model was extended with a length and velocity reflex loop. Together with the reflexive parameters, intrinsic stiffness and damping were estimated by means of one value representing the amount of cocontraction that scales the intrinsic stiffness and damping values estimated under the highest admittance condition (see also Appendix A.1).

2.2.6 Spectral analyses

The combined system is perturbed by the independent external force perturbation signal $d(t)$. The measured hand reaction force $f_h(t)$ and hand position $x_h(t)$ are dependent signals inside the closed loop. The admittance of arm and combined system were non-parametrically estimated in the frequency domain, expressed as frequency response functions (FRFs). The estimator for the admittance of the com-

bined system is:

$$\hat{H}_{DX}(f) = \frac{\hat{G}_{dx}(f)}{\hat{G}_{dd}(f)} \tag{2.3}$$

with $\hat{H}_{DX}(f)$ the estimated admittance of the combined system (arm plus environment). $\hat{G}_{dx}(f)$ is the estimated cross spectral density between force perturbation, $d(t)$, and hand displacement, $x_h(t)$, and $\hat{G}_{dd}(f)$ the estimated auto spectral density of $d(t)$. The spectral densities were obtained using the Fast Fourier Transformation (FFT) of the corresponding time signals (Van Lunteren 1979).

To verify the usage of linear models, the coherence function is estimated. This function is a measure for the amount of linearity of the system in response to the external force perturbation and is determined according to:

$$\hat{\Gamma}_{DX}(f) = \sqrt{\frac{|\hat{G}_{dx}(f)|^2}{\hat{G}_{dd}(f)\hat{G}_{xx}(f)}} \tag{2.4}$$

The coherence function $\hat{\Gamma}_{dx}(f)$ equals one when there is no noise (linearization or measurement noise), and zero in the worst case.

As the human controller is embedded in a closed-loop configuration, the estimate for the arm admittance was obtained using the closed-loop estimator:

$$\hat{H}_{arm}(f) = \frac{\hat{G}_{dx}(f)}{\hat{G}_{df}(f)} \tag{2.5}$$

with $\hat{H}_{arm}(f)$ the estimated arm admittance and $\hat{G}_{df}(f)$ the estimated cross spectral density between the external force perturbation, $d(t)$, and reaction force $f_h(t)$. In all estimators, (2.3), (2.4) and (2.5), the estimated of the auto and cross spectral densities were averaged over eight frequency points to reduce the variance (Jenkins and Watts 1969).

2.2.7 Parametric model

The intrinsic model includes arm and hand dynamics. The derivation of the intrinsic model is given in Appendix A.1. The intrinsic parameters to be estimated are: arm mass, m_a; arm damping, b_a; arm stiffness, k_a; hand grip viscosity, b_h; and elasticity, k_h. Including the hand dynamics significantly improved the estimation of the intrinsic arm parameters, especially arm mass. This is because hand stiffness and viscosity appeared to be much larger than those of the arm (Sec. 2.3) such that hand dynamics are present in the frequency range (about 10 Hz) where also the arm mass is dominant. In the following, when referring to the arm dynamics, the combined arm and hand dynamics are meant.

From the estimated intrinsic values, the MB-combinations for each subject were determined as described in Sect. 2.2.5. Only for this purpose, hand dynamics were

neglected such that the combined system can be described as a second order system that facilitates the calculation of relative damping and eigenfrequencies.

The second order dynamics of the intrinsic combined admittance $H_{DX_i}(s)$ follow from Eq. (2.2):

$$H_{DX_i}(s) = \frac{H_{arm}(s)H_e(s)}{H_{arm}(s)+H_e(s)} = \frac{1}{H_{arm}^{-1}(s)+H_e^{-1}(s)}$$

with

$$H_{arm}(s) = \frac{1}{m_a s^2 + b_a s + k_a}$$
$$H_e(s) = \frac{1}{m_e s^2 + b_e s + k_e}$$

the combined intrinsic system becomes:

$$H_{DX_i}(s) = \frac{1}{(m_a+m_e)s^2+(b_a+b_e)s+(k_a+k_e)} = \frac{1/k_{tot}}{\frac{1}{\omega_0^2}s^2+\frac{2\beta}{\omega_0}s+1} \quad (2.6)$$

where $m_{tot} = m_a + m_e$, $b_{tot} = b_a + b_e$ and $k_{tot} = k_a + k_e$ and with the eigenfrequency, f_{0_i} and β the relative damping according to:

$$f_{0_i} = \frac{1}{2\pi}\sqrt{\frac{k_{tot}}{m_{tot}}} \quad (2.7)$$

$$\beta = \frac{b_{tot}}{2\sqrt{k_{tot}m_{tot}}} \quad (2.8)$$

Substituting b_{tot} in (2.8) and rewriting it gives:

$$b_e = 2\beta\sqrt{k_{tot}m_{tot}} - b_a \quad (2.9)$$

Using the controlled values for β and the external mass m_e, the external damping b_e follows from (2.9).

To estimate the reflex gains and the amount of cocontraction, the intrinsic model was extended with a reflex loop consisting of three elements: (1) reflexive length and velocity feedback gains; (2) third order Pade approximation of neural transportation delay; and (3) first order activation dynamics (see Appendix A.2). The parameters to be estimated were: reflexive length feedback gain, $\hat{k}_p$, reflexive velocity feedback gain, $\hat{k}_v$, and cocontraction level $\hat{u}_0$ (hat denotes the values derived from the estimated FRFs).

For each set of estimated parameters $\{\hat{k}_p, \hat{k}_v, \hat{u}_0\}$ the Variance Accounted For (VAF) was calculated indicating the 'goodness of fit' of the estimated combined model (arm plus environment) to the recorded values:

$$VAF = \left[1 - \frac{\sum_{i=1}^{n}|x_h(t_i) - x_{h,sim}(t_i)|^2}{\sum_{i=1}^{n}|x_h(t_i)|^2}\right]\cdot 100\% \quad (2.10)$$

with $x_{h,sim}(t_i)$ the forward simulated hand position and $x_h(t_i)$ the measured hand position, where i indexes the time vector. The hand position, $x_{h,sim}(t_i)$, is obtained by simulations using the model of the combined system, $H_{DX}(s)$ (Appendix A.3, Eq. A.9) including the estimated parameter values and the input force disturbance $d(t)$ identical as used in the experiments.

For each MB combination, the recorded smooth EMG signals were averaged over four trials. Then, the root mean square (RMS) values were calculated. To compare variations between EMG (in mVolts) and corresponding estimated cocontraction $\hat{u}_0$, the RMS values were scaled. This scaling was such that the mean of the RMS values (for each muscle over all MB combinations and for each subject) equals the corresponding mean value of the estimates. The goodness of the estimate was represented as the difference between the scaled RMS and $\hat{u}_0$.

2.2.8 Model optimization

A model optimization was performed to asses the effect on the adjustments of reflexive feedback of: (1) the task variable (in this case the instruction to 'minimize displacements'); (2) the mechanical properties of the environment; and (3) the force perturbation. The task instruction was replaced by a performance criterion that weights displacements of the hand from the reference point. Another criterion was implemented to minimize control effort. The goal of the optimization is to minimize the combined criterion functions. The parameters to be optimized were the reflexive length and velocity feedback gains, k_p^* and k_v^* respectively (asterisks denote optimized values).

The performance criterion is formulated as:

$$J_x = E\{{x_h}^2(t)\} \tag{2.11}$$

where $E\{\cdot\}$ is the expectation operator. Because the model is expressed in the frequency domain, J_x is rewritten into its corresponding frequency form (see Appendix A.4 for derivation):

$$J_x = \int_{f_l}^{f_h} |H_{DX}(f)|^2 df \tag{2.12}$$

with $H_{DX}(f)$ the closed loop transfer function of the combined system. J_x therefore depends on the gain of the closed loop dynamics inside the input frequency range $f_l \leq f \leq f_h$. The mean estimated intrinsic values of all subjects were averaged for each MB-combination and used in $H_{DX}(s)$ (see Table 2.1). Control effort weighting was added by a criterion function J_a and similar to the performance criterion is written in its frequency form:

$$J_a = E\{a^2(t)\} = \int_{f_l}^{f_h} |H_{DA}(f)^2| df \tag{2.13}$$

with $H_{DA}(s)$ the closed loop transfer function from force perturbation $d(t)$ to reflexive activation $a(t)$ (Appendix A.3, Eq. A.11).

From (2.12) and (2.13) it is clear that the optimal closed loop behavior is determined by the frequency range of the input perturbation. Due to the performance criterion J_x, the reflex gains tend to increase, i.e. reducing the admittance $H_{DX}(f)$, while the control effort criterion $J_a(f)$ tends to limit the gains.

The parameters of the postural control model will be optimized by minimizing the summed cost function:

$$J = J_x + pJ_a \tag{2.14}$$

In addition to this cost function, the poles of the combined system $H_{DX}(s)$ were constrained to be in the left half of the complex plane to ensure stability.

Evidently, increasing the weighting factor p worsens performance and reduces control effort. One value for p was chosen for all conditions such that the optimized reflex gains were comparable in a qualitative way to the estimated ones (see Results).

The optimization is performed in the frequency domain where Eqs (2.12) and (2.13) were numerically integrated between f_l and f_h at each optimization step.

The optimization is also used to calculate the sensitivity of the estimated feedback gains to the differences between measured EMG (scaled RMS) and estimated cocontraction levels. Therefore, the model was optimized using the estimated $\hat{u}_0$ plus and minus the standard deviation of these differences.

The optimization uses a multidimensional constrained non-linear minimization method. All calculations for estimation and optimization are performed using MATLAB (The MathWorks, Inc.).

An overview of the experimental and optimization procedures performed is shown in Fig. 2.4 in the form of a flow chart.

2.3 Results

2.3.1 Experiments

The MB combinations derived from the intrinsic values for subject HB are plotted in Fig. 2.5 as an example. Every open circle in this figure represents a single condition applied. The mutually shifted square root curves indicate lines of constant relative damping (β) according to Eq. (2.9). Vertical shifted points indicate conditions with the same eigenfrequency (f_{0_i}), i.e. where the mass of the environment is the same. The additional three conditions are shown on the horizontal axis, indicating the lowest relative damping applied being 0.50, 0.32 and 0.24 for this subject.

In Fig. 2.6 the estimated gain and phase of $H_{arm}(f)$ of four extreme conditions for subject HB are shown, corresponding to the conditions indicated with large circles in Fig. 2.5. The corresponding admittances of the combined system $H_{DX}(f)$ are given in Fig. 2.7. Comparable responses were found for all other subjects.

For all conditions, the estimated mean reflex gains amongst all subjects (mean and standard deviation) are given in Fig. 2.8 where the four conditions are indicated by vertical arrows.

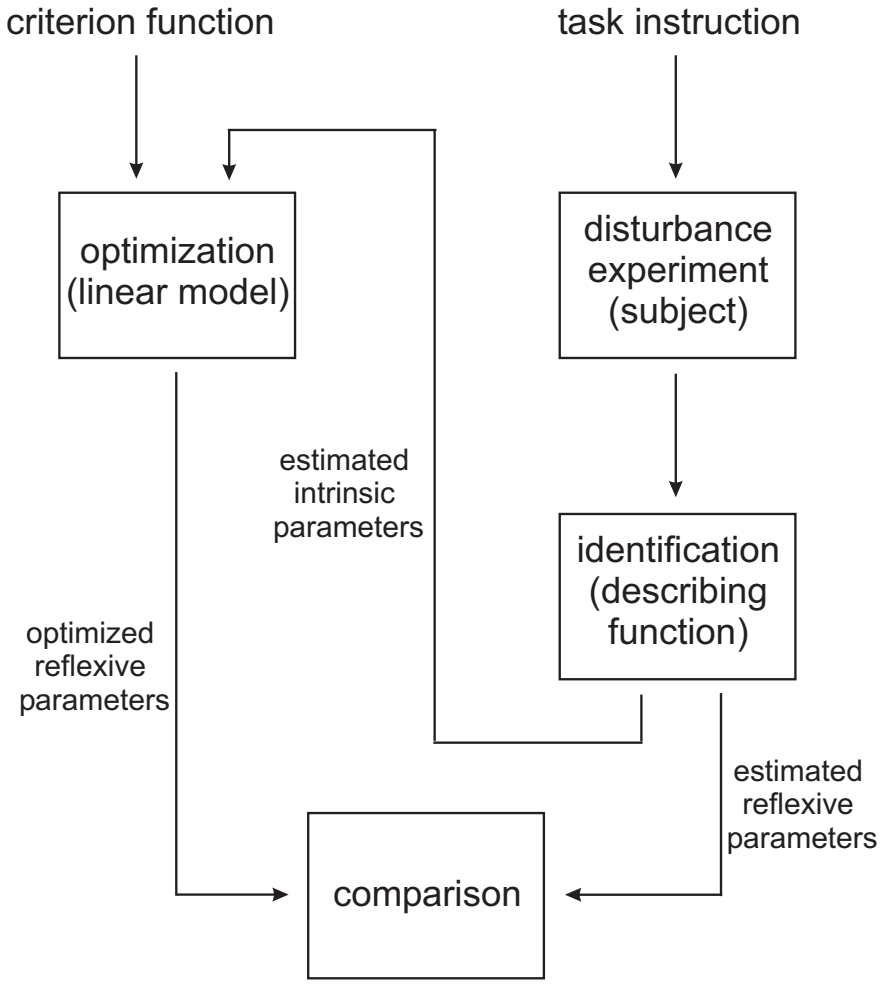

Figure 2.4: *Flowchart of the procedure followed in this study. The right path is the experimental execution with the subject taken as an optimal controller to minimize hand displacements. Its input-output behaviour (admittance) is estimated as a describing function from which lumped intrinsic and reflexive parameters were obtained by model fitting, as described in the text. Left path represents the optimization of the combined arm-environment model as to simulate the experimental procedure where the criterion function mimics the task instruction given to the subject. Optimized reflex parameters were compared with the estimated ones.*

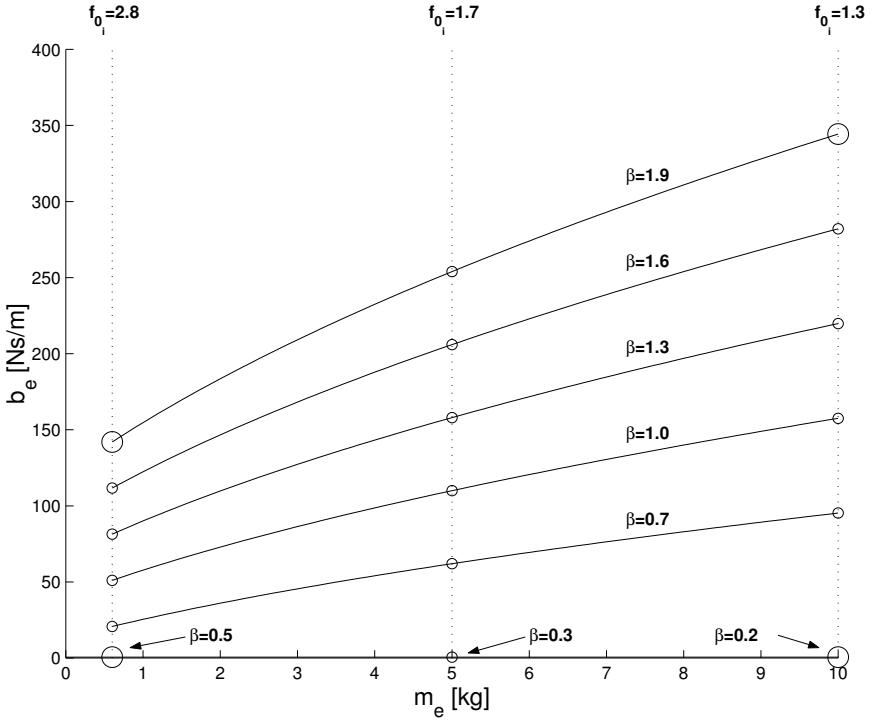

Figure 2.5: *MB combinations of parameters of the environment admittance based on intrinsic properties of subject HB, represented by open circles. Each combination is an applied experimental condition. Square root (interpolated) curves connect conditions with constant relative damping β (controlled variable) of the combined intrinsic system. Combinations on verticals have equal eigenfrequencies f_{0_i} (controlled variable) of the combined intrinsic system. Circles on the horizontal axis denote the three conditions with the lowest external damping $b_e = 0.6$ Ns/m. Large circles denote four extreme conditions (see Text). The large circle at the left on the horizontal axis denotes the condition where no reflexes were present, i.e. where the intrinsic parameters were determined.*

The left plot of Fig. 2.6 (dashed curves) shows $H_{arm}(s)$ in the case of the largest environmental admittance $H_e(s)$. From this condition the intrinsic parameters were estimated because likely no reflexes were present, as can be seen from Fig. 2.8 (leftmost arrow). Table 2.1 gives the average estimated intrinsic values among all subjects. The mean eigenfrequencies (Eq. 2.7) were $f_{0_i} = \{2.8, 1.7, 1.3\}$ Hz (see Table 2.1).

For the highest eigenfrequency, $f_{0_i} = 2.8$ Hz ($m_e = 0.6$ kg) the arm admittance showed a significant oscillation peak when relative damping is largest ($\beta = 1.9$, Fig. 2.6, *left column*, solid curves). This can be explained by an increased length feedback gain of approximately 500 N/m, which is about 75% of the intrinsic stiff-

Table 2.1: *Estimated intrinsic arm parameters and eigenfrequencies of all subjects ($n = 5$) and their standard deviation (SD).*

	Mean (SD)	Unit	Description
m_a	1.88 (0.290)	kg	arm mass
b_a	37.3 (6.30)	Ns/m	intrinsic arm damping
k_a	733 (175)	N/m	intrinsic arm stiffness
b_h	178 (45.5)	Ns/m	intrinsic hand damping
k_h	14998 (50.5)	N/m	intrinsic hand stiffness
f_{0_i}	2.77 (0.191)	Hz	eigenfrequency combined
	1.69 (0.157)		intrinsic system
	1.31 (0.129)		

ness. Decreasing the eigenfrequency f_{0_i} to 1.3 Hz ($m_e = 10$ kg) results in an even more underdamped response of the arm admittance. In case of the smallest relative damping ($\beta = 0.24$), there is already significant amplification at the eigenfrequency that still further increases to extremely underdamped behavior for the largest relative damping ($\beta = 1.9$, Fig. 2.6, *right column*, solid curves). At these combinations of small eigenfrequencies and large values for relative damping, the arm sometimes became unstable. Note that arm instability never led to instable behavior of the combined system $H_{DX}(f)$. The length feedback gains (Fig. 2.8, arrows in third column) were high and exceeded the intrinsic stiffness by approximately a factor 1.5. Generally, $\hat{k}_p$ increases with relative damping and its characteristics are shifted to larger values with increasing eigenfrequency f_{0_i}.

The velocity feedback gain $\hat{k}_v$ showed opposite variations, decreasing moderately with relative damping at all eigenfrequencies. Typically, the estimates became negative with increasing relative damping.

In contrast to the arm admittance, the combined system was almost critically damped for the lowest values of β and severely overdamped for the highest values (Fig. 2.7). Comparison with the arm admittance, $H_{arm}(f)$ immediately reveals that the low frequency gain of $H_{DX}(f)$ is determined by $H_{arm}(f)$, and that the undesired oscillation peak of $H_{arm}(f)$ is suppressed by the environment. For the largest values of β the arm compliance showed the highest oscillation peak whereas the combined system was severely overdamped by the environment.

Since reflexive length feedback increases the stiffness of the arm and consequently of the combined system, the eigenfrequencies based on the MB combinations shift to higher frequencies. This is indicated by vertical lines in Fig. 2.7 and short vertical bars on the horizontal axis at f_{0_i}. The largest increase in eigenfrequency occurs at the largest values for β where $\hat{k}_p$ is largest (right arrows in first and third column of Fig. 2.8). For these conditions, the eigenfrequencies were shifted from 2.8 to 3.8 Hz and from 1.3 to 2.1 Hz respectively.

In nearly all cases the estimated coherence $\hat{\Gamma}_{DX}(f)$ was high (> 0.9) for all frequencies which validates the linear model approximation and proves that measure-

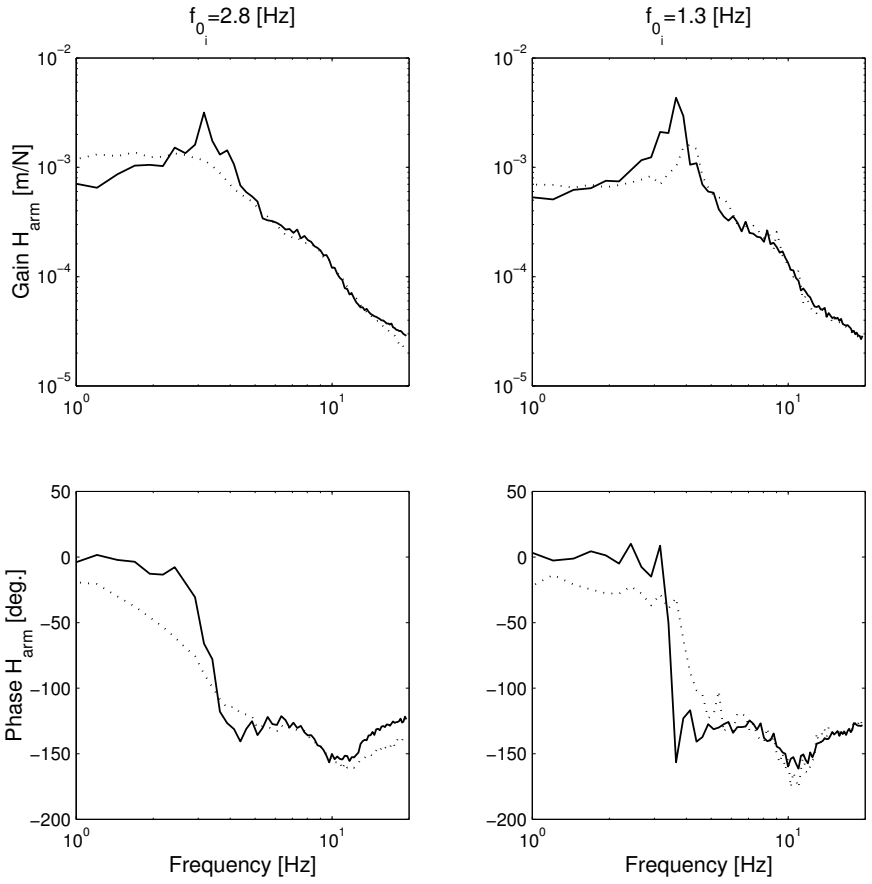

Figure 2.6: *Estimated transfer functions of the arm $\hat{H}_{arm}(f)$ for subject HB (averages of four trials).* Top row*: gain (m/N),* bottom row*: phase (deg.).* Left column*: largest eigenfrequency $f_{0_i} = 2.8$ Hz ($m_e = 0.6$ kg) and two different values for relative damping: $\beta = 0.5$ (*dashed curves*), at which the intrinsic parameters were measured, and $\beta = 1.9$ (*solid curves*) of combined intrinsic system,* right column*: $f_{0_i} = 1.3$ Hz ($m_e = 10$ kg) with $\beta = 0.24$ (*dashed curves*) and $\beta = 1.9$ (*solid curves*).*

ment noise was negligible. Comparable values were found for all other conditions and subjects.

Except for the smallest relative damping β at the smallest eigenfrequency f_{0_i}, high VAF values ($> 83\%$) were obtained (Fig. 2.8, bottom row) which can be considered very good. This means that the linear model structure with the estimated parameter values $\hat{k}_p$, $\hat{k}_v$ and $\hat{u}_0$, is an accurate approximation of the real system dynamics (arm plus environment) under these experimental conditions.

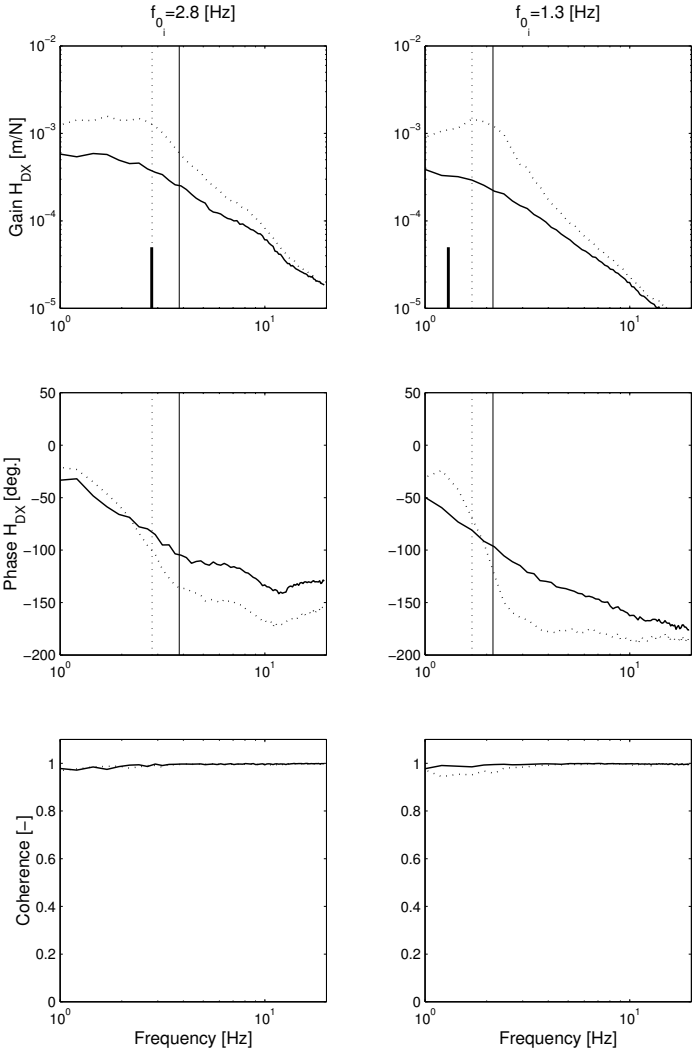

Figure 2.7: *Estimated transfer functions of combined system (arm plus environment)* $\hat{H}_{DX}(f)$ *for subject HB (averages of four trials).* Top row*: gain (m/N),* middle row*: phase (deg.),* bottom row*: coherence function* $\hat{\Gamma}_{DX}(f)$. Left column*: largest eigenfrequency* $f_{0_i} = 2.8$ *Hz (*$m_e = 0.6$ *kg) and two different values for relative damping:* $\beta = 0.5$ *(*dashed curves*) and* $\beta = 1.9$ *(*solid curves*) of the combined intrinsic system,* right column*:* $f_{0_i} = 1.3$ *Hz (*$m_e = 10$ *kg) with* $\beta = 0.24$ *(*dashed curves*) and* $\beta = 1.9$ *(*solid curves*). Short vertical bars on the horizontal axis indicate the eigenfrequencies (*f_{0_i}*) of the combined intrinsic system without reflexes. Vertical lines indicate the corresponding eigenfrequencies as the result of increased stiffness due to reflexes.*

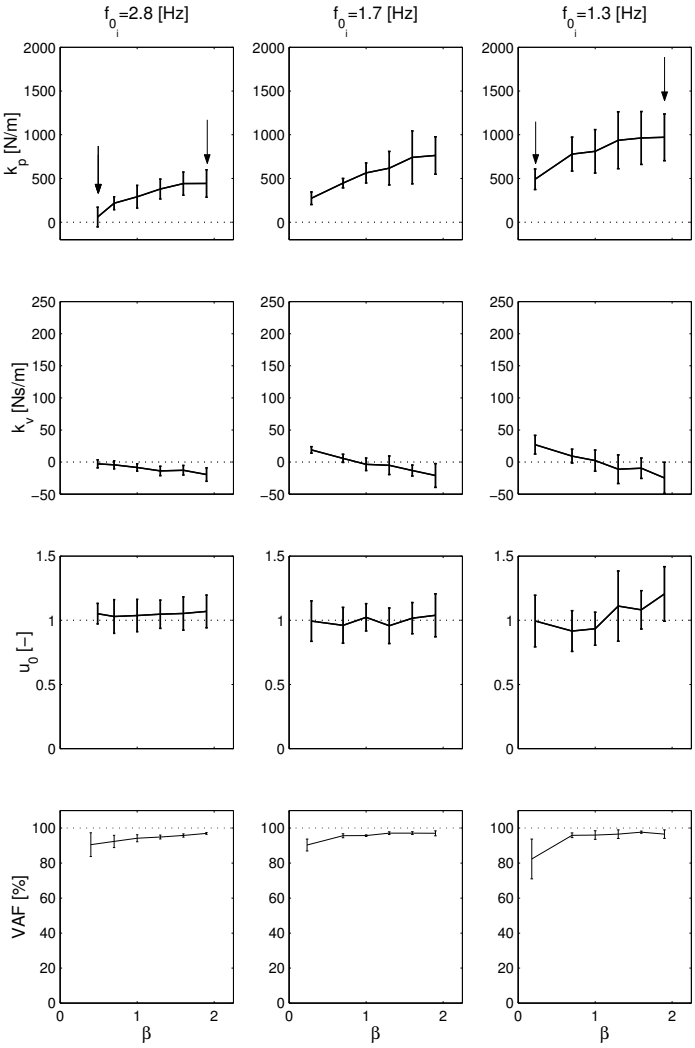

Figure 2.8: *Estimated mean reflex gains and standard deviation (*errorbars*) for subject HB. Rows from* top *to* bottom*: length feedback gain $\hat{k}_p$, velocity feedback gain $\hat{k}_v$, cocontraction level $\hat{u}_0$ and VAF values. Columns:* left*, $f_{0_i} = 2.8$ Hz;* middle*, $f_{0_i} = 1.7$; right $f_{0_i} = 1.3$ Hz. Vertical arrows indicate the conditions for which the FRFs of the combined system and the arm are shown in Figs 2.6 and 2.7 (i.e. the large circles in Fig. 2.5).*

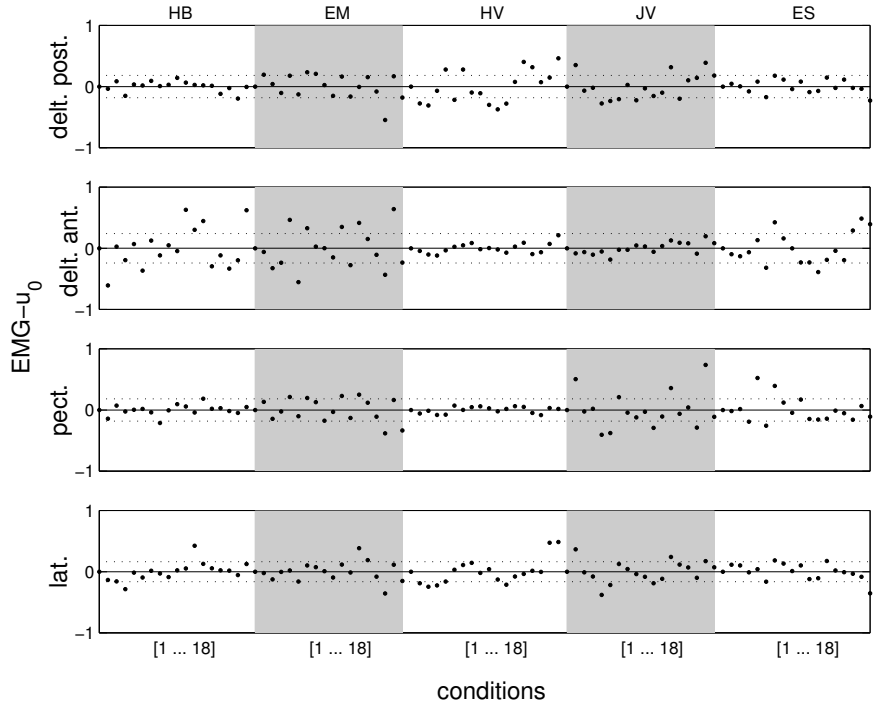

Figure 2.9: *Difference of measured EMG (scaled RMS) and estimated cocontraction $\hat{u}_0$ indicated by points for all of the MB-combinations for each muscle (*rows*) and all subjects (*white-gray columns*) with standard deviations (*horizontal dotted lines*). Each column shows all eighteen MB-combinations per subject.*

In Fig. 2.9 the difference between the scaled RMS of the EMG signals and corresponding estimated cocontraction levels $\hat{u}_0$ are shown. Since the RMS values were scaled such that their means coincide with the estimations, the mean of the difference is zero. For each muscle, the standard deviations amongst all subjects are indicated by dotted lines. EMG of the m. deltoideus anterior showed the largest differences (24% st. dev.) while the discrepancies of the other muscles were smaller ($\leq 18\%$). For subjects HV and JV the differences were small for m. deltoideus anterior, meaning that the variations of the estimated cocontraction levels approximated those of the EMG recordings very well. The same accounts for the m. pectoralis major (subjects HB, HV) and m. deltoideus posterior (subject HB). The mean standard deviation of all muscles and subjects was $\approx 20\%$. The effect of these variations in cocontraction level on the estimated feedback gains is analyzed by optimizations and described at the end of the next subsection.

2.3.2 Optimization

Metabolic energy weighting was not incorporated in our model such that unrealistic high values of intrinsic stiffness and damping resulted when the amount of cocontraction was taken as a free parameter to be optimized. Therefore, its value (i.e. u_0) was fixed to the corresponding estimated value for each condition.

In Fig. 2.10 the averaged estimated length and velocity feedback gains are shown together with the optimized values for a number of different values of control effort weighting factor p. Both optimized reflex gains outranged the estimated values by far ($k_p^* > 8000N/m, k_v^* > 500N/m$) for $p = 0$ (not shown). The optimized gains decreased with increasing control effort weighting. Negative values for k_v^* were also not found for very large p values. All values of the estimated length feedback gains are within the range of the optimized values for different p. The predicted velocity feedback gains were substantially lower in all cases. This indicates that the estimated reflexive velocity feedback is suboptimal under these experimental conditions.

To show the role of velocity feedback, Fig. 2.11 displays the optimized length feedback gains again for the same p values but without velocity feedback, i.e. k_v^* was set to zero as an approximation of the estimated values. The curvatures of k_p^* are nearly similar except in case of the lowest relative damping β at the two largest eigenfrequencies f_{0_i}.

The impact of control effort weighting on performance and afferent feedback is shown in Fig. 2.12 for three values of β $(0.7, 1.3, 1.9)$ at each eigenfrequency. The performance expectedly worsens with control effort weighing for all conditions, as can be seen by the increase of the performance criterion function J_x (Fig. 2.12, *top row*). For the highest eigenfrequency the performance without control effort weighting ($p = 0$) was the worst and therefore the relative increase of J_x was smallest. Control effort is effectively reduced for small weightings and saturated when weighting was further increased (Fig. 2.12, *middle row*). Slightly weighting J_a with p also improved converging of the parameters significantly. The contribution of J_x to J is much higher than that of pJ_a, as can be seen by comparing J_x and J (Fig. 2.12, *bottom row* and *top row*). One value for control effort weighting was chosen for all conditions: $p = 0.5 \cdot 10^{-7}$, as indicated by the gray vertical lines in Fig. 2.12. With this value the control effort J_a was substantially reduced ($\approx 60-80\%$) while performance J_x decreased to a far lesser extent ($\leq 20\%$, see Fig. 2.12). The corresponding optimized length reflex gains k_p^* are shown in Fig. 2.13 (k_v^* set to zero). Apart from the two largest eigenfrequencies and smallest relative damping, the gains were predicted quite well and captured by the standard deviations of the corresponding estimates.

In Fig. 2.14 the effect of variations in cocontraction level on the reflex gains were simulated ($p = 0.5 \cdot 10^{-7}$). When estimated cocontraction levels were increased by 20% (i.e. a proportional increase of muscle stiffness and damping), both the reflex gains decreased only slightly ($\leq 10\%$) for all conditions and vice versa in case of lower cocontraction.

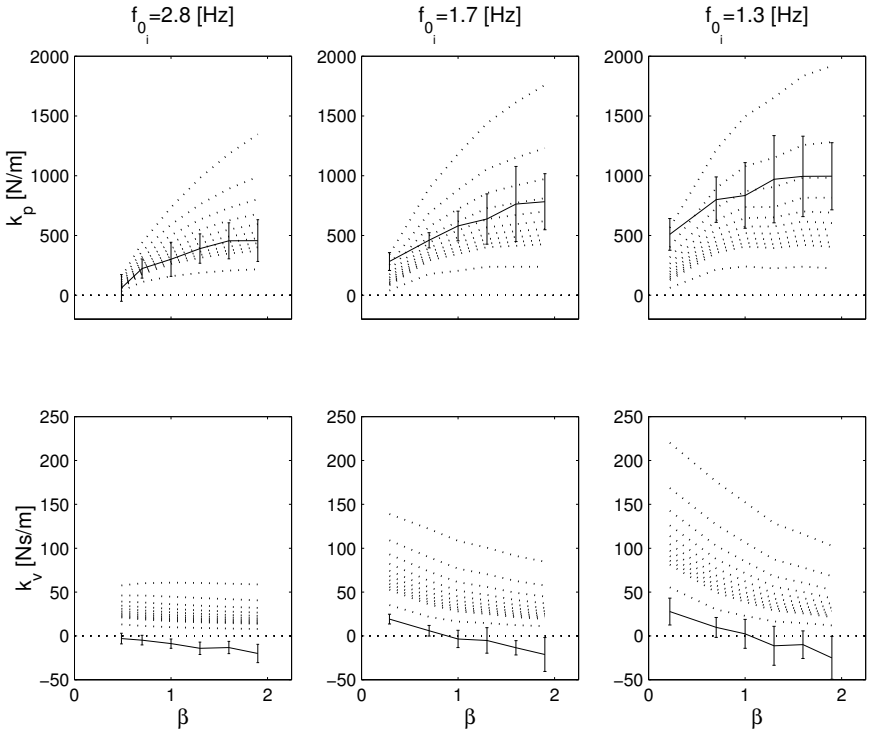

Figure 2.10: *Optimized (*dashed curves*) and estimated (*solid curves*) reflex gains (averaged over all subjects* $n = 5$*).* Errorbars *denote the standard deviation of the estimated mean values. Each dotted line corresponds to one value of* p *ranging from* $\{0.1 - 2.0\} \cdot 10^{-7}$*. Largest optimized gains occurred at the lowest values of* p*.*

2.4 Discussion

Stability of the combined system was guaranteed for all conditions. Apart from the smallest relative damping at each eigenfrequency, the combined system was sufficiently damped (Fig. 2.7). This is because the external dynamics provided substantial damping. Consequently, the human controller was indemnified from critically controlling the stability margins of the total system by being only partly able to change the admittance of the combined system. The adjustments of reflexive feedback gains under those current experimental conditions were therefore particularly determined by performance and control effort criteria and not constrained by stability demands, as was the case in previous studies (De Vlugt et al. 2001; Schouten et al. 2001).

To clarify the changes in reflex gains it must be repeated that performance J_x is related to the combined system of arm plus environment (Eq. 2.12) and the only way to improve performance is to modify the arm admittance. To what extent the

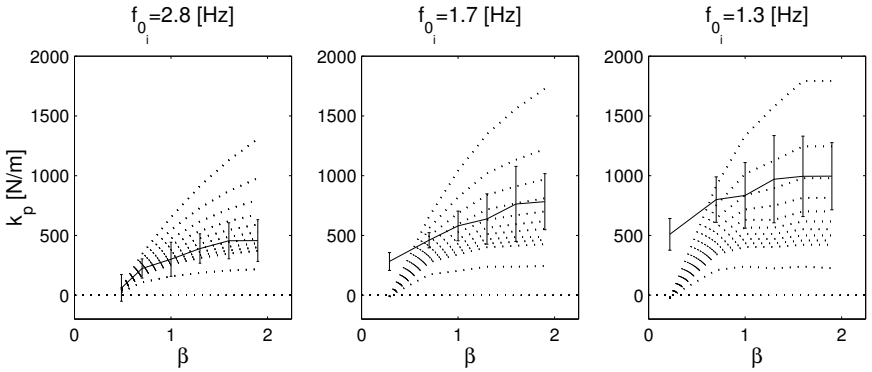

Figure 2.11: *Optimized (*dashed curves*) and estimated (*solid curves*) length reflex gain, averaged over all subjects ($n = 5$). Velocity feedback is not optimized and set to zero.* Errorbars *denote the standard deviation of the estimated mean values. Each dotted line corresponds to one value of p ranging from $\{0.1 - 2.0\} \cdot 10^{-7}$. Largest optimized gains occurred at the lowest values of p.*

performance is determined by the arm also depended on the mechanical properties of the environment. Because only damping and mass of the environment were increased, the stiffness was always determined by the arm only, i.e. by intrinsic and reflexive feedback. This is the reason why increasing arm stiffness by high length feedback gains was effective in general for nearly all experimental conditions.

In the case of the highest eigenfrequency f_{0_i} and the smallest relative damping β (minimal mass and damping of the environment), the combined system was dominated by the mechanical properties of the arm. For this condition, both reflex gains were found to be very small (Fig. 2.10), as was also found in a comparable study by Van der Helm at al. (2002) and in previous simulation studies (De Vlugt et al. 2001; Schouten et al. 2001). The absence of reflexes for this condition can be explained from the effect of k_p on J_x, which is twofold. First, as already stated above, it increases stiffness which is beneficial. Second, it directly decreases relative damping, according to Eq. (2.8) and due to the neural time delay. Obviously, smaller relative damping increases the amplification at system's eigenfrequency (oscillation) that deteriorates performance. Apparently, a negative contribution of an oscillation peak is larger than a profitable increase of stiffness for this condition. The absence of feedback also validated the estimation of the intrinsic parameters which were estimated at this condition.

When relative damping increases, the influence of an increased oscillation peak of the arm dynamics has little effect on the combined system and consequently worsens performance to a lesser extent. This is simply because the overall damping is larger. Therefore, k_p can be increased to improve performance in these cases. Generally, the higher the total relative damping the larger the efficiency of length feedback because amplification at the eigenfrequency of the arm is suppressed by

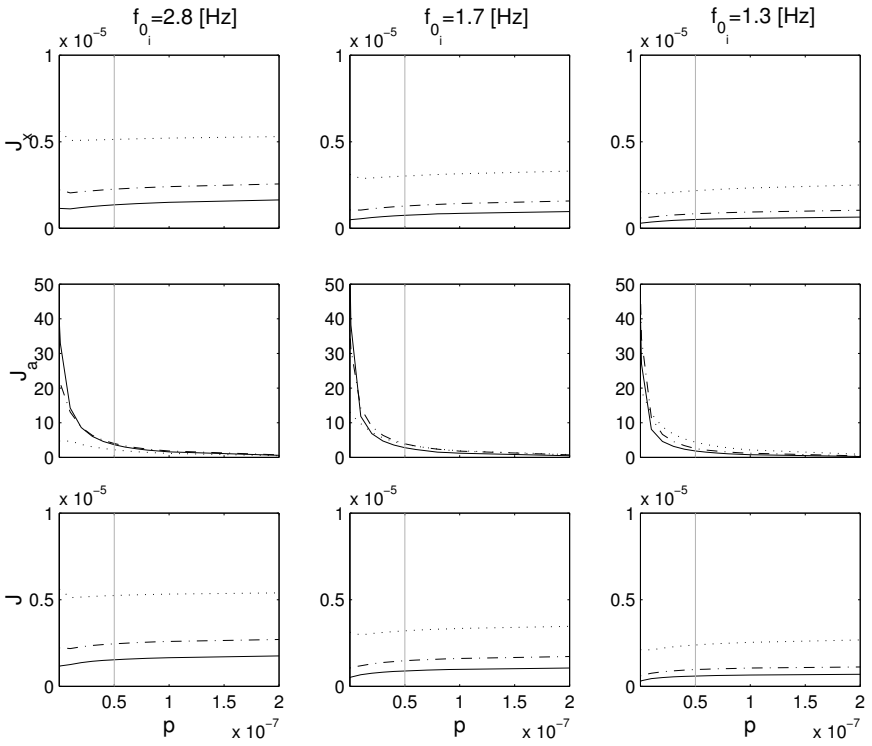

Figure 2.12: *Criterion functions for different values of control effort weighing* p. Top row*: performance criterion* J_x, bottom row*: control effort criterion* J_a. Dotted *curves:* $\beta = 0.7$*;* Dashed dotted *curves:* $\beta = 1.3$*;* Solid *curves:* $\beta = 1.9$. *Criterion values at* $p = 0.5 \cdot 10^{-7}$ *are indicated by gray vertical lines.*

the environment.

The velocity feedback gain $\hat{k}_v$ was very small, decreased slightly and even became negative for larger relative damping. Negative reflex gains were also found by Van der Helm et al. (2002), were close to optimal under the experimental conditions (De Vlugt et al. 2001) and were attributed to autogenic excitation (Schouten et al. 2003). On the contrary, the simulation results showed k_v^* was substantial and effectively suppressed the resonance peak in particular for the smallest eigenfrequency and smallest relative damping. This is shown in Fig. 2.15 (right upper plot, dashed-dotted curves). The estimated $\hat{k}_v$ therefore seems suboptimal and leaves the arm and combined system underdamped, in particular for this condition (Fig. 2.15, right upper plot, solid curves). When velocity feedback gain was fixed to zero, the lack of damping is evidently predicted but now the optimized length feedback gains were much smaller than estimated for these particular conditions, resulting in an increase of the low frequency gain of $H_{DX}(f)$ (Fig. 2.15, right upper plot, dotted

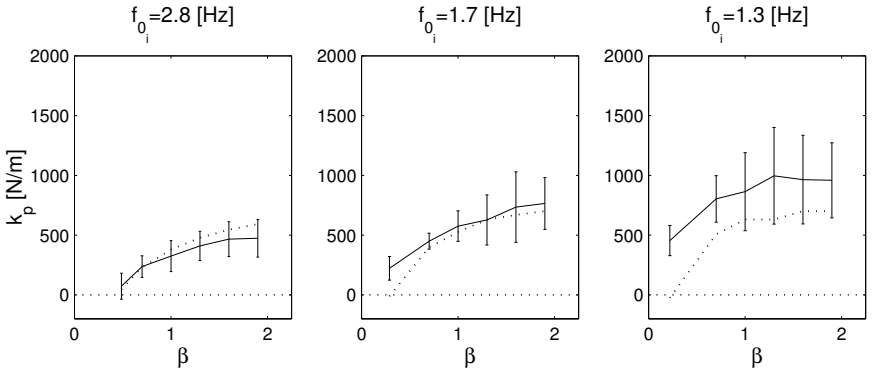

Figure 2.13: *Optimized (*dashed curves*) and estimated (*solid curves*) length feedback gains, averaged over all subjects ($n = 5$). Velocity feedback is not optimized and set to zero. Control effort weighting $p = 0.5 \cdot 10^{-7}$.* Errorbars *denote the standard deviation of the estimated mean values.*

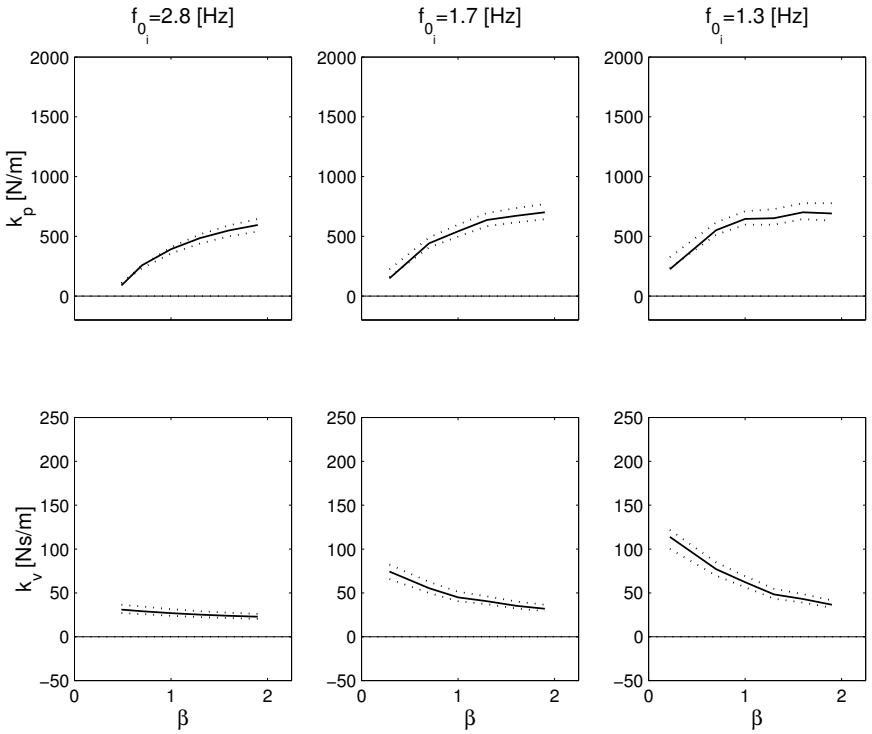

Figure 2.14: *Model optimization ($p = 0.5 \cdot 10^{-7}$) showing the effect of variations in cocontraction level on the reflex gains.* Solid *curves: optimed gains using the corresponding estimated values for u_0.* Dotted *curves: u_0 is increased (below) and decreased (above) with 20%.*

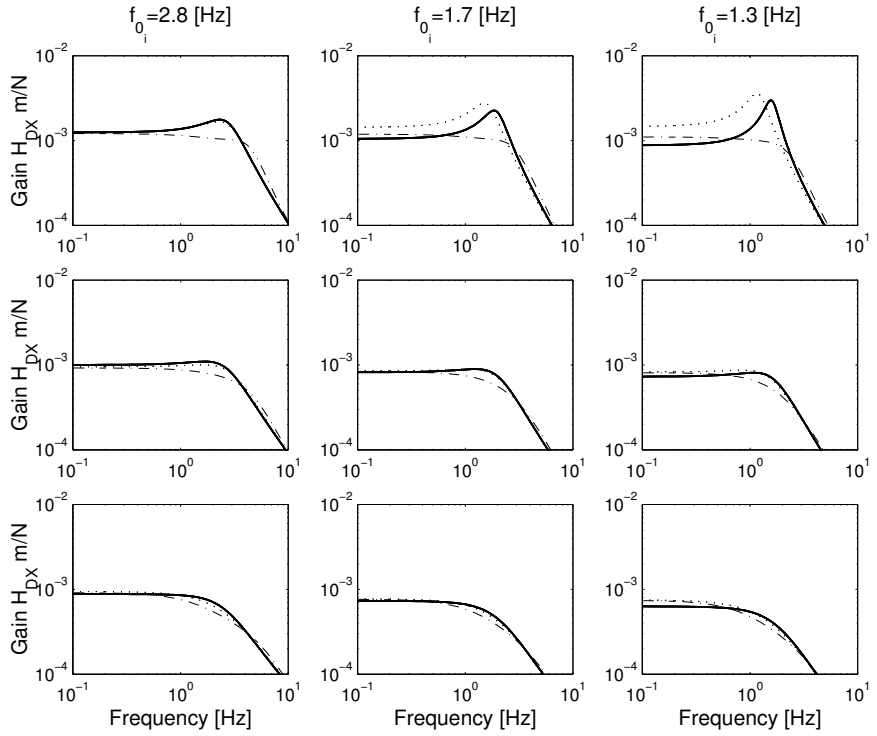

Figure 2.15: *FRFs of modelled combined system $H_{DX}(f)$ for smallest relative damping β (*top row*), $\beta = 1.0$ (*middle row*) and $\beta = 1.6$ (*bottom row*) at all three eigenfrequencies f_{0_i}.* Solid *curves are the combined model parametrized with the estimated parameters $\hat{k}_p$, $\hat{k}_v$ and $\hat{u}_0$ (mean of all subjects).* Dashed dotted *curves: the optimized FRFs parametrized with optimal gains k_p^* and k_v^* for $p = 0.5 \cdot 10^{-7}$.* Dotted *curves: the optimized FRFs parametrized with the optimal gain k_p^* and k_v^* set to zero for the same weighting factor.*

curves). Apart from this extreme condition, the length feedback appears to be close to optimal and the estimated FRFs of the combined system $H_{DX}(f)$ were very similar to the optimized ones.

Possibly, the length and velocity feedback gains are somehow restricted by a mutual gain limiting relation which was not incorporated in our model (Schaafsma et al. 1991). For instance, if muscle spindle output was dependent on the amplitude of velocity such that at large velocities the sensitivity for lengthening was reduced and vice versa, at low velocities length feedback would be more dominant. Apparently, if such mechanisms somehow exist, the movements in our experiments were slow enough to exhibit pronounced length feedback in nearly all cases. Omitting the velocity feedback from the optimization was a means to mimic such a property. Further research on spindle transferfunction identification is necessary to explain

such input selectivity and to clarify the restricted velocity gains found under the current experimental conditions.

Summarizing the findings it is stated that 1) length feedback effectively reduces the admittance of the combined system and 2) the strength of length feedback is the result of weighting of admittance reduction against the control effort needed for this reduction.

We have also applied slower time constants (30-50 ms) for the activation process and found that the estimated velocity feedback gains increased while length feedback did not noticeably change (not shown). This is because activation acts as a low pass filter (≈ 5 Hz) to afferent signals such that higher velocity gains would be estimated to obtain the same behavior. This sensitivity of velocity feedback on activation time constant can account for the unexpected negative values. However the same sensitivity also follows from the model optimization and so the discrepancy with the estimated velocity gains still remains.

Mean EMG and estimated cocontraction levels were almost constant over the conditions. Since increasing intrinsic stiffness and damping always improves performance, cocontraction was apparently at maximum during all conditions. The difference between recorded EMG and estimated cocontraction level had a standard deviation of $\approx 20\%$ accounting for measurements noise and inaccuracy of the estimation procedure. Higher cocontraction levels decreased the admittance of the combined system due to larger intrinsic stiffness and damping of the arm. Consequently, at the same weighting of control effort, the effectiveness of additional reflexive feedback was less and the gains were smaller (Fig. 2.14). The opposite effect was shown for smaller cocontraction levels. However, the effect of fluctuations in cocontraction did not affect the values of the feedback gains substantially and therefore do not change the findings of this study. A 20% variation merely changed the gains by less than 10%. This indicated the estimation procedure was accurate enough to quantify intrinsic and reflexive properties which was confirmed by high VAF values.

Subjects felt themselves to have the least control over the combined system at the lowest eigenfrequencies f_{0_i}. In these cases, both mass and damping of the environment were large. This was reflected by increased variations in cocontraction ($\hat{u}_0$ and EMG) and larger standard deviations in estimated length reflex gains (Fig. 2.8). This varying behavior is most likely the result of decreased relative contribution of the arm damping to the damping of the combined system such that subjects possibly varied slightly around their optimal adjustments without affecting performance seriously.

Despite the rather good resemblance of estimated cocontraction level and measured EMG, it must be mentioned that EMG is not a direct measure for muscle force. Since (non-linear) activation dynamics separate those quantities a direct comparison seems not possible. However, in a mean sense for almost constant cocontraction levels, the activation dynamics can be neglected such that muscle force can be taken as a scaled version of the corresponding EMG. Since EMG and u_0 were both used as normalized variables in this study a direct comparison was justified.

2.5 Conclusions

Afferent length and velocity feedback gains were shown to adapt to different mechanical properties of the environment. In particular, length feedback gain increased substantially with relative damping of the combined system. Increasing the eigenfrequency by larger masses of the environment increased the length feedback gains to a lesser extent. These gains modulations served the optimization of a performance criterion concerning the combined system of arm plus environment, i.e. the minimization of displacements of the hand during a continuous force perturbation. It is likely the CNS controls the reflex gains within seconds after the perturbation was applied. This specialized feedback behavior followed directly from optimal control theory. Length feedback effectively improved performance because it enlarges stiffness but only when its negative side-effect of increased resonance is suppressed by the environment.

Model optimizations show strong similarities with the estimated length feedback gains indicating that: (1) the performance criterion is a realistic description of the task instruction; (2) the control effort weighting is somehow apparent in the feedback loop; and (3) because of the high VAF values, the model is an adequate description of intrinsic and reflex mechanisms at endpoint level.

The results are valid for the system being perturbed with continuous random forces while the subject is performing a position task. Because these conditions correspond to real life posture maintenance, it is believed that these conditions are necessary to explain neuromuscular functioning of human posture control in vivo.

Chapter 3

Quantifying reflexes with mechanical admittance and reflexive impedance

Alfred Schouten, Erwin de Vlugt, J.J. (Bob) van Hilten, Frans C. T. van der Helm
submitted to *Journal of NeuroScience Methods*

This study aimed to analyze the dynamic properties of the muscle spindle feedback system of shoulder muscles during a posture task. External continuous force disturbances were applied at the hand while subjects had to minimize their hand displacements. The results were analyzed using two frequency response functions (FRFs) from which the model parameters were derived, being a) the mechanical admittance and b) the reflexive impedance. These FRFs were analyzed by a neuromusculoskeletal model that implicitly separates the reflexive feedback properties (position, velocity and acceleration feedback gains) from intrinsic muscle visco-elasticity. The results show substantial changes in estimated reflex gains under conditions of variable bandwidth of the applied force disturbance or variable degrees of external damping. Position and velocity feedback gains were relatively larger when the force disturbance contained only low frequencies. With increasing damping of the environment, acceleration feedback gain decreased, velocity feedback gain remained almost constant and position feedback gain increased. It is concluded that under the aforementioned circumstances, the reflex system increases its gains to maximize the mechanical resistance to external force disturbances while preserving sufficient stability.

3.1 Introduction

Studies addressing the role of spinal reflexes in the regulation of movement and posture have been informative in understanding the impact of diseases with abnormal muscle tone including spasticity, dystonia or Parkinson's disease (Mirbagheri et al., 2001; Schouten et al., 2003a; Lee and Tatton, 1975). Studies on the role of spinal reflexes in the regulation of muscle tone have mainly applied qualitative approaches (Doemges and Rack, 1992a,b; Akazawa et al., 1983; Kanosue et al., 1983). From these studies important features of the proprioceptive reflex system emerged showing the influence of position and force tasks on proprioceptive reflex magnitude. However these studies have not provided insight into the functional contribution of proprioceptive reflexes to the dynamic relation between force and position (mechanical admittance), which is crucial in the understanding of how these reflexes control stable movement and posture. Few studies have focused on qualitative characterization of proprioceptive reflex regulation (Zhang and Rymer, 1997; Kearney et al., 1997; Van der Helm et al., 2002). These studies have used quantification methods that basically rely on specific neuromuscular models and optimization algorithms to minimize the difference between measured and predicted variables. Hitherto, all studies have used an indirect approach by estimating reflex parameters from the mechanical admittance. In the mechanical response, intrinsic muscle visco-elasticity and reflexive contributions coexist. Therefore assumptions on the reflexive component were necessary to separate the intrinsic and reflexive contributions. Such assumptions on reflex behavior may introduce a bias in the model. Consequently, there is a need for methods that directly quantify reflex behavior. In a recent study (Schouten et al., 2003b) a method was introduced to estimate the frequency response functions of the mechanical admittance and the reflexive impedance, i.e. the dynamic relation between position and muscle activation. This study aims to quantify spinal reflexes directly by fitting a neuromusculoskeletal (NMS) model of the arm on both the mechanical admittance and reflexive impedance obtained simultaneously during posture tasks.

3.2 Methods

3.2.1 Subjects

Two experiments were carried out. In the main experiment ten healthy subjects (4 women, 3 left handed) participated with a mean (SD) age of 25.8 (7.0) years. In a second experiment, to estimate the muscle activation dynamics, five subjects (2 women, 2 left handed) participated with a mean (SD) age of 25.4 (3.2) years. All subjects gave informed consent prior to the experiment. All experiments were conducted on the right arm.

3.2.2 Apparatus

Force disturbances were applied to the hand by means of a linear manipulator. The manipulator is extensively described in Chapter 2 and is introduced briefly. The subjects sat in a chair and had to hold a handle with their right hand. Movement of the handle resulted in ante-/retroflexion movements of the shoulder-joint. To the subject the manipulator behaved like a mass-spring-damper system. The parameters of the spring (k_e), damper (b_e), and mass (m_e) are adjustable. In this study the mass, m_e, was set to a fixed value of 1 kg. The damping, b_e, was varied between the trials, see Section 3.2.3. No stiffness was used ($k_e = 0$ N/m).

3.2.3 Procedures

Main experiment

In the main experiment subjects had to hold the handle and were instructed to *'minimize the displacements'* of the handle, while continuous random force disturbances were applied for 30 seconds (task *stiff*). The actual position of the handle was shown on a display to assist the subjects and to prevent drift. Only a few trials were necessary to get the subject acquainted with the task. The following experimental conditions were applied:

- Wide bandwidth (WB) disturbance without external damping (WB *stiff*). The WB disturbance signal had power between between 0.5 and 20 Hz. This condition is referred to as the reference condition.
- WB disturbance without external damping and the task *slack* (WB *slack*). Here the task instruction was different from the other: the subject was asked to relax his/her arm muscles and not to react to the disturbance. This task was only used to improve to estimate of the arm mass.
- WB disturbance with external damping. The damping was assigned values of 50, 100, 150, 200 Ns/m (B50, B100, B150, B200).
- Narrow bandwidth disturbance type 1 (NB1) without external damping. The disturbance signals had a variable bandwidth; the lowest frequency was fixed at 0.5 Hz and the highest frequency, f_h, varied between 1.2 and 3.7 Hz (1.2, 1.5, 1.8, 2.4, 3.1, 3.7 Hz).
- Narrow bandwidth disturbance type 2 (NB2) without external damping. The signals had a bandwidth of 0.3 Hz concentrated around a variable center frequency, f_c, of 1.3 up to 7 Hz (1.3, 1.8, 2.3, 3, 4, 5, 6, 7 Hz).

The twenty different conditions were repeated four times, resulting in eighty trials of 30 seconds each. The trials were presented in a random order. In between the trials the subject could rest as long as he/she wanted to prevent fatigue. All disturbance signals were designed in the frequency domain as so-called multisine signals with optimized crest factor (Schoukens et al., 1993; Pintelon and Schoukens, 2001;

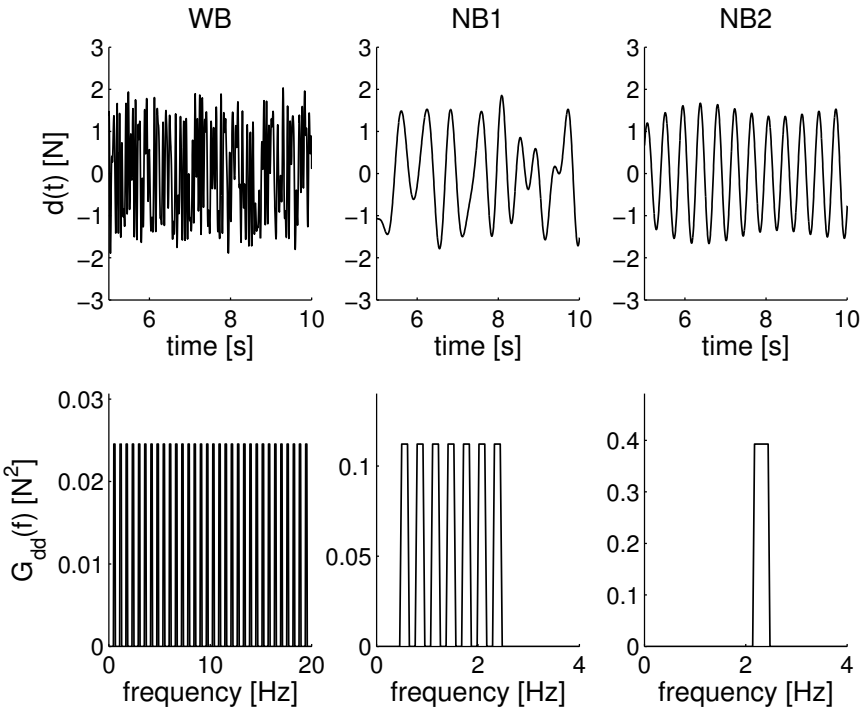

Figure 3.1: *Examples of disturbance signals; left: WB; middle: NB1 $f_h = 2.4$ Hz; right: NB2 $f_c = 2.3$ Hz. Upper plots: 5 seconds fragment of the signals; lower plots: power spectral densities of the signals. The signals are scaled to a root mean square (RMS) value of one. Each peak in the power spectral densities represents a cluster of 4 (WB, NB1) or 8 (NB2) adjacent frequencies.*

Schouten et al., 2003b). Because multisine signals are deterministic, no bias or variance were introduced in the estimated spectral densities (Pintelon and Schoukens, 2001; De Vlugt et al., 2003a).

To improve the signal-to-noise ratio (SNR) of the EMG and to allow reliable identification of the reflexive impedance, the power of the disturbance signal was distributed over a limited number of frequencies within the bandwidth. For the WB disturbance the signal power was uniformly distributed over 32 equidistantly spaced clusters of 4 adjacent frequencies, i.e. 25% of the frequencies within the bandwidth are excited (Schouten et al., 2003b). The data analysis required clusters of 4 adjacent frequencies for averaging. For the NB1 disturbances 50% of the frequencies within the bandwidth were excited, and consequently each NB1 signal contained a different number of clusters (ranging from 3 clusters for $f_h = 1.2$ Hz up to 11 clusters for $f_h = 3.7$ Hz). For the NB2 disturbances the power was distributed in one cluster of 8 adjacent frequencies. Fig. 3.1 shows examples of the disturbance

signals, the lower plots show the power spectral densities of the signals.

To justify the use of linear model approximations the position deviations must be kept small within each condition. Prior to the trials each condition was tested and the amplitude of the force disturbance was adjusted for each condition to obtain a root-mean-square (RMS) value for the position of approximately 3 mm.

Since recorded EMG is an electric signal which is meaningless to the mechanical properties, the EMG to force ratio was determined to obtain a relative measure of the muscle force. Therefore, subjects were required to perform isometric push and pull tasks, prior and after the main experiment. The subjects had to maintain constant force levels for 10 seconds (-25, -20, -15, 0, 15, 20, 25 N) by pushing or pulling against the handle, which was controlled to be in a fixed (rigid) position. During these isometric trials the reference force together with the actual force at the handle were shown on the display to assist the subject in performing the task. The EMG to force ratio was determined by linear regression.

Activation dynamics

The EMG to force ratio provides the static relation between muscle activation and muscle force. The dynamic relation between muscle activation and muscle force was determined in a secondary isometric experiment. The secondary experiment started and ended with the same push/pull tasks as the main experiment. The experiment consists of 8 trials of 30 seconds. During these trials the subjects performed isometric tasks and were asked to make block-shaped forces between approximately 25 N push and pull.

3.2.4 Data processing

Signal recording and processing

During a trial the force disturbance, $d(t)$, the position of the handle, $x_h(t)$, the force at the handle, $f_h(t)$, and the EMG of four relevant shoulder muscles (e_1: m. pectoralis major, e_2: m. deltoideus anterior, e_3: m. deltoideus posterior, and e_4: m. latissimus dorsi) were recorded at 2500 Hz sample frequency with a 16 bit resolution. Before recording, the EMG signals were high pass filtered to remove DC components and movement artifacts (20 Hz, 3th order Butterworth), and low pass filtered to prevent aliasing (1 kHz, 3th order Butterworth). This study investigates stationary behavior and to remove any initial transient effect the first 9464 samples ($\approx$ 4 s) were eliminated, leaving 2^{16} samples ($\approx$ 26 s) for further processing.

The EMG signals were used (1) to estimate the amount of co-activation expressed by the mean EMG and (2) to construct the muscle activation, $a(t)$. The procedure of EMG treatment is described previously in Schouten et al. (2003b) and will be briefly summarized. To improve the quality of the EMG signals a prewhitening filter is implemented, following the procedures as described in Clancy et al. (2002). The power spectral densities of the EMGs during the maximum isometric push and pull tasks (25 N) are used to obtain the parameters of the prewhitening filter (6th order).

For small variations in muscle co-activation it reasonable to assume that the intrinsic muscle visco-elasticity linearly scale with the co-activation level (Agarwal and Gottlieb, 1977a). Therefore mean EMG, u_0, was determined as a measure for muscle co-activation. To calculate the mean EMG the integrated rectified EMG, IEMG, of each muscle during a trial was calculated.

$$\text{IEMG}_i = \frac{1}{n}\sum_{k=1}^{n} |e_{w,i}(t_k)| \tag{3.1}$$

in which $e_{w,i}$ is the prewhitened EMG of muscle i, k indexes the time vector, and n is the number of samples. The mean EMG was calculated, according to:

$$u_0 = \frac{1}{4}\sum_{i=1}^{4} \frac{\text{IEMG}_i}{\text{IEMG}_{ref,i}} \tag{3.2}$$

where $\text{IEMG}_{ref,i}$ denotes the IEMG for muscle i of the reference disturbance averaged over the four repetitions.

To calculate the muscle activation, $a(t)$, the EMG signals are scaled and expressed into Newtons. The force to EMG ratio of each muscle, K_i, is estimated from the push/pull tasks by linear regression. The (lumped) muscle activation is obtained by combining the rectified prewhitened EMGs of the four recorded muscles:

$$a(t) = \frac{1}{2}\left(K_1 |e_{w,1}(t)| + K_2 |e_{w,2}(t)|\right) + \frac{1}{2}\left(K_3 |e_{w,3}(t)| + K_4 |e_{w,4}(t)|\right) \tag{3.3}$$

In this equation it is assumed that both 'push' muscles (1 and 2) have equal relevance and consequently the total push force is equal to the mean of both muscles. The same holds for the 'pull' muscles (3 and 4). Note that K_1 and K_2 are positive and K_3 and K_4 are negative, as the muscles operate in opposite direction.

Nonparametric analysis

The time records ($x_h(t)$, $f_h(t)$, $d(t)$, and $a(t)$) of the four repetitions for one condition are averaged to reduce the variance due to noise in the signals. The signals are transformed to the frequency domain using the fast Fourier transform (FFT). Because force disturbances are applied, interaction between the subject and manipulator existed, i.e. the position of the handle depends on both the dynamics of the subject and the virtual environment imposed by the manipulator. Because of this interaction closed loop identification algorithms are required to estimate the frequency response functions (FRFs) of the mechanical admittance, $\hat{H}_{fx}(f)$, and reflexive impedance, $\hat{H}_{xa}(f)$ (Schouten et al., 2003b).

$$\hat{H}_{fx}(f) = \frac{\hat{G}_{dx}(f)}{\hat{G}_{df}(f)} \tag{3.4}$$

$$\hat{H}_{xa}(f) = \frac{\hat{G}_{da}(f)}{\hat{G}_{dx}(f)} \tag{3.5}$$

where $\hat{G}_{dx}(f)$ is the estimated cross spectral density between d and x_h (hat denotes estimate). The spectral densities are averaged over 4 adjacent frequencies to reduce the variance of the estimations (Jenkins and Watts, 1968). As a measure for linearity between the signals the coherence for the position, $\hat{\gamma}_x^2(f)$, and muscle activation, $\hat{\gamma}_a^2(f)$, were estimated.

$$\hat{\gamma}_x^2(f) = \frac{\left|\hat{G}_{dx}(f)\right|^2}{\hat{G}_{dd}(f)\hat{G}_{xx}(f)} \tag{3.6}$$

$$\hat{\gamma}_a^2(f) = \frac{\left|\hat{G}_{da}(f)\right|^2}{\hat{G}_{dd}(f)\hat{G}_{aa}(f)} \tag{3.7}$$

The coherence varies between 0 and 1 and decreases due to external noise and nonlinearities. The FRFs and coherences were only evaluated at the frequencies where the perturbation signal had non-zero power.

Quantification of activation dynamics

During isometric experiments the relationship between the muscle activation, $a(t)$, and handle force, $f_h(t)$, depends on the activation dynamics only. As the muscle activation was scaled to force the muscle dynamics have unity static gain. The activation dynamics, $\hat{H}_{act}(f)$, were estimated by dividing the appropriate spectral densities with the aid of an independent instrument variable (Pintelon and Schoukens, 2001):

$$\hat{H}_{act}(f) = \frac{\hat{G}_{wf}(f)}{\hat{G}_{wa}(f)} \tag{3.8}$$

$$\hat{\gamma}_{af}^2(f) = \frac{\left|\hat{G}_{af}(f)\right|^2}{\hat{G}_{aa}(f)\hat{G}_{ff}(f)} \tag{3.9}$$

with w as the instrument variable for which a signal with power uniformly distributed between 0.1-20 Hz was used. To improve the estimations the spectral densities are averaged over 4 adjacent frequencies.

The activation dynamics are described by with a second order model (Olney and Winter, 1985; Bobet and Norman, 1990; Potvin et al., 1996):

$$H_{act}(s, p_{act}) = \frac{1}{\frac{1}{{\omega_0}^2}s^2 + \frac{2\beta}{\omega}s + 1} \tag{3.10}$$

with

$$p_{act} = [f_0, \beta]$$

in which s the Laplace operator equals $j2\pi f$, f_0 is the eigenfrequency ($f_0 = \frac{\omega_0}{2\pi}$), β the relative damping of the activation dynamics model, and p_{act} is the parameter vector.

The activation dynamics were obtained by fitting the model (Eq. 3.10) onto the estimated activation dynamics (Eq. 3.8) by minimizing the criterion function:

$$L_{act}(p_{act}) = \sum_k \frac{\hat{\gamma}^2_{af}(f_k)}{1+f_k} \left| \ln \hat{H}_{act}(f_k) - \ln H_{act}(f_k, p_{act}) \right|^2 \tag{3.11}$$

where k indexes the frequency vector. Only the frequencies to 10 Hz were used for the criterion. For higher frequencies the force signal contained little power such that the activation dynamics can not be estimated reliably. This is reflected by the low coherence for these frequencies, see Results. Because of the large range of the FRF gain a least squares criterion with logarithmic difference was used (Pintelon et al., 1994). The criterion was weighted with the coherence to reduce emphasis on less reliable frequencies in the FRF and with $(1+f_k)^{-1}$ to prevent excessive emphasis on the higher frequencies. To obtain a better fit one set of parameters was used to fit the model simultaneously on all 8 trials for each subject. Finally the activation parameters were averaged over all subjects and used to quantify the intrinsic and reflexive parameters.

Quantification of intrinsic and reflexive properties

The model used to quantify the proprioceptive reflexes along with the intrinsic muscle visco-elasticity and limb mass is given in Fig. 3.2. Basically, the model is a lumped description of the mechanical behavior at endpoint. The position of the handle, $X_h(s)$, results from (1) the external force disturbance, $D(s)$, (2) human arm admittance, $H_{fx}(s)$, and (3) the admittance of the external environment, $H_e(s)$.

$$H_e(s) = \frac{1}{m_e s^2 + b_e s + k_e} \tag{3.12}$$

The parameters of the model are summarized in Table 3.1.

$H_g(s)$ represents the grip dynamics of the hand.

$$H_g(s) = b_g s + k_g \tag{3.13}$$

The intrinsic model, $H_{int}(s)$, includes the arm mass and the visco-elasticity of the co-contracting muscles. For small displacements the intrinsic visco-elastic properties of muscles can be described by a linear spring-damper system (Winters et al., 1988).

$$H_{int}(s) = \frac{1}{ms^2 + bs + k} \tag{3.14}$$

The reflexive dynamics, $H_{ref}(s)$, represents the muscle spindle sensory system as modelled by an acceleration, k_a, velocity, k_v, and position, k_p, term in series with a neural time delay, τ_d.

$$H_{ref}(s) = \left(k_a s^2 + k_v s + k_p\right) e^{-\tau_d s} \tag{3.15}$$

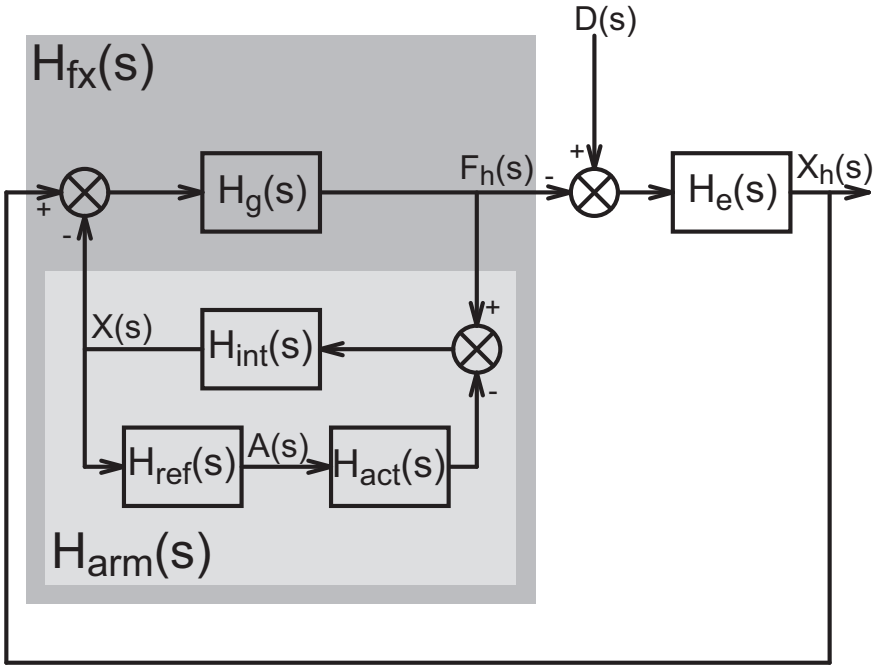

Figure 3.2: *NMS model, $H_{fx}(s)$, in conjunction with the environment, $H_e(s)$. The external force disturbance $D(s)$, hand force $F_h(s)$, position of the handle $X_h(s)$, and muscle activation $A(s)$, are measured. $H_g(s)$ represents grip dynamics, $H_{int}(s)$ intrinsic properties, $H_{act}(s)$ activation dynamics, $H_{ref}(s)$ reflexive feedback, and $X(s)$ position of the arm. The light grey box ($H_{arm}(s)$) represents the arm model without grip.*

Table 3.1: *Model parameters to be quantified.*

m [kg]	arm mass
b [Ns/m]	muscle damping
k [N/m]	muscle stiffness
b_g [Ns/m]	grip damping
k_g [kN/m]	grip stiffness
k_a [Ns^2/m]	acceleration feedback gain
k_v [Ns/m]	velocity feedback gain
k_p [N/m]	position feedback gain
τ_d [ms]	neural time delay

From the equations (Eqs. 3.10-3.15) the arm dynamics, excluding grip dynamics, can be derived:

$$\begin{aligned} H_{arm}(s) &= \frac{X(s)}{F_h(s)} = \frac{H_{int}(s)}{1 + H_{int}(s)H_{ref}(s)H_{act}(s)} \\ &= \frac{1}{ms^2 + bs + k + (k_a s^2 + k_v s + k_p)\, e^{-\tau_d s} H_{act}(s)} \end{aligned} \tag{3.16}$$

where $X(s)$ and $F_h(s)$ are the Laplace transforms of the arm position and hand force respectively. Finally the mechanical admittance and the reflexive impedance are modelled by:

$$H_{fx}(s,p) = \frac{X_h(s)}{F_h(s)} = H_{arm}(s) + {H_g}^{-1}(s) \tag{3.17}$$

$$H_{xa}(s,p) = \frac{A(s)}{X_h(s)} = H_{ref}(s)\frac{H_g(s)}{H_g(s) + H_{arm}^{-1}(s)} \tag{3.18}$$

in which p is the parameter vector:

$$p = [m, b, k, b_g, k_g, k_a, k_v, k_p, \tau_d]$$

Note that when the grip becomes very stiff, ${H_g}^{-1}(s)$ approaches to zero, such that the mechanical admittance, $H_{fx}(s)$, will become equal to $H_{arm}(s)$ while the reflexive impedance, $H_{xa}(s)$, to $H_{ref}(s)$.

The model parameters are quantified by fitting the models (Eqs. 3.17 and 3.18) to the corresponding FRFs (Eqs. 3.4 and 3.5) simultaneously, by minimizing the following criterion function:

$$\begin{aligned} L(p) &= \sum_k \frac{\hat{\gamma}_x^2(f_k)}{1 + f_k} \left| \ln \hat{H}_{fx}(f_k) - \ln H_{fx}(f_k, p) \right|^2 \\ &\quad + q \sum_k \frac{\hat{\gamma}_a^2(f_k)}{1 + f_k} \left| \ln \hat{H}_{xa}(f_k) - \ln H_{xa}(f_k, p) \right|^2 \end{aligned} \tag{3.19}$$

with q as a weighting factor. Only frequencies where the perturbation signal contained power were included in the criterion. A weighting factor of 0.09 was chosen such that both terms in Eq. (3.19) had approximately equal values in the optimal fit.

The parameters of the conditions with WB disturbances, i.e. with and without damping and WB task *slack*, were estimated simultaneously (six conditions). During this simultaneous model fit one variable for the mass and one for the neural time delay were used for all six conditions. Except for the WB condition task *slack*, the damping and stiffness for the arm and the grip scaled between the conditions simultaneously with the mean EMG, u_0.

$$\begin{aligned} b &= u_0 \cdot b_{ref} \\ k &= u_0 \cdot k_{ref} \\ b_g &= u_0 \cdot b_{g,ref} \\ k_g &= u_0 \cdot k_{g,ref} \end{aligned} \tag{3.20}$$

in which $_{ref}$ denotes the parameter value in the reference condition. For the condition with task *slack* only the admittance was fitted ($q = 0$) and the reflexive parameters were omitted. The only function of the *slack* condition was to get a better estimate for the mass. Finally the number of parameters was reduced from 54 (6 condition with 9 parameters) to 25 (1 mass, 1 time delay, 4 muscle and grip parameters for the reference condition, 4 idem for task *slack* and 3 reflex gains for 5 conditions).

For the NB conditions the FRFs can only be estimated for the limited bandwidth and therefore contain not enough information to estimate the nine model parameters. To overcome this, it was assumed that the intrinsic parameters (muscle and grip) scaled with mean EMG using the intrinsic parameters estimated from the reference condition (WB *stiff*), see Eq. (3.20). Furthermore the mass and the neural time delay were fixed to the values found with the WB conditions. consequently the parameter vector for the NB conditions was reduced to the reflexive parameters only:

$$p = [k_a, k_v, k_p]$$

Model validation

The variance accounted for (VAF) is calculated to obtain a validity index for the quantified parameters. A VAF of 100% indicates that the linear model fully predicts the measurements. Noise, nonlinearities and other unmodelled behavior reduce the VAF. Note that a low coherence (noise or nonlinearities) always results in a low VAF values.

To calculate the VAF the model is simulated in time with the disturbance, $d(t)$, as input and the simulated position, $\hat{x}_h(t)$, and simulated muscle activation, $\hat{a}(t)$, as the outputs. Because both the hand position and muscle activation are available from measurements, the VAF is calculated for both:

$$\text{VAF}_x = 1 - \frac{\sum_n |x_h(t_n) - \hat{x}_h(t_n)|^2}{\sum_n |x_h(t_n)|^2} \tag{3.21}$$

$$\text{VAF}_a = 1 - \frac{\sum_n |a(t_n) - \hat{a}(t_n)|^2}{\sum_n |a(t_n)|^2} \tag{3.22}$$

in which n indexes the time sampled vector. All signals are high pass filtered to remove drift, before calculating the VAF (3th order Butterworth, 1 Hz). The lumped muscle activation signal is reconstructed from rectified EMG signals and consequently contains high frequency components. To remove these components the lumped muscle activation is low pass filtered (3th order Butterworth, 10 Hz) before calculating the VAF.

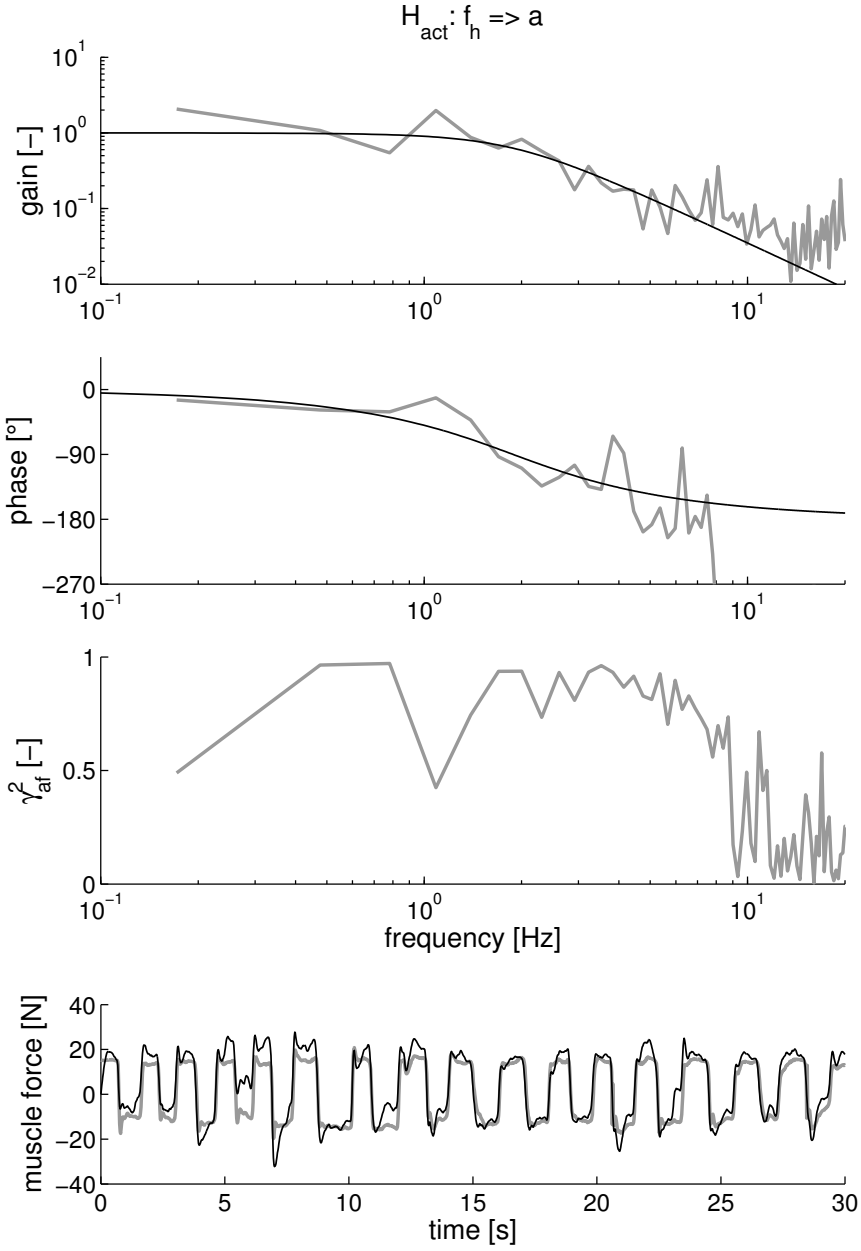

Figure 3.3: *From top to bottom: gain and phase of the FRF of activation dynamics, coherence, and a 10 seconds fragment of the recorded hand force. Black lines: model/simulation; grey lines: estimation/measurement.*

Table 3.2: *Estimated eigenfrequency, f_0, and relative damping, β, of the activation dynamics for all subjects.*

subject	f_o [Hz]	β [-]
1	1.88	0.80
2	2.58	0.77
3	2.03	0.74
4	2.00	0.74
5	2.37	0.64
mean (SD)	2.17 (0.29)	0.74 (0.06)

3.3 Results

3.3.1 Activation dynamics

Fig. 3.3 shows the estimated FRFs of the activation dynamics and the coherence for a typical trial of one subject. For this trial the coherence was relatively high to 8 Hz, meaning that the estimate of the FRF is reliable to this frequency. For frequencies beyond 8 Hz the coherence dropped, which was likely the result of low input power at these frequencies. Similar figures were found for other trials and subjects. Fig. 3.3 also shows the fitted model for the activation dynamics for this subject. The lower plot of Fig. 3.3 shows the time course of the measured and predicted hand force. The predicted force resembled the recorded force very well, only at the sharp transits, i.e. higher frequencies, the force slightly deviated from the measurements. However during the main experiment these higher frequencies were dominated by the arm mass and the mismatch will be of little concern.

In Table 3.2 the estimated parameters are given for all subjects. The average values over the subjects were 2.17 Hz for the eigenfrequency and 0.74 for the relative damping. These values were used for the estimation of the intrinsic and reflexive parameters.

3.3.2 Nonparametric FRFs

In Table 3.3 the average RMS of the hand position over the subjects is given. The RMS of the hand position was always approximately 3 mm, except for NB Type 2 disturbances with center frequencies higher than 5 Hz. These disturbances only contained power above the eigenfrequency of the arm, which is approximately 3 Hz. The admittance at these frequencies was primarily determined by the arm mass, which would require uncomfortably large forces to accelerate the arm. For this reason the amplitude of the force disturbance was reduced explaining the smaller amplitudes. The mean EMG varied slightly around one, indicating that the co-activation of the muscles was almost equal for all *stiff* conditions (Table 3.3).

Figs. 3.4-3.6 show the FRFs and coherences for one and the same subject during the WB, NB1, and NB2 conditions respectively. For all conditions the coherence of the handle position was higher than 0.95. The coherence of the muscle activation

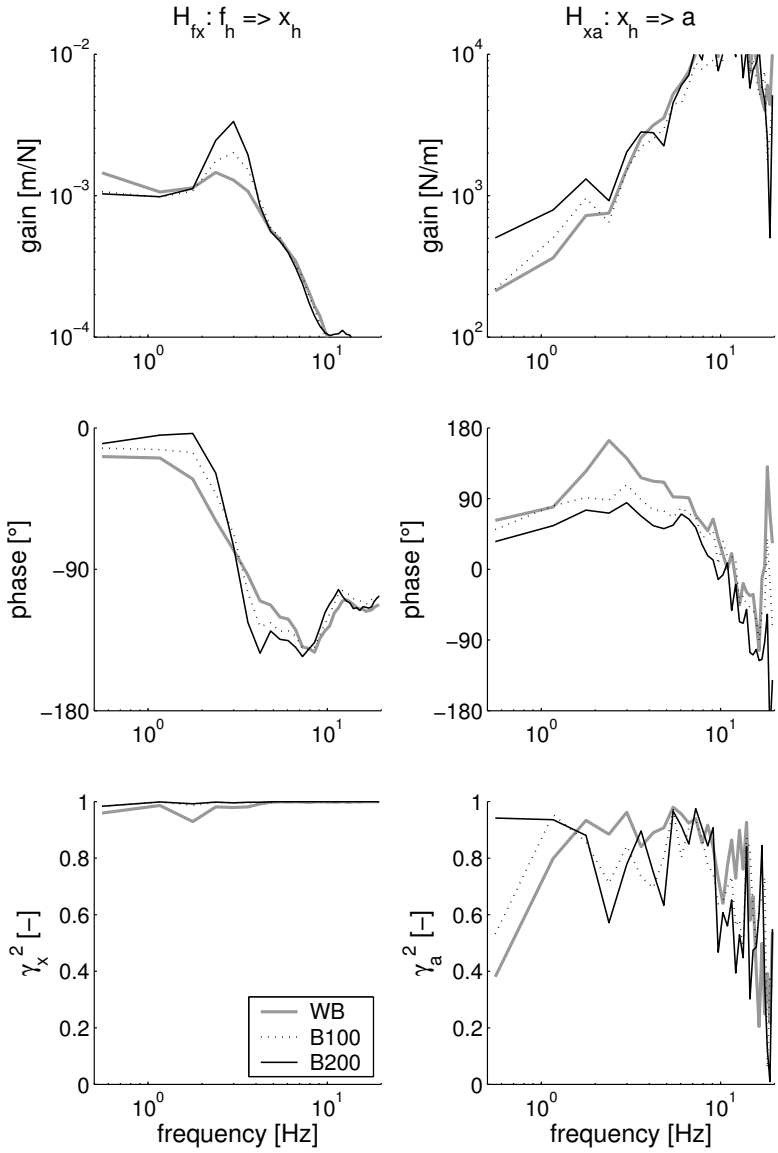

Figure 3.4: *The FRFs of a typical subject for the mechanical admittance (left) and the reflexive impedance (right) together with corresponding coherences for WB disturbances with increasing damping. Upper row: gain; middle row: phase; bottom row: coherences.*

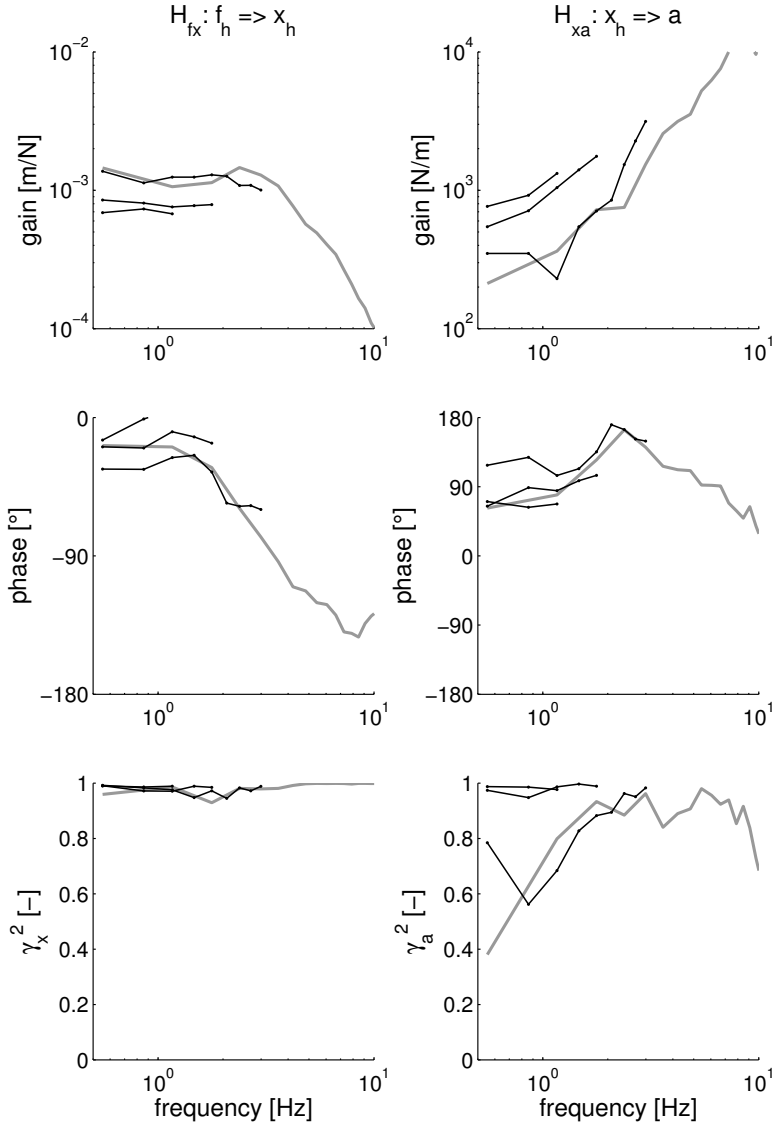

Figure 3.5: *The FRFs of a typical subject for the mechanical admittance (left) and the reflexive impedance (right) together with corresponding coherences for NB1 disturbances. Upper row: gain; middle row: phase; bottom row: coherences. The grey line denotes the reference condition*

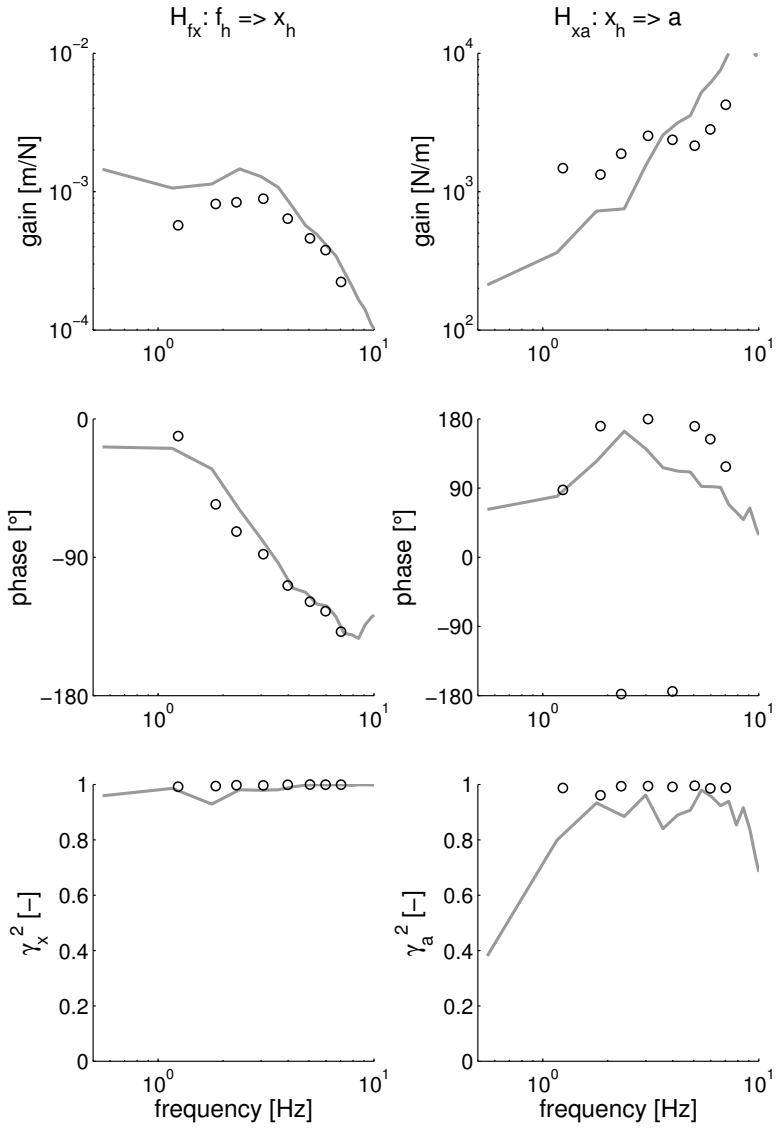

Figure 3.6: *The FRFs of a typical subject for the mechanical admittance (left) and the reflexive impedance (right) together with corresponding coherences for NB2 disturbances. Upper row: gain; middle row: phase; bottom row: coherences. The power of the disturbances is concentrated in a small bandwidth around a centre frequency denoted with the circles. The grey line denotes the reference condition*

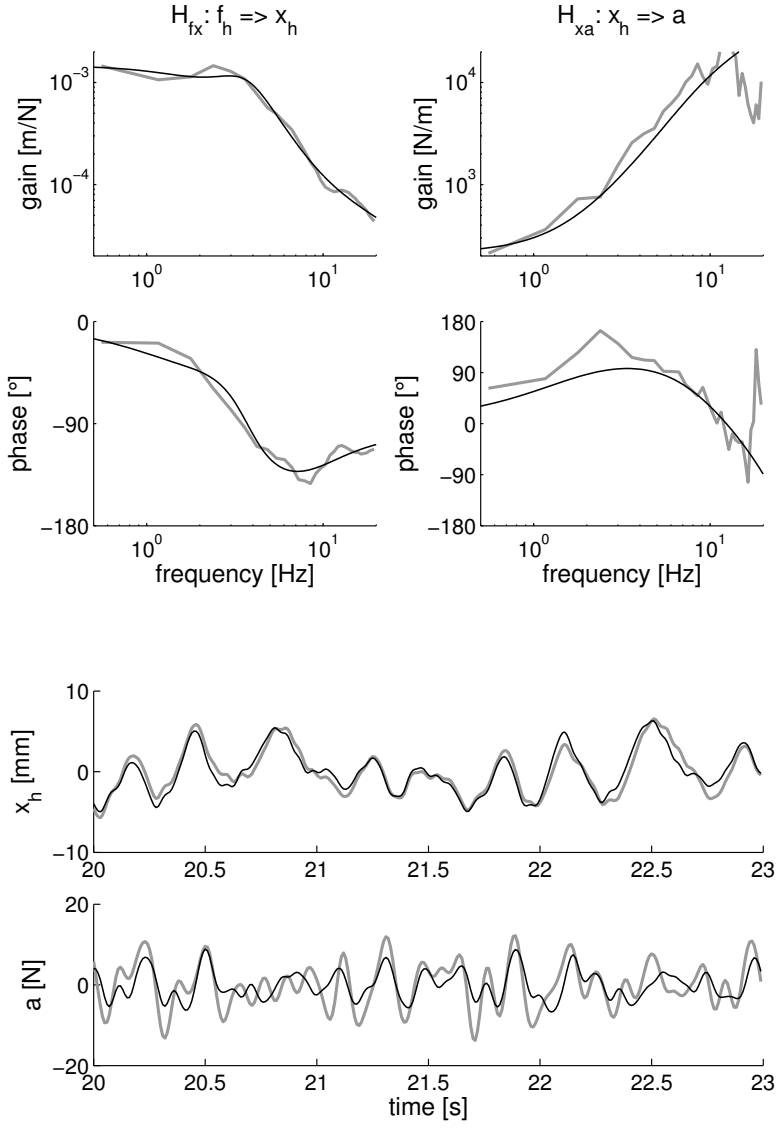

Figure 3.7: *Top: FRFs of the admittance (left) and reflexive impedance (right) for reference condition for a typical subject. Grey lines: estimates; black lines: model fits. Bottom: a 3 second time fragment of the handle position, $x_h(t)$, and the muscle activation, $a(t)$. Grey: measurements; black: model simulations.*

Table 3.3: *Root-mean-square (RMS) value of the hand position and muscle activity for all conditions. Mean (SD) over all subjects.*

condition		RMS [mm]	u_0 [-]
WB		3.3 (0.4)	1 (-)
B50	50 Ns/m	3.1 (0.6)	1.02 (0.05)
B100	100 Ns/m	3.1 (0.4)	0.95 (0.05)
B150	150 Ns/m	3.2 (0.5)	0.96 (0.09)
B200	200 Ns/m	3.2 (0.5)	0.93 (0.10)
NB1	1.2 Hz	3.1 (0.8)	0.95 (0.11)
NB1	1.5 Hz	3.2 (0.8)	0.94 (0.11)
NB1	1.8 Hz	3.2 (0.7)	0.95 (0.12)
NB1	2.4 Hz	3.5 (0.9)	1.01 (0.11)
NB1	3.1 Hz	3.7 (0.6)	1.01 (0.09)
NB1	3.7 Hz	3.3 (0.6)	0.99 (0.12)
NB2	1.3 Hz	3.0 (0.5)	0.98 (0.12)
NB2	1.8 Hz	2.9 (0.7)	1.05 (0.11)
NB2	2.3 Hz	3.0 (0.8)	0.99 (0.10)
NB2	3.0 Hz	2.7 (0.5)	1.03 (0.13)
NB2	4.0 Hz	3.0 (0.7)	1.06 (0.16)
NB2	5.0 Hz	2.5 (0.4)	0.95 (0.11)
NB2	6.0 Hz	2.1 (0.4)	0.97 (0.16)
NB2	7.0 Hz	1.8 (0.3)	0.98 (0.16)

was relatively high for the frequencies between 1 and 10 Hz. With external damping the admittance decreased at low frequencies compared to the WB condition (i.e. the arm became stiffer), and the peak at the eigenfrequency around 3 Hz increased. Note that the combined arm-environment system remained well damped due to the external damping. The gain of the reflexive impedance increased with damping (upper-right plot in Figure 3.4). The phase of the reflexive impedance is primarily determined by velocity feedback (differential action introducing 90 degrees phase advance at all frequencies), position feedback (zero degrees for all frequencies) and a time delay (zero phase lag at 0 Hz and increasing lag with higher frequencies). With the reference condition (WB *stiff*) the phase advance at 0.5 Hz was approximately 70 degrees, indicating that at these frequencies velocity feedback was substantial. With the increase of the external damping the phase advance at 0.5 Hz decreased, indicating that position feedback was more pronounced.

Figure 3.5 shows that for the NB1 condition the admittance decreased with decreasing bandwidth. The peak around the eigenfrequency was not visible since the eigenfrequency was not excited by the NB1 disturbances. The reflexive impedance increased for smaller disturbance bandwidth and was almost 3 times larger for the smallest bandwidth compared to the reference condition.

For all NB2 conditions the gain of the admittance was lower compared to the reference condition (Fig. 3.6). However the reflexive impedance was increased for center frequencies up to 3 Hz, and smaller for higher center frequencies. The phase

Table 3.4: *Estimated parameters for the reference condition and the condition with task slack. Mean (SD) over the subjects.*

	reference (WB *stiff*)		WB *slack*
m [kg]	2.02 (0.39)	$\Longleftrightarrow$	2.02 (0.39)
b [Ns/m]	32.5 (10.1)		14.4 (4.2)
k [N/m]	382 (181)		169 (45)
b_g [Ns/m]	228 (94)		44 (32)
k_g [kN/m]	11.7 (6.0)		2.6 (1.9)
k_a [Ns^2/m]	2.3 (0.5)		zero
k_v [Ns/m]	37.4 (16.3)		zero
k_p [N/m]	91 (145)		zero
τ_d [ms]	28.4 (4.9)		-

lead of the reflexive impedance was larger compared to the reference condition at nearly all frequencies.

3.3.3 Intrinsic and reflexive parameters

In Fig. 3.7 the model fit is shown for a typical subject during the reference condition. In Table 3.4 the estimated parameters for the reference condition are given, together with the parameters for the condition with task *slack*. Fig. 3.8 shows the quantified parameters averaged over all subjects for all conditions together with the VAF values for position and muscle activation. The values for VAF$_x$ (solid lines in Fig. 3.8) were generally high, i.e. higher than 90%. Only for the NB1 conditions with f_h smaller than 2 Hz the VAF$_x$ was slightly smaller. The values for VAF$_a$ varied around 50% for most conditions. Both the coherence and the VAF for the muscle activation were smaller than one, most likely due to the presence of noise in the EMG recordings. To severely reduce the noise in the signals all irrelevant frequencies, i.e. not excited by the force disturbance, were removed from the measured position and muscle activation. Noise reduction was performed by applying FFT, setting power to zero at all irrelevant frequencies, and then inverse transformation to time domain (by inverse FFT). The VAF values for these noise-reduced signals are indicated with gray lines in Fig. 3.8. The usage of the noise-reduced signals increased the VAF$_a$ to values around 60% for the damping conditions and even to 90% for the NB2 conditions. The VAF$_x$ increased to values above 90% for all conditions.

The acceleration feedback decreased with damping from around 2 Ns^2/m for the reference condition to 1 Ns^2/m for the highest external damping. As expected from the FRFs of the reference condition, the reflexive impedance was dominated by velocity feedback, which was approximately equal to the intrinsic damping. The position feedback gain increased with external damping, while velocity feedback remained almost constant. For the condition with the highest external damping the position feedback was in the same size as the intrinsic stiffness. This implicates that for this condition approximately 50% of the overall stiffness is of reflexive origin.

For the NB1 conditions both position and velocity feedback increased with de-

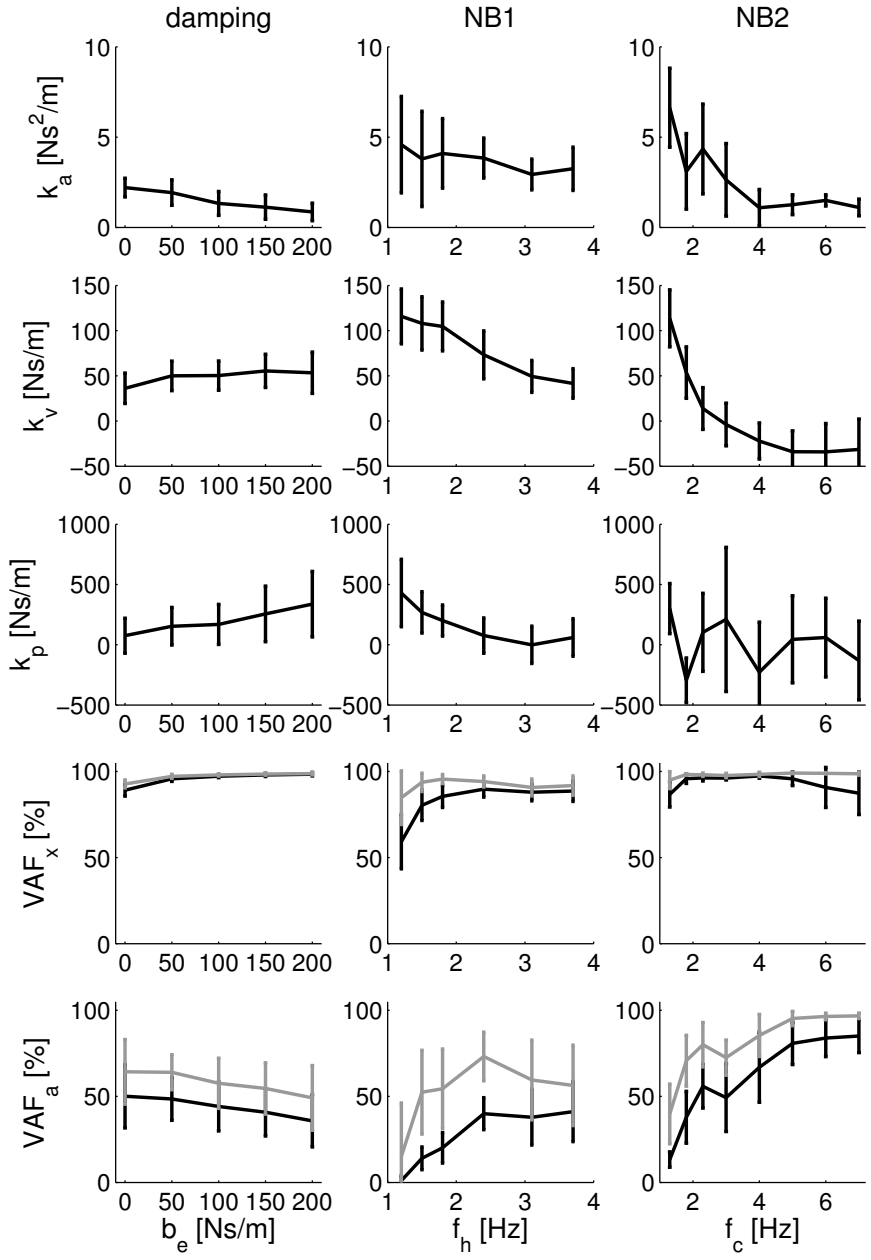

Figure 3.8: *Estimated reflex gains (k_a, k_v, k_p) and corresponding VAF values (VAF_x, VAF_a). Left column: external damping conditions; middle column: NB1 conditions; right column: NB2 conditions.*

creasing bandwidth. For the largest bandwidth the reflex gains approached to the values corresponding to the reference condition. The mean values for the acceleration feedback gains did not show a clear trend with external damping. For the smallest bandwidth the standard deviations was relatively high, most likely as acceleration feedback has minor effect on low frequencies.

For the NB2 conditions both the acceleration and velocity feedback increased with decreasing center frequency. The standard deviation of the position feedback is high and no trend is seen over the conditions. The high standard deviation indicates that the position feedback gain can not be quantified accurately for these conditions and has minor effect for these disturbances.

3.4 Discussion

3.4.1 Methodology

In this study a method is developed to quantify the dynamic properties of proprioceptive reflexes in vivo. This method is an important tool to evaluate the regulation of spinal reflexes during posture tasks. The use of force disturbances appeared natural to the subjects, facilitating the application of an unambiguous position task. Reflex gains were quantified by fitting linear models onto estimated input-output behavior. Both the mechanical admittance and reflexive impedance were estimated on which a linear NMS model was fitted. The incorporation of the reflexive impedance into the quantification method is new and gives direct insight into the contribution of the underlying reflexive feedback system to the overall mechanical behavior of the arm. The method has the advantage that intrinsic and reflexive parameters, including the neural time delay, can be estimated simultaneously.

The estimated coherences were high, justifying the usage of linear models. Below 1 Hz and above 10 Hz the coherence of the muscle activation was relatively low, which is likely is the result of uncorrelated corrective muscle contractions to prevent drifting of the hand position and noise inherent to EMG. The estimated FRFs of the arm admittance showed that reflexes are effective in increasing the mechanical resistance to external force disturbances, as indicated by smaller mechanical admittance and higher reflexive impedance (Figs. 3.4-3.6). The quantified parameters resulted in accurate model predictions of both hand position and muscle activation, as proved by the high VAF values for almost all experimental conditions. The small standard deviation of the estimated time delay indicates that this parameter is obtained with high accuracy. A mean value of $\pm$ 29 ms means that the identified reflexive feedback system is mediated via monosynaptic neural connections, i.e. the short latency spinal pathways. Clear trends in the estimated reflex gains were seen which indicate that the reflex system adapts to the external conditions applied. This study shows that for some condition half of the joint stiffness is of reflexive origin.

3.4.2 Functionality of reflexes

The findings of this study add to understanding of the functionality of proprioceptive reflexes. The feedback controller is the series conjunction of muscle activation dynamics, muscle spindle dynamics and a time delay. The effect of the feedback controller is explained graphically from the feedback model shown in Fig. 3.9, using two different estimated parameter sets corresponding to the reference condition (black lines) and to the NB1 (f_h=1.2 Hz) condition (gray lines). The muscle spindles tend to increase the feedback gain with frequency (left column) while activation dynamics causes attenuation with increasing frequency (middle column). As a result, length and velocity feedback are most effective because these properties are manifest within the bandwidth of the activation dynamics ($\pm$ 2 Hz). Beyond this bandwidth, high frequency gain from acceleration feedback (10^2 amplification per frequency decade) is canceled due to the same amount of attenuation from the activation dynamics. Hence, the feedback system acts as a proportional-differential-proportional (PDP) controller in series with a time delay, as can be seen from Figure 3.9 (right column). The effectiveness of the reflexive controller is strongly limited by substantial phase lag at higher frequencies due to the neural time delay. Attenuation of the gain at higher frequencies by the activation dynamics is therefore advantageous to facilitate position and velocity feedback, which are effective at low and intermediate frequencies. Without such an attenuation, position and velocity feedback gains would be severely limited to avoid unstable behavior.

Besides stability as an ultimate bound, the feedback gains are determined by performance demands. High position and velocity feedback gains decrease the admittances at frequencies below the eigenfrequency of the arm ($\pm$ 3 Hz), i.e. decrease the sensitivity to external force disturbance (De Vlugt et al., 2001; Schouten et al., 2001). However, due to the presence of phase lags from neural time delays and activation dynamics, high feedback gains also result in oscillatory behavior around the eigenfrequency which worsen performance. In the case of the NB1 condition containing only low frequencies, the eigenfrequency is not excited and oscillations will not occur. Therefore large feedback gains are beneficial to the performance for NB1 conditions (Fig. 3.9, gray lines). Furthermore, external damping suppresses the oscillation of the arm such that large feedback gains are also beneficial for these conditions (see Fig. 3.4). Taken together, high feedback gains improve performance at low frequencies but tend to destabilize the arm around the eigenfrequency. Apparently, the CNS modulates the feedback gains by trading off performance against stability. Future model optimization studies could determine to what extent the quantified feedback gains found in this study are optimal.

3.4.3 Comparison with previous work

The experimental conditions applied in the present study were similar to those used in previous studies by our group (De Vlugt et al., 2002; Van der Helm et al., 2002). The main trends in the quantified position and velocity feedback gains are comparable, albeit that in the previous studies the velocity feedback gains were

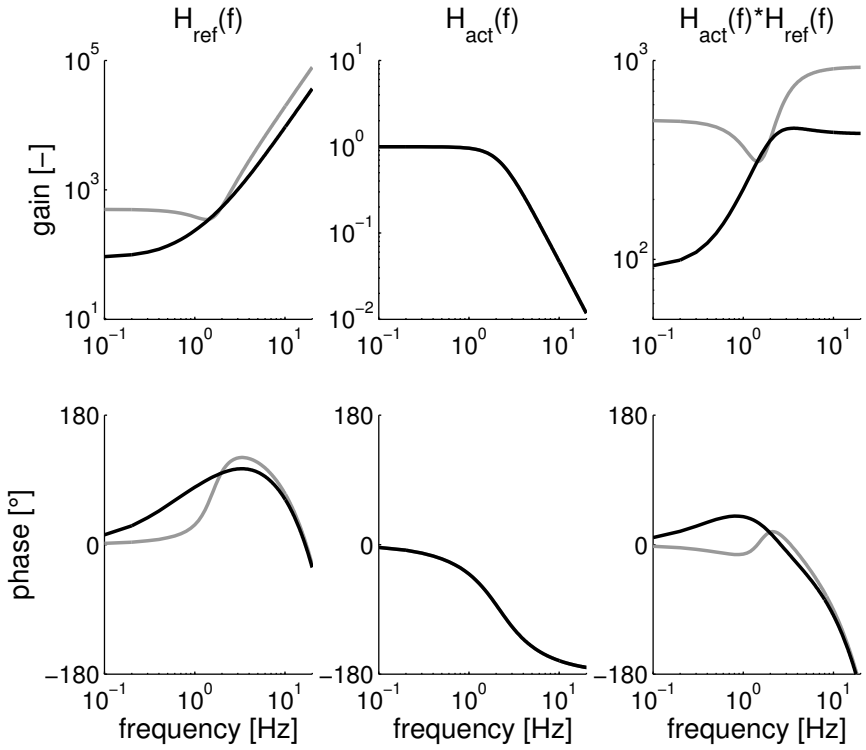

Figure 3.9: *Gain (upper row) and phase plots (bottom row) of the reflexive feedback $H_{ref}(f)$ (left column), the activation dynamics $H_{act}(f)$ (middle column) and the combined feedback controller as the cascade of both models $H_{act}(f) * H_{ref}(f)$ (right column). Parameter sets corresponding to the estimated values for the reference condition (black lines) and the NB1 ($f_h = 1.2Hz$) condition (grey lines).*

underestimated. The explanation is twofold. The first is presence of reflexive feedback during the reference condition and the second is the smaller bandwidth of the muscle activation dynamics. In the previous studies the reflexive feedback could not be identified directly and therefore it was assumed that the reflexes were negligible for wide bandwidth disturbances (reference condition) in order to separate the intrinsic and reflexive contributions. This study showed that velocity feedback was indeed present during the reference, hence velocity feedback was underestimated in the previous studies. In this study the activation dynamics were quantified, where in the previous studies a general model was adopted a-priori from literature, having a bandwidth of 5 Hz. This study proves that such a bandwidth is too high, and therefore the previously estimated velocity feedback gains were lower as a compensation.

In this study muscle activation dynamics was modelled as a second order sys-

tem. The quantified cut off frequency is 2.17 Hz and the relative damping is 0.75. These values are comparable to those found in the literature. Potvin et al. (1996) found a rather wide range for trunk extensor muscles (2.0-3.3 Hz) while Bobet and Norman (1990) identified the elbow flexor and extensor muscles and found values of 1.9-2.8 Hz. Olney and Winter (1985) estimated values of 1.0-2.8 Hz for lower limb muscles during walking.

In this study, an acceleration term was included in the reflexive feedback to describe the reflexive impedance at higher frequencies. Kukreja et al. (2003) showed that linearization of an unidirectional velocity sensitivity results in higher order terms including a pronounced acceleration term. In a recent study, the reflexive impedance was estimated from a nonlinear NMS model including unidirectional velocity sensitivity (Stienen et al., 2003). The gain and phase characteristics were comparable to those found in this study (Figs. 3.4-3.6) showing a clear second order (acceleration) response. This suggests that acceleration feedback is an artifact of muscle spindle unidirectionality rather than a distinct sensory function.

Chapter 4

The effect of position and force tasks on human arm admittance

David Abbink, Erwin de Vlugt, Alfred C. Schouten, Frans C. T. van der Helm
to be submitted to *Biological Cybernetics*

The goal of this study is to determine the effect of position and force tasks on human arm dynamics. Endpoint arm dynamical properties are described by the mechanical admittance which determines the hand position as a dynamic function of an external force imposed at the hand. Endpoint admittance incorporates the effects of underlying neuromuscular properties and is gives direct insight into the disturbance rejection of the human limb. It is known that humans are able to modify their admittance by adaptation of three mechanisms: a) intrinsic muscle visco-elasticity, b) muscle spindle stretch and stretch velocity feedback, and c) muscle force feedback from golgi tendon organs (GTOs). The effect of different posture tasks on these three mechanisms are qualified from a functional perspective. These qualifications are judged on the basis of two hypotheses. The first is that during position tasks, the mechanical resistance to external forces increases (admittance decreases) due to intrinsic muscle visco-elasticity and reflexive properties from muscle spindles. The second is that during complementary force tasks, the mechanical resistance decreases from reduced intrinsic and reflexive spindle contributions and additionally from a pronounced force feedback of the GTOs.

Experiments were performed to estimate the arm admittance by frequency response functions (FRFs). Continuous force and position perturbations were applied at the hand alternately, while subjects ($n = 10$) were instructed to minimize either their hand displacements or hand reaction force. Inspection of the estimated admittance and comparison with model simulations confirmed the hypotheses qualitatively. All estimated admittances roughly resemble that of a second-order system, with 4 subjects showing a distinct local increase in the FRF gain and phase around 10 Hz for all experimental conditions. From the model it was found that there is strong interdependence between reflexive feedback and intrinsic properties in their potential contribution to endpoint arm admittance. Particularly between GTO and

muscle spindle feedback. The local increase is explained by a subject dependent relatively large GTO feedback gain.

It is concluded that position tasks entail considerably lower admittances and more co-contraction than force tasks. GTO activity was most likely present for 4 subjects irrespective they performed a position or force task and probably was invariant for each subject. Muscle spindle feedback appeared to be reduced during the force tasks and therefore seems not functional to control endpoint force.

4.1 Introduction

The neuromusculoskeletal system is equipped with different mechanisms that are potentially effective in compensating for external disturbances. This study focuses on the peripheral mechanisms that control the motion and forces of the human arm, being: 1) intrinsic visco-elasticity from activated muscles and 2) monosynaptic reflexive feedback from muscle spindles and golgi tendon organs (GTO). The effectiveness of these mechanisms - especially reflexive feedback - and their combined effect on the mechanical properties of the human arm are largely unknown. In this study the contributions of those mechanisms are analyzed for two different tasks: posture maintenance and force maintenance. In daily life, both tasks occur frequently and are characterized by small variations around a working point.

For the maintenance of posture, intrinsic stiffness and damping from cocontracting muscles is effective though energy-consuming. Muscle stiffness and damping vary simultaneously with muscle activation that is determined by supra-spinal commands. Muscle spindles provide reflexive information on muscle stretch and stretch velocity, and excite the alpha motor neuron, increasing overall stiffness and damping. Reflexive muscle activity only occurs in response to perturbations, and is therefore energy-efficient. However, the effectiveness of the feedback loop is limited by its inherent time delay. Experimental studies have shown that muscle spindle activity depends on task instruction (Doemges and Rack 1992a; 1992b), the level of muscle contraction (e.g. Jaeger et al. 1982), the displacement amplitude (Cathers et al. 1999), the bandwidth of the perturbation signal (Van der Helm et al., 2002) and the mechanical properties of the environment the subject interacts with (De Vlugt et al. 2002).

The influence of the task instruction is very difficult to determine from the literature. Doemges and Rack (1992a; 1992b) used transient perturbations to study the influence of position and force tasks. They found that position tasks entailed more reflexive activity than force tasks. Cathers et al. (1999) applied continuous position perturbations to the wrist while the subjects had to maintain a background force. They estimated frequency response functions (FRFs) between the wrist displacement and muscle activation from electro-myography (EMG) and attributed the results to muscle spindle feedback. In general, they showed that feedback gains increase with decreasing perturbation amplitude and increase with the level of background torque. Agarwal and Gottlieb (1977a) applied continuous force perturbations to the ankle joint where the subjects had to maintain a constant torque.

Table 4.1: *Four hypotheses to be tested in the present study.*

		Position Task	Force Task
1)	Admittance	low	high
2)	Co-contraction	high	low
3)	Muscle spindle feedback gain	high	low
4)	GTO feedback gain	low	high

Based on the estimated FRFs, they concluded that there was no indication of reflex contributions. Another study by Jaeger et al. (1982) used transient torque perturbations to the wrist and found that the fastest (monosynaptic) response in EMG was not modified when the subjects had to change their tasks from 'do not intervene' to 'maximally resist'. Comparisons and results between the different studies are difficult to interpret due to the abundance of different experimental conditions: the type of perturbation (force or position, transient or continuous) and the task required by the subject (position or force tasks, minimal or maximal level of intervention). Additionally, very scarce information of the GTO functionality exists. It is known that GTOs provide force feedback and have an inhibitory effect onto alpha motor neurons. Whether the amount of force feedback can be modified is not known. In this study it is expected that this inhibitory effect reduces the overall mechanical resistance of the joints to external force disturbances.

When studying the effect of task instruction on motion control, it is important to understand the functional difference between position tasks and force tasks. Position tasks are present in many daily situations like driving a car or riding a bike, in which cases the limb is disturbed by force perturbations (position perturbations render the task impossible). High stiffness and damping (i.e. small endpoint admittance) are functional to suppress the effect of force perturbations. It is therefore hypothesized that during position tasks intrinsic muscle visco-elasticity (by co-contraction) dominate over GTO feedback.

Force tasks (implying position perturbations) require a constant force to be exerted on an object, and occur less frequently in daily life, e.g. maintaining the pressure on a pen when writing in a train. Force tasks are best accomplished when the subject is compliant (i.e. large endpoint admittance) and moves along perfectly with the imposed displacements, whereas a high resistance to movements results in undesired high reaction forces. Intrinsic muscle visco-elasticity and muscle spindle feedback are therefore counterproductive. It is hypothesized that during force tasks GTO feedback is pronounced and that muscle spindle feedback and intrinsic visco-elasticity is reduced.

Both hypotheses are summarized in Table 4.1. The contribution to endpoint behavior of visco-elastic muscle properties, spindle and GTO feedback were determined by analysis of the estimated admittance FRFs and by qualitative comparison with a linear neuromusculoskeletal (NMS) model.

The results indicated that the estimated endpoint admittance is lower for position tasks primarily due to large levels of co-contraction compared to force tasks. A sensitivity analysis made clear that severe interchange existed between muscle spindle and GTO feedback parameters due to the complementary effect of both to the overall endpoint admittance. As a result, the contribution of GTO feedback could not be clearly derived from the estimated FRFs. In 4 subjects and irrespective the task, a local change in the admittance was clearly visible. A systematic model analysis indicated that this effect is the result of a substantial and invariant GTO feedback, which is different amongst subjects. Muscle spindle feedback was found to be reduced during force tasks and therefore seems not functional to control endpoint force.

4.2 Methods

4.2.1 Subjects

Ten subjects (5 females) between the age of 20 to 25 participated in the experiment. All subjects were right-handed, and had no medical record of neurological disease or arm injuries and were not familiar with the purpose of this study. Subjects gave informed consent to the experimental procedure.

4.2.2 Apparatus and signals

A hydraulic manipulator is used that generates either force or position perturbations in one direction. The subjects interacted with the manipulator through a handle, which they were instructed to hold firmly with their right hand (see Fig. 4.1). On a computer monitor in front of the subject, position (or force) was plotted against a reference line that represented the target position (or force). The hand force on the manipulator handle $f_h(t)$ and its position $x_h(t)$ were measured.

Two types of perturbation signals were used: force perturbations and position perturbations. During force perturbations the manipulator acts as an impedance controller with negligible stiffness and viscosity, and a minimum virtual mass of 0.6 kg. The force perturbation enters the system by adding it to the measured hand force. In the case of position perturbations, the handle was controlled by a strong position servo that simply dictates the motion, irrespective of the applied hand reaction force.

Force perturbations were generated off-line in the frequency domain. Four rectangular spectra were used containing power at frequencies from 0.5 Hz to 1.5 Hz, 2.5 Hz, 3.5 Hz or 20 Hz. Within each bandwidth, the power was equal for all frequencies present in the signal. The mutual phase shift between all sinusoidal components had random values with a uniform distribution between 0 and 2π rad. Inverse fourier transform resulted in unpredictable time signals with a duration of 40 seconds. Intrinsic visco-elastic properties (co-contraction level) and reflexive properties that are of interest in this study, can be taken as time invariant in response to these disturbances (Van der Helm et al. 2002). The magnitude of the force

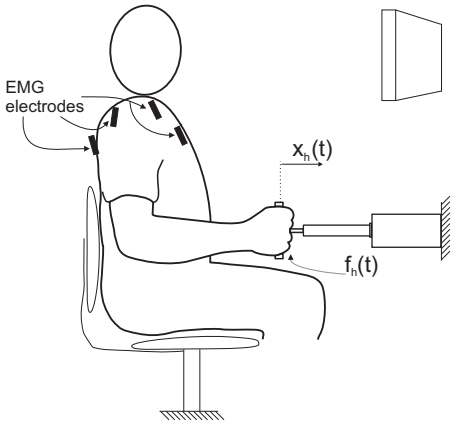

Figure 4.1: *The experimental setup, showing a subject seated in front of the the monitor, holding the handle of the manipulator. The forearm is horizontally aligned and the elbow is 90 degrees flexed. Four EMG electrodes were placed to record activation signals of relevant shoulder muscles. The hand motion $x_h(t)$ and the force of the hand on the stick $f_h(t)$ are measured. Hand motion is constrained by the manipulator, so that only movements in anterior-posterior direction are possible.*

perturbations was determined for each bandwidth during test trials, so that the resulting average absolute displacements were comparable (6-8 mm). The recorded displacements during the force perturbations were stored and applied as position perturbations, when required. Such a strategy guarantees that displacements have approximately the same magnitude for each combination of task and perturbation, so that non-linear effects due to amplitude dependencies are avoided.

EMG signals of four muscles were measured by differential surface electrodes. Latissimus dorsi and deltoid posterior muscles cause a backward arm motion (pull, antagonists) from the target position, while deltoid anterior and pectoralis major muscles cause a forward motion (push, agonists). All EMG signals were preamplified, high-pass filtered (20 Hz, third-order Butterworth), amplified, rectified and smoothed (100 Hz low pass, third order Butterworth). Position, force and EMG signals were measured via analogous to digital conversion with 16-bit resolution at 250 Hz sample frequency and digitally stored for further analysis.

4.2.3 Experimental Procedure

The experiment consists of two parts, each with a different task. In the first part subjects were instructed to maintain a constant position (position task, PT), in the face of different bias forces (constant over a trial). In the second part they were required to maintain constant force levels (force task, FT). All non-zero force levels required the subject to push forward. Without informing the subject, position perturbations (PP) and force perturbations (FP) were randomly applied for each of

Table 4.2: *Structure of the experiment. Each combination of task and position was applied eight times (four different bandwidths, two repetitions). During the functional tasks (PT-FP and FT-PP) three additional force levels were investigated. Illogical tasks (PT-PP and FT-FP) were only investigated for one level of (bias) force. A single trial lasted 40 seconds.*

Task		Perturbation type: Position	Perturbation type: Force
Position (Part 1)	Notation	PT-PP	PT-FP
	Bias Force	0 %MVC	0, 15, 25 %MVC
	#trials	8	3×8 = 24
	Functionality	Illogical task, any effort is useless	Logical combination
Force (Part 2)	Notation	FT-PP	FT-FP
	Force Level	0, 15, 25 %MVC	25 %MVC
	#trials	3×8 = 24	8
	Functionality	Logical combination	Illogical task, considerable drift expected

these two tasks. Note that PT-FP and FT-PP are logical combinations of task and perturbation. The other two combinations are illogical: for PT-PP it is impossible to minimize the hand displacements, while for FT-FP the hand position is not determined (neither by the task, nor by the perturbation) and is therefore liable to drift. The illogical combinations are only used to investigate the influence of the perturbation type on the admittance.

Subjects were trained for the logical combinations only and during 15 minutes prior to the start of the actual experiment. A 15 minute break separated both halves of the experiment. Each trial is defined by a combination of a) task, b) perturbation type, c) mean generated force (called bias force for PT, and force level for FT) and d) signal bandwidth. Each trial was presented twice, for averaging purposes.

Before the main experiment, subjects were asked to alternately push and pull as hard as they could for three seconds. Maximal pushing and pulling forces were measured by an AMTI force transducer (type MC3-6-500). Startup effects were excluded by rejecting the first second. Subsequently, force and EMG signals were averaged over the trial time, and these averages were again averaged over three repeating trials, yielding the MVC force and a value EMG_{max} for each muscle. Mean EMG signals measured during the main experiment were scaled with EMG_{max} of the corresponding muscles. This method yields a normalized EMG signal $nEMG$ ($=\frac{EMG}{EMG_{max}}$) for each of the four muscles, which is used for comparison between subjects.

Position task

In the first part subjects were instructed to minimize deviations during 32 trials. During PT-FP trials an additional bias force was added to the force perturbation, equaling 0%, 15% or 25% of the subjects' maximal voluntary contraction (MVC). This bias force was compensated for when subjects succeeded in maintaining their position. Note that a bias force is impossible to apply during PT-PP trials. The total number of force perturbation trials (FP) is 24 (three bias forces, four bandwidths, two repetitions), while the total number of position perturbation trials (PP) is 8 (four bandwidths, two repetitions).

The top row of Table 4.2 summarizes the trials presented during position tasks. The trials were presented in random order with a 40 second rest period between each trial to prevent fatigue.

Force task

In the second part, subjects were instructed to maintain a steady force during 32 trials. During FT-PP trials the force levels were 0%, 15% and 25% of the MVC. During FT-FP only the maximal force level was used (25%), since the inherent position drift appeared to be smaller for larger force levels. The applied force perturbations were scaled down so that approximately the same displacements occurred as during PT-FP. The total number of PP trials is 24 (three force levels, four bandwidths, two repetitions), while the total number of FP trials is 8 (four bandwidths, two repetitions).
The bottom row of Table 4.2 summarizes the trials presented during force tasks. The trials were presented in random order with a rest period of 15 seconds in between, because force tasks are less fatiguing than position tasks.

4.2.4 System identification

The first 8 seconds of the signal were not used for identification, to eliminate the effects of initial adaptation after the perturbation onset. The measured position and force signals were transformed to the frequency domain using the fast fourier transform (FFT). Non-parametric estimations of the human arm FRF were calculated using cross-spectral densities.

Application of position perturbations excludes any interaction between the subject and the manipulator. Therefore, an open-loop identification procedure is used for PT-PP and FT-PP trials with the position perturbation as the input and the hand reaction force as the output. The transfer function, or impedance, is estimated by:

$$\hat{H}_{XF}(f) = \frac{\hat{G}_{xf}(f)}{\hat{G}_{xx}(f)} \tag{4.1}$$

where $\hat{H}$ denotes the estimated FRF. $\hat{G}_{xf}$ is the cross-spectral density of $x_h(t)$ and $f_h(t)$, while $\hat{G}_{xx}$ is the auto-spectral density of $x_h(t)$.

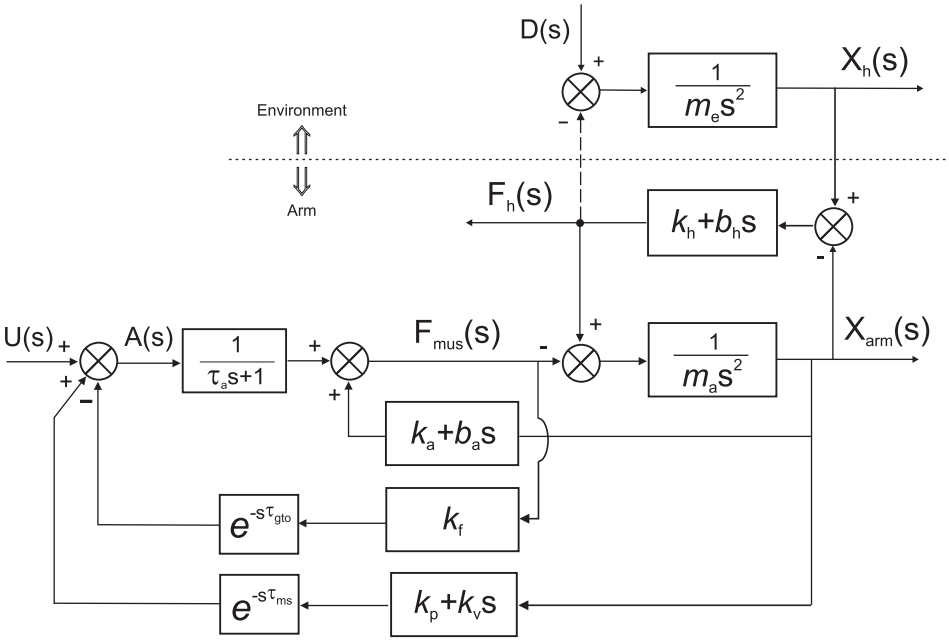

Figure 4.2: *Linear blockscheme comprising the human arm, hand and the environment (s is the laplace operator). The reflexive and intrinsic parameters are lumped. All parameters are discussed in the text. $U(s)$ represents the variations of a lumped supraspinal signal representing neural projections on the alpha motoneuron. These variations are assumed to be zero during the experiments. $A(s)$ is the muscle activation signal; $F_{mus}(s)$: lumped muscle force; $F_h(s)$: (measured) hand reaction force; $X_h(s)$: (measured) hand position; $X_{arm}(s)$: arm position; $D(s)$ external force perturbation. In case position perturbations are applied, there is no interaction between the human arm and the environment: the dotted connection (vertical arrow) is void (see text).*

For force perturbations (PT-FP, FT-FP) a closed-loop identification procedure is required (De Vlugt et al., 2002; Van der Helm et al., 2002). The closed loop configuration emerges because interaction exists between the manipulator ($m_e = 0.6$ kg) and the human arm. To separately estimate the FRF of the human arm, an external signal is needed from outside the closed loop for which the external force perturbation $d(t)$ is used. The relationship between the hand reaction force (input) and the hand position (output), i.e. the arm admittance, is estimated by:

$$\hat{H}_{FX}(f) = \frac{\hat{G}_{dx}(f)}{\hat{G}_{df}(f)} \tag{4.2}$$

The term $\hat{G}_{dx}$ is the cross-spectral density of $d(t)$ and $x_h(t)$, whereas $\hat{G}_{df}$ is the the cross-spectral density of $d(t)$ and $f_h(t)$. All spectral densities were averaged over eight adjacent frequencies to reduce the variance.

To verify the appropriate usage of linear models, the coherence function is estimated. For Eqs 4.1-4.2 the coherence is determined according to:

$$\hat{\Gamma}_{XF}(f) = \sqrt{\frac{|\hat{G}_{xf}(f)|^2}{\hat{G}_{xx}(f)\hat{G}_{ff}(f)}} \tag{4.3}$$

$$\hat{\Gamma}_{FX}(f) = \sqrt{\frac{|\hat{G}_{dx}(f)|^2}{\hat{G}_{dd}(f)\hat{G}_{xx}(f)}} \tag{4.4}$$

This function is an indication of the amount of linearity of the system in response to the external perturbation. The coherence varies between 0 and 1 and decreases due to external noise and nonlinearities.

4.2.5 Linear arm model

A linear model comprising arm and hand dynamics is given in Figure 4.2. The model contains: the environment; intrinsic muscle stiffness and damping; handgrip visco-elasticity; muscle activation dynamics; position and velocity feedback from muscle spindles; and force feedback from GTOs. The model is represented in the frequency domain where s denotes the laplace operator.

The motion of the arm inertia is defined by

$$X_{arm}(s) = H_i(s)\left[F_h(s) - F_{mus}(s)\right] \tag{4.5}$$

where

$$H_i(s) = \frac{1}{m_a s^2}$$

with m_a the lumped endpoint inertia of the arm. The total force acting upon the arm is the sum of the hand reaction force $F_h(s)$ and the opposed force exerted by the muscles $F_{mus}(s)$.

$$F_{mus}(s) = H_{act}(s)A(s) + H_{ve}(s)X_{arm}(s) \tag{4.6}$$

Equation (4.6) defines the muscle force, which exists of an intrinsic and an activation component. Intrinsic muscle stiffness and damping is described by

$$H_{ve}(s) = k_a + b_a s$$

with k_a the lumped muscle stiffness and b_a the lumped muscle damping at endpoint level. The stiffness and damping are increased by activating the muscles. Muscle activation describes the process of active muscle force build-up following a neural activation signal $A(s)$, and is approximated by a first order process having a time constant τ_a of 30 ms (Winters and Stark, 1985)

$$H_{act}(s) = \frac{1}{\tau_a s + 1}$$

The activation signal $A(s)$ is the result of muscle spindle and GTO feedback, according to

$$A(s) = H_{ms}(s)X_{arm}(s) - H_{gto}(s)F_{mus}(s) + U(s) \tag{4.7}$$

with

$$H_{ms}(s) = (k_p + k_v s)\, e^{-s\,\tau_{ms}}$$

the muscle spindle dynamics. The parameters k_p and k_v represent the gains of the monosynaptic stretch and stretch velocity feedback. $U(s)$ represents the variations in the supraspinal signal, which are thought to be zero. A time delay of τ_{ms}=30 ms is taken that approximates the time elapse of the neural signal traveling from the spindles to the spinal cord and back to the muscle (De Vlugt et al. 2002). GTO dynamics are described by a force feedback gain k_f and a time delay equal to that used for spindle feedback (τ_{gto}= 30 ms).

$$H_{gto}(s) = \; k_f\, e^{-s\,\tau_{gto}}$$

Compared to muscle spindle afferents that excite the alpha motoneuron (i.e. activate the muscle), GTO feedback has an inhibitory effect. Hence the minus sign in Eq. (4.7).

Displacements of the handle within the handgrip, due to skin displacement and movement of the fingers, is represented by a first order system

$$F_h(s) = H_h(s)\,[X_h(s) - X_{arm}(s)] \tag{4.8}$$

with

$$H_h(s) = k_h + b_h s$$

Hand elasticity and viscosity are represented by k_h and b_h respectively.

Because the FRF of the arm is always estimated separately, the environment is excluded from the model analysis (indicated by the dotted horizontal line in Figure 4.2). The complete lumped model of the arm at endpoint level follows from (4.5)-(4.8). By default, the arm model is expressed as an admittance, i.e. from $F_h(s)$ to $X_h(s)$. The following model equation is the result:

$$\frac{X_h}{F_h} = \left[H_h^{-1} + \frac{H_i\,[1 + H_{act}H_{gto}]}{1 + H_{act}H_{gto} + H_i\,[H_{act}H_{ms} + H_{ve}]}\right] \tag{4.9}$$

Substituting the parameters and structuring the terms in Eq. (4.9) results in a well-organized model equation

$$\frac{X_h}{F_h} = \frac{1}{b_h s + k_h} + \frac{1}{m_a s^2 + Bs + Ks} \tag{4.10}$$

with B and K the compound damping and stiffness, respectively

$$B = \frac{b_a + k_v H_{act}\, e^{-\tau_{ms}}}{1 + k_f H_{act}\, e^{-\tau_{gto}}}$$
$$K = \frac{k_a + k_p H_{act}\, e^{-\tau_{ms}}}{1 + k_f H_{act}\, e^{-\tau_{gto}}}$$

The blockscheme (Fig. 4.2) is a proper representation in case force perturbations are applied. However, the model can also be used for position perturbations. In that case, interaction between the human arm and the manipulator is absent, which is represented by the dotted vertical arrow in the blockscheme (Fig. 4.2). Consequently, the hand position is only determined by the external force perturbation $D(s)$, according to

$$X_h(s) = \frac{1}{m_e s^2} D(s) \tag{4.11}$$

When the perturbation signal is amplified (multiplied) by $m_e s^2$, than (4.11) changes into

$$X_h(s) = \frac{1}{m_e s^2} m_e s^2 D(s) = D(s) \tag{4.12}$$

The force perturbation signal actually has become the position perturbation signal, assuming the attached payload of the human arm has negligible effect on the imposed position. For this condition, $X_h(s)$ can be considered as the input and $F_h(s)$ as the output of the system.

4.3 Results

4.3.1 Experimental results

All estimated FRFs are shown as admittances to facilitate comparison. The admittance - denoted by H_{est} - represents $\hat{H}_{XF}^{-1}$ in case of position perturbations, and $\hat{H}_{FX}$ in case of force perturbations. Admittance can be thought of as a measure of the displacement magnitude due to a force. A large admittance represents low stiffness and damping, entailing large displacements. Functional force tasks (FT-PP) with force levels of 0%, 15% and 25% of MVC are denoted as FT-0, FT-15 and FT-25. Functional position tasks (PT-FP) with force levels are denoted as: PT-0, PT-15 and PT-25. The most important results are summarized in Table 4.3.

Influence of task on admittance

Figure 4.3 shows the admittance gain, phase and coherence for a typical subject, during perturbations with a 20 Hz bandwidth for both PT-0 and FT-0. Coherence

Table 4.3: *Summarized results for all four combinations of task and type of perturbation. Different (bias) force levels and perturbation bandwidths are only applied for the two functional combinations (PT-FP and FT-PP). An increase is indicated by upward arrows (↑); a decrease is indicated by downward arrows (↓).*

Task		Perturbation type: Position	Perturbation type: Force
Position (Part 1)	Notation	PT-PP	PT-FP
	Functionality	-	low admittance, high co-contraction
	Bias Force ↑	-	admittance: similar EMG: agonist ↑
	Bandwidth ↓	-	admittance: ↓ EMG: constant
	Comment	Strongly resembles PT-FP any effort is useless Force (EMG) not determined	
Force (Part 2)	Notation	FT-PP	FT-FP
	Functionality	high admittance, little co-contraction	-
	Force Level ↑	admittance: ↓ EMG: agonist ↑	-
	Bandwidth ↓	admittance: similar EMG: constant	-
	Comment		Strongly resembles FT-PP Position not determined

was generally high (>0.9) for all subjects and for all trials, indicating that the estimated (linear) FRFs almost completely describe the input-output behavior. Lower coherence values (≈ 0.6) were found during FT-0, only at very low frequencies.

Three important differences were seen between behavior during position tasks and during force tasks. First, at low frequencies, force tasks cause a larger admittance than position tasks. The top-right figure in Fig. 4.3 shows the relative admittance for eight subjects (two are excluded since they could not perform a force task well). The relative admittance is the FT-0 admittance normalized by the PT-0 admittance. Values above one signify an increase in admittance during FT-0 compared to PT-0, which was found to be statistically significant up to 2.5 Hz (Student's two-tailed T-test, $p < 0.05$).

Second, force tasks cause a larger admittance than position tasks at higher frequencies also. During FT-0 tasks the increase was especially strong for four subjects, as can be seen in the relative admittance (Fig. 4.3, top-right).

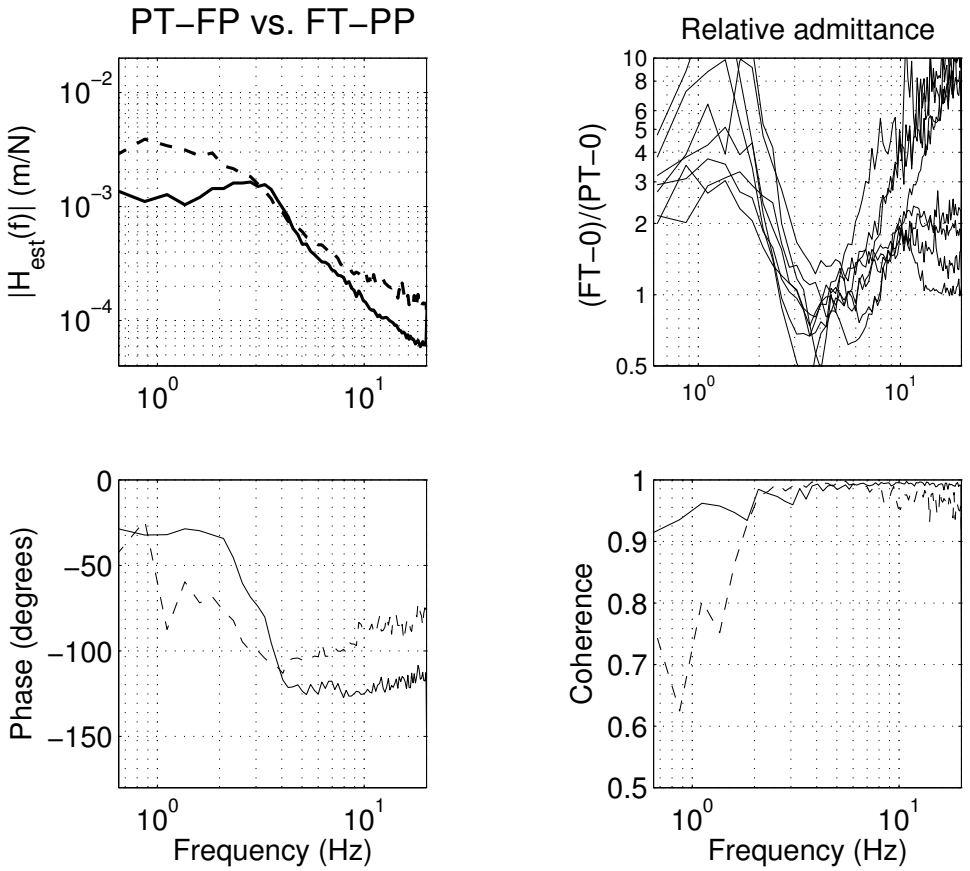

Figure 4.3: *Gain, phase and coherence of the estimated admittance H_{est} of a typical subject (DW), for position tasks during force perturbations (solid), and force tasks during position perturbations (dashed). The force level was 0% MVC for both tasks. The top right figure shows the relative admittance (for n=8), which is the admittance during FT-0 divided by the admittance during PT-0.*

Third, during PT the admittance shows a slight oscillation peak around 3 Hz, which is accompanied by a more apparent sharper phase descent (Fig. 4.3, left). FT admittances display a more damped nature, with an accompanying moderate phase descent. This effect was seen for most subjects (n=8).

Influence of perturbation type on admittance

All subjects indicated they did not notice that two different perturbation types were applied during a single task.

The top row of Fig. 4.4 shows the admittance during position tasks for both

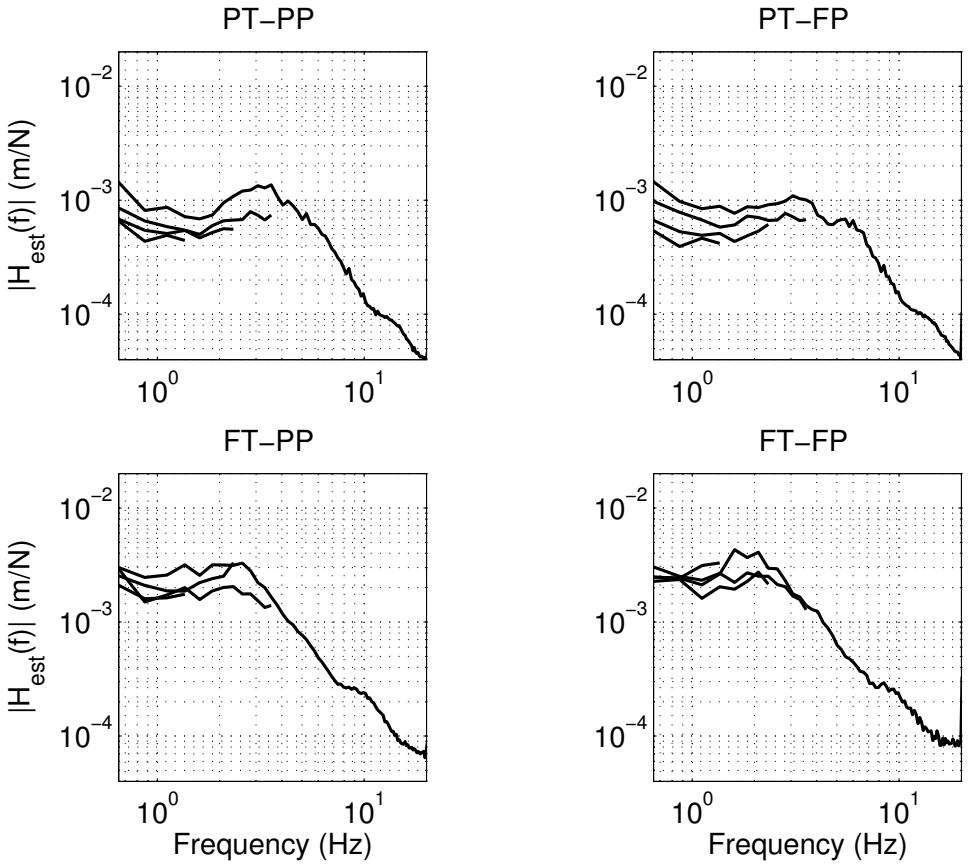

Figure 4.4: *Gain of the estimated admittance H_{est} of a typical subject (LK) shown for position tasks (top row) and force tasks (bottom row), with position perturbations (left column) and force perturbations (right column). The bias force level during position tasks was 0, and during force tasks 25% MVC.*

position and force perturbations. The admittances are similar, even though most subjects showed considerable and abrupt fluctuations in force during the illogical task PT-PP. The fluctuations were uncorrelated to the perturbations, and were also encountered in EMG measurements.

The bottom row of Fig. 4.4 shows the admittances during force tasks: FT-PP (left) and FT-FP (right). Both admittances are larger than during the PT admittances. During FT-FP, most subjects showed considerable (low-frequency) drift of the hand position, as was expected. Despite these fluctuations, it was still possible to estimate the admittance properly, although the coherence was slightly lower. The applied perturbation type does not substantially affect the admittance.

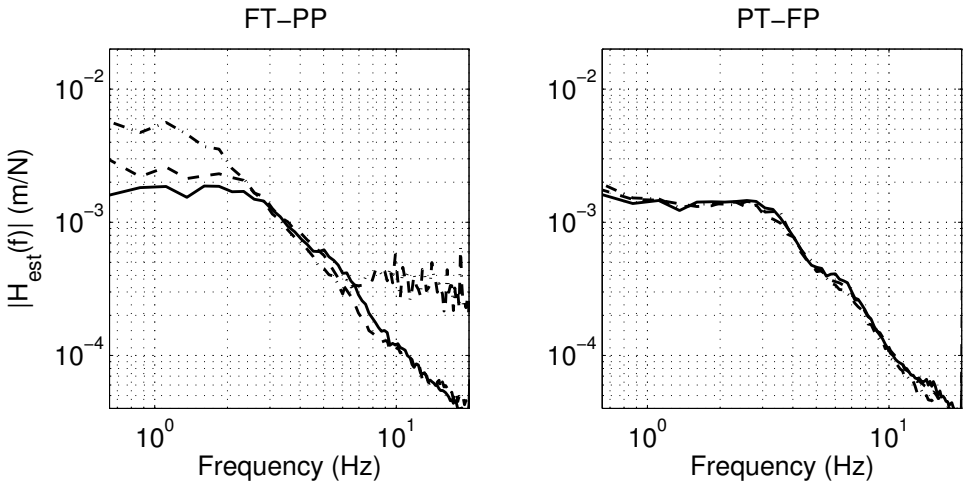

Figure 4.5: *Gain of the estimated admittance H_{est} of a typical subject (AS), for the functional tasks FT-PP (left) and PT-FP (right). For trials with a 20 Hz bandwidth, all force levels (or bias forces) are shown: 0% MVC (dash-dotted line), 15% MVC (dashed line) and 25% MVC (solid line).*

Influence of bandwidth on admittance

For all bandwidths, the admittance during PT-0 is shown in Fig. 4.4 (top row). For lower bandwidths the admittance was found to be smaller. This phenomenon was also found previously by (Van der Helm et al., 2002) for PT-FP trials. The present study adds the observation that the effect is independent of perturbation type (top row), and of bias force level (not shown here).

During force tasks the admittance did not change unambiguously with bandwidth. For most subjects the admittance did not change at all. Some difference between the four bandwidths was seen for three subjects. A clear trend, as during position tasks, could not be discerned (Fig. 4.4).

Influence of force level on admittance

During force tasks the admittance decreases at low frequencies for increasing force level, which is clearly visible in Fig. 4.5 (left). FT-0 yields the largest admittances and FT-25 the smallest, which was expected since larger muscle activation was required that simultaneously increase muscle stiffness. Most subjects (n=8) showed the decrease in admittance, which can be seen upon comparison of the top row of Fig. 4.6 with the top right figure in Fig. 4.3. The admittances during FT-15 and FT-25 are both larger than during PT-0 (statistically significant up to 2.5 Hz, p <0.05). During FT-0 the admittance is larger than during FT-15 and FT-25 (statistically significant up to 2 Hz, Student's two-tailed T-test, p <0.05, not shown).

During position tasks, admittance did not vary significantly with the bias force,

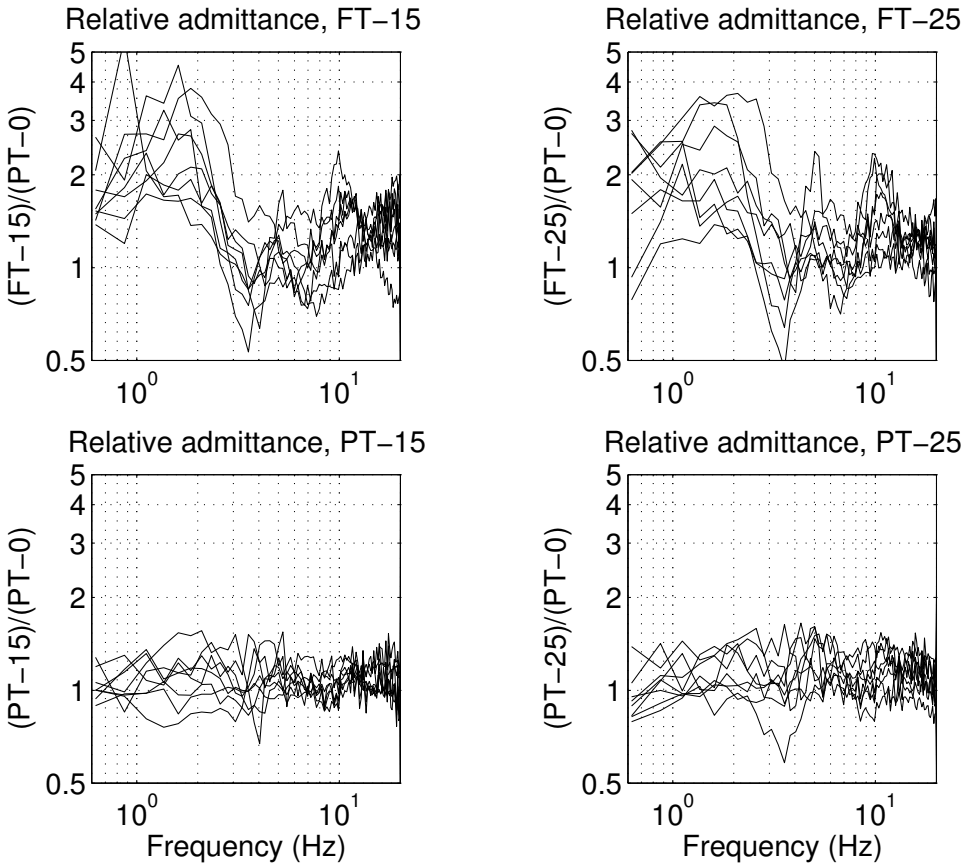

Figure 4.6: *Relative admittance for eight subjects, for the logical combinations PT-FP and FT-PP. The top row shows the relative admittances during FT-15 (left) and FT-25 (right). The bottom row shows the relative admittances during PT-15 and PT-25. A relative admittance of one means that the admittance is the same as during PT-0.*

which is illustrated for a typical subject in Fig. 4.5 (right) and for all subjects in the bottom row of Fig. 4.6.

The local increase around 10 Hz

Four out of ten subjects, all female, showed a distinct local increase in the gain and phase of their admittance around 10 Hz. This group of subjects is called group A. Fig. 4.7 shows a typical group A subject. The local increase is apparent during each combination of task and perturbation (logical or illogical), as can be seen in the admittance of another group A subject (Fig. 4.4). Shape and size of the local increase did not vary substantially with task, perturbation or (bias) force level, and

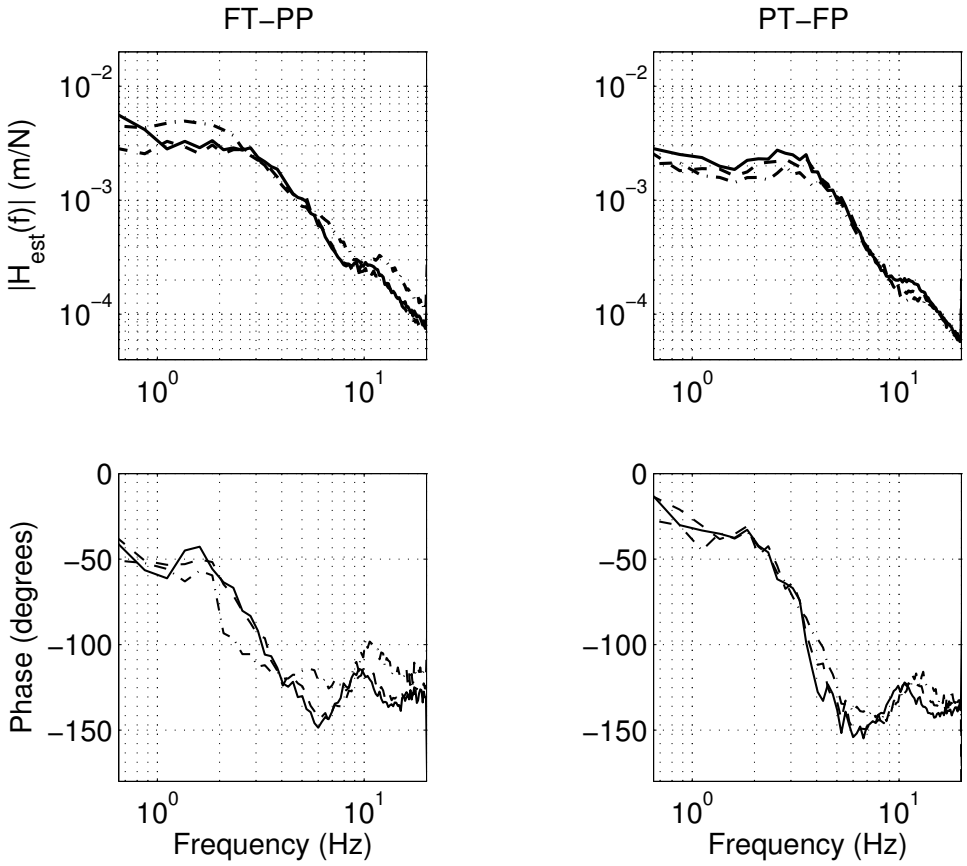

Figure 4.7: *Gain and phase of the estimated admittance H_{est} of a typical group A subject (SP), for FT-PP (left) and PT-FP (right). Notice the local increase in gain and phase around 10 Hz. For trials with a 20 Hz bandwidth, all force levels (or bias forces) are shown: 0% MVC (dash-dotted line), 15% MVC (dashed line) and 25% MVC (solid line).*

was approximately the same for the entire group A. The other six subjects (Group B) did not show this local increase, not for any task or perturbation (Fig. 4.8).

EMG results

During position task trials, $nEMG$ was highest for all muscles, usually 20-30% MVC for agonists and 10-20% mVC for antagonists. It is known that higher forces can be generated in a short burst (3 seconds) compared to when longer activity (40 seconds) is required, hence the 'low' percentages. $nEMG$ of each muscle was constant for different bandwidths of the signal, which agrees with previous studies in our group (van der Helm et al. 2002; De Vlugt et al. 2002). When a bias force was required, most subjects generated the extra force through increased agonist activity.

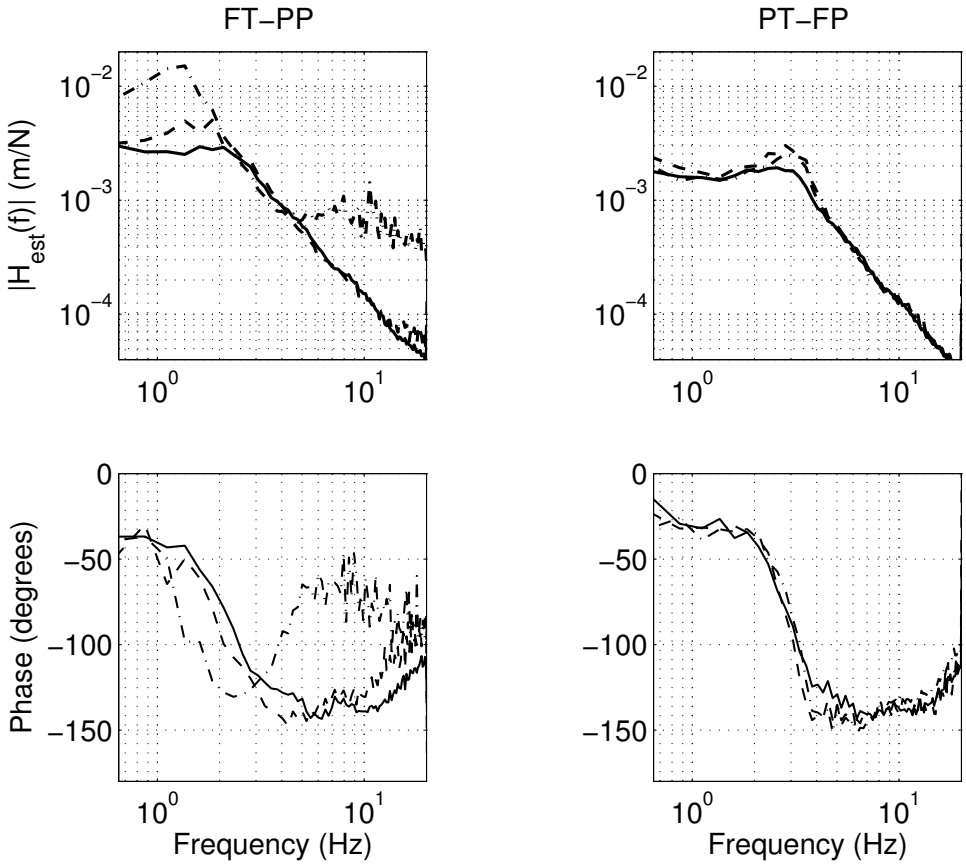

Figure 4.8: *Gain and phase of the estimated admittance H_{est} of a typical group B subject [PG], for FT-PP (left) and PT-FP (right). For trials with a 20 Hz bandwidth, all force levels (or bias forces) are shown: 0% MVC (dash-dotted line), 15% MVC (dashed line) and 25% MVC (solid line). The large values for the gains below 2 Hz (upper left) and above 5 Hz were the result of a slack handgrip, that occurred often for the FT-PP at 0% MVC.*

Two subjects showed an accompanying decrease in antagonist $nEMG$.

During FT-PP trials where subjects had to maintain a force level of zero (FT-0), $nEMG$ of both agonists and antagonists was very small (0-3%), indicating that active intrinsic feedback was almost absent. When the force level increased in magnitude (FT-15, FT-25), agonist activity increased considerably (to 10-20%). Antagonist activity usually remained smaller than 5%, indicating little co-contraction. For all FT trials, $nEMG$ signals did not change substantially with different bandwidths.

In short: $nEMG$ did not change with bandwidth of the perturbation signals; increased with bias force, and was higher during position tasks compared to force tasks.

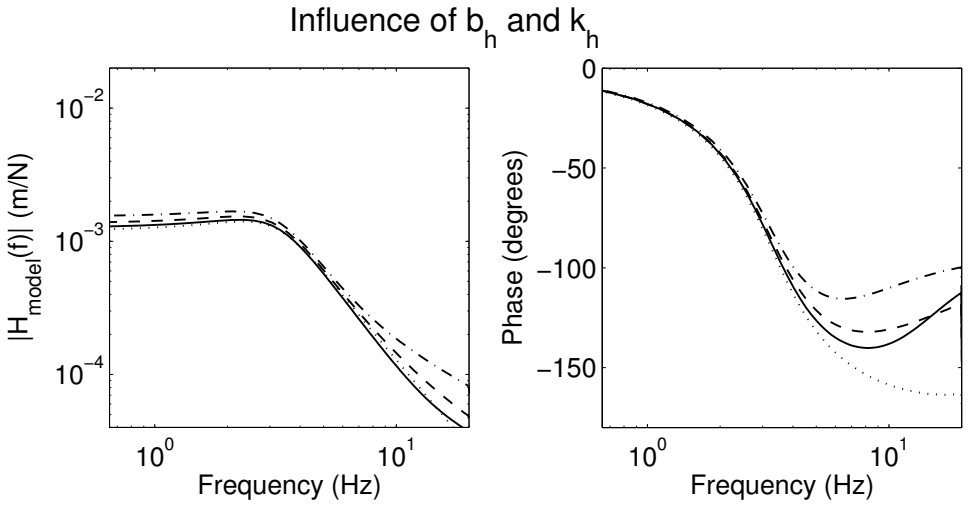

Figure 4.9: *Influence of decreasing handgrip parameters b_h and k_h on the model admittance gain and phase. The dotted line represents a simple MBK model (infinitely stiff handgrip), with $m_a = 2$, $b_a = 40$ and $k_a = 800$. The solid line represents the standardized handgrip (b_h=200, k_h=15000). The dashed line represents a slack handgrip (b_h=200, k_h=6000), whereas the dash-dotted line depicts a very loose handgrip (b_h=100, k_h=3000).*

4.3.2 Sensitivity analysis

The linear model (Eq. 4.10) is used to investigate the effect of lumped model parameters on endpoint arm admittance. The purpose of the model study is twofold: to search for characteristics of reflexive feedback in the arm admittance, and to explain experimental results such as: the presence of the local increase around 10 Hz; the slight oscillation peak (3-4 Hz); and the difference at high frequencies between position and force tasks.

Intrinsic parameters

The general dynamics of all estimated admittances roughly resemble that of a simple second order mass-spring-damper (MBK) system. When reflexive contributions are absent and the handgrip is infinitely stiff, all dynamics of the system can be described by a simple MBK system, as can be derived from (4.10) by setting all reflex gains to zero. The inertia m_a decreases high-frequency admittance, viscosity b_a increases damping and decreases medium-frequency admittance, and stiffness k_a decreases low-frequency admittance. Parameter values were chosen such that the modelled admittance resembles the estimated admittance for the PT-0 (20 Hz) condition. The parameter values are: $m_a = 2$ [kg], $b_a = 40$ [Ns/m] and $k_a = 800$ [N/m]) and are comparable with previous findings from our group (De Vlugt et al. 2002; Van der Helm et al. 2002).

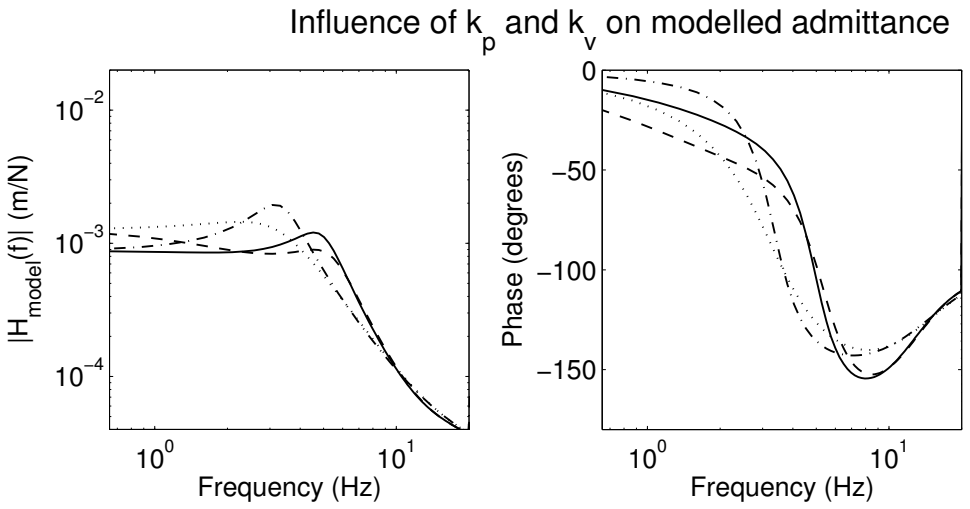

Figure 4.10: *Influence of increasing muscle spindle feedback gains k_p and k_v on the model admittance gain and phase. The dotted line represents the standard MBK model with the standardized handgrip. Dash-dotted line: k_p=400 and k_v=0. Dashed line: k_p=0 and k_v=40. Solid line: k_p=400 and k_v=40.*

Handgrip parameters

The model simulation in Figure 4.9 shows deviations due to decreasing grip viscosity b_h and grip stiffness k_h. The model admittance resembles PT admittances more closely for handgrip parameters b_h=200 and k_h=15000 (solid line), hereafter referred to as the standardized handgrip. For lower values of the handgrip parameters (dashed and dash-dotted lines) the high frequency admittance increase is more pronounced and approximates the estimated admittance (above 5 Hz) during force tasks (especially FT-0). Apparently, subjects did not maintain a constant grip over all trials, as some indicated after the experiment. Handgrip parameters are not the cause of an oscillatory peak around 3-4 Hz or the local increase around 10 Hz. Such deviations from an MBK system are most likely the effect of reflexive activity.

Muscle spindle parameters

As can be seen in Fig. 4.10, a high length feedback gain k_p decreases the admittance considerably at lower frequencies. An additional effect of high values of k_p can be seen in an oscillation peak around 3-4 Hz, with an accompanying sharp phase descent around that frequency. These effects strongly resemble those found from the estimated admittances during the PT conditions. Increasing the velocity feedback gain k_v also decreases the admittance (at lower and medium frequencies) and attenuates the oscillatory peak around 3 Hz. A combination of the two can result in a small admittance over a relatively large bandwidth.

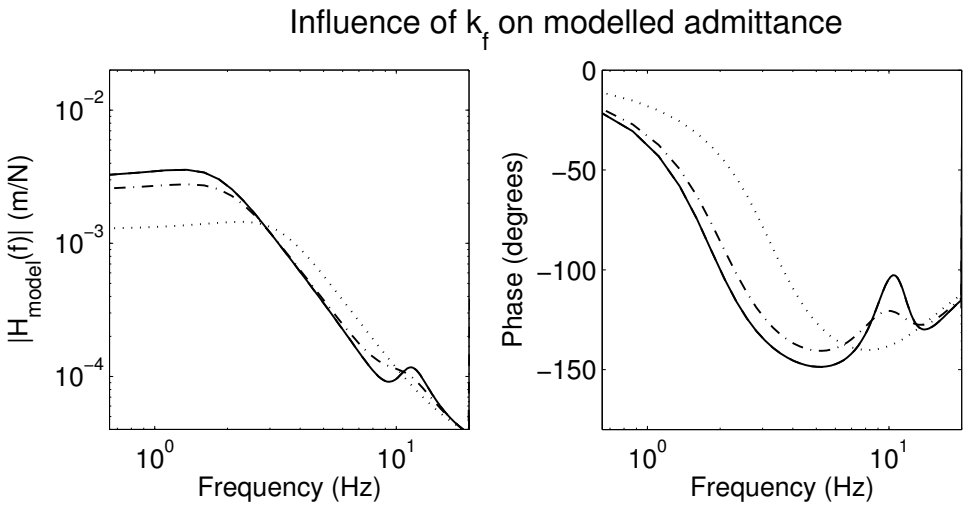

Figure 4.11: *Influence of increasing GTO feedback gains k_f on the model admittance gain and phase. The dotted line represents the standard MBK model with the standardized handgrip. Dash-dotted line: k_f=1. Solid line: k_f=1.5.*

GTO parameter

Figure 4.11 shows the effect of the GTO force feedback gain: when k_f is increased, the admittance will be larger at low and medium frequencies, counteracting the admittance-decreasing effect of muscle spindles and intrinsic feedback. For k_f gains higher than approximately 1, a local increase around 10 Hz arises, in the gain as well as in the phase. The local increase strongly resembles the local increase observed in estimated group A admittances.

Compensatory effect of reflexive parameters

Model results show that muscle spindles and GTO have an opposite effect on admittance, as was hypothesized. The extent to which muscle spindle activity can compensate for GTO activity can be seen in Fig. 4.12, where all lines are shown with the same force feedback gain (k_f=1.5). At low frequencies, length feedback k_p can compensate for the admittance-increasing effect of k_f, but at medium frequencies an accompanying oscillation peak at 3-4 Hz arises. Increasing velocity feedback gain k_v attenuates the oscillation peak, and also reduces the local increase at high frequencies (due to k_f). Theoretically muscle spindle feedback can *totally* compensate for GTO activity, which is illustrated by the solid line. Appendix B shows the remarkable (theoretical) interplay between both feedback contributions from muscle spindles and golgi tendon organs, given certain fixed values of intrinsic viscoelasticity. The simulations show that large reflex gains (solid line) result in the same admittance as a simple MBK system without any reflexes (dotted line). Due to the

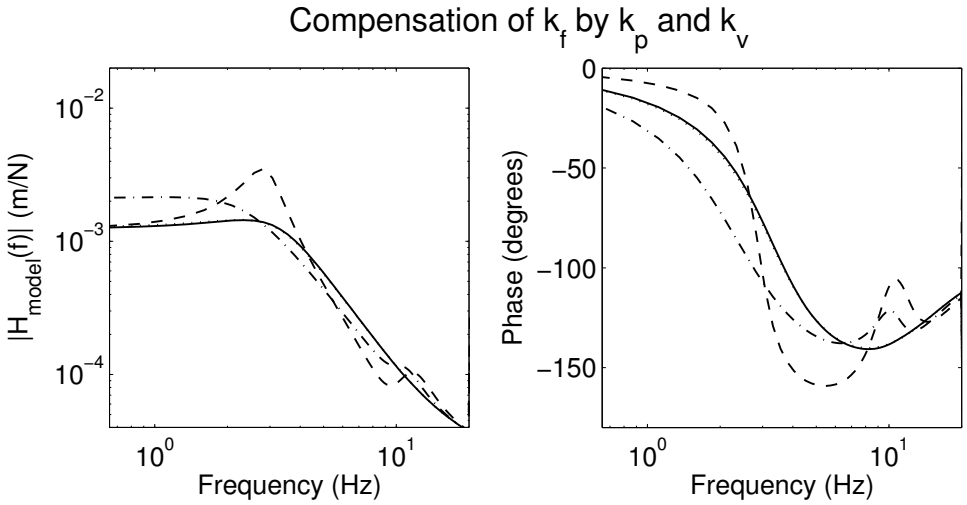

Figure 4.12: *Compensation of GTO gain k_f=1.5 by muscle spindle feedback gains k_p and k_v. The dotted line represents the standard MBK model without reflexes, with standardized handgrip dynamics(b_h=200, k_h=15000). Dashed-dotted line: k_f=1.5, k_p=400 and $k_v = 40$. Dashed line: k_f=1.5, k_p=1200 and $k_v = 0$. Solid line: k_f=1.5, k_p=1200 and $k_v = 60$.*

interplay between the model parameters, it is very difficult to identify intrinsic and reflexive contributions to the estimated endpoint admittance. Clues to the presence of reflexive activity can only be found in the deviations from an MBK model: a large local increase around 10 Hz indicates relatively high GTO activity, and a large peak around 3-4 Hz indicates relatively high muscle spindle activity. Unfortunately, such clues are not consistently found in all subjects.

4.4 Discussion

4.4.1 Experimental results

The experimental results (Table 4.3) support the hypothesis that subjects exhibit a smaller endpoint admittance during PT-FP than during FT-PP. Apparently, humans modify their arm admittance to optimally perform a task. All subjects indicated that position tasks were easier to learn and perform than force tasks. Two subjects even reported considerable difficulty in performing the force task. Inspection of the $nEMG$ showed that these subjects used relatively higher levels of co-contraction (higher antagonist activity) during force tasks compared to other subjects. This likely reflects the difficulty these subjects had in relaxing their antagonist muscles and generating an unilateral contraction, that would be optimal to the force task.

At frequencies below 1 Hz the estimated coherence function was relatively low for all subjects and conditions. This is probably due to corrective muscle contrac-

tions to prevent drifting of the hand position. Visual and tactile mechanisms involve long neural delays and are therefore considered unlikely to contribute to relatively fast changes in endpoint position or force above 1 Hz during the present experiment (De Vlugt et al., 2002). High values of the coherence above 1 Hz proves that the input output behavior at endpoint can be described accurately by a linear model. Non-linear properties, like e.g. the unidirectional sensitivity of muscle spindles, apparently had no effect on the endpoint behavior for the conditions applied.

Influence of perturbation type

During both position and force tasks, position and force perturbations were randomly applied to the subjects. During each task the estimated admittance was similar irrespective the type of perturbation, confirming the dominance of the subject's task perception. During the illogical conditions (PT-PP, FT-FP), all subjects were apparently fooled into functional behavior. The only differences with logical conditions were fluctuations of the hand force and position respectively. These fluctuations exist at very low frequencies only and were uncorrelated to the perturbation.

Influence of bandwidth

With decreasing bandwidth of the perturbation signal, the admittance decreases during PT. Since intrinsic feedback is independent of the bandwidth ($nEMG$ was constant), any changes in admittance are most likely due to reflexive activity (De Vlugt et al., 2002; Van der Helm et al., 2002). Results during FT show no consistent change with bandwidth, suggesting that GTO and muscle spindle feedback gains were not modified.

The results during PT are similar to those found by a previous PT study from our laboratory (Van der Helm et al., 2002). In that study, a similar model without GTO feedback was used to quantify the parameters by a model fitting procedure. On the assumption that GTO feedback was absent, reflexive and intrinsic parameters were quantified. It was also found that muscle spindle gains were higher for smaller perturbation bandwidths. The local increase around 10 Hz as simulated by our model and measured in the admittance, suggests the presence of GTO feedback even during PT trials. Theoretically, the decrease in admittance for lower bandwidths could also be the result of decreased GTO activity. However, the idea of modifying arm stiffness and damping properties by adjusting the gain of GTOs seems less appealing than gain regulation by muscle spindles. Moreover, there were no indications that subjects changed GTO feedback gain substantially, as discussed in Sec. 4.4.2). Therefore, it is likely that muscle spindles are responsible for the admittance decrease at lower bandwidths.

Influence of force level

During force tasks (FT), endpoint admittance decreased substantially with increasing force levels. However, during position tasks (PT), endpoint admittance did not

decrease for increasing bias force levels, in spite of higher agonist $nEMG$. Apparently, additional agonist activation does not further increase endpoint visco-elastic properties at high levels of co-contraction.

4.4.2 Simulation results

The model analysis gives much insight in how different feedback mechanisms contribute to the endpoint arm admittance. Two clues to the presence of substantial GTO and muscle spindle feedback were revealed: the local increase around 10 Hz and the oscillation peak around 3-4 Hz, respectively. Both effects were unfortunately not distinctive enough to provide the information necessary to further quantify the experiments: too much interplay between the parameters complicates accurate parametrization of individual feedback mechanisms.

At low frequencies ($<$ 3 Hz) the admittance is decreased by k_a (intrinsic stiffness) and by k_p and k_v (length and velocity feedback), while it is increased by k_f (force feedback). At medium frequencies (3-7 Hz) the admittance is decreased by b_a (intrinsic damping) and k_v. An oscillation peak arises for high values of k_p, yet it can be reduced by b_a, k_v and k_f. At high frequencies ($>$7 Hz) the admittance is decreased by k_h and b_h (handgrip) and by m_a (inertia). The local increase around 10 Hz (encountered in subjects A) is caused by a high k_f, yet it can be reduced by k_v and also by b_a (not shown). The fact that handgrip was not constant for different tasks complicated the interpretation of other parameters that influence high-frequency admittance. A more slack handgrip will result in lower mass estimations, and complicated comparisons between PT and FT. Therefore it is recommended for future studies that a constant, stiff grip is assured (possibly by using a cast), and that a separate estimation of endpoint inertia is used. This reduces the number of variable parameters substantially.

Although the reported interplay between intrinsic and reflexive feedback is undeniably present, the actual freedom in combinations of muscle co-contraction and afferent reflex gains is probably not as large as the model suggests. Reflex gains cannot be increased indefinitely, and might not be modified with full independence from intrinsic feedback. It is likely that an optimum is found between performance on one hand, and energy consumption and control effort on the other (Schouten et al. 2001). Intrinsic feedback is characterized by energy consumption, reflexive feedback by control effort.

Because position (and velocity) and force feedback are interdependent and even cancel eachother's effect in the case the arm admittance resembles a second order transfer function (Appendix B), quantitative measures of the reflexive system were not possible from the current analysis. The challenge remains to identify the relationship between reflexive and intrinsic activity for different tasks.

Muscle spindle activity

Muscle spindle activity is likely to be large during PT, and small or absent during FT, which is supported by two observations. First, an oscillation peak and a sharp

phase descent around 3-4 Hz. These characteristics were more prominent during PT than during FT for all subjects. The model study showed that these characteristics were the explicit results of muscle spindle feedback. The model study further confirms the hypothesis that muscle spindle activity decreases admittance (functional for PT, counterproductive for FT: Hypothesis 3 from Table 4.1).

Second, the bandwidth dependency encountered during PT is absent during FT. This effect is attributed to muscle spindle feedback: higher muscle spindle gains can increase the performance during PT for lower bandwidths. Muscle spindles are presumably not modified during FT, and are probably as low as possible. The second observations implies that muscle spindle gains are indeed much smaller for FT than for PT.

GTO activity

The local increase around 10 Hz is a clear indication of high GTO activity ($k_f > 1$). Experimental results suggest that - when present - GTO activity is constant, because: 1) the local increase is of approximately constant shape and size for all combinations of task, perturbation and force levels, 2) the local increase is even present during PT, where less GTO activity would result in a better performance, 3) the bandwidth dependency encountered during PT is absent during FT, suggesting that reflexive behavior was not modulated during FT, where extra GTO activity would result in a better performance. Apparently, subjects did not modify GTO feedback during the experimental conditions, either because it was not functional for the task, or because GTO activity can not be modified at all.

The question remains by what experimental condition GTO activity is provoked: under exactly the same experimental conditions 6 out of 10 subjects did not display the local increase, while the others did. Position and force tasks are not successful in isolating GTO feedback: the goal to be reached by the subjects can apparently be accomplished with different settings of the feedback mechanisms.

Comparing group A and group B subjects

The presence of the local increase did not relate to other subject characteristics like subject size, sportive activities, MVC, $nEMG$ level, magnitude of oscillation peak around 3-4 Hz, or the magnitude of their arm admittance. In other words: subjects from group A were not better or worse in their tasks, nor did they have anything in common that subjects from group B lacked. All four group A subjects were female, but group B also contained one female subject. Furthermore, upon inspection of PT-FP results from previous research in our group, some male group A subjects were found as well.

Intrinsic behavior is likely to be of comparable magnitude between both groups: group A subjects did not show higher values for $nEMG$ and F_{max} than group B subjects. We can only speculate on the difference in reflexive behavior between group A and B. A large local increase (group A) indicates a relatively large force feedback gain k_f, compared to group B subjects. More GTO activity should result

in a higher admittance, if all other feedback mechanism are constant. However, apart from the local increase there was no distinct difference in the magnitude of the admittance. Apparently the admittance-increasing effect of high GTO gains was somehow compensated for by a combination of intrinsic feedback and muscle spindle activity. Since intrinsic feedback is presumably comparable between group A and B and since it is highly energy consuming, it is not likely to have a large part in such compensation. Muscle spindle activity is more likely to compensate for the effects of GTO activity. After all, the absence of the local increase does not have to say that there is no GTO feedback, because muscle spindle feedback can cancel GTO feedback (Appendix B).

The length feedback gain k_p has been shown to compensate for most of the lower frequency effects but with an accompanying oscillation peak at 3-4 Hz. The velocity feedback gain k_v reduces the size of both the local increase and the oscillation peak. All group A subjects display a pronounced local increase, but not a particularly large oscillation peak (especially not during force tasks). Therefore it is considered likely that predominantly muscle stretch feedback (k_p) is present for Group A subjects, while enough k_v is present to attenuate the oscillation peak without diminishing the local increase. Unfortunately, such a speculation could not be proved by the current study.

4.5 Conclusions

From the estimated endpoint admittance of the human arm, it can be concluded that:

- Position tasks produce a smaller endpoint admittance than force tasks
- Position tasks result in higher levels of co-contraction than force tasks
- Task interpretation influences admittance substantially, while perturbation type does not. Subjects were fooled into displaying 'functional' behavior in an environment where their strategies were useless.

A linear model study was used to investigate the effect of reflexive feedback and intrinsic visco-elasticity on the endpoint arm admittance. The modelled admittance was compared to the experimental ones, bringing forward the following qualitative results:

- Substantial interplay was found between feedback mechanisms (muscle spindle and GTO) and intrinsic muscle visco-elasticity, facilitating many combinations of to obtain the same endpoint admittance.
- There was no indication of muscle spindle feedback during force tasks. The conclusion is based on the absence of a sharp phase descent an an oscillation peak of the endpoint admittance around 3-4 Hz. Force tasks are therefore considered not logical when the functionality of muscle spindle reflexes is to be investigated.

- There is strong indication that GTO feedback is present during both force tasks as well as position tasks. GTO feedback increases the endpoint admittance and is therefore functional to force tasks only. For large values of the GTO loop gain a local increase emerged in our model simulations around 10 Hz. Such an increase was also seen in 4 out of 10 subjects which is most likely the result of GTO feedback. For the conditions where GTO was discernibly present in the measurements, its feedback gain was rather constant even during position tasks where the admittance-increasing effect is counterproductive.

Chapter 5

Closed-loop multivariable system identification using force disturbances

Erwin de Vlugt, Frans C. T. van der Helm, Alfred C. Schouten
Journal of NeuroScience Methods 2003; 122: 123-140

This study presents a multivariable closed loop identification technique for estimating the dynamic compliance of the multijoint human arm during posture maintenance. The method is suited for the application of continuous force disturbances that facilitate interaction of the limb with the environment. The dynamic compliance of the arm arises from different physiological mechanisms and is important for maintaining stable postures and to suppress disturbances. Estimates can be useful to analyze the ability of the nervous system to adapt the arm compliance to different types of disturbances and environments. The technique is linear and requires no a priori knowledge of the system. Linear system behavior is justified for posture tasks where the hand position deviates slightly from a reference position. Interaction results in a closed-loop configuration of arm and environment. The problem with previous methods is the restriction to open-loop systems. With the current technique, the dynamic arm compliance is separately estimated from the closed-loop. The accuracy of the identification technique is tested by simulations for different values of the dynamic compliance of the arm and environment and for different methodological parameters. It is concluded that the identification technique is accurate, even for short observation periods and severe noise.

5.1 Introduction

Human arm posture maintenance is the result of coordinated forces around the joints at particular joint angles. The goal of posture control is to maintain a certain mean position and to minimize deviations in the presence of force disturbances. With respect to the displacements, the restoring forces result from elastic, viscous and inertial properties. Elastic and viscous properties of a limb can be adapted and originate from intrinsic muscle stiffness and damping and additionally from reflexive feedback from muscle spindles (Doemges and Rack, 1992a; Kearney et al., 1997; Kirsch et al., 1993; Toft et al., 1991). Both intrinsic and reflexive contributions depend on (a) the task instruction given to the subjects (Doemges and Rack, 1992b; Gomi and Osu, 1998; Smeets and Erkelens, 1991), (b) the properties and type of the disturbance signal (Cathers et al., 1999; Stein and Kearney, 1995; Van der Helm et al., 2002), (c) the configuration of the arm (Mussa-Ivaldi et al., 1985; Dolan et al., 1993) and (d) the mechanical properties of the environment (De Vlugt et al., 2002; Milner and Cloutier, 1993).
Most of these studies used transient position disturbances to identify only the stiffness of single joints and some have retrieved stiffness ellipses for the two-joint case (Mussa-Ivaldi et al., 1985; Dolan et al., 1993; Gomi and Kawato, 1996). Since position is imposed, the reaction force was taken as the free output variable. The task instruction is mostly formulated so as to maintain a certain force level in certain directions. Other studies analyzed the transient response in EMG signals to separate the reflexive contributions by isolating the delayed response from the instantaneous. Only the first hundreds of milliseconds were analyzed where voluntary reactions are likely not to take place (Stein and Kearney, 1995; Toft et al., 1991).
A few studies applied continuous stochastic position disturbances to determine the mechanical properties of the limb (Cathers et al., 1999; Kirsch et al., 1993; Kearney et al., 1997; Perreault et al., 2001; Zhang and Rymer, 1997). Compared to transient disturbances, this method allows a faster and more accurate quantification of limb stiffness, damping and mass because a richer frequency range is applied.
However, since position is simply imposed by a manipulator that is assigned a stiffness much larger than that of the concerned limb, the 'responding' forces can by no means change the limb position or muscle lengths. For (ideal) position disturbances, position and force are fully decoupled and there is no matter of active stabilization, i.e. the position servo provides inherent stability. Because of the decoupling, the system can be regarded as an open-loop, facilitating straight forward open loop identification techniques (Bendat and Piersol, 1986; Ljung, 1999).

In contrast to position disturbances, force disturbances facilitates a functional dynamic analysis of the limb compliance during natural interaction with the environment. Deviations of the endpoint position, as a result of the force disturbance, are determined by the dynamic compliance of both the arm and environment. Efforts of the central nervous system (CNS) to preserve stability by adjusting both intrinsic and reflexive properties have a direct effect on the responding limb position. The interacting behavior results in a closed-loop control configuration of limb

and environment together. The problem with previous estimation techniques is the restriction to open-loop systems.

The goal of this study is to develop a closed-loop identification technique which is appropriate for application of continuous force disturbances and interaction with environments during posture control. The technique is non-parametric, meaning that no *a priori* knowledge of the system is needed. An important requirement is that the system to be estimated is stationary. This means that its properties remain constant over the observed time period. In fact, the interest is in the system response to the continuous force disturbance. Therefore, anticipatory muscle activation which changes the arm compliance (and acts as an additional force input) should be avoided. This is achieved by using random force disturbances such that prediction is likely excluded. If the system is indeed stationary for these types of force disturbances, the arm compliance can only be the result of constant intrinsic muscle properties and peripheral feedback mechanisms.

Kearney and Hunter (1990) already indicated the great usefulness of closed-loop responses since they characterize joint behavior under natural behavioral conditions. They described the basics for the application of closed-loop estimators for single-joint dynamics. In a recent study from our laboratory, this experimental paradigm is applied to quantify the compliance of the shoulder joint (De Vlugt et al., 2002; Van der Helm et al., 2002).
The present study extends the estimation method for single-joint dynamics to a two-input two-output planar case for estimating arm compliance at the point of interaction or endpoint. In this case the hand reaction force acts as the input and the hand position as the output. The application is also suitable for larger input-output systems. The estimated dynamic compliance is expressed in the frequency domain by means of a matrix frequency response function (MFRF).
In addition to the closed-loop estimator, a signal design method is used for the generation of the force disturbance signals. This method produces unpredictable deterministic signals having exact power at specific frequencies. The main advantage of deterministic signals is that their periodicity prevents bias in the estimates, which would otherwise emerge in the case of application of stochastic signals (Schoukens et al., 1993).
The goodness of the estimation method is verified by simulations for different properties of arm and environmental compliance. Various experimental and methodological conditions are simulated and discussed. The results indicate that the endpoint compliance is estimated very accurately, having negligible bias and variance at rather erroneous conditions, reflected by high values of the multiple coherence functions.

5.2 Closed-loop system description

Any (bio)mechanical system in its complete dimension and normal functioning, is properly described when a driving force is taken at the input and a movement (po-

sition or velocity) as the output. Only in this way the system states follow from integration of inputs, and the output is determined as a (linear) combination of the system states. To understand the underlying mechanisms subserving the mechanical response, the system therefore should be analyzed in its causal dynamic structures wherein it is defined, i.e. as a dynamic compliance (Hogan, 1985b). The compliance comprises stiffness, damping and inertia properties, together with feedback loops, and is expressed in meters per Newton (m/N), i.e. the inverse of the mechanical impedance.
Figure 5.1 shows schematically a manipulator to realize an environment. The Cartesian components of the signals are defined in the subjects frame having its origin in the right shoulder. To analyze human arm posture control effectively, the influence of the environment should be kept small compared to the arm. This means that the inertia, damping and stiffness of the environment should be as low as possible. Despite lightweight designs and advanced control strategies to increase the apparent (virtual) endpoint compliance, the additional contribution cannot be neglected in practice. Figure 5.2 shows the nonlinear blockscheme representing the mechanical interaction of the arm with the environment. The total force acting upon the environment is the summation of an independent external force disturbance $\mathbf{D}(t)$ and the opposing hand reaction force $\mathbf{F}(t)$. The hand force is an internal variable and the hand position $\mathbf{X}(t)$ is the output of the total system. It is assumed that the force disturbance, hand reaction force and hand position are available from measurements.

Figure 5.2 can also be interpreted in terms of classical control theory. In that case, the environment represents a mechanical system of which the compliance can be modified by an additional compliance of the human arm, which acts as the dynamic compliance controller.

5.2.1 Linear closed-loop system description

Most system identification techniques are designed for linear systems, whereas biological systems are highly nonlinear in nature (Winters and Stark, 1985; Kirsch et al., 1994; Stein and Kearney, 1995). To use linear techniques, a nonlinear system should be excited such that it behaves almost linearly. This means that only small variations of system states around a working point are allowed. For human posture maintenance, this requirement is easily met because it is the primary goal of posture control to keep the position deviations small with respect to a reference position. The approximation around a specific reference point will never be perfect. The imperfection of the linearized system with respect to the original nonlinear system is accounted for by an additional residual signal or model remnant $\mathbf{R}(f)$ at the output which is uncorrelated with the input $\mathbf{D}(f)$, see Fig. 5.3A. The linear dynamic compliance of the human arm is indicated by the MFRF $H_{xf}(f)$. Note that the arm is expressed as the anticausal MFRF $H_{xf}^{-1}(f)$ to preserve the causal definition of the dynamic compliance. The (virtual) compliance of the environment is indicated by the MFRF $E_{xz}(f)$. Any nonlinearities in the virtual compliance are also accounted for by the model remnant $\mathbf{R}(f)$. Volitional force contribution, which is

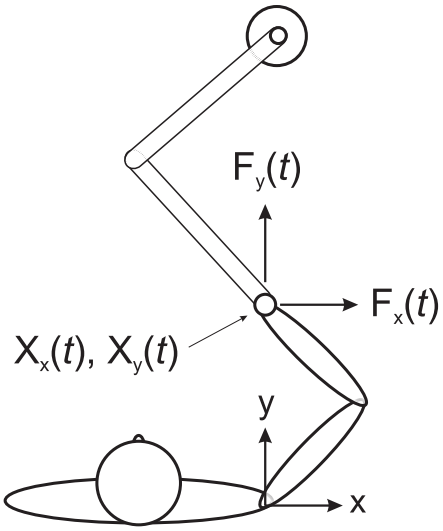

Figure 5.1: *Schematical configuration of a typical experimental setup to measure the planar dynamic compliance of the human arm. The hand is physically attached to the manipulator. Forces and motions are constrained to a horizontal plane and decomposed in cartesian $(x - y)$ coordinates in the subjects frame. The origin of the frame is usually located in the subject's shoulder rotation centre. $\mathbf{F}$ is the (2×1) vector of the hand reaction force and $\mathbf{X}$ is the vector of the endpoint or hand position.*

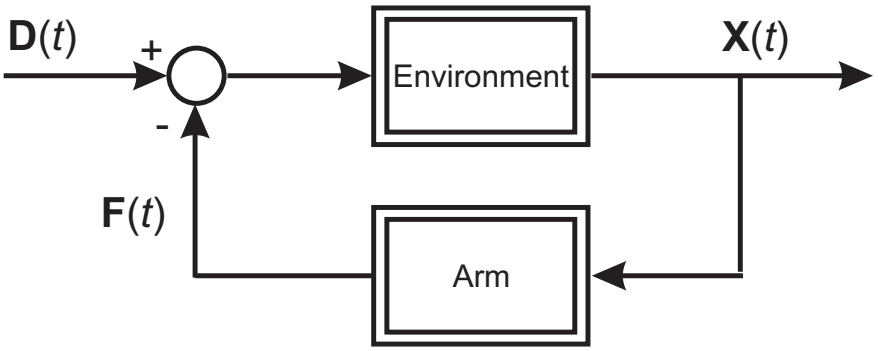

Figure 5.2: *Basic (nonlinear) closed-loop configuration of the mechanical interaction between the human arm and the manipulator acting as the environment. The total system is excited by a force disturbance $\mathbf{D}(t)$. The force applied by the human arm $\mathbf{F}(t)$ acts in addition, and opposite, to the external force. The system output is the common endpoint or hand position $\mathbf{X}(t)$.*

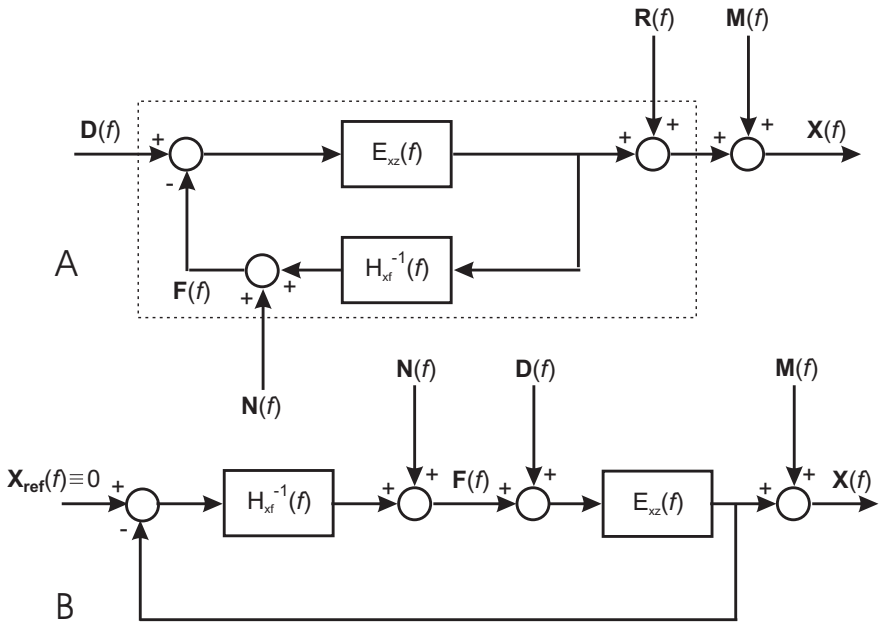

Figure 5.3: *A, Linear system approximation of the nonlinear system (dotted box) between input force disturbance $\mathbf{D}(t)$ and output (hand) position $\mathbf{X}(t)$, expressed in the frequency domain. $\mathbf{R}(f)$ is the model remnant, $\mathbf{N}(f)$ system input noise and $\mathbf{M}(f)$ measurement noise. All noise signals are unknown and assumed uncorrelated with $\mathbf{D}(t)$. The dynamic compliance of the arm $H_{xf}(f)$ is configured in a closed loop with the environmental compliance $E_{xz}(f)$. The arm compliance is presented as its inverse to preserve its causal definition. $\mathbf{F}(f)$ is the hand reaction force, applied via the hand of the subject to the manipulator. B, redrawn of A into a disturbance control scheme where the goal is to reduce deviations around a reference position. The posture task is represented by the reference position to be maintained ($\mathbf{X_{ref}} \equiv 0$) which means that the effect of the force disturbance is to be minimized. The output noise $\mathbf{M}(f)$ also includes the model remnant $\mathbf{R}(f)$.*

not correlated with the imposed force disturbance $\mathbf{D}(t)$, is represented by the input noise signal $\mathbf{N}(t)$. Finally, measurement noise is indicated by $\mathbf{M}(t)$ and is also assumed uncorrelated with $\mathbf{D}(t)$. Since the control of posture is a disturbance task, the blockscheme of Fig. 5.3A is redrawn into a disturbance blockscheme (Fig. 5.3B) with a reference position at the input which has to be maintained. Since model remnant and measurement noise cannot be separated from each other, both noise sources are taken together in one noise source $\mathbf{M}(f)$.

As a result of the closed-loop configuration, the input noise $\mathbf{N}(f)$ also appears in the hand reaction force $\mathbf{F}(f)$ and consequently is correlated with it. It is therefore impossible to separate that part in the measured hand position $\mathbf{X}(f)$ that comes from the hand reaction force only. Identification of the arm compliance $H_{xf}(f)$ from

$\mathbf{F}(f)$ and $\mathbf{X}(f)$ is therefore inadequate. An external signal from outside the loop is needed to eliminate the contribution of the noise source $\mathbf{N}(t)$. The only requirement is that the external signal is uncorrelated with the noise inside the loop. The force disturbance signal $\mathbf{D}(t)$ is taken as the most obvious choice.

The closed-loop estimator of the arm compliance is derived from the system equations in which $\mathbf{F}(t)$ and $\mathbf{X}(t)$ are to be expressed in terms of all the inputs to the closed loop system, being $\mathbf{D}(t)$, $\mathbf{N}(t)$ and $\mathbf{M}(t)$. First define the frequency transforms of the signals into their x-y components:

$$\begin{aligned}
\mathbf{F}(n\Delta f) &= [F_x(n\Delta f)\ F_y(n\Delta f)]^T \\
\mathbf{X}(n\Delta f) &= [X_x(n\Delta f)\ X_y(n\Delta f)]^T \\
\mathbf{D}(n\Delta f) &= [D_x(n\Delta f)\ D_y(n\Delta f)]^T \\
\mathbf{N}(n\Delta f) &= [N_x(n\Delta f)\ N_y(n\Delta f)]^T \\
\mathbf{M}(n\Delta f) &= [M_x(n\Delta f)\ M_y(n\Delta f)]^T
\end{aligned}$$

where ^{T} denotes the vector transposed and $n\Delta f$ the discrete frequencies. Hereby, $n \in [0, 1, 2, \ldots \frac{N}{2}]$, $N = f_s T$, f_s the sample frequency and T the observation time period. The signals are transformed by the standard Fast Fourier Transform (FFT) algorithm. The system MFRFs $H_{xf}(n\Delta f)$ and $E_{xz}(n\Delta f)$ are defined as two-by-two matrices according to:

$$H_{xf}(n\Delta f) = \begin{bmatrix} H_{x_x f_x}(n\Delta f) & H_{x_x f_y}(n\Delta f) \\ H_{x_y f_x}(n\Delta f) & H_{x_y f_y}(n\Delta f) \end{bmatrix} \tag{5.1}$$

$$E_{xz}(n\Delta f) = \begin{bmatrix} E_{x_x z_x}(n\Delta f) & E_{x_x z_y}(n\Delta f) \\ E_{x_y z_x}(n\Delta f) & E_{x_y z_y}(n\Delta f) \end{bmatrix} \tag{5.2}$$

with $z_x = f_x - d_x$ and $z_y = f_y - d_y$. Then the system equations are:

$$\mathbf{F} = [I + H_{xf}^{-1} E_{xz}]^{-1} H_{xf}^{-1} E_{xz}\, \mathbf{D} + [I + H_{xf}^{-1} E_{xz}]^{-1} \mathbf{N} \tag{5.3}$$

$$\mathbf{X} = [I + E_{xz} H_{xf}^{-1}]^{-1} E_{xz}\, \mathbf{D} + [I + E_{xz} H_{xf}^{-1}]^{-1} E_{xz}\, \mathbf{N} + \mathbf{M} \tag{5.4}$$

where I is the unit matrix. In Eqs (5.3) and (5.4) the arguments are omitted for readability. Making use of the following algebraic rule:

$$[I + H_{xf}^{-1} E_{xz}]^{-1} H_{xf}^{-1} = H_{xf}^{-1} [I + E_{xz} H_{xf}^{-1}]^{-1}$$

and substituting:

$$L^T = [I + E_{xz} H_{xf}^{-1}]^{-1}$$

into the transposed Eqs (5.3) and (5.4), results in:

$$\mathbf{F}^T = \mathbf{D}^T E_{xz}^T L^T H_{xf}^{-1^T} + \mathbf{N}^T H_{xf}^T L^T H_{xf}^{-1^T} \tag{5.5}$$

$$\mathbf{X}^T = \mathbf{D}^T E_{xz}^T L^T + \mathbf{N}^T E_{xz}^T L^T + \mathbf{M}^T \tag{5.6}$$

The cancellation of noise can be established by the use of spectral densities. The spectral densities are obtained by premultiplication of the loop signals (Eqs (5.5)

and (5.6)) with the complex conjugate of the external signal $\mathbf{D}(n\Delta f)$ and then taking the expectation value of the products according to:

$$G_{d_i f_j} = E\{\mathbf{D}_i^* \mathbf{F}_j^T\} \tag{5.7}$$

$$G_{d_i x_j} = E\{\mathbf{D}_i^* \mathbf{X}_j^T\} \quad i,j \in [x,y] \tag{5.8}$$

where * denotes the complex conjugate, G the spectral density matrix and $E\{\cdot\}$ the expectation operator. Application of spectral densities to the system equations (Eqs (5.5) and (5.6)) gives:

$$G_{df} = G_{dd} E_{xz}^T L^T H_{xf}^{-1^T} + G_{dn} H_{xf}^T L^T H_{xf}^{-1^T} \tag{5.9}$$

$$G_{dx} = G_{dd} E_{xz}^T L^T + G_{dn} E_{xz}^T L^T + G_{dm} \tag{5.10}$$

with

$$G_{df} = \begin{bmatrix} G_{d_x f_x} & G_{d_x f_y} \\ G_{d_y f_x} & G_{d_y f_y} \end{bmatrix}, \quad G_{dx} = \begin{bmatrix} G_{d_x x_x} & G_{d_x x_y} \\ G_{d_y x_x} & G_{d_y x_y} \end{bmatrix}, \quad G_{dd} = \begin{bmatrix} G_{d_x d_x} & G_{d_x d_y} \\ G_{d_y d_x} & G_{d_y d_y} \end{bmatrix}$$

The external force disturbance is assumed uncorrelated with both noise signals such that G_{dm} and G_{dn} equal the nulmatrix. As a result, the corresponding cross-spectra vanish from Eqs (5.9) and (5.10). The arm compliance follows from multiplication of both cross spectral densities, according to:

$$\begin{aligned} G_{df}^{-1} G_{dx} &= H_{xf}^T L^{-1^T} E_{xz}^{-1^T} G_{dd}^{-1} G_{dd} E_{xz}^T L^T \\ &= H_{xf}^T \end{aligned} \tag{5.11}$$

A sufficient requirement for the external force disturbance signals is that the matrix G_{dd} is invertible (Eq. (5.11)), which means that both signals may not be fully coupled to avoid matrix singularity. This still allows the signals in both directions to be correlated with each other. The closed-loop estimator is therefore indifferent to input coupling, which follows directly from Eq. (5.11) where the product $G_{dd}^{-1} G_{dd}$ vanishes.

The purpose of the closed-loop estimator is to obtain an accurate estimate of the arm compliance H_{xf}.

5.2.2 Closed loop system estimation

The derivation of the arm compliance (Eq. (5.11)) is a theoretical one, based on expectation values in the definition of the spectral densities (Eqs (5.7) and (5.8)). In fact, these definitions only hold for infinitely long observations. A practical approximation of spectral densities, based on finite time records, is obtained by multiplication of the FFT-transformed signals according to:

$$\hat{G}_{d_i f_j} = \mathbf{D}_i \mathbf{F}_j^* \approx E\{\mathbf{D}_i \mathbf{F}_j\} = G_{d_i f_j} \quad i,j \in [x,y] \tag{5.12}$$

where $\hat{G}$ denotes the estimate of the true spectral density G (Bendat and Piersol, 1986). Applying the approximation also to G_{dx} in Eq. (5.11) gives the final closed-loop estimator:

$$\hat{H}_{xf} = \hat{G}_{dx}^{T}\hat{G}_{df}^{-1^{T}} \tag{5.13}$$

with $\hat{H}_{xf}$ the estimated MFRF of the dynamic arm compliance. Dividing the above equation into the matrix components gives:

$$\hat{H}_{x_x f_x} = \frac{\hat{G}_{d_x x_x}\left[1 - \frac{\hat{G}_{d_y x_x}\hat{G}_{d_x f_y}}{\hat{G}_{d_x x_x}\hat{G}_{d_y f_y}}\right]}{\hat{G}_{d_x f_x}\left[1 - \frac{\hat{G}_{d_y f_x}\hat{G}_{d_x f_y}}{\hat{G}_{d_x f_x}\hat{G}_{d_y f_y}}\right]} \quad \hat{H}_{x_x f_y} = \frac{\hat{G}_{d_y x_x}\left[1 - \frac{\hat{G}_{d_x x_x}\hat{G}_{d_y f_x}}{\hat{G}_{d_y x_x}\hat{G}_{d_x f_x}}\right]}{\hat{G}_{d_y f_y}\left[1 - \frac{\hat{G}_{d_y f_x}\hat{G}_{d_x f_y}}{\hat{G}_{d_y f_y}\hat{G}_{d_x f_x}}\right]}$$

$$\hat{H}_{x_y f_x} = \frac{\hat{G}_{d_x x_y}\left[1 - \frac{\hat{G}_{d_y x_y}\hat{G}_{d_x f_y}}{\hat{G}_{d_x x_y}\hat{G}_{d_y f_y}}\right]}{\hat{G}_{d_x f_x}\left[1 - \frac{\hat{G}_{d_y f_x}\hat{G}_{d_x f_y}}{\hat{G}_{d_x f_x}\hat{G}_{d_y f_y}}\right]} \quad \hat{H}_{x_y f_y} = \frac{\hat{G}_{d_y x_y}\left[1 - \frac{\hat{G}_{d_x x_y}\hat{G}_{d_y f_x}}{\hat{G}_{d_y x_y}\hat{G}_{d_x f_x}}\right]}{\hat{G}_{d_y f_y}\left[1 - \frac{\hat{G}_{d_y f_x}\hat{G}_{d_x f_y}}{\hat{G}_{d_y f_y}\hat{G}_{d_x f_x}}\right]}$$

The left terms in both numerator and denominator corresponds to the case of no cross coupling between the x and y components in the closed-loop system, i.e. of two decoupled single-input single-output (SISO) systems. The fractions within brackets are corrections for the case of nonzero coupling, i.e. the existence of off-diagonal terms in the MFRFs, which is normally the case in human arm endpoint compliance.

A common indicator of the amount of noise entering the system, are the multiple coherence functions (Bendat and Piersol, 1986):

$$\begin{aligned}
\hat{\gamma}^2_{x_x d_{xy}} &= \frac{\hat{P}_{x_x d_x}\hat{G}_{d_x x_x} + \hat{P}_{x_x d_y}\hat{G}_{d_y x_x}}{\hat{G}_{x_x x_x}} \\
\hat{\gamma}^2_{x_y d_{xy}} &= \frac{\hat{P}_{x_y d_x}\hat{G}_{d_x x_y} + \hat{P}_{x_y d_y}\hat{G}_{d_y x_y}}{\hat{G}_{x_y x_y}}
\end{aligned} \tag{5.14}$$

with $\hat{\gamma}^2_{x_x d_{xy}}$ the multiple coherence function from both inputs (D_x and D_y) to the output in x-direction (X_x) and $\hat{\gamma}^2_{x_y d_{xy}}$ from both inputs to the output in y-direction (X_y). When both the multiple coherence functions are close to one, the power of any noise is small and the output $\mathbf{X}$ is almost linearly related to the input $\mathbf{D}$. In the case where the multiple coherence functions are close to zero, the power of noise entering the system is large. The multiple coherence functions (Eq. (5.14)) make use of $\hat{P}_{x_i d_j}$ $(i, j \in [x, y])$, which is the open-loop estimated MFRF of the complete system from force disturbance to hand position, according to:

$$\hat{P}_{xd} = \hat{G}_{dx}^{T}\hat{G}_{dd}^{-1^{T}} \tag{5.15}$$

and specified into its components gives:

$$\hat{P}_{x_i d_x} = \frac{\hat{G}_{d_x x_i}\left[1 - \frac{\hat{G}_{d_x d_y}\hat{G}_{d_y x_i}}{\hat{G}_{d_y d_y}\hat{G}_{d_x x_i}}\right]}{\hat{G}_{d_x d_x}\left[1 - \hat{\gamma}^2_{d_x d_y}\right]} \quad \hat{P}_{x_i d_y} = \frac{\hat{G}_{d_y x_i}\left[1 - \frac{\hat{G}_{d_y d_x}\hat{G}_{d_x x_i}}{\hat{G}_{d_x d_x}\hat{G}_{d_y x_i}}\right]}{\hat{G}_{d_y d_y}\left[1 - \hat{\gamma}^2_{d_x d_y}\right]} \quad i \in [x, y] \tag{5.16}$$

where $\hat{\gamma}^2_{d_x d_y}$ is the estimated coherence function between both disturbance signals and defined as:

$$\hat{\gamma}^2_{d_x d_y} = \frac{|\,\hat{G}_{d_x d_y}|^2}{\hat{G}_{d_x d_x}\hat{G}_{d_y d_y}} \tag{5.17}$$

Partial coherence functions provide estimates of the linear relationships between one input (D_x or D_y) and one output (X_x or X_y) and is given by (Bendat and Piersol, 1986):

$$\hat{\gamma}^2_{d_i x_j \cdot d_k} = \frac{|\,\hat{G}_{d_i x_j \cdot d_k}|^2}{\hat{G}_{d_i d_j \cdot d_k}\hat{G}_{x_i x_j \cdot d_k}} \quad i, j, k \in [1, 2], \;\; i \neq k \tag{5.18}$$

where the residual spectra $\hat{G}_{d_i x_j \cdot d_k}$ are defined as:

$$\hat{G}_{d_i x_j \cdot d_k} = \hat{G}_{d_i x_j}\left[1 - \frac{\hat{G}_{d_i d_k}\hat{G}_{d_k x_j}}{\hat{G}_{d_k d_k}\hat{G}_{d_i x_j}}\right] \tag{5.19}$$

Working out the substitution of Eq. (5.19) into Eq. (5.18) gives:

$$\hat{\gamma}^2_{d_i x_j \cdot d_k} = \frac{|\,\hat{G}_{d_i x_j}\hat{G}_{d_k d_k} - \hat{G}_{d_k x_j}\hat{G}_{d_i d_k}|^2}{\hat{G}^2_{d_k d_k}\hat{G}_{d_i d_i}\hat{G}_{x_j x_j}(1 - \hat{\gamma}^2_{d_k d_i})(1 - \hat{\gamma}^2_{d_k x_j})} \tag{5.20}$$

with $\hat{\gamma}_{d_k d_i}$ the ordinary coherence function between both inputs (Eq. (5.17)) and $\hat{\gamma}_{d_k x_j}$ the ordinary coherence function between one input and one output and defined as:

$$\hat{\gamma}^2_{d_k x_j} = \frac{|\,\hat{G}_{d_k x_j}|^2}{\hat{G}_{d_k d_k}\hat{G}_{x_j x_j}} \tag{5.21}$$

Partial coherence functions are equivalent to ordinary coherence functions after the effects of all other inputs have been removed from both input and output of interest (Bendat and Piersol, 1986). Because the input coherence (Eq. (5.17)) is part of their expressions, multiple and partial coherence functions compensate for coupling between the input signals.

5.2.3 A particular case: the open-loop estimator

Normally, the arm is interacting with an environment and it was argued that a closed-loop estimator was necessary to obtain an estimate of the arm compliance. A typical application of open-loop estimators accounts in the case position disturbances are applied using a strong servo controlled manipulator that simply imposes (or dictates) a prespecified movement irrespective of the generated hand force. The corresponding open-loop estimator, as used by Perreault et al. (1999), can be derived from the closed-loop estimator in the following way.
Let the environment be dominant over the arm, i.e. $E_{xz} \ll H_{xf}$ or $E_{xz} \to 0$, then $L \to I$. Additionally, let the external force disturbance increase proportionally such that $\mathbf{D} \gg \mathbf{F}$. Now, Eqs (5.5) and (5.6) become:

$$\begin{aligned} \mathbf{F}^T &= \mathbf{D}^T E_{xz}^T {H_{xf}^{-1}}^T + \mathbf{N}^T \\ \mathbf{X}^T &= \mathbf{D}^T E_{xz}^T + \mathbf{M}^T \end{aligned}$$

The product $\mathbf{D}^T E_{xz}^T$ actually describes the imposed position disturbance. Taking $\mathbf{D}^T E_{xz}^T = {\mathbf{X_{dist}}}^T$ as the position disturbance, and substituting it into the above equations gives:

$$\begin{aligned} \mathbf{F}^T &= {\mathbf{X_{dist}}}^T {H_{xf}^{-1}}^T + \mathbf{N}^T \\ \mathbf{X}^T &= {\mathbf{X_{dist}}}^T + \mathbf{M}^T \end{aligned}$$

Effectively, $\mathbf{X_{dist}}$ has become the exciting input of the arm and this is true as long as $\mathbf{X} = \mathbf{X_{dist}}$ (assuming $\mathbf{M} \ll \mathbf{X_{dist}}$). Evidently, the hand reaction force $\mathbf{F}$ must be taken as the responding output. Assuming that both noise sources are uncorrelated with the input $\mathbf{X_{dist}}$, the open-loop estimator becomes:

$$\hat{G}_{xx}^{-1} \hat{G}_{xf} = \hat{H_{xf}}^{-1^T}$$

For correctness of terms, in the above equation the arm impedance (inverse of compliance) is given because the force is assumed as an output. Accordingly, the coherences functions need to be expressed between $\mathbf{X}$ and $\mathbf{F}$.
The other situation for which an open-loop estimator can be derived is the ideal case that the manipulator has no dynamics. This means that $E_{xz} \to \infty$ and similar steps can easily be followed to arrive at an open-loop estimator for the arm compliance. In that case, $\mathbf{F}$ is the exciting input and is equal to $\mathbf{D}$.

5.2.4 Variance and bias of spectral density estimators

The goodness of the estimation is judged by the bias and variance of the applied estimator. Variance is the result of random parts in the signals and is reduced by averaging the raw spectra ($\hat{G}_{df}$ and $\hat{G}_{dx}$) over m adjacent frequencies (Jenkins and Watts, 1968). As the result, the frequency resolution decreases to $m\Delta f$ such that the estimated compliance is defined at the following frequencies:

$$\hat{H}_{xf}(n\Delta f) \overset{aver.}{\to} \hat{H}_{xf}(\Delta f_1 + p\, m\Delta f) \qquad p \in \left[1, 2, ..., \frac{N-m}{m}\right]$$

with Δf_1 the lowest frequency after averaging according to:

$$\Delta f_1 = \frac{1}{m} \sum_{n=m+1}^{n=2m} n\Delta f$$

From the above equation it can be seen that the zeroth frequency is removed from the spectral densities (related to the mean values of the signals) by omitting the first averaging window.

To preserve a certain minimal frequency resolution in order not to average out peaks in the (M)FRFs, m should be limited. Alternatively, the record time can be increased, albeit restrictively to avoid fatigue effects during experiments with humans in vivo.

Bias is the result of structural differences between the estimated value and the real value. The largest bias contribution is caused by the finiteness of the time records (Bendat and Piersol, 1986; Perreault et al., 1999). In the case of long observations and a large number of averaging frequencies, the bias of the spectral densities approaches zero (Jenkins and Watts, 1968).

Variance of the estimated MFRFs is also reflected by variance of the multiple coherence functions and bias results in a decrease of the multiple coherence (Bendat and Piersol, 1986; Perreault et al., 1999). Therefore, multiple coherence functions will be taken as the explicit indicators for the robustness of the estimator.

In addition to noise, the disturbance signal also enters the system. In many studies this signal has been taken to be stochastic too (Kirsch et al., 1993; Cathers et al., 1999; Perreault et al., 1999, 2001), leading to a further increment of bias and variance (Schoukens et al., 1993). This is because the spectral properties of stochastic signals are captured only from infinitely long observations and defined on a continuous frequency scale, while for a finite observation time the system can only be defined at discrete frequencies $n\Delta f$. To exclude this negative effect, a specific signal design method has been adopted which is described in the following section.

5.2.5 Disturbance signal design

The disturbance signal will be designed in the frequency domain such that the signal is completely determined within T seconds in order to avoid bias. Any spectrum can be realized, resulting in a sum of sine waves with different frequencies. Using these multisine signals (Schoukens et al., 1993), the system is identified at those frequencies $(n\Delta f)$ constituting the disturbance signal. To make the signal unpredictable for subjects, the phases between all frequency components are randomized.

The structure of the Fourier transform $\mathbf{\Psi}(n\Delta f)$, of the time signal $\psi(l\Delta t)$ to be constructed, is determined as follows:

$$\begin{aligned} \mathbf{\Psi}(n\Delta f) &= \sum_{n=1}^{\frac{N}{2}} \mathbf{\Lambda}(n\Delta f) e^{j\mathbf{\Theta}(n\Delta f)} \\ &= \lambda_1(\cos\theta_1 + j\sin\theta_1) + \ldots + \lambda_{\frac{N}{2}}(\cos\theta_{\frac{N}{2}} + j\sin\theta_{\frac{N}{2}}) \end{aligned} \tag{5.22}$$

with $\mathbf{\Theta}(n\Delta f)$ a sequence of randomly generated phases in the range $[0 \dots 2\pi]$:

$$\mathbf{\Theta}(n\Delta f) = \left[\theta_1 \dots \theta_{\frac{N}{2}}\right] \tag{5.23}$$

and $\mathbf{\Lambda}(n\Delta f)$ a sequence of vector magnitudes:

$$\mathbf{\Lambda}(n\Delta f) = \left[\lambda_1 \dots \lambda_{\frac{N}{2}}\right]$$

The amplitude of each sine wave λ_n is adjusted to obtain the appropriate spectral power distribution. For the random generation of the phases, any type of distribution will suffice. In this case, a uniform distribution is applied. Application of the Inverse Fast Fourier Transform (IFFT) to the N-point frequency vector, i.e. $[\mathbf{\Psi}(-n\Delta f)\ \mathbf{\Psi}(0)\ \mathbf{\Psi}(n\Delta f)]$ directly gives the corresponding time signal $\psi(l\Delta t)$, with $l = 1 \dots N$.

5.3 Simulations

The accuracy of the estimator of the dynamic arm compliance (Eq. (5.13)) is analyzed for different controlled conditions. For this purpose, computer simulations are performed for varying properties of:

- the compliance of the arm
- the compliance of the environment
- input and output noise
- the number of averaging frequencies
- the length of the observation time

5.3.1 Arm-environment model

If both arm and environment were coupled mass-damper-spring systems, the hand reaction force $\mathbf{F}(t)$ would not be observable, i.e. could not be a system output. This is because force is also a function of the second derivative while only the zeroth (positions) and first derivatives (velocities) are part of the state space. To obtain the hand reaction force, handgrip visco-elasticity is incorporated into the model which represents the dynamics between the arm and the environment. In fact, the handgrip visco-elasticity decouples the mass of both arm and environment such that the hand reaction force is determined by the difference in velocity and position between both masses. A representation of the complete system of arm and environmental compliance is given in Fig. 5.4. The representation is simplified to one degree-of-freedom (for the drawing only) and taken to be linear. A linear approximation of the planar endpoint dynamics is justified for small amplitude displacements (Dolan et al., 1993; Acosta et al., 2000).

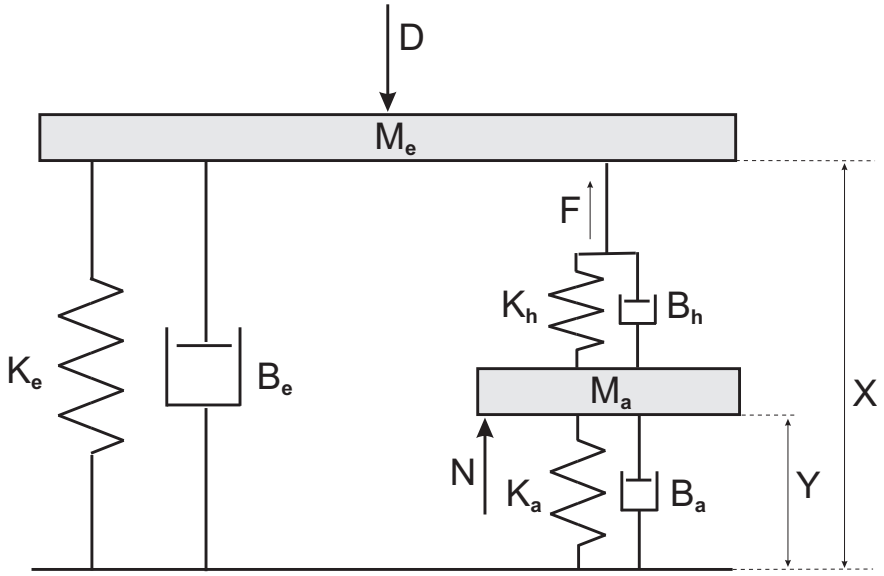

Figure 5.4: *Model representation of the mechanical compliance of the arm and the environment as used for simulation. The representation is merely to illustrate the model equations and is simply reduced here to one degree of freedom.* M_e, B_e, K_e *represent the mass-damper-spring system of the environment.* B_h, K_h *represent the visco-elasticity of the handgrip and* M_a, B_a, K_a *represent the mass-damper-spring system of the arm.* $\mathbf{D}$ *is the external force disturbance acting upon the whole system.* $\mathbf{Y}$ *is the arm position and* $\mathbf{X}$ *the position of the endpoint or hand.* $\mathbf{F}$ *is the hand reaction force and* $\mathbf{N}$ *is the input noise from uncorrelated activation of the muscles. Note that both masses are decoupled by the handgrip visco-elasticity.*

The model is described in state-space form (see Appendix C). The state vector is:

$$\mathbf{X} = [\dot{X}\, X\, \dot{Y}\, Y]^T$$

with X and Y the position and $\dot{X}$ and $\dot{Y}$ the velocity of the hand and arm respectively. The inputs are $\mathbf{D}(t)$ and $\mathbf{N}(t)$, and the outputs are $\mathbf{X}(t)$ and $\mathbf{F}(t)$. The output noise $\mathbf{M}(t)$ is added to the model output $\mathbf{X}(t)$. Figure 5.5 shows an example of an input signal that is used for simulation. The lowest frequency in this signal was approximately 0.03 Hz ($= 1/T$ for $T = 32.768$) and the highest approximately 20 Hz, which is a sufficient bandwidth to capture all arm dynamics (Perreault et al., 2001). The signals are scaled such that the standard deviation is 1 N.

Model simulations were performed in Matlab/Simulink (The MathWorks, Inc.) using a variable time step Runge-Kutta (Dormand-Prince) solver. The resulting signals were linearly interpolated to obtain equidistant time samples at 125 Hz ($N = 2^{12}$ samples for $T = 32.768$ s) reconstruction frequency (zero order hold).

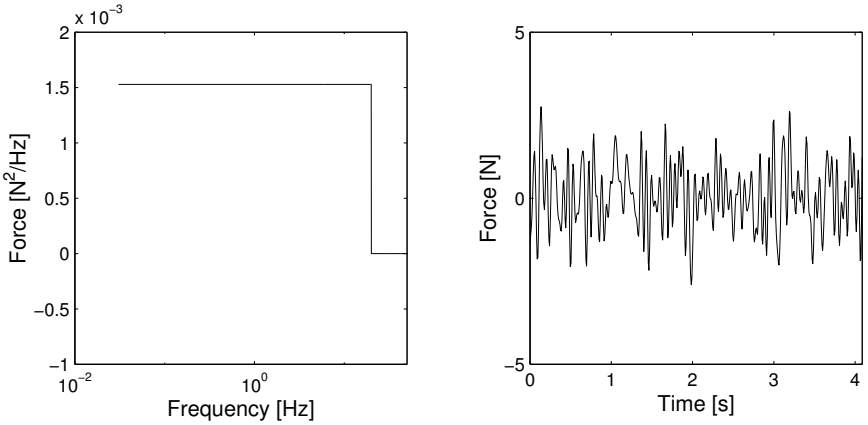

Figure 5.5: *Realization of an input disturbance signal. Left: power spectral density. Right: corresponding time signal (only the first 4 seconds). Standard deviation: 1 N.*

Table 5.1: *Parameters of the dynamic compliance of the arm (set one and two), adopted from Tsuji et al. (1995) (their Table 4, subject A, position 1 and 2 respectively). M_a: mass matrix; B_a: damping matrix and K_a: stiffness matrix. The third parameter set contains a value for damping which is 25% of that of the first parameter set while the mass and stiffness were taken as equal. Asterisk indicates the default parameter set.*

	M_a [kg]		B_a [Ns/m]		K_a [N/m]	
1^*	1.22	-0.31	12.2	-9.68	131	-123
	-0.28	0.57	-10.1	16.9	-141	283
2	0.96	-0.57	5.03	-4.13	58.3	-45.6
	-0.55	0.98	-3.99	30.0	-54.0	506
3	1.22	-0.31	3.05	-2.42	131	-123
	-0.28	0.57	-2.53	4.23	-141	283

5.3.2 Model parameters

Two typical sets of arm-model parameters were taken from the experiments of Tsuji et al. (1995), given in Table 5.1. To evaluate the effect in the case where the arm compliance contains a high resonance peak, a third parameter set is used containing a reduced arm damping of 25% of the default value (see Table 5.1). The default parameter set is indicated with an asterisk.

The visco-elastic handgrip parameters were taken from recent experiments from our group (De Vlugt et al., 2002):

$$B_h = \begin{bmatrix} 200 & 0 \\ 0 & 200 \end{bmatrix} [Ns/m], \quad K_h = \begin{bmatrix} 15000 & 0 \\ 0 & 15000 \end{bmatrix} [N/m]$$

Table 5.2: *Parameters of the environment used for simulation, with M_e: mass matrix; B_e: damping matrix and K_e: stiffness matrix. The first combination represents a high environmental compliance and is used for the application of force disturbances. The second combination represents a low compliance having a flat bandwidth of 10 Hz, typically used for position disturbances. Asterisk indicates the default parameter set.*

	M_e [kg]	B_e [Ns/m]	K_e [N/m]
1*	$\begin{matrix} 1 & 0 \\ 0 & 1 \end{matrix}$	$\begin{matrix} 0 & 0 \\ 0 & 0 \end{matrix}$	$\begin{matrix} 0 & 0 \\ 0 & 0 \end{matrix}$
2	$\begin{matrix} 2.53 & 0 \\ 0 & 2.53 \end{matrix}$	$\begin{matrix} 223 & 0 \\ 0 & 223 \end{matrix}$	$\begin{matrix} 10000 & 0 \\ 0 & 10000 \end{matrix}$

with B_h the grip viscosity and K_h the grip elasticity matrix. These parameter values were taken the same for all simulations.

Table 5.2 gives the parameter sets of two extreme environments. The first set (default) corresponds to a high compliance, appropriate for the application of force disturbances. A symmetric endpoint mass of 1 kg is taken which, to our experience, is a minimum for a typical two-linkage manipulator. The second parameter set represents a very low compliance, typically that of a position controlled (stiff) manipulator and appropriate for the application of position disturbances. This parameter set was chosen such that the MFRF is flat (critically damped) having a bandwidth of 10 Hz.

The power of the noise contribution is expressed as the signal-to-noise ratio (SNR) in decibels $[dB]$:

$$SNR = 10\,^{10}\log\left(\frac{G_{nn}}{G_{dd}}\right) \quad [dB] \tag{5.24}$$

With G_{nn} the power spectrum of the input noise, and G_{dd} the power spectrum of the disturbance signal. In case of output noise: G_{nn} is replaced by G_{mm} and G_{dd} by G_{xx}.

5.3.3 Methodological parameters

The accuracy of the estimator is judged for different values of noise levels, observation time period and width of the frequency window used for averaging. The values are given in Table 5.3 where the defaults are indicated with an asterisk. The most meaningful combinations of these different parameter values are evaluated and the results are described in following section.

Table 5.3: *Estimator and simulation parameters. SNR_f and SNR_x: signal to noise ratios for input and output noise respectively; T: observation time length; m number of averaging frequencies. Asterisk indicates the default parameter set.*

SNR_f, SNR_x [dB]	T [s]	m [-]
-20^*	32.768^*	4^*
-10	16.384	8
0	8.192	16

5.4 Results

5.4.1 Arm compliance

Figure 5.6 shows the estimated dynamic compliance $H_{xf}(n\Delta f)$ for parameter sets one and two of Table 5.1. All other parameters were set at their default values. For almost all frequencies, the estimated MFRFs are very good approximations of the modelled MFRFs (dotted lines). Any deviation from the modelled compliance is the result of noise and the application of frequency averaging that increase the variance and bias. For the off-diagonal elements, the estimates deviate the most. Especially for parameter set two where the off-diagonal elements of the compliance were smallest (less contribution to the output) such that the SNR was highest. The accuracy of the compliance estimates is reflected by the coherence functions shown in Fig. 5.7. For the diagonal elements, the output is almost linearly related to the input for all frequencies as indicated by high values of the corresponding partial coherence functions. The deviations of the estimated compliance for the off-diagonal elements are reflected by smaller values of the partial coherence functions. The multiple coherence functions are high for all frequencies, indicating a predominant linear behavior between force disturbance and hand position.

Hereafter, only the multiple coherence functions will be shown for convenience of comparison.

5.4.2 Environmental compliance

For high compliance of the environment, the multiple coherence is mainly determined by the arm compliance. In the case where the compliance of the environment is severely lowered (second parameter set, Table 5.2) the overall system MFRF will mainly be determined by the compliance of the environment. Consequently, any bias around the resonance frequency of the arm, due to averaging out it's resonance peak, will vanish. For a clear illustration of this effect, the highly resonant arm compliance (third parameter set in Table 5.1) is used for both types of environments. The increase of the multiple coherence functions is clearly demonstrated as being due to the dominance of the environment (Fig. 5.8, from solid lines to dotted lines).

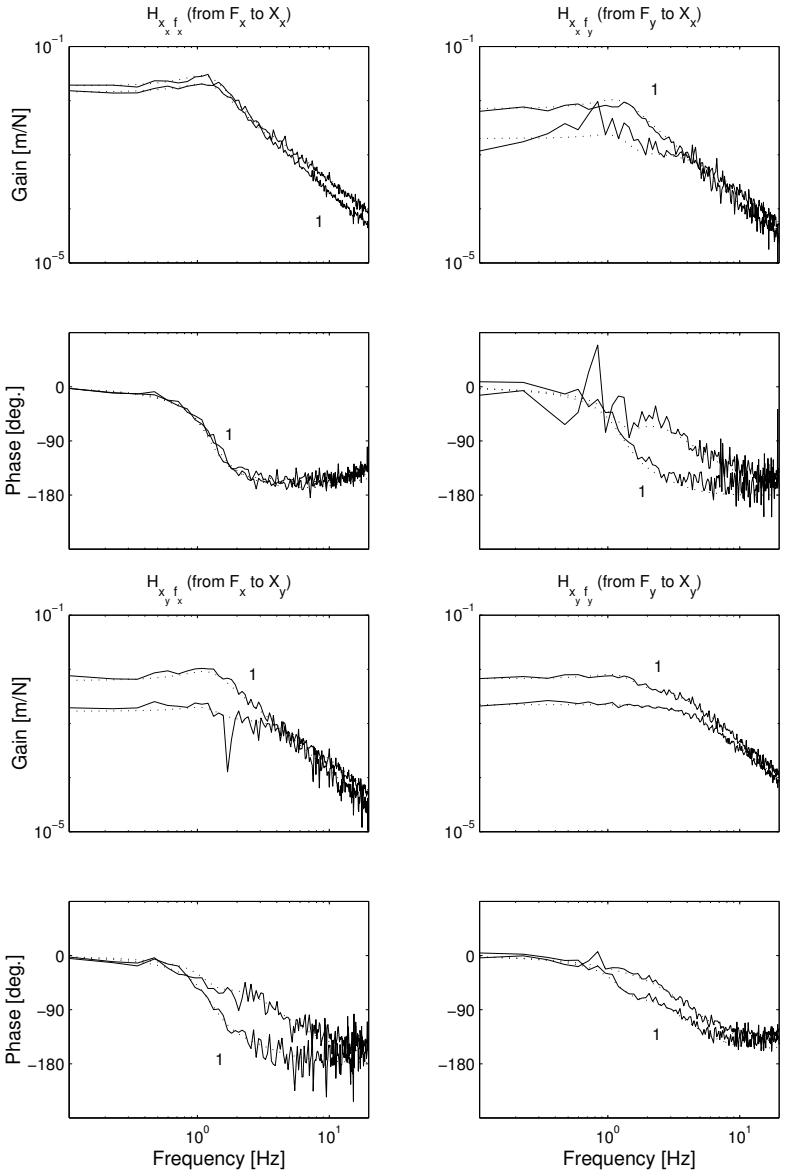

Figure 5.6: *Estimated dynamic compliance H_{xf} of the arm for parameter sets one and two (set one labeled by 1's). Solid lines: estimations; dotted lines: model. All other parameters are set at the default values.*

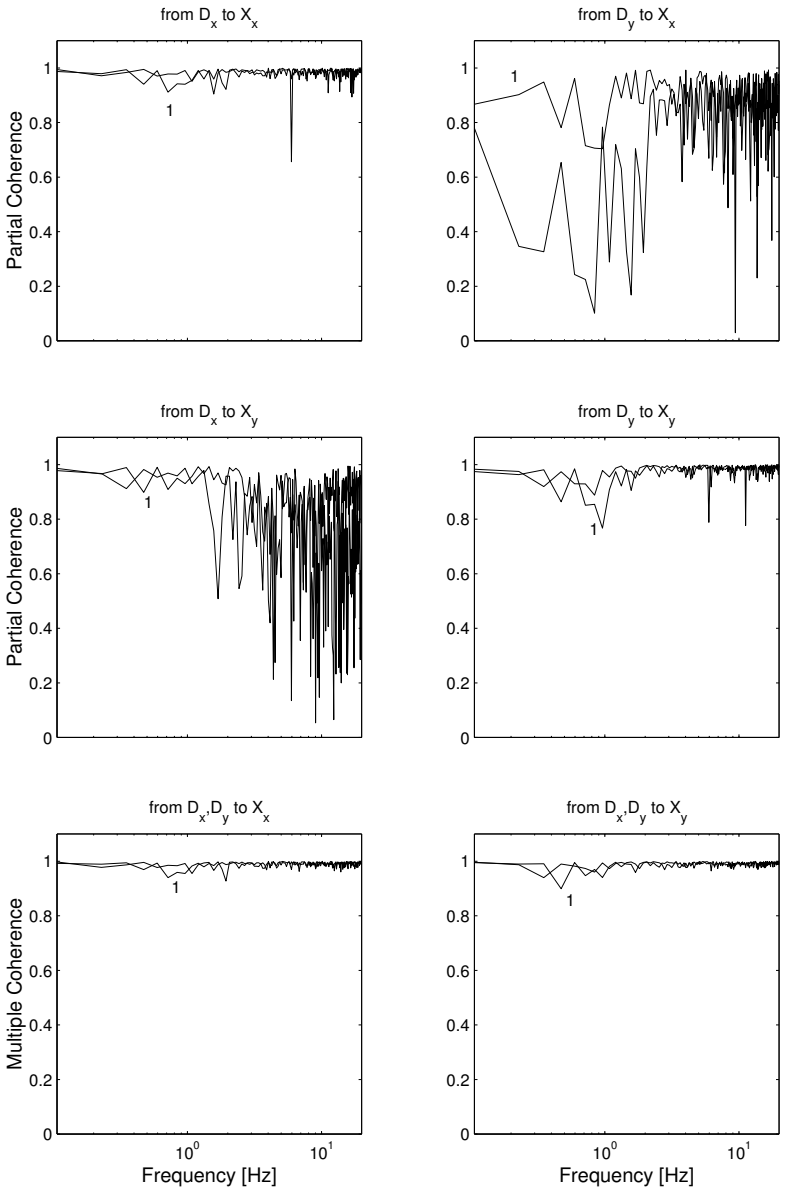

Figure 5.7: *Estimated coherence functions corresponding to the complete system from force disturbance D to end point position X corresponding to the estimates shown in Fig. 5.6 (parameter set one labeled by 1's). Upper two rows: partial coherence functions; bottom row: multiple coherence functions.*

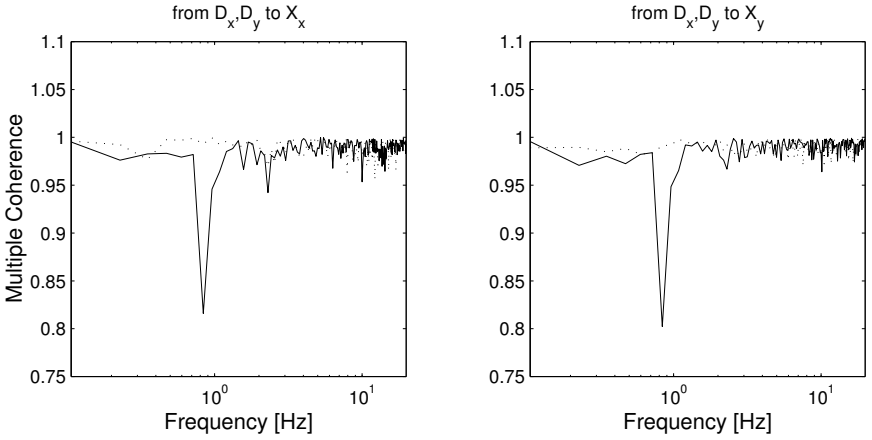

Figure 5.8: *Multiple coherence estimates in the case of different admittances of the environment. Arm damping B_a is set to 25% of its default value. Solid lines: large (default) compliance of the environment. Dashed dotted lines: low compliance of the environment. Note the lowest value on the ordinate is 0.75.*

5.4.3 Input and output noise

Both noise signals are generated as a stochastic sequence of time samples and filtered at 20 Hz (fourth order Butterworth) to avoid aliasing. With increasing power level of both input and output noise, the estimated multiple coherence functions decrease, as was expected (Fig. 5.9). The coherence functions are still very high (> 0.8) for SNRs of -10 dB. When the power of the noise is as large as that of the signal itself (SNR=0 dB), the estimated multiple coherence functions remain mostly above 0.4.

5.4.4 Frequency averaging and observation time length

The smoothing effect of averaging is largest in the case of severe noise. For large stochastic noise power (SNR=0 dB) at both input and output in combination with only four averaging frequencies ($m = 4$), variance and bias of the estimated coherence functions are large (Fig. 5.10). For $m = 16$, the variance is smaller resulting in smoother estimates of the coherences.

The effect of the observation time length is analyzed for the default conditions, except that no noise is applied. Then the only cause for bias is the width of the frequency window used for averaging, which is directly dependent on the number of averaging frequencies (m) and reciprocally on the observation time length (T). Figure 5.11 shows the estimated multiple coherence functions for 32.768, 16.384 and 8.192 s ($m = 4$). The multiple coherence functions decrease to a minimum for the shortest record length at the eigenfrequency of the arm where the variation of the MFRFs is largest. For this short observation, the width of the frequency window

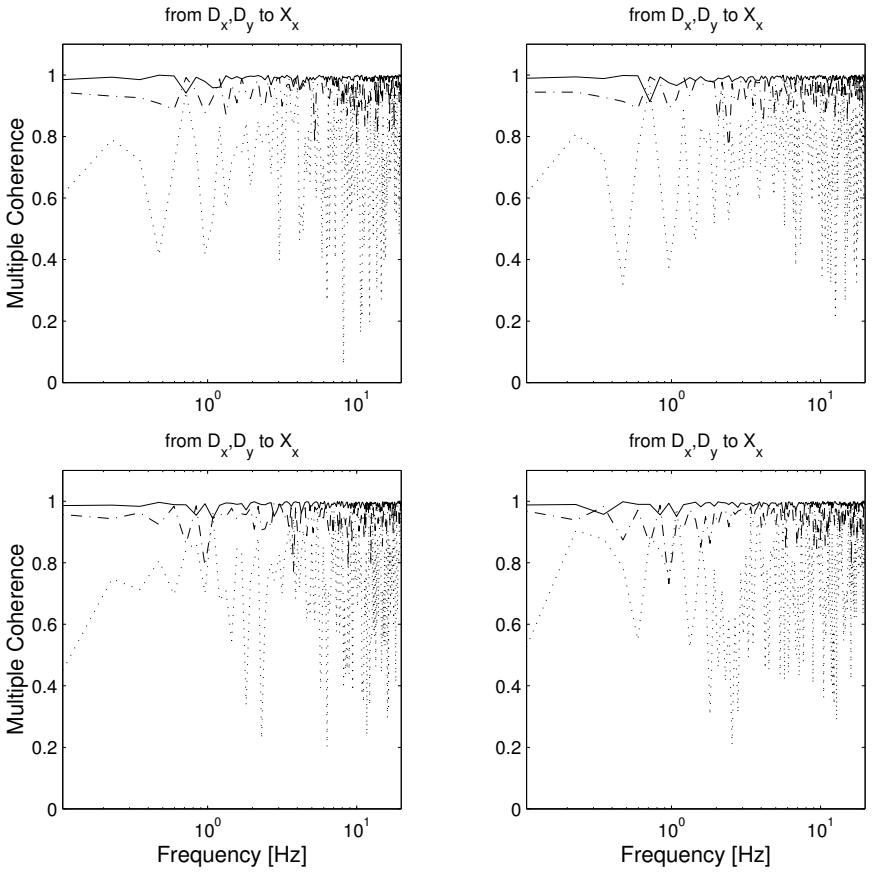

Figure 5.9: *Estimated multiple coherence functions for different signal-to-noise ratios at the input (upper row) and output (bottom row): -20 dB (solid lines); -10 dB (dashed-dotted lines) and 0 dB (dotted lines).*

was largest, i.e. $\frac{m}{T} = \frac{4}{8.192} \approx 0.5$ Hz. The multiple coherence was still very high ($>$ 0.8, Fig. 5.11, upper row). For comparison, the same exercise is performed but now with different window widths to preserve the same frequency resolution. Therefore $m = 16$, 8 and 4 for $T = 32.768$, 16.384 and 8.192 s respectively. Figure 5.11 (bottom row) now shows that all estimated multiple coherence functions exhibit a minimum which is more or less the same.

5.5 Discussion

This article presents a new multivariable closed loop identification method to estimate the compliance of the arm during excitation with continuous force distur-

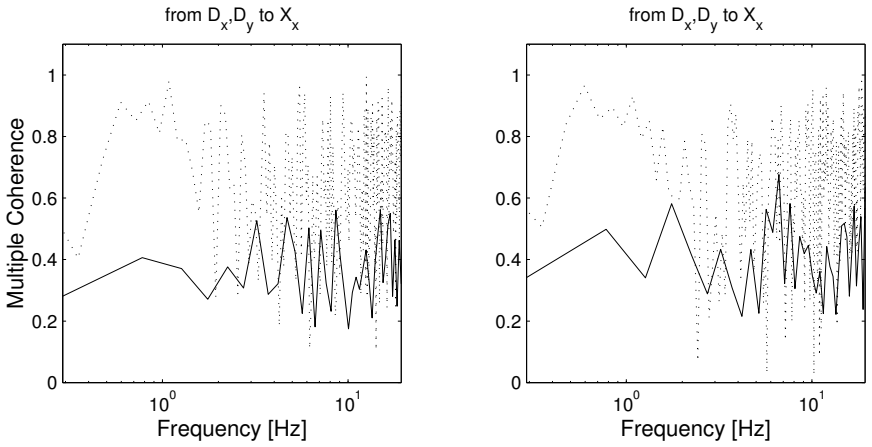

Figure 5.10: *Estimated multiple coherence functions for two different numbers of averaging frequencies (m) in case of large noise power at both input and output (SNR=0 dB). $m = 4$ (dotted lines), $m = 16$ (solid lines).*

bances. The method is applicable to posture tasks where interaction with an environment takes place which always results from the application of force disturbances. The accuracy of the estimator is tested for different parameters of the dynamic compliance of the arm and several methodological conditions.

In the following, the performance and limitations of the estimator, the validity of the arm model, the properties of the disturbance signals and the relevance of applying force disturbances are discussed.

5.5.1 Estimator performance

Estimates are always contaminated with bias (structural errors) and variance (random errors). Both are primarily the result of noise. Input noise comes from additional inputs that are uncorrelated with the force disturbance signal, like uncorrelated muscle activation, and can be minimized by preventing anticipatory behavior of the subject. To rule out anticipation, unpredictable (random) disturbances are necessary. Output noise is mainly caused by system nonlinearities and time variant behavior of the limb and environment. Nonlinearities can be minimized using small amplitude disturbances and application of high performance (linear) manipulators. Time variant behavior is likely to be minimal with clear and natural task instructions that are translated by the CNS into unambiguous motion control actions.

For modelling purposes, noise at the input can easily be replaced by noise at the output, accounting for the difference of the MFRF of the combined system. The input noise power was almost constant over frequency while the power of the output

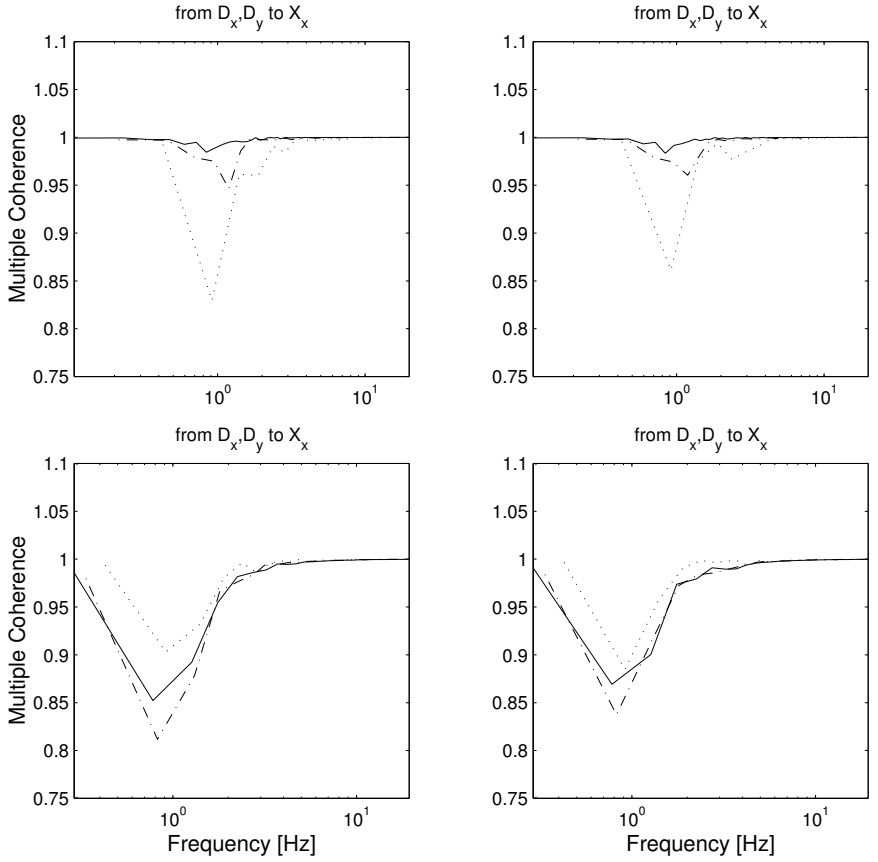

Figure 5.11: *Estimated multiple coherence functions for different observation time lengths (upper row) without noise.* $T = 32.768$ *s (solid lines);* $T = 16.384$ *s (dashed-dotted lines) and* $T = 8.192$ *s (dotted line). Bottom row:* $T = 32.768$ *s with* $m = 16$ *(solid lines);* $T = 16.384$ *s with* $m = 8$ *(dashed-dotted lines) and* $T = 8.192$ *s with* $m = 4$ *(dotted line). Note the lowest value on the ordinate is 0.75.*

noise was taken as a scaled version of the output itself, according to the expression of the SNR (Eq. (5.24)). Hence, the difference between the input and output noise power is determined (approximately) by the gain of the MFRF of the combined system such that their net effects are the same at the output (Fig. 5.9). Despite this rather simplistic combination of input and output noise power, it clearly demonstrates that high frequency input noise deteriorates the estimates to a lesser extent than high frequency output noise. This is due to the filtering effect of the system compliance.

Averaging of the raw spectra over adjacent frequencies is applied, which effectively reduces the variance (Fig. 5.10). Another positive effect of averaging is

that bias in the estimates of the partial and multiple coherence functions decreases (Jenkins and Watts, 1968). This is also clear from Fig. 5.10 where the estimates are apparently too high for $m = 4$ compared to those for $m = 16$. The disadvantage of frequency averaging is the increase of bias due to the decrease of the frequency resolution. Bias is particularly large at frequencies where the MFRF of the system to be identified contains abrupt changes, e.g. from oscillatory behavior (Fig. 5.8). The trade-off between the positive and negative effects of frequency averaging can primarily be solved with increasing the observation time length (Fig. 5.11).
Another source of bias and variance originate from the application of stochastic disturbance signals (Schoukens et al., 1993). The bias can be reduced by substantially increasing the observation time length, as mentioned before. However, to avoid time variant behavior due to fatigue in the case of in-vivo experiments, long observations are undesirable. Application of deterministic disturbances, like the multisine signals in this study, instead of stochastic noise has been proved to reduce bias in the estimates (Peeters et al., 2001).

An important property of the estimator is the accurateness for short observations. For instance, a 8.192 s observation time length and only four averaging frequencies still results in high multiple coherence functions (> 0.8, Fig. 5.11), at a frequency resolution of $\Delta f = 4/8.192 \approx 0.5$ Hz.

An alternative averaging method, as used in the study by Perreault et al. (1999), is the periodogram approach or Welch method (Welch, 1967). This method relies on segmentation in the time domain of the measured signals and performing spectral estimates on each segment. The raw estimates of each periodogram are averaged and used to calculate the final estimate of the arm compliance, using the same estimator as used in this study. The Welch method is therefore less suitable to deterministic signals as used in this study because the requirement was that the observation time length should be the same as the period of the disturbance signal in order to achieve the exclusion of bias. Because segmentation introduces bias, a deterministic disturbance is not preferred anymore to a stochastic one for application of the Welch method. Hence, the advantage of deterministic signals does not apply to the Welch method.
For the same model parameters and noise power, Perreault et al. (1999) showed values of the estimated multiple coherences of about 0.7 with a 2.56 s (Welch)window ($\Delta f = 1/2.56 \approx 0.4$ Hz). Our results showed somewhat higher values (> 0.8, Fig. 5.11) for a comparable frequency resolution ($T = 8.192, m = 4, \Delta f \approx 0.5$). Similarly, for higher frequency resolutions, i.e. $T = 16.384$ and $T = 32.768$ s in our case (with a constant number of averaging frequencies of $m = 4$) against Welch-window sizes of 5.12 and 10.24 s respectively, the estimates of the multiple coherences are comparable. However, their results required a total observation time length of 60 s, which is more than seven times longer than in our case for $T = 8.192$, and four times and two times longer in the case of $T = 16.384$ and $T = 32.768$ s respectively. Generally, the identification method presented here requires relatively short observations and moderate averaging to preserve sufficient frequency resolution with reasonably high values of the multiple coherence functions. It is proved by

this study that the current identification method together with the application of the deterministic disturbances offers accurate estimations, within observation times that are substantially shorter than required by the Welch method. Evidently, experiments should be conducted to verify high multiple coherences during such a short observation times in practice.

Perreault et al. (1999) used a sampling frequency of 50 Hz against 125 Hz in this study. However, sampling frequency has no influence on the frequency resolution and therefore does not change the results. The advantage of a higher sampling rate is that low-pass anti-aliasing filters can be applied with cut-off frequencies sufficiently above the frequency range of interest, which is approximately 20 Hz for mechanical properties of the arm.

Coherence functions apply to independent inputs and the outputs of the combined closed loop system. In the case where the compliance of the environment is substantially lower than that of the arm, the estimated multiple coherence function is largely determined by the (linear) environment instead of the arm (Fig. 5.8). An open-loop estimator should be used in these cases to circumvent this problem. However, in the case of force disturbances, a high environmental compliance is primarily desired resulting in an input-output behavior that is mainly determined by the arm compliance. In these cases, coherence functions therefore are largely determined by the arm compliance.

5.5.2 Frequency vs time domain identification

An alternative to the frequency domain is identification in the time domain. The corresponding nonparametric time domain identification then provides estimates of the system's matrix impulse response function (MIRF). For linear open-loop systems, both time and frequency domain identification obtain comparable estimates (Perreault et al., 1999). Besides numerical differences, there is a preference for MFRFs to MIRFs with respect to visual presentation. Where MIRFs are poor indicators of the system dynamics and give only insight in the time extent or memory of the system, MFRFs show important global properties of dynamic systems such as the order of the system, relative damping and regions of oscillatory behavior.

Apart from these general differences, a detailed comparison cannot be made because nonparametric identification in the time domain has not been studied previously for closed loop systems. Usually, parametric estimators in the time domain are applied using a fixed model structure of the system to be estimated. Parametric identification is less attractive in the first stage when detailed knowledge of the system structure is not at hand. A proofed method to quantify the parameters of a single-joint arm model is the application of a non-parametric estimator in the first stage, followed by (least squares) fitting of a parametric model onto the estimates as the second stage (Van der Helm et al., 2002).

5.5.3 Validity of the arm model

The arm model used is very simple, only consisting of a linear mass-damper-spring system. This model is frequently used to describe the input-output behavior of limbs at endpoint (mostly the hand) for small continuous displacements around a reference point under different experimental conditions (Dolan et al., 1993; Tsuji et al., 1995; Gomi and Kawato, 1996; Gomi and Osu, 1998; Perreault et al., 2000, 2001). Despite its limited descriptive ability, since it is only a lumped representation of intrinsic and reflexive dynamics together, these studies showed that this model is quite accurate for the conditions studied. In previous studies from our group, we extended the mass-damper-spring system with linear position and velocity feedback to separately identify the gains of muscle spindles (De Vlugt et al., 2002; Van der Helm et al., 2002). For the experimental conditions applied, we found that both gains depend on the frequency content of the force disturbance and damping of the environment. Despite the highly non-linear behavior of the muscle spindles, mainly due to their unidirectional sensitivity to stretch (Kirsch et al., 1994; Stein and Kearney, 1995; Kearney et al., 1997; Zhang and Rymer, 1997; Mirbagheri et al., 2000), high values for the variance accounted for (VAF) were found with the linear endpoint model.

Other nonlinearities on the muscle level are the different calcium activation-deactivation rates, and mechanical properties of the contractile elements like the force-length and force-velocity characteristics (Winters and Stark, 1985). Apparently, in multiple muscle systems these nonlinearities cancel out at endpoint level under specific conditions. Application of the linear identification method as developed in this study seems therefore justified. Summarized: 1) the application of small amplitude disturbances simply do not excite appreciable nonlinearities; 2) unidirectional presumably turns into bidirectional behavior in case of muscles acting as antagonistic pairs and 3) from a functional anatomical point of view, different muscles likely act at different lengths hence distributing their characteristics over a wider range of motion which smoothes out the nonlinearities.

5.5.4 Relevance of force disturbances

Application of force disturbances while performing a position task offers insight into the disturbance rejecting behavior of the human controller, i.e. the properties of the arm compliance. This experimental condition equates to natural posture tasks that aim to minimize deviations around a fixed desired position. Examples are holding a steering wheel or positioning a drilling machine (in the lateral direction). The magnitude of positional deviations is dependent on the total compliance at the endpoint (hand) and evidently from the power of the disturbance. The total compliance is the sum of the compliance of the arm and the environment, i.e. the dynamic compliance of the steering wheel in this example. Because there is mutual interaction, the endpoint compliance can be adapted through changing the compliance of the human arm.

The advantage of continuous disturbances is that subjects have the opportunity

to adapt to the disturbance, in contrast to transient disturbances. In particular for unpredictable continuous disturbances, the arm compliance can only be changed by different (constant) levels of intrinsic and reflexive contributions. In general, high (co)contraction and large feedback from muscle spindles can potentially decrease the arm compliance and hence improve the disturbance rejection.

Simulation studies have shown that intrinsic and reflexive mechanisms were effective for continuous unpredictable force disturbances where the task was to minimize hand displacements. In particular, high afferent position feedback was predicted for small bandwidth force disturbances (De Vlugt et al., 2001; Schouten et al., 2001). These results were very similar to a comparable experimental study by Van der Helm et al. (2002), and were explained from an optimal controller perspective, i.e. adjustment of the dynamic arm compliance to minimize displacements of the hand. Such an explanations are only possible if the system is being perturbed by force disturbances such that all compliance mediating mechanisms have direct effect on the task performance (or hand displacement)

In the case of continuous position disturbances a force task seems logical (compared to force disturbances and a position task) and one is likely interested in mechanisms that are suited to control force, probably by Golgi tendon organs. Studies based on such an approach are not known to us. The challenge remains to clarify the role of different mechanisms, in particular reflexes, that contribute to whole limb compliance for different tasks and during continuous disturbances. The degree of interaction and the type of disturbance signals are important aspects in 1) understanding the adaptability of the arm compliance by the CNS and 2) the choice (open or closed loop) of the identification method. Unfortunately, these aspects were not fully recognized in the literature.

5.6 Conclusions

Closed-loop identification is necessary to estimate the mechanical properties of the arm using force disturbances where interaction with the environment always exists. This study proposes a new frequency-domain estimator that estimates the arm compliance from the closed loop. The major advantages of the estimator are summarized below.

- The estimator is nonparametric such that no *a priori* system knowledge is required.
- The estimator is very accurate and requires only short observations periods.
- The application of deterministic multisine disturbance signals do not introduce bias and variance, and facilitates full control of the input spectra.

To understand the functionality of mechanisms controlling the dynamic compliance of the arm during posture tasks, the application of force disturbances and manipulable environments is important because it establishes a natural experimental

condition. In order to estimate the arm compliance under such conditions, a closed-loop identification method as described in this study is indispensable.

Chapter 6

A planar haptic device for movement control analysis of the human arm

Erwin de Vlugt, Alfred C. Schouten, Frans C. T. van der Helm, Piet C. Teerhuis, Guido G. Brouwn

Journal of NeuroScience Methods 2003; 129: 151-168

This paper describes the design and application of a haptic device to study the mechanical properties of the human arm during interaction with compliant environments. Estimates of the human endpoint admittance can be obtained by recording position deviations as a result of force perturbations. Previous studies attempted to estimate the impedance by recording force as a result of position perturbations, but these experiments do not require a feasible task of human beings. A general problem of force-controlled haptic devices is the occurrence of contact instability, especially where a small virtual mass is required. This negative effect is reduced by the use of a lightweight but stiff manipulator and a robust servo-based admittance controller. The virtual admittance is accurate to at least 13 Hz, attaining a minimum virtual mass of 1.7 kg (isotropic, without damping and stiffness). The properties of known test loads were estimated with an accuracy higher than 98 %, up to 20 Hz. The application of the manipulator is evaluated by an experiment with a subject performing a position maintenance task. With this device it is possible to study the adaptability of the neuromuscular system to a variety of environments, enabling a new and functional approach to human motion research.

6.1 Introduction

Many daily life human arm motion tasks imply physical interaction with objects, hereafter referred to as the environment, of which the mechanical properties can be diverse. Most environments are well manipulable, meaning that humans are able to control their hand position by generating the appropriate muscle forces. By changing the arm admittance the combined admittance of arm plus environment can be modified. From the combined admittance, important dynamic properties can be derived such as mechanical stability margins and the resistance to external force perturbations (De Vlugt et al. 2002; Van der Helm et al. 2002). The admittance is defined as the dynamic ratio of position to force (m/N), and equal to the inverse of the mechanical impedance. A low admittance ($\sim$ high impedance) is desirable, which means small position deviations for a given magnitude of force perturbations. The arm admittance comprises inertial, viscous and elastic properties from intrinsic structures (muscles, connective tissues, bones) and reflexive feedback properties through muscle spindles, golgi tendon organs and the central nervous system.

In previous studies that have aimed to characterize the admittance of human limbs, a manipulator was used to impose a mechanical perturbation while the human reaction did not have an effect on the position of the manipulator (Acosta et al. 2000; Cathers et al. 1999; Dolan et al. 1993; Gomi an Osu 1998; McIntyre et al. 1996; Mussa-Ivaldi et al. 1985; Perreault et al. 2001, 2002; Tsuji et al. 1995; Won and Hogan 1995; Zhang and Rymer 1997). In those studies, the subjects were required to exert a constant force while the hand was displaced by the use of different position perturbations, which is considered not to be a very natural task. Resulting viscoelastic properties from intrinsic and reflexive origin were often explained in terms of contributions to movement stability. However, there is no functional relevance to actively preserve stability because the movement is simply imposed by an inherently stable, position-controlled manipulator having an extremely low admittance.

Force-controlled manipulators, on the contrary, facilitate interaction with compliant environments such as presented in this study. With these manipulators, force perturbations can be applied in combination with position related tasks which comply to natural movement conditions. The effect of the combination of perturbation type and task instruction on the neuromuscular response has been previously studied (Akazawa et al. 1983; Kanosue et al. 1983; Doemges and Rack 1992; Mirbagheri et al. 2000). These studies showed that muscle spindle responses to force perturbations during a position-holding task where significantly larger than in the case of position perturbations while maintaining a constant force.

In this report, a force-controlled two-degree-of-freedom (2DOF) haptic device is described consisting of a two-linkage anthropomorphic arm having a force sensor at the tip. The manipulator is driven by two powerful hydraulic actuators. A position-servo-based haptic controller is used to increase the endpoint admittance, i.e. decrease the real mass of the linkages to a virtual mass experienced by the subject. The bandwidth is sufficient to capture all the dynamic properties of the human

arm, which can be identified using a multivariable system identification method (De Vlugt et al. 2003). With the use of this device, the adaptability of the admittance of the human arm to different environments and types of force perturbations can be analyzed in the horizontal plane, which has never been done before.

Existing, comparable haptic devices are the MIT-MANUS (Colgate 1988) and the Hopkins manipulandum (Shadmehr and Brashers-Krug 1997). These manipulators have been designed to study slow, human induced motions and have never been used for the identification of the arm admittance. Another manipulator, which is rather strong and compliant at the endpoint, is the PFM manipulandum (Gomi and Kawato 1996). The PFM has been used to measure the planar stiffness and viscosity properties of the human arm using force pulses (Gomi and Kawato 1996; Gomi and Osu 1998). However, the design and constructional aspects of the present manipulators have never been formulated from the perspective of functional control of the human arm during continuous interaction with (virtual) environments. Also, previous applications were directed at relatively low frequency properties only (stiffness and damping), while the purpose of the present manipulator is to identify the arm admittance over a broad frequency range.

A fundamental problem in haptic control is the occurrence of contact instability when the subject firmly grips the handle (Carignan and Cleary 2000; Hogan and Colgate 1989; Van der Linden 1997). Since the haptic device actively generates mechanical energy, contact instability can pose a direct physical threat to the human subject and needs to be avoided at all times. Contact instability is the result of limited controller bandwidth, which in turn is the result of mechanical resonances of the linkage system. Consequently, the manipulator admittance can only be 'replaced' adequately over a limited frequency range. Outside this range, stability cannot be guaranteed. Within the current design, we maximized the bandwidth of the haptic device by the choice of strong and lightweight materials and the optimal adjustment of a servo-based controller. The result is the realization of a compliant and stable environment for worst case loading conditions. The accuracy of the load estimates is tested by comparing the estimated values with the true values of different technical mass-spring systems. Its final application is demonstrated by showing the estimated arm admittance of a subject performing a posture maintenance task.

6.2 Haptic device

6.2.1 Manipulator-actuator chain

A diagram of the two-linkage manipulator is shown in Figure 6.1A. Both linkages ($l = 0.60$ m) are constructed as hollow cages and made of 3 mm thick aluminum alloy having a high stiffness to mass ratio. Each linkage rotates on a vertical axis, indicated by the angles θ_1 (around the main axis) and θ_2 (the secondary axis). The motion is constrained to the horizontal plane. Torques are generated by two identical direct drive hydraulic motors around each axis (supply pressure 120 bar; max. torque 480 Nm; max. angular velocity 15 rad/s). The actuators are vertically aligned

on the main axis. One actuates the (inner) first linkage and the other the (outer) second linkage by means of two parallel bars. The mass of the inner linkage is 5.4 kg (including the pull bars) and that of the outer linkage is 3.6 kg. Angular rotation is measured by optical encoders (Heidenhain ROC417, 17 bits per 360 deg.). Angular velocities are derived analogously. Oil flow is controlled by critical four way valves (Moog D760-2817A) with valve position feedback (300 Hz bandwidth from input voltage to valve position). Pressure difference between both sides of the rotor vane is measured (Paine transducers). Each motor is equipped with a pressure controller (150 Hz bandwidth) to compensate for pressure fluctuations due to movements, leakage and oil compressibility (Heintze et al. 1995). Strain gauges are mounted in the handle to measure the hand reaction force (range -300 to 300 N) in two orthogonal directions.
Interaction of the human arm with the environment, as simulated by the manipulator, is clarified in the control scheme of Figure 6.1B. The total force acting upon the environment is the summation of the hand reaction force $\mathbf{F}$ and an independently generated external force perturbation signal $\mathbf{F_{ext}}$. The hand position $\mathbf{X}$ is the output of the total system.

6.2.2 Safety system

To prevent the subject from entering the area of motion of the manipulator, the body is securely strapped to the chair back by two shoulder belts (see Fig. 6.1A). The shoulder rotation center is horizontally aligned with the hand grip by adjusting the height of the chair.
The manipulator is equipped with an autonomous safety system which is approved by the local board on human experiments. The absolute endpoint velocity is limited to 1.0 ms^{-1}, to guarantee a safe range of operation. The absolute hand reaction force is limited to 100 N. In addition, the power (dot product of endpoint velocity and hand reaction force) transferred by the manipulator to the subject's hand is limited to 40 Watts. At all times, the subject is able to stop the manipulator immediately by pressing an emergency button with his or her free hand. To prevent the manipulator from swaying when the subject loosens contact, the manipulator is stopped when the absolute hand reaction force is below 0.1 N for 10 ms.

6.2.3 Haptic controller

The haptic controller is optimized using linear analysis tools. This implies that optimal controller settings are determined for movements of the manipulator around different positions that are small enough to approximately describe the system behavior by linear transfer functions. Linear transfer functions facilitate direct access to important system properties in the frequency domain, like resonance frequencies, phase lags and system bandwidth. In accordance with notations used in previous studies, the endpoint admittance, force and position are defined in the Cartesian frame having its origin in the subject shoulder rotation center.

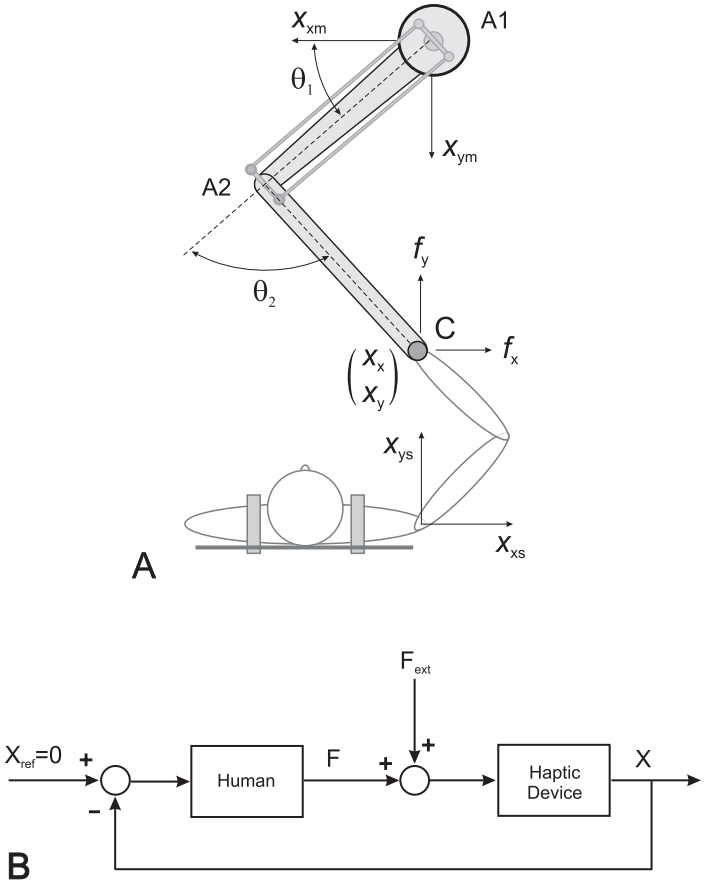

Figure 6.1: *A: Schematic configuration of the experimental setup. The inner link rotates around the main axis (A1) and the outer link rotates around the secondary axis (A2); θ_1: rotation angle of the innerlink, θ_2: the rotation angle of the outer link relative to the inner link. The subject is physically attached to the manipulator by taking a firm grip on the handle (C). Hand reaction forces $\mathbf{F}$ and hand position $\mathbf{X}$ are constrained to the horizontal plane and decomposed into Cartesian coordinates in the subject's frame (x_{x_s}, x_{y_s}). The origin of this frame is located in the rotation center of the shoulder. The manipulator kinematics are defined in the manipulator's frame (x_{x_m}, x_{y_m}) having its origin at the main rotation axis. B: General (nonlinear) disturbance block scheme of the mechanical interaction between the human (arm) and the haptic device, acting as the environment. The manipulator position is being calculated from the hand force ($\mathbf{F}$) recorded at the handle. The external force perturbation $\mathbf{F_{ext}}$ is added to the hand force. The system output is the common endpoint or hand position $\mathbf{X}$. $\mathbf{X}_{ref} \equiv 0$ indicates the posture task, i.e. a reference position to be maintained.*

The admittance controller configuration is shown in Figure 6.2. The desired trajectory is given by:

$$\mathbf{X}_{des}(s) = V(s)(\mathbf{F_{ext}}(s) - \mathbf{F}(s)) \tag{6.1}$$

with $s = j2\pi f$ the Laplace operator (f the frequency in Hz). In Eq. (6.1), $\mathbf{X}_{des}(s) = [x_{des,x}(s)\ x_{des,ys}(s)]^T$ is the desired endpoint position (^{T} indicates the transposed), $\mathbf{F}(s) = [f_x(s)\ f_y(s)]^T$ the hand reaction force, $\mathbf{F_{ext}(s)} = [f_{ext,x}(s)\ f_{ext,y}(s)]^T$ the external force perturbation, and $V(s)$ the multivariable transfer function (MTF) of the virtual endpoint admittance according to:

$$V(s) = \left(\begin{bmatrix} m_{xx} & m_{xy} \\ m_{yx} & m_{yy} \end{bmatrix} s^2 + \begin{bmatrix} b_{xx} & b_{xy} \\ b_{yx} & b_{yy} \end{bmatrix} s + \begin{bmatrix} k_{xx} & k_{xy} \\ k_{yx} & k_{yy} \end{bmatrix} \right)^{-1} \tag{6.2}$$

with m_{ij} the virtual mass, b_{ij} virtual damping and k_{ij} the virtual stiffness components ($i, j \in [x, y]$).

The servo is angular based such that kinematic transformations to, and from, the Cartesian frame are required. The servo is the closed-loop subsystem from $\mathbf{\Theta}_{des}(s)$ to $\mathbf{\Theta}(s)$ (Fig. 6.2), with $\mathbf{\Theta}(s) = [\theta_1(s)\ \theta_2(s)]^T$ the vector of rotation angles. For small deviations around a mean (not necessarily fixed) reference position, the variation of the reference angles are obtained by inverse transformations from the Cartesian frame:

$$\partial\mathbf{\Theta}(s) = J^{-1}\partial\mathbf{X}(s)$$

with J the Jacobian (Craig 1989):

$$J = \begin{bmatrix} -l_1 \sin\bar{\theta}_1 - l_2 \sin(\bar{\theta}_1 + \bar{\theta}_2) & -l_2 \sin(\bar{\theta}_1 + \bar{\theta}_2) \\ l_1 \cos\bar{\theta}_1 + l_2 \cos(\bar{\theta}_1 + \bar{\theta}_2) & l_2 \cos(\bar{\theta}_1 + \bar{\theta}_2) \end{bmatrix}$$

and $\bar{\theta}_1$ and $\bar{\theta}_2$ the means of θ_1 and θ_2 respectively.

The stability of the haptic device is determined by the loop MTF. Since the admittance control configuration consists of a servo (inner) loop and a force (outer) loop (see Fig. 6.2), the dynamic properties of both loop MTFs are important to the overall behavior of the haptic device.
The open loop servo MTF from $\epsilon_\theta(s)$ to $\mathbf{\Theta(s)}$ equals:

$$\overleftrightarrow{H}_{servo}(s) = \mathbf{\Theta}(s)\epsilon_\theta^{-1}(s) = G(s)K(s) \tag{6.3}$$

with $K(s)$ the servo controller to be designed. $G(s)$ is the combined admittance of the manipulator $P(s)$ (in joint coordinates) loaded with the human arm $H(s)$ (in Cartesian coordinates), i.e. from $\mathbf{T}_{act}(s)$ to $\mathbf{\Theta}(s)$, according to:

$$G(s) = \left[I + P(s)J^{-1}H^{-1}(s)J\right]^{-1} P(s) \tag{6.4}$$

where $H^{-1}(s)$ is the impedance of the human load and I the 2×2 identity matrix.
For the force loop (from $\epsilon_f(s)$ to $\mathbf{F}(s)$), the open loop MTF $\overleftrightarrow{H}_{force}(s)$ equals:

$$\mathbf{F}(s)\epsilon_f(s)^{-1} = \overleftrightarrow{H}_{force}(s) = H^{-1}(s)JH_{servo}(s)J^{-1}V(s) \tag{6.5}$$

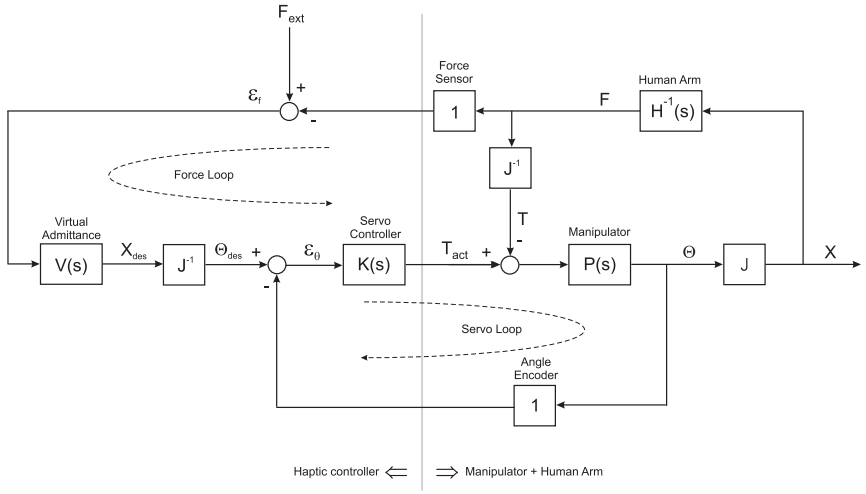

Figure 6.2: *Linear block scheme of the admittance controller for the multivariable two-linkage manipulator. The controller consists of two loops: the servo loop having high loop gain to track the desired angles ($\mathbf{\Theta}_{des}$) and the force loop to include the measured interaction force. Both force sensors and angular encoders are assumed to be ideal. The desired angles are obtained from the virtual dynamics ($V(s)$). Based on the difference between desired and measured angles (ϵ_θ), an actuating torque $\mathbf{T_{act}}$ is obtained from the servo controller $K(s)$. The load comprises that of the manipulator $P(s)$ and the subject's arm $H(s)$. The actual position ($\mathbf{X}$) is imposed to the subject's arm, which therefore appears as an impedance ($H^{-1}(s)$). The cascade of the virtual dynamics and the servo offers the virtual admittance the subject experiences (from $\mathbf{F}$ to $\mathbf{X}$). The external force perturbation signal ($\mathbf{F_{ext}}$) is added to the subject's hand reaction force. The difference ($\epsilon_\mathbf{f}$) is the input to the virtual admittance. Transformation from small angular deviations (around a working point) to Cartesian coordinates is indicated by the Jacobian J.*

where $H_{servo}(s)$ is the closed loop servo MTF according to:

$$\begin{aligned} H_{servo}(s) &= \mathbf{\Theta}(s)\mathbf{\Theta}_{des}^{-1}(s) \\ &= \left[I + \overleftrightarrow{H}_{servo}(s)\right]^{-1} \overleftrightarrow{H}_{servo}(s) \end{aligned} \tag{6.6}$$

The constraint to the servo controller, $K(s)$, is that both the servo loop (Eq. 6.3) and force loop (Eq. 6.5) must be unconditionally stable.

The performance of the haptic device becomes clear when considering the MTF from $\mathbf{F}_{ext}(s)$ to $\mathbf{X}(s)$, which is derived as follows. From Eq. (6.5) it follows that:

$$\overleftrightarrow{H}_{force}(s)\epsilon_f(s) = \mathbf{F}(s)$$

Substituting, $\mathbf{F}(s) = H^{-1}(s)\mathbf{X}(s)$ gives:

$$\epsilon_f(s) = \overset{\hookleftarrow}{H}{}^{-1}_{force}(s)H^{-1}(s)\mathbf{X}(s) \tag{6.7}$$

Substituting $\epsilon_f(s)$ in Eq. (6.7) by:

$$\epsilon_f(s) = \mathbf{F}_{ext}(s) - \mathbf{F}(s) = \mathbf{F}_{ext}(s) - \mathbf{H}^{-1}(s)\mathbf{X}(s)$$

gives:

$$\mathbf{F}_{ext}(s) = \left[I + \overset{\hookleftarrow}{H}{}^{-1}_{force}\right] H^{-1}(s)\mathbf{X}(s)$$

and finally the combined admittance at endpoint is:

$$\mathbf{X}(s)\mathbf{F}_{ext}(s)^{-1} = H(s)\left[I + \overset{\hookleftarrow}{H}{}^{-1}_{force}\right]^{-1} \tag{6.8}$$

The general purpose of the controller $K(s)$ is to obtain high loop gains such that the gains of $\overset{\hookleftarrow}{H}_{servo}(s)$ are high and consequently $H_{servo}(s) \rightarrow 1$ and $\mathbf{\Theta}(s) \rightarrow \mathbf{\Theta}_{des}(s)$. Also, the force loop (Eq. 6.5) will converge to $H^{-1}(s)V(s)$ such that the combined admittance at endpoint (Eq. 6.8) becomes:

$$\begin{aligned} \mathbf{X}(s)\mathbf{F}_{ext}(s)^{-1} &\approx H(s)\left[I + V^{-1}(s)H(s)\right]^{-1} \\ &\approx \left[V^{-1}(s) + H^{-1}(s)\right]^{-1} \end{aligned} \tag{6.9}$$

Eq. (6.9) describes the ideal input-output behavior from external force to endpoint position that is formed by the parallel configuration of the human arm ($H(s)$) and the virtual environment ($V(s)$), i.e. the manipulator admittance ($P(s)$) is perfectly masked.

The virtual filter and the position servo are designed in Simulink and implemented in a 16 bit DSP signal processor (DS1003 60 MHz, DSpace GmBh) at 1 kHz sample frequency.

6.3 Method

6.3.1 Servo controller optimization

The servo controller $K(s)$ is optimized to realize a maximum bandwidth of the closed loop servo (Eq. 6.6). The servo controller is implemented as a proportional-differential (PD) controller for each axis:

$$\tau_{act,n} = k_{p,n}(\theta_{n,des} - \theta_n) + k_{d,n}(\dot{\theta}_{n,des} - \dot{\theta}_n) \tag{6.10}$$

with $\tau_{act,n}$ the actuator torque and $k_{p,n}$ and $k_{d,n}$ the gains of proportional and differential action respectively (n denotes the actuator, i.e. $n \in [1, 2]$).

Because the dynamics of the manipulator and the human arm change with configuration, the servo controller is optimized at five different endpoint positions of the manipulator, being: central $[0, 0.45]$ [m], left $[-0.2, 0.35]$ [m], right $[0.2, 0.35]$ [m], proximal $[0, 0.35]$ [m] and distal $[0, 0.55]$ [m] (numbers adopted from Gomi et al. 1998). These coordinates are defined in the subject's frame and cover a sufficiently wide range of human arm positions. To obtain a stable servo for many different loading conditions, the worst case load is taken, being the subject generating maximum resistance to the force perturbations. Stability is the constraint to the optimizations for which different margins are taken, ranging from wide to rather narrow (Sec. 6.3.3). Optimizations for all positions are performed simultaneously, resulting in one set of optimal controller gains for each size of the servo stability margin. The optimization is performed independently from the force loop.

6.3.2 Force loop optimization

Given the optimized servo, the force loop (Eq. 6.5) is optimized to find the maximum attainable stable virtual admittance. Apart from the servo, the force loop also comprises the human arm impedance and the virtual admittance. Similar to the optimization of the servo, the worst case loading condition occurs when the human arm generates maximum resistance resulting in a high impedance and consequently in potentially destabilizing high loop gains. The worst contribution of the virtual admittance is when it only has mass terms which at the same time are small, causing high loop gains at low frequencies and 180 degrees phase lag at all frequencies. Also, five different stability margins are taken as constraints to the optimization of the force loop (Sec. 6.3.3).

6.3.3 Identification

To determine the effect of the controller $K(s)$ on both force and servo loop, the MTFs of the manipulator ($P(s)$) and that of the human arm ($H(s)$) are estimated to calculate $\overleftrightarrow{H}_{force}(s)$ and $\overleftrightarrow{H}_{servo}(s)$ (i.e. Eqs. (6.5) and (6.3) respectively). To capture all important dynamics, both MTFs are estimated using a broad bandwidth force perturbation signal containing frequencies up to 100 Hz. Using the closed-loop multivariable identification method from De Vlugt et al. (2003), the (two-input two-output) multivariable frequency response function (MFRF) of the corresponding MTFs can be estimated. The method requires the hand reaction force, hand position and the independent external force perturbation.

For the estimation of the test loads, a force disturbance signal including frequencies to 20 Hz is used. The reason for this range is that all important mechanical properties of the human arm are excited by these frequencies (Perreault et al. 1999). Estimation accuracy beyond 20 Hz is therefore considered not relevant. The time period of observation is 20 sec in all cases.

Table 6.1: *Gain and phase margins corresponding to M-circles (> 1) used to impose the stability boundaries. The phase and amplitude margins are determined with respect to the point [-1,0] in the complex plain: phase margin φ equals the remaining angle at unity gain; amplitude margin A equals the remaining amplitude at -180 deg phase shift.*

M	φ [deg]	A [-]
1.3	50	0.44
2	30	0.33
3	20	0.25
4	15	0.20
5	12	0.17

Since MFRFs are only valid descriptions of input-output systems when the underlying system behaves almost linearly, the partial and multiple coherence functions are also estimated as an indication of linearity (De Vlugt et al. 2003; Van der Helm et al. 2002). These functions are equal to one if the system output ($\mathbf{X}$) is a linear function of it's input ($\mathbf{F_{ext}}$) and decrease with system nonlinearities, or additional unmeasured inputs like voluntary forces or measurement noise.

Characteristic loci and M-circles

An adequate method to infer stability and performance properties of systems under feedback control is to plot the characteristic loci of the open-loop system transfer functions, i.e. the MFTFs of the force and servo loops in the present case (Maciejowski 1989). Characteristic loci are the frequency-dependent complex eigenvalues of a multivariable system, describing the dynamic relation between a system input and output signal vector. Another useful tool in control engineering practice is the use of M-circles. These circles apply to the (open-loop) loci and mark the points in the complex plane where the gain of the (closed-loop) system is equal to M. M-circles greater than one are used to determine the stability margins. For instance, if all characteristic loci lie outside the $M = 1.3$ circle, the maximum overshoot of the closed-loop system following an input step is less than 30 %. Stability margins corresponding to five different M-circles are used for both the servo (M_s) and the force (M_f) loop, ranging from 1.3 to 5 (Table 6.1). M-circles smaller than one are used to determine the performance of the closed servo loop. One standard value of $M = \frac{1}{2}\sqrt{2}$ is used. The frequency where the loci cross this circle equals the bandwidth of the closed-loop MTF, i.e. where $|H_{servo}(s)| = \frac{1}{2}\sqrt{2}$.

As an example, Figure 6.3 shows the characteristic loci of the servo loop for the central position and an initial (stable) set of controller gains, being: $k_{p,1} = k_{p,2} = 2400$ and $k_{d,1} = k_{d,2} = 24$. The direction of increasing frequency (f) is indicated by arrows. The circle on the left is the $M_s = 1.3$ circle and the larger circle on the right is the $M_s = \frac{1}{2}\sqrt{2}$ circle. The loci do not cross the $M_s = 1.3$ circle, meaning that the servo is stable and sufficiently damped for these initial controller gains. These gains

appeared to be stable for the other positions also, so that all the necessary MFRFs of the manipulator and those of the subject's arm admittance were estimated and used to determine the optimal controller gains (Sec. 6.3.3). The $M_s = \frac{1}{2}\sqrt{2}$ circle is crossed at 2 Hz and 6 Hz for the first and second locus respectively (Fig. 6.3).

Implementing the optimization

The servo controller gains are optimized by minimizing the following cost function:

$$P(k) = P_s(k) + P_h(k) \tag{6.11}$$

where $P_s(k)$ is related to the servo performance (desired effect) and $P_h(k)$ to high frequency amplification beyond the servo bandwidth (undesired effect, i.e. actuator overdrive). Both functions are dependent on the controller parameter vector $k = \{k_{p,1}, k_{p,2}, k_{d,1}, k_{d,2}\}$ (see Eq. 6.10).

For the servo performance, the bandwidths of both servo loci are taken as direct measures according to:

$$P_s(k) = \frac{1}{f_{b,1}(k)} + \frac{1}{f_{b,2}(k)} \tag{6.12}$$

with $f_{b,1}$ and $f_{b,2}$ the bandwidth of the first and second locus respectively.

The usage of P_h in Eq. (6.11) is to prevent the actuator torque from varying too quickly. For the hydraulic actuators in the present case, the pressure differences in the valves would otherwise be too large leading to undesired noise in the pressure control loops and annoying 'sawing' sounds from highly turbulent oil flows. High frequency excitation is undesired in general and not a specific issue in the hydraulic case in this study. In a preliminary experimental setup we experienced comparable high-frequency noise in the current controller of an electrically powered wrist manipulator. The common problem is that differential (D)-action is required inside the servo bandwidth to induce the necessary phase lead, which at the same time amplifies the gains at frequencies beyond the bandwidth. Therefore, excessively high differential (D)-action in the servo controller is penalized by weighting the gains of the servo loci above 25 Hz in the present case, which approximately equals the frequency where the first locus of the manipulator admittance starts to increase again (Fig. 6.4A). The following cost function P_h to be minimized is therefore taken:

$$P_h = c \sum_{n\Delta f=25}^{n\Delta f=100} |\lambda_{s_1}(2\pi n\Delta f j)| + |\lambda_{s_2}(2\pi n\Delta f j)| \tag{6.13}$$

with $\lambda_{s_1}, \lambda_{s_2}$ the servo loci and c a weighing factor. Different values for c are used, being 0.25, 0.50, 0.75, 1.00, 1.25 and 1.50.

The constraint to the minimization of Eq. (6.11) is that the servo loci may not cross the stability boundaries given by the M_s-circles. For each value of c and for

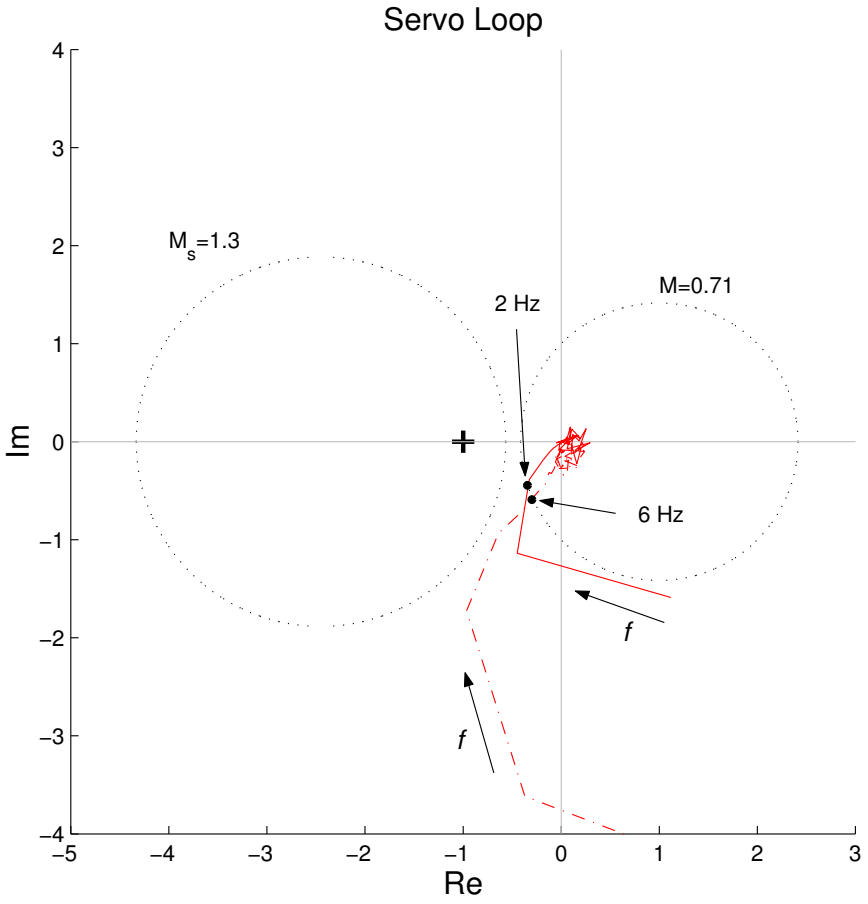

Figure 6.3: *Characteristic loci (solid: first locus; dashed dotted: second locus) for initial and stable controller gains ($k_{p,1} = k_{p,2} = 2400$ and $k_{d,1} = k_{d,2} = 24$) of the servo loop $\overleftrightarrow{H}_{servo}(s)$ in the case the subject is attached. The force loop is opened (hand reaction force was not fed back). The endpoint is in the central position. The stability area is represented by the $M_s = 1.3$ circle which is not crossed by the loci. The $M = \frac{1}{2}\sqrt{2} \approx 0.71$ circle on the right indicates the bandwidth, i.e. where the gains of the closed loop servo equals $\frac{1}{2}\sqrt{2}$ ($f_{b,1} \approx 2$ Hz, $f_{b,2} \approx 6$ Hz). The direction of increasing frequency is indicated by f along the arrows.*

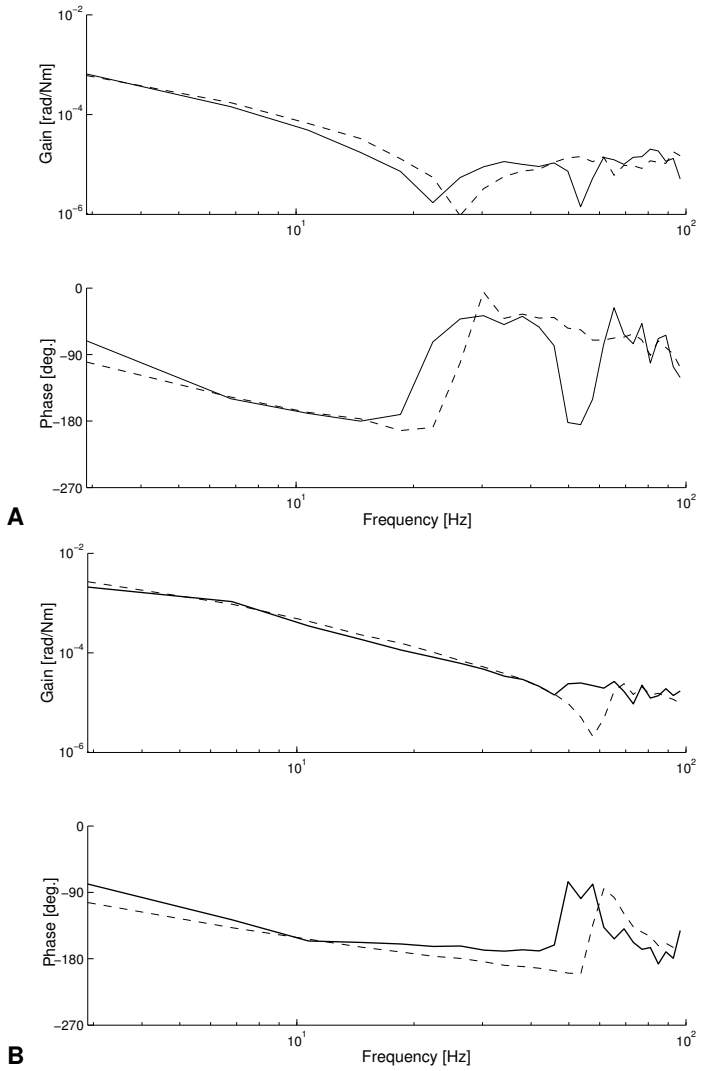

Figure 6.4: *Estimated frequency response functions (FRFs) of the characteristic loci (gain and phase plots) of the manipulator. A: first locus of the admittance of the manipulator loaded with the human arm, i.e. the combined admittance $G(s)$ (solid lines), and that of the unloaded manipulator $P(s)$ (dashed lines). B: the second locus; loaded (solid lines) and unloaded (dashed lines). The loci correspond to the MFRF between the actuator torque ($\mathbf{T_{act}(s)}$) and rotation angles ($\mathbf{\Theta(s)}$).*

each value of the stability margin M_s (25 combinations), the characteristic loci of the servo loop MTFs (Eq. 6.3) are optimized by minimizing $P(k)$.

Given the optimized servo, the force loop is optimized by determining the minimal virtual mass for each combination of M_s and c and for the five different values of M_f (resulting in 75 values of the virtual mass). This is achieved by sizing the loci of the force loop for different values of the virtual mass such that the loci just touch, but do not intersect the M_f-circle. The virtual mass is taken isotropically for simplicity, such that it can be described by one parameter: $m_v = m_{xx} = m_{yy}$ with $m_{xy} = m_{yx} = 0$.

6.3.4 Test loads

The overall quality of the optimally controlled haptic device is judged on two properties: the accuracy with which the desired virtual admittance is simulated and the ability to retrieve reliable estimates of the human arm.
The estimator is tested by identification of known mass-spring loads. The estimated load is then compared to the true one. For this purpose, different combinations of masses and springs are attached to the handle of the manipulator in the central position. All loads are taken symmetrically. Three different isotropic masses were used, weighing 0.99, 1.30 and 1.61 kg. With the smallest mass, four spring configurations were applied: the combination (k_{xx}, k_{yy}) was taken equal to (300,300), (600,300), (300,600) and (600,600) respectively (values in Nm^{-1}). The values are taken as a representative range for the human arm stiffness (Tsuji et al. 1995). Due to the configuration of the springs, the actual stiffness in one direction is increased by the springs in the perpendicular direction. A schematic representation of the spring configuration and the derivation of the true stiffness values is presented in Appendix D. To judge the accuracy of the estimates, a second order mass-spring model has been fitted in the frequency domain through the diagonal elements of the estimated FRFs using a straight forward least squares algorithm. For all combinations of the test loads, the virtual admittance of the manipulator was set at zero stiffness and a symmetric mass of 5 kg. A small amount of virtual damping (5 Nsm^{-1}) was used to suppress oscillations of the endpoint. In the case where the test load includes no springs, the virtual stiffness was set to a small value of 50 Nm^{-1} to exclude drifting of the endpoint position.
After the estimation accuracy is determined, the admittance of the virtual environment is estimated and compared to the real admittance of the manipulator. The estimation is performed while the subject holds the handle and performs the maximal resistance position maintenance task. The difference is expressed as the ratio in eigenvalues of the estimated virtual mass ellipse and the real mass ellipse. The mass ellipse is graphically displayed as a force vector in response to a unit acceleration vector generated by sin and cos functions, according to:

$$\begin{bmatrix} f_1 \\ f_2 \end{bmatrix} = M \begin{bmatrix} \cos\phi \\ \sin\phi \end{bmatrix} \tag{6.14}$$

for $0 < \phi < 2\pi$ and where

$$M = \begin{bmatrix} m & 0 \\ 0 & m \end{bmatrix}$$

is the endpoint mass matrix (for small excursions of the endpoint around a fixed position). Since the mass is taken isotropically, the ellipse is a circle of which the two eigenvalues are equal, i.e. $\lambda_1 = \lambda_2 = m$. In contrast, the real mass of the manipulator at endpoint is displayed as an ellipse having non-zero off-diagonal terms and unequal diagonal terms, which is a general property of a chain of rotating linkages (Craig 1989).

6.3.5 Subject

The arm admittance of one subject (male, 29 years) was estimated. The subject gave informed consent to the experimental procedure. The experiment was carried out with the right arm. The subject was asked to take a firm grip on the manipulator handle (Fig. 6.1). Gravitational forces were compensated for by supporting the upper arm with a brace that was fixed by a rope to the ceiling. The subject was instructed to minimize the displacements of the hand that resulted from the force perturbations, evoking high stiffness and damping of the arm (Van der Helm et al., 2002). On a monitor screen 65 cm in front of the subject, the reference position was visualized by means of a 3 cm diameter circle inside which the subject had to keep a smaller (0.5 cm diameter) filled circle representing the actual hand position. The force perturbation always started after the subject had positioned his or her hand in the center of the reference circles.

6.4 Results

6.4.1 Manipulator dynamics

Figure 6.4 shows the estimated characteristic loci, presented as FRFs, of the manipulator loaded with the human arm, i.e. the combined admittance, $G(s)$ (dark lines), and the unloaded manipulator, $P(s)$ (dashed lines). Distinct troughs and strongly alternating phase shifts are clearly seen, especially for the first locus (Fig. 6.4A), and are typical for systems with distributed regions of low stiffness. The gain of the first locus of the combined admittance exhibits two collapses around 22 Hz and 53 Hz. The loci of the manipulator only are largely comparable to those of the combined admittance. The main differences are the increase of the frequency where the first trough occurs and the absence of the second trough. Both differences are the result of changes in eigenfrequencies due to the additional load of the human arm.

6.4.2 Controller gains

The optimized servo bandwidth and minimal virtual mass are given in Figure 6.5 for high frequency weighting $c = 1.25$. Lower weighting of the high frequency gains in the servo loop ($c < 1.25$) resulted in hydraulic overdrive meaning that the corresponding controller gains were not of practical use. For the largest weighting ($c = 1.5$) the controller was too conservative resulting in a smaller bandwidth and a slightly larger minimum for the virtual mass. Because the bandwidth of the second locus is substantially higher (> 30 Hz), only the bandwidth of the first locus, $f_{b,1}$, is given. The bandwidth increases with decreasing servo stability margins (increasing values of M_s). The minimal virtual mass also increases with M_s for the smallest stability margins of the force loop ($M_f = 5$) and remains almost the same for the largest margins ($M_f = 1.3$). It is clear that there is a trade-off between bandwidth and minimal attainable virtual mass. As the best choice between smallest virtual mass and highest bandwidth, we have chosen $m_v = 1.72$ kg and $f_{b,1} = 12.9$ Hz, corresponding to $M_s = 2$ and $M_f = 5$ as indicated by the encircled values in Figure 6.5. The corresponding controller parameters are $k_{p,1} = 12432.0$, $k_{p,2} = 6240.0$, $k_{d,1} = 244.8$, $k_{d,2} = 8.6$.

The values of the bandwidth are minima, and always occurred at the proximal position where the manipulator was highly extended. The highest bandwidth always occurred at the distal position and was approximately 20 % higher.

The optimal loci of the servo are shown in Figure 6.6A for the proximal (limiting) position. The bandwidths are indicated by filled dots on the crossing point of the loci with the $M = \frac{1}{2}\sqrt{2}$ circle. Figure 6.6B shows the loci of the force loop. The 'touch' with the corresponding M-circles is clearly visible and always occurred for the second locus.

Figure 6.7 shows the four FRFs of the two-by-two servo MFRF in the Cartesian frame. The decomposition of the endpoint MFRF into its four Cartesian FRFs is a common way of studying the planar admittance and is used as the default representation hereafter. The x-direction is restrictive, having a bandwidth comparable to the first locus of the MFRF (≈ 13 Hz). In the y-direction, the bandwidth is much higher (> 20 Hz) and comparable with the second locus of the MFRF. Within the smallest bandwidth, the Cartesian directions are reasonably decoupled, as indicated by the reduced gains of the cross terms. For both loading conditions in all positions, the multiple coherence is higher than 0.85, indicating highly linear behavior of the servo.

6.4.3 Test load estimation

Figure 6.8A shows the estimations and model fits in the case of the smallest test mass without springs. Figure 6.8B shown the results in the case of added springs. The estimated FRFs show the typical responses of mass-spring systems. In the case of the mass load, the gain decreases monotonically with -100 [N/m] per frequency decade at a constant phase lag of -180 degrees. Added springs decrease the low frequency gain and introduce an undamped oscillation peak at the eigenfrequency.

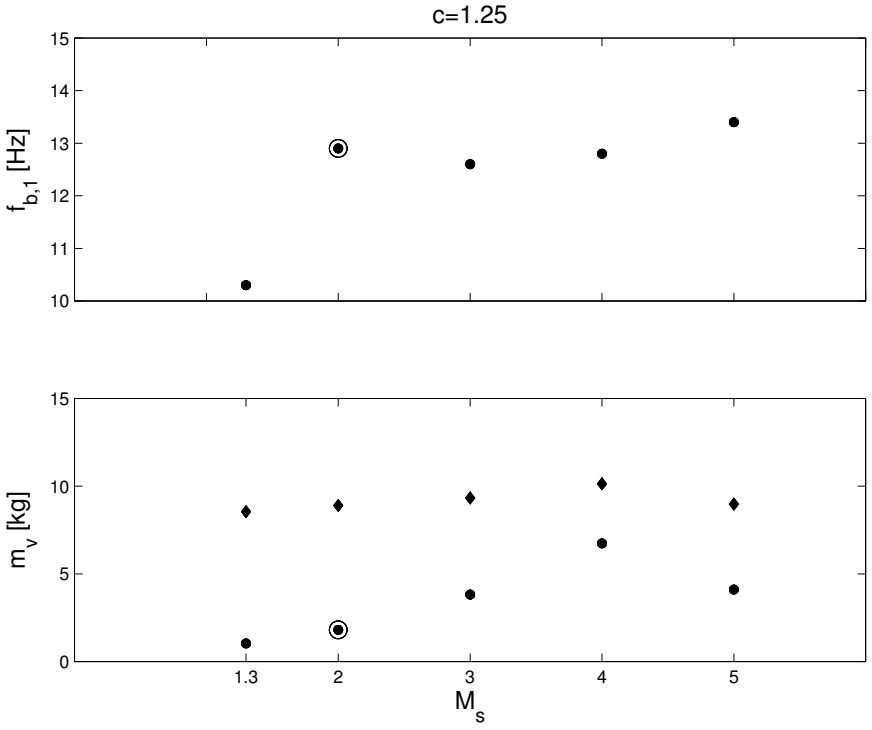

Figure 6.5: *Optimized servo bandwidth and virtual mass for different stability margins of the servo M_s (abscissae) and high frequency weighting $c = 1.25$. Upper: minimal bandwidth (main axis) $f_{b,1}$. Those mimimal values always occurred at the proximal position. Bottom: minimal virtual mass m_v corresponding to the smallest stability margins ($M_f = 5$, filled circles) and largest stability margins ($M_f = 1.3$, diamonds) of the force loop. The encircled values mark the best choice, i.e. the smallest attainable virtual mass at the highest bandwidth.*

The estimated cross terms are much smaller compared to the diagonal terms. This is expected because all loads are purely diagonal. An additional indication of the amount of coupling in the (combined) system is given by the partial coherence functions, shown in Figure 6.9. For the cross-terms, the partial coherence functions are almost zero within the servo bandwidth. On the contrary, values close to one are found for the diagonal terms indicating that the output in one direction is mainly determined by the input in the same direction within the bandwidth.
The estimated multiple coherence functions are high (> 0.85 up to 15 Hz), indicating highly linear behavior. The model fits are accurate for all load combinations and yield parameter estimates showing negligible deviations from the true values ($R > 0.9995$) with absolute differences smaller than 2% of the true value.

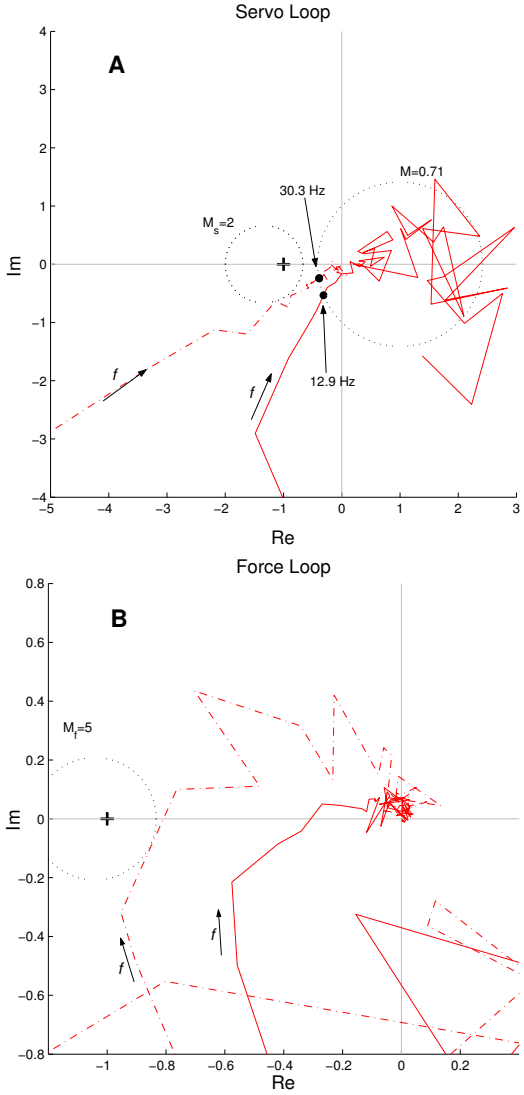

Figure 6.6: *Estimated characteristic loci (solid: first locus; dashed dotted: second locus) corresponding to the optimal controller gains of the servo loop (A) and force loop (B). The servo loci correspond to the proximal position where the locus of the secondary axis touches the $M_s = 2$ circle. The force loci correspond to the central position where the second locus touches the $M_f = 5$ circle. The minimal attainable virtual mass is 1.72 kg. Note the scale difference between the figures. Dots at the crossing point of the loci and the $M = \frac{1}{2}\sqrt{2}$ circle indicate the bandwidths of both loci.*

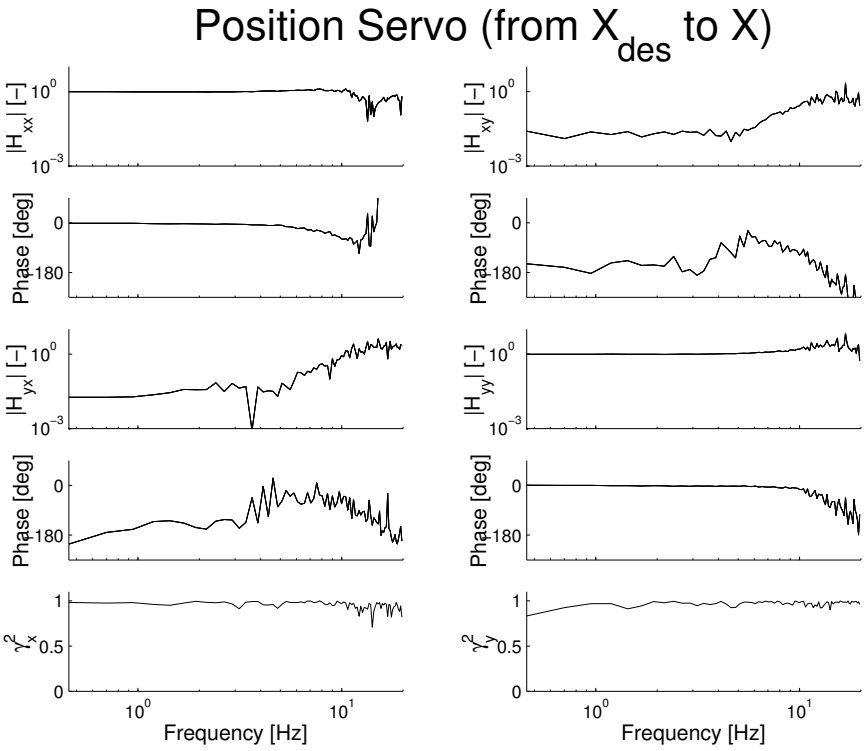

Figure 6.7: *Estimated optimal FRFs (gain and phase plots) of the position servo in the Cartesian frame (from X_{des} to X) in the proximal position, comprising the four elements of the servo MFRF in $x-$ and $y-$direction (from 0.4-20 Hz). Bottom row: corresponding multiple coherence functions γ_x^2 and and γ_y^2.*

6.4.4 Human arm admittance estimation

Figure 6.10A shows the estimated MFRF of the subject in the central position. The estimated FRFs show rather flat or slightly declining gains with frequency to approximately 6 Hz and decline steeper with further increase of frequency. The corresponding phase lag increases from zero to -180 degrees for the diagonal terms. Oscillatory behavior appears around 6 Hz. In the other positions, the magnitudes of these oscillations were different (or sometimes absent) while the oscillation occurred within the same frequency range (not shown). Multiple coherence functions are high (> 0.75). The estimated FRFs of the virtual admittance closely resemble those of the desired admittance, being an isotropic mass of 1.72 kg (Fig. 6.10B). Around 13 Hz, the FRFs deviate slightly from the intended ones (dotted lines), in particular in the x-direction. The multiple coherence functions indicate highly linear behavior over the whole frequency range.

Figure 6.11 shows the ellipses of the real mass of the manipulator (dotted) and

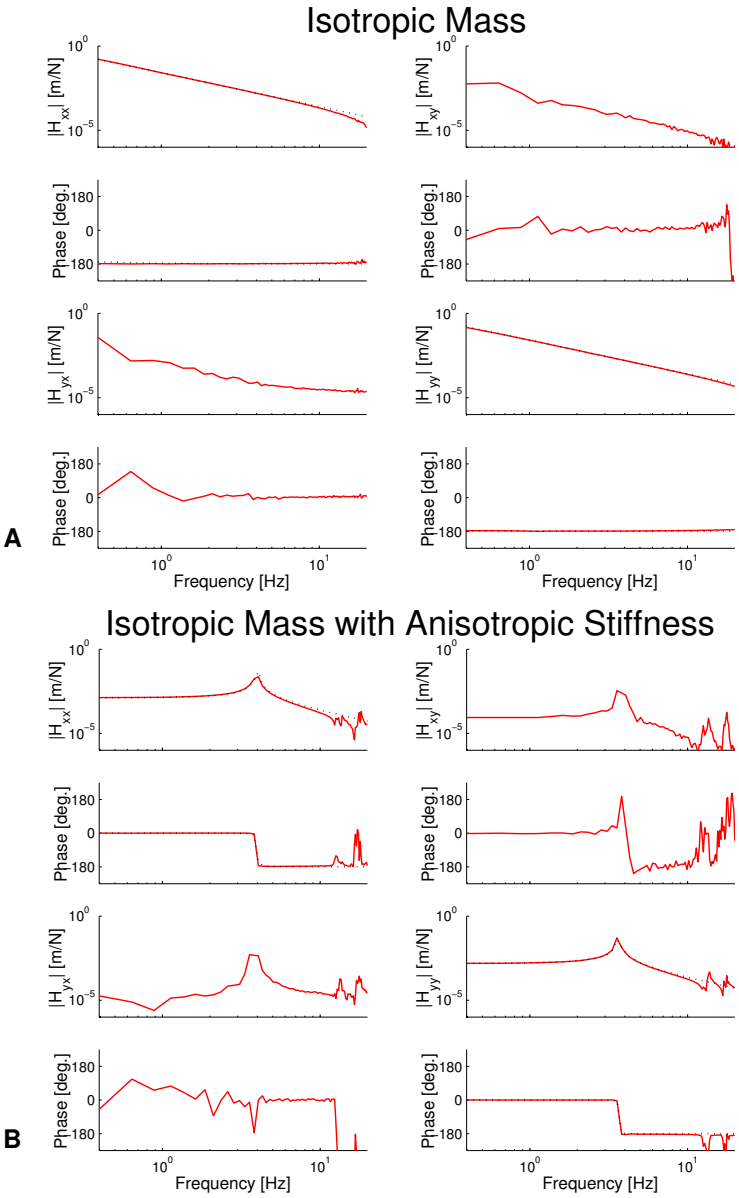

Figure 6.8: *Estimated FRFs (solid lines) and model fits (dotted lines) for two different test loads: isotropic mass of 0.99 kg (A) and the same mass with diagonal spring stiffness in x-direction k_{xx}=600 Nm^{-1} and in y-direction k_{yy}=300 Nm^{-1} (B).*

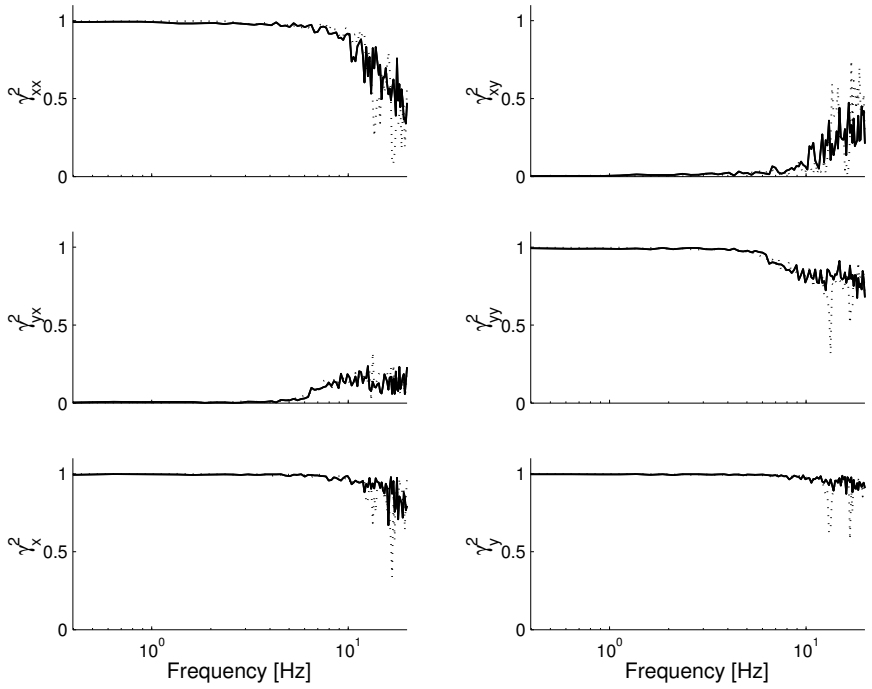

Figure 6.9: *Estimated partial coherence functions (first and second row) and multiple coherence functions (bottom row) corresponding to both test loads of Fig. 6.8. Isotropic mass (solid lines) and additional springs (dotted lines). Partial coherence functions are defined as follows: γ^2_{xx} is the linear contribution from input force perturbation $f_{ext,x}$, to the output hand position, x_x; γ^2_{xy} : from $f_{ext,y}$ to x_x; γ^2_{yx} : from $f_{ext,x}$ to x_y and γ^2_{yy} : from $f_{ext,y}$ to x_y. Multiple coherence functions: γ^2_x and γ^2_y from both external inputs ($f_{ext,x}$, $f_{ext,y}$) to one output x_x and x_y respectively.*

the estimated virtual environment (solid). The eigenvalues of the real mass matrix of the manipulator are $\lambda_{1,real} = 4.97$ kg and $\lambda_{2,real} = 0.90$ kg. The eigenvalues of the estimated virtual mass ellipse are equal to the minimal attainable mass, i.e. $\lambda_{1,vir} = \lambda_{2,vir} = 1.72$ kg. The real mass is therefore reduced by $\lambda_{1,vir} = \lambda_{1,real} = 1.72/4.97 = 35\%$ while in the opposite direction the real mass is increased by a factor $\lambda_{2,vir} = \lambda_{2,real} = 1.72/0.90 = 1.9$ (almost doubled).

6.5 Discussion

6.5.1 Stability and performance of the haptic device

The servo controller has a minimal bandwidth of 12.9 Hz. Within this frequency range, the virtual admittance is almost equal to the desired one provided by the virtual dynamics (Fig. 6.10). The real mass of the manipulator is strongly reduced in

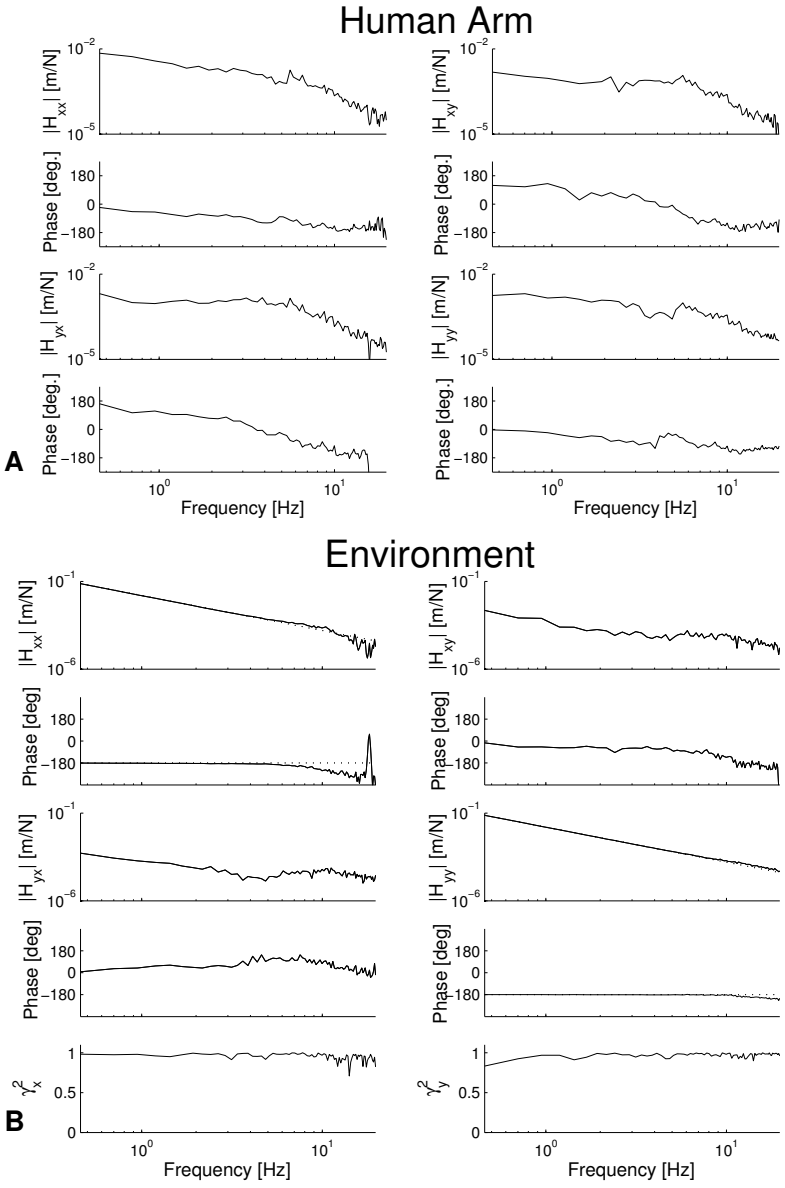

Figure 6.10: *A: Estimated MFRFs (gain and phase) of the subject's endpoint admittance and of the virtual environment it interacts with (B) in the central position. Bottom row: multiple coherence functions. The desired endpoint admittance, corresponding to the minimal virtual mass of 1.72 kg, is also shown (dotted lines).*

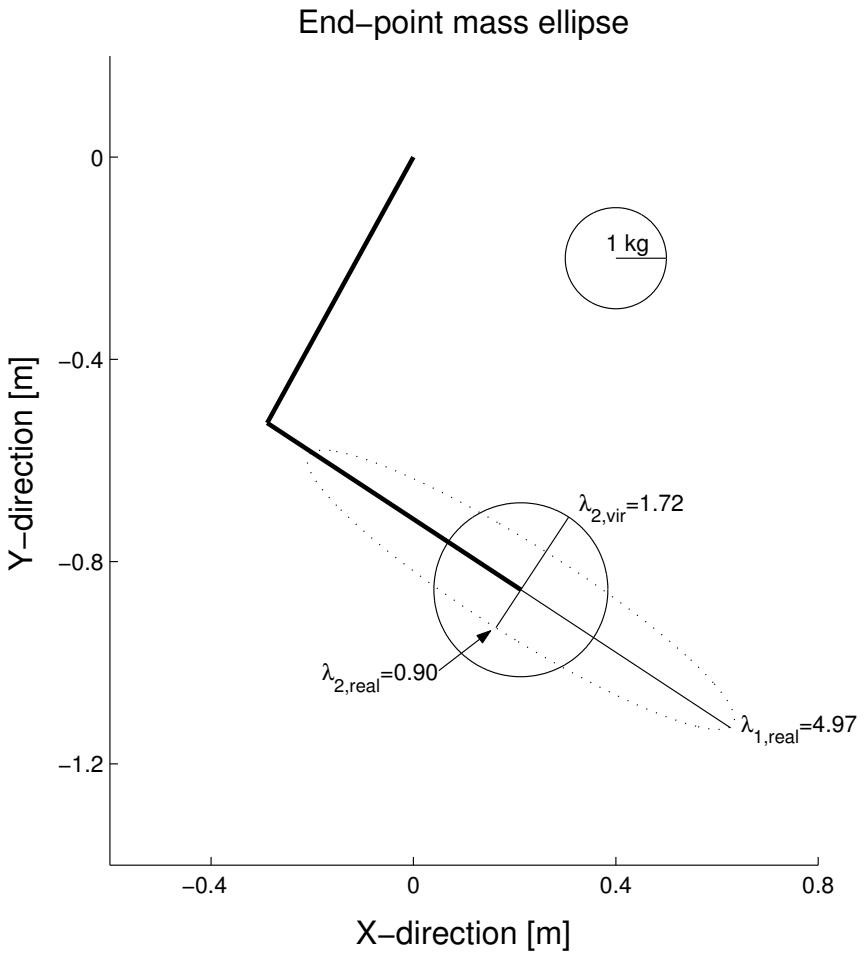

Figure 6.11: *Mass ellipses at the endpoint of the manipulator (central position) in the subject's coordinate frame. Grey lines schematically represent the linkages of the manipulator. Estimated virtual mass (solid) and real mass of the manipulator (dotted). The radius of the calibration circle corresponds to 1 kg. Mass values in both principle directions are indicated by the corresponding eigenvalues.*

the linear direction of the outer linkage (35%) but is almost doubled in the opposite direction. Because the virtual mass is minimized in two directions (x and y) equally, due to its prescribed isotropic form, the minimum is probably not the ultimate for each direction individually. That is, the optimum perhaps elicits a virtual mass that is more ellipsoidal when optimized in both directions independently. The facility to use an ellipsoidal virtual mass however, is not of prime interest. Rather, changing the virtual stiffness or damping in different directions seems a more logical approach to investigate the direction dependent visco-elastic disturbance behavior of the human arm (De Vlugt et al. 2002).

The minimal value of the virtual mass is 1.72 kg and is the result of the most appropriate choice between a least dominant environment and a large servo bandwidth. The phase and amplitude margins are sufficient for the servo loop ($M_s = 2$) but narrow for the force loop ($M_f = 5$). We have successfully validated stable interaction in the case of several goal-directed movements within the boundaries given by the separate positions. In the case contact instability still occurs, more conservative controller gains (at the cost of bandwidth) or a larger virtual mass should be taken.

Due to the material stiffness, the gain of the manipulator admittance does not decay for higher frequencies (Fig. 6.4A). Consequently, the increase of the servo loop gain by the controller is limited to avoid actuator overdrive, and thus the desired virtual admittance cannot accurately be realized (Eq. 6.9). This indicates the need to use stiff and lightweight materials for all moving parts (Carignan and Cleary 2000).

When wide servo stability margins are imposed ($M_s = 1.3$), D-action is necessary at the cost of additional P-action. In contrast, for small stability margins D-action is not required and is therefore directly penalized by high frequency weighting. In that case, additional P-action is allowed and beneficial for increasing the bandwidth at the cost of a higher virtual mass. The latter is explained by the lack of phase advance from the D-action. The trade-off illustrates the conflict of two desired effects: high phase advance inside the bandwidth and sufficient gain attenuation outside the bandwidth. Therefore, the application of several stability boundaries and control effort weighting at high frequencies is a practical and efficient method to adjust the servo controller.

An important aspect regarding the stability of the haptic device in general is the sampling frequency of the controller. Discretization (sample and hold circuits) introduces phase lags that increase with frequency. For the present case, the sampling frequency of 1 kHz appeared to be the upper limit gained with our hardware, which can be regarded as sufficient for these types of admittance controlled applications (Carignan and Cleary 2000).

Regarding contact instability as the result of badly controllable and oscillatory states, the addition of any dissipative elements can be used to suppress those oscillations. The first location where those elements could be applied is in the force loop, by simply providing the virtual dynamics (Eq. 6.2) with damping terms that directly reduces phase lags from -180 to -90 at the lower frequencies. In this case

one has to accept a certain minimal virtual damping to be present which limits the haptic device in its range of virtual admittances. Energy dissipative elements can also be applied in the servo loop, by adding an arrangement of physical dashpots to the linkage system. It is expected that such a facility will improve the servo but also at lower frequencies only. Furthermore, such an arrangement will increase the inertia of the device which in turn will enhance oscillatory behavior.

6.5.2 Test load estimation

The estimation of the load is accurate over the whole frequency range to 20 Hz. The reason is that the applied closed-loop estimator separately estimates the load admittance irrespective of the properties of the environment (De Vlugt et al. 2003). This property only holds for the condition that the servo does not introduce too much noise beyond its bandwidth. Since the combined system response is highly linear, as proved by the high multiple coherence functions in all cases (Figs 6.9 and 6.10), the limited bandwidth does not affect the estimation of the MFRF of the human arm admittance.

High correlations between the true and estimated parameters of the mass-spring loads validate the accuracy of the identification procedure. The validation is performed on the diagonal elements only. This is because it was not possible to create cross-terms in the load configuration with the test frame as used in this study (Appendix D, Fig. D.1). For that purpose, a more sophisticated test bed would have to be used that is morphologically comparable with the human arm. Such a facility comprises multi-DOF rotating levers with additional (and adjustable) joint viscoelasticity. Such an elaborate mechanism is much harder to construct and was not at hand.

If springs are used as test loads, wave propagation (longitudinal and transversal) of the springs probably causes additional reaction forces that are (partly) uncorrelated with the external force perturbation and therefore reduce the multiple coherence above 10 Hz (Fig. 6.9).

6.5.3 Human arm admittance estimation

Some general features seen in the estimated arm MFRF that reflect underlying mechanical properties will be briefly discussed. The endpoint MFRF measured at the hand is comprised of the rotational dynamics around the wrist, elbow and shoulder joint. Assuming that the joint impedance MTF is of second order, the joint admittance MTF (matrix inverse of the impedance MTF) is then of sixth order, i.e. three second order systems in series. Consequently, the endpoint admittance of the arm is also of sixth order, as it follows from pre- and post-multiplication of the joint admittance MTF by the Jacobian (J) and its transposed (J^T) respectively. For the shoulder-elbow combination (fixated wrist) a moderate amplification around 2 Hz was measured (amongst others) by Gomi et al. (1998) and Perreault et al. (2001). In those studies, the subjects performed a submaximal force task while in the present study maximal performance position tasks were performed resulting in higher joint

stiffness values. Such an oscillation was not clearly seen in our estimates (Fig. 6.10A, upper part). The resonance at 6 Hz probably indicates the influence of the wrist.

6.5.4 Other control strategies

Generally, there are two control strategies that can be used in haptic control: feedforward and feedback control.

Feedforward control

Feedforward control is based on forward coupling of either the measured interaction force or the endpoint position. Feedforward controllers enforce accurate models of the manipulator admittance to completely cancel out all the dynamics and insert any virtual admittance instead. The cancellation is performed using the inversed admittance model (impedance) yielding high amplification at high frequencies, resulting in unacceptably fast changes of the actuator control signals, i.e. actuator overdrive. Accurate modeling of the admittance is possible for the low frequency dynamics but is almost impossible for higher frequencies due to mechanical resonance resulting from material weakness. Imperfect cancellation will easily lead to unstable interaction. Additionally, the resonance frequencies shift with configuration of the linkages, such that a generic model will end in an excessively high computational burden. For these reasons, feedforward control is not appropriate for the current application.

Feedback control

The other control strategy is based on feedback control which does not require accurate system knowledge (Hogan 1985). Feedback control for haptic applications comes within two basic configurations: impedance and admittance control. The latter is applied in this study. Both consist of an inner feedback loop to track the desired endpoint force (impedance control) or endpoint position (admittance control). The interaction force is included by an outer feedback loop. The benefit of feedback is that excellent high bandwidth tracking can be established when high gain of the inner feedback loop can be realized. Again, mechanical resonance prevents high gains which leads to limited servo bandwidths.

As the result of a limited bandwidth, and therewith an improper (but stable) realization of the virtual admittance, the force loop can become unstable for high loop gains, i.e. the problem of contact instability (Adams and Hannaford 1999; Carignan and Cleary 2000; Hannaford and Ryu 2002; Van der Linden 1997). High force loop gain occurs when the human impedance is high, e.g. when one tightens the grip and fully cocontracts the muscles around the shoulder, elbow and wrist joints. In that case, the human load causes force loop gains that increase with frequency.

Comparing both feedback controllers, impedance control has a practical drawback and that is the requirement to measure the acceleration for adaptation of the virtual mass. Accelerometers are commercially available in different types but are

less accurate than force sensors. Also, on-line differentiation of the position is very susceptible to noise and slow drift. Considering this drawback, an admittance controller has been chosen for the current application.

6.6 Conclusions

The haptic manipulator presented in this study facilitates the analysis of human arm motion control during natural interaction with compliant environments. It offers a stable and accurate testbed to estimate the mechanical admittance of the human arm at different positions in the horizontal plane. From the mechanical admittance, important physiological properties related to intrinsic and reflexive muscle mechanisms can be analyzed to study the adaptability of the human arm neuromusculature to deal with different types of environments.

6.7 Acknowledgements

This project (under the working title "ARMANDA", from ARm Movement ANd Disturbance Analysis) is realized with the help of several persons who deserve our grateful thanks. Being, for the mechanical and hydraulical part: Ad van der Geest and John Dukker; for the electrical part: Leo Beckers and Kees Slinkman and for the controller part Peter Valk. All persons are engaged at the faculty of Mechanical Engineering at the Delft University of Technology, Delft, the Netherlands.

Chapter 7

Intrinsic and reflexive properties during a multi-joint posture task

Erwin de Vlugt, Frans C. T. van der Helm
to be submitted

This study estimates the intrinsic and reflexive properties of single-joint and two-joint muscles acting around the shoulder, elbow and the wrist during posture maintenance of the arm in the horizontal plane. External force disturbances were applied to the hand while the subjects were instructed to minimize their hand displacements that resulted from the disturbance. To examine how the nervous system modifies intrinsic and reflexive muscle properties, external damping was increased and also the amplitude of the disturbance was varied. Different hand positions were also used to find any effect of the joint configuration on muscular control. By a two-step identification method model parameters describing intrinsic, activation and reflexive properties were estimated. The latter representing afferent feedback gains from muscle spindles and golgi tendon organs. Consistent time delays and activation cut-off frequencies were found for mono-articular and bi-articular muscle groups. The results showed also consistent reflexive parameter estimates, however no modification with external damping or disturbance amplitude was found. Single-joint shoulder muscles showed minimal intrinsic properties, that was compensated for by reflexive feedback. Two-joint shoulder-elbow muscles showed a significant intrinsic and reflexive contribution in contrast to two-joint elbow-wrist muscles. The results from this study indicate that during multijoint posture maintenance, the mechanical properties are controlled on the joint level and not on the endpoint level.

7.1 Introduction

To maintain the hand at a specific point in space, humans need to control their muscles around the shoulder, elbow and wrist joints simultaneously. If external disturbing forces act upon the arm, a sufficient amount of muscle visco-elasticity is needed to suppress joint displacements that result from the disturbance. It is known from previous experimental studies that joint resistance is produced by intrinsic muscle visco-elasticity and reflexive feedback from muscle spindles. Most intriguing to the majority of motor control studies that focus on posture maintenance is the functionality of the reflexive feedback mechanism because it shows how the nervous system modifies the feedback gains to minimize deviations from a desired position. It has been shown that the position and velocity feedback gains of the monosynaptic Ia reflex increases for decreasing amplitude (Poppele, 1981; Stein and Kearney, 1995; Cathers et al., 1999) and decreasing frequency of the disturbance (Van der Helm et al., 2002). A recent study also reported enhanced position feedback with increasing damping of the environment (De Vlugt et al., 2002). These results indicate that the CNS is adaptive to cope with different disturbance conditions.

These previous single joint studies together with numerous others, have contributed to the fundamental understanding of neuromuscular functioning. However, these studies were all based on single joint experiments that give no insight into more natural multiple degree-of-freedom (DOF) posture control. Quantitative two joint (shoulder-elbow) studies have been done to measure the net stiffness and damping at the hand and joint level (Mussa-Ivaldi et al., 1985; Dolan et al., 1993; Tsuji et al., 1995; Gomi and Kawato, 1996; McIntyre et al., 1996; Gomi and Osu, 1998; Perreault et al., 2001; Perreault, 2002). Endpoint stiffness fields in the horizontal plane have been measured by most of these studies and was found to be strongly dependent on arm posture, joint stiffness and endpoint force. Stiffness determines the low frequency response to external disturbances while damping and inertia are important at higher frequencies. Because these previous studies made no distinction between underlying intrinsic and reflexive mechanisms, the role of the CNS during multiple DOF posture maintenance remains unknown.

The goal of this study is to quantify intrinsic and reflexive muscle properties of the shoulder, elbow and wrist joint simultaneously during arm posture maintenance in the horizontal plane. Since the number of DOF at joint level (three) is higher than the DOF at endpoint level (two), there is kinematic and dynamic redundancy. This means that there exists many different combinations of joint angles to obtain the same endpoint position. And similarly, endpoint stiffness (and damping) is not uniquely determined by joint stiffness (and damping). Does redundancy changes the way intrinsic and reflexive muscle properties are controlled?

In redundant joint system, there exists a null-space which is that part of the joint space in which parameter variations do not affect the endpoint properties. Consequently, joint properties could not be found algebraically from endpoint measurements. We solved this problem by model based optimization. Multivariable frequency response transfer functions were estimated from the recorded hand po-

sition and hand force with the aid of a newly developed two DOF manipulator and a multivariable subspace identification technique. Highly accurate estimates of the endpoint admittance were obtained on which a detailed three-joint neuromusculoskeletal (NMS) model was fitted by minimizing the difference of the modelled and the estimated endpoint admittance. Interchange of the parameters due to redundancy was restricted by using a proper model structure, the absence of tri-articular muscles and feasible bounds of the parameters. Consistent intrinsic and reflexive joint parameters were estimated. The adaptability of the intrinsic and reflexive properties were studied by varying the disturbance amplitude, external damping and hand position. The set of experimental conditions largely overlaps with those applied in the previously referred studies. In addition to the reflexive properties of Ia afferents, we also estimated the cut-off frequency of the muscle activation process and force feedback gains from golgi tendon organs (Ib-afferent) of which no comparable data exists.

7.2 Materials and Method

7.2.1 Experimental

Apparatus

Endpoint arm admittance was estimated using continuous force disturbances applied by a planar two-joint robotic manipulator which properties are described in detail previously (De Vlugt et al., 2003b) and are summarized briefly here. Figure 7.1 shows this device which acted as a mechanical mass-damper-spring system, hereafter referred to as the environment. The mechanical properties of the subject's arm are measured in endpoint coordinates in the horizontal plane and estimated as an admittance. Admittance is the dynamic relationship between displacements (output) in response to forces (input). Here, the measured displacements are those of the handle of the manipulator that approximately coincides with the handgrip of the subject. The driving forces are those generated by the subject's arm in addition to those externally imposed by the manipulator. Subjects were strapped rigidly in a chair with custom supports to constrain both lateral and anterior-posterior trunk movements. The subjects could freely take the handle of the manipulator and were asked to hold the handle firmly during the experiments. The elbow was supported by a long rope (2 m) attached to the ceiling. The handle was free to rotate in the horizontal plane around its attachment point. The manipulator was instrumented to measure the displacements of the subject's hand and the forces applied by the subject to the environment. Endpoint forces in two orthogonal directions were measured by strain gauges mounted inside the handle with a range of $\pm$ 300 N. Endpoint displacements were measured by two optical angular encoders (Heidenhain ROC417, 17 bits per 360 deg.) for each joint of the manipulator.

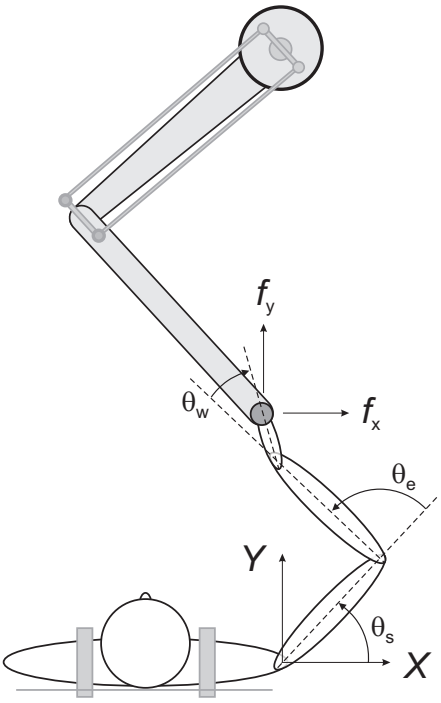

Figure 7.1: *Experimental setup. The two-joint manipulator was used to apply continuous random forces in two directions (X and Y) onto the subject's hand. The manipulator represented a virtual mechanical environment that consisted of a mass-damper-spring system in the horizontal plane. The subjects were instucted to minimize the hand displacements that resulted from the force disturbances.*

EMG measurements

The considered movements of the human arm were: wrist flexion/extension, elbow flexion/extension and horizontal shoulder adduction/abduction. Muscle activity was recorded using bipolar surface electrodes from eight arm muscles being: flexor carpi radialis (wrist flexor, single-joint); extensor carpi radialis brevis (wrist extensor, single-joint); brachioradialis (elbow flexor, single-joint); biceps short head (shoulder adductor, elbow flexor, two-joint); triceps lateralis (elbow extensor, single joint); triceps long head (shoulder abductor, elbow extensor, two-joint); deltoideus anterior (shoulder adductor, single-joint) and the deltoideus posterior (shoulder abductor, single-joint). Before digital recording, the raw EMG signals were high pass filtered (20 Hz, 3th order Butterworth) to remove movement artifacts, rectified and low pass filtered (100 Hz, 3th order Butterworth) to prevent aliasing. From the EMG recordings, mean muscle activity was derived and used to test whether the mean muscle activation levels changed between the conditions. Handle displacements, hand force, external disturbance and EMG signals were recorded at 250 Hz sam-

Table 7.1: *Experimental parameters, showing humural length (l_{hume}), forearm length (l_{fore}) and hand length (l_{hand}, measured from wrist joint to centre of manipulator handle) for each subject, as well as the three joint angles (shoulder: θ_s, elbow: θ_e, wrist: θ_w) corresponding to each endpoint location. Mean wrist angle (θ_w) remained almost constant at 15 degrees extension in all cases.*

Subject	Link lengths (cm)			Arm orientation (deg)					
				Left		Central		Right	
	l_{hume}	l_{fore}	l_{hand}	θ_s	θ_e	θ_s	θ_e	θ_s	θ_e
1	29	26	7	87	58	54	82	29	83
2	26	25	6	99	36	59	70	35	71
3	29	25	8	88	58	54	82	29	82
4	32	28	8	79	75	48	93	23	94
5	35	31	10	70	88	40	104	15	104

ple frequency (16 bit resolution) for further analysis. All signals, except EMG, were digitally re-sampled to 66.25 Hz to speed up the parametric estimation.

Subjects and protocol

Five healthy subjects (4 women, 2 left handed) with a mean (standard deviation, SD) age of 26.8 (8.1) years and a mean length of 175.8 (14.4) m, with no history of neurological impairments participated in this study. Subjects gave informed consent to the procedures and were free to withdraw from the study at any time. All measurements were made on the right arm.

To observe the variation of the intrinsic and reflexive muscle properties with configuration of the arm, measurements were made at three different hand locations in the horizontal workspace at the vertical level of the gleno-humeral joint. All locations were 0.4 m anterior to the acromion. The left position (Left) was 0.2 m to the left of the acromion, the central position (Central) in front of the acromion and the right position (Right) 0.2 m tot the right of the acromion. Due to kinematic redundancy the hand position could be attained by many different combinations of joint angles. However, all subjects chose an arm orientation where the wrist angle was at $\pm$ 15 degrees extension. The wrist angle was read from a goniometer at several instants during the experiments. Limb lengths were measured by a tape measure as the distance between corresponding joint rotation centers. The position of the gleno-humeral joint in the horizontal plane was measured in manipulator coordinates such that the shoulder and elbow angles were calculated from the measured handle position, limb lengths and known wrist angle. Table 7.1 showes the joint angles corresponding to the three endpoint positions for each subject.

For all trials, the force disturbance contained power at frequencies between 0.06 to 20 Hz and was designed as a sum of sinusoids with equal amplitudes and mutually random phase shifts to prevent any anticipation (Van der Helm et al., 2002). Figure 7.2 shows an example of the autospectrum and a time sample of the force disturbance. In each position, the following experimental conditions were applied:

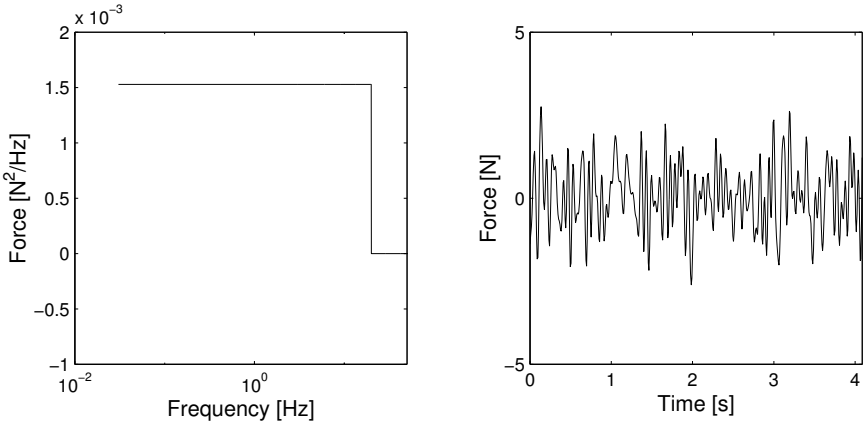

Figure 7.2: *Example of the force disturbance signal used in this study. Left: autospectrum. Right: 4 second time sample.*

- Different hand displacement amplitudes to test on the existence of nonlinear behavior that might be the result of underlying neuromuscular properties. The power of the force disturbance was adjusted such that hand displacements in either the x- or y-direction had a root-mean-square (RMS) value of 4 mm, 5.5 mm and 7 mm.

- Different viscosity fields to test if the CNS takes advantage of increased stability margins at the endpoint. For each displacement the external damping of the environment, B_e, was assigned four different values, being 0, 50, 100 and 150 Ns/m (isotropic field).

In total, the number of conditions equals 36 (3 positions, 3 hand displacements, 4 damping fields). Each condition was repeated four times to evaluate the consistency of the estimated model parameters, giving a total number of 144 trials. Each trial lasted 20 s, of which the first 4 seconds were omitted from the analysis to exclude any responses from start-up transients. The remaining 16 seconds (2^{10} samples at 62.5 Hz) of each signal was used for further processing.

Subjects were given a clear position task by the instruction to minimize their hand displacements as good as possible. To assist the subject in performing the task, the reference position was visualized on a monitor screen 65 cm in front of the subject, by means of a 3 cm diameter circle inside which the subject had to keep a smaller (0.5 cm diameter) filled circle representing the actual hand position. The force perturbation always started after the subject had positioned his or her hand in the center of the reference circles.

Before the trials were recorded, each condition was applied once to obtain the appropriate magnitude of the handle displacements by adjusting the power of the force disturbance. The power was equal in both directions and increased by small

Table 7.2: *RMS values of the handle displacements in the x-direction, averaged over 16 trials (four different external damping values and four repetitions). Target values were 4 mm, 5.5 mm, 7 mm (RMS). The figures only show the values for the x-component because the displacements were largest in this direction in all cases.*

Subject	Hand displacements in the x-direction (mm RMS)								
	Left			Central			Right		
RMS	4	5.5	7	4	5.5	7	4	5.5	7
1	3.7	5.3	6.2	4.1	4.7	6.9	4.2	5.2	6.8
2	4.3	5.3	7.1	4.0	6.2	8.8	4.2	5.4	7.3
3	3.8	5.1	6.4	3.9	5.4	6.4	3.9	5.7	6.3
4	3.7	4.9	6.6	3.8	5.5	7.2	3.4	5.2	6.3
5	3.6	5.1	6.8	3.7	5.6	7.1	3.4	4.9	6.8
mean	3.8	5.1	6.6	3.9	5.5	7.3	3.8	5.3	6.7

steps until the appropriate RMS value was obtained. These trials were also used to make the subjects familiar with the experiment and were not used for further analyses. Table 7.2 gives the final RMS values of the displacements for all trials and all subjects. The figures only show the values for the x-component of the displacement because the RMS value was largest in this direction in all cases. On average, the measured RMS values corresponded well to the intended values.

7.2.2 Identification and parameter estimation

Endpoint arm admittance is the transfer function describing the dynamic relationship between hand force and hand displacement, and captures all underlying mechanisms that contribute to this relationship, such as intrinsic and reflexive muscle properties and inertia of the segments. The goal was first to identify the horizontal plane arm admittance at endpoint level from measurements in two horizontal directions. Secondly, model parameters describing the NMS properties constituting the arm admittance on joint level, were estimated from the identified endpoint admittance. This two step estimation procedure is described in the following sections.

Parametric identification of the arm admittance

As the first step, a parametric description of the arm admittance is to be quantified without using any a-priori knowledge of the neuromuscular system. This was achieved by using a time domain identification method based on linear ARX models. This method uses open-loop system descriptions which can easily be derived from the blockscheme in Figure 7.3.

The first open-loop system equation is derived by expressing the output $X(t)$ as a function the inputs $D(t)$ and $N(t)$:

$$\begin{aligned} X(t) &= H(q^{-1})(N(t)+D(t)) - H(q^{-1})E(q^{-1})X(t) \\ &= (I+H(q^{-1})E(q^{-1}))^{-1}H(q^{-1})D(t) + (I+H(q^{-1})E(q^{-1}))^{-1}H(q^{-1})N(t) \end{aligned} \quad (7.1)$$

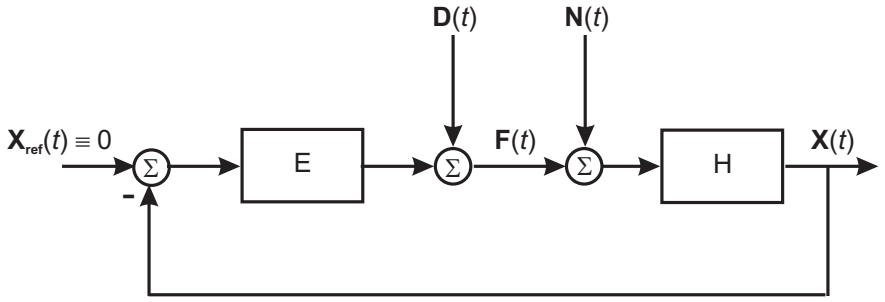

Figure 7.3: *Linear closed loop system configuration of the human arm interacting with the environment. The human arm is modelled as an admittance (H) and consequently the environment is modelled as an impedance (E). The system is excited by the external force disturbance ($D(t)$) and a noise source ($N(t)$). The latter representing any contributions from muscle forces that are not correlated with the external force disturbance and also any model remnant due to linearization. The measured variables are the hand force $F(t)$, the hand displacement $X(t)$ and the external force disturbance. $X_{ref} \equiv 0$ mimics the posture task, i.e. minimize hand displacements.*

By using the following algebraic property:

$$(I + H(q^{-1})E(q^{-1}))^{-1}H(q^{-1}) = H(q^{-1})(I + E(q^{-1})H(q^{-1}))^{-1}$$

Eq. (7.1) becomes:

$$\begin{aligned} X(t) &= H(q^{-1})(I + E(q^{-1})H(q^{-1}))^{-1}D(t) + H(q^{-1})(I + E(q^{-1})H(q^{-1}))^{-1}N(t) \\ &= H(q^{-1})S(q^{-1})D(t) + H(q^{-1})S(q^{-1})N(t) \end{aligned} \quad (7.2)$$

with $S(q^{-1}) = (I + E(q^{-1})H(q^{-1}))^{-1}$. Common notation for discrete systems is adopted with q the backward shift operator such that $q^{-1}X(t) = X(t - \Delta t)$.

The second open-loop system equation is derived by expressing the input $F(t)$ of the arm admittance as a function of the inputs:

$$\begin{aligned} F(t) &= (I + E(q^{-1})H(q^{-1}))^{-1}D(t) + (I + E(q^{-1})H(q^{-1}))^{-1}E(q^{-1})H(q^{-1})N(t) \\ &= S(q^{-1})D(t) + S(q^{-1})E(q^{-1})H(q^{-1})N(t) \end{aligned} \quad (7.3)$$

Rearranging Eqs (7.2) and (7.3) gives:

$$S(q^{-1})^{-1}H(q^{-1})^{-1}X(t) = D(t) + N(t) \quad (7.4)$$

$$H(q^{-1})^{-1}E(q^{-1})^{-1}S(q^{-1})^{-1}F(t) = H(q^{-1})^{-1}E(q^{-1})^{-1}D(t) + N(t) \quad (7.5)$$

Equations (7.4) and (7.5) are structured in the ARX format:

$$A(q^{-1}, \theta)y(t) = B(q^{-1}, \theta)u(t - nk) + e(t) \quad (7.6)$$

with

$$\begin{aligned} A(q^{-1},\theta) &= 1 + a_1 q^{-1} + a_2 q^{-2} + \ldots + a_{na} q^{-na} \\ B(q^{-1},\theta) &= b_0 + b_1 q^{-1} + b_2 q^{-2} + \ldots + b_{nb-1} q^{-nb+1} \end{aligned}$$

and θ the parameter vector:

$$\theta := [a_1\ a_2 \ldots a_{na}\ b_0\ b_1 \ldots b_{nb-1}]^T$$

$A(q^{-1},\theta)y(t)$ is the AutoRegressive part, $B(q^{-1},\theta)u(t)$ the eXogenous part and $e(t)$ an additional noise term that has no linear relationship with $u(t)$. Any delay from the input to the output is modelled by nk. The only source of delay in this study comes from one sample and hold execution in the discrete controller of the manipulator, which operates at 1kHz. Such a small delay completely vanishes for the signals at 62.5 Hz sample frequency as used in the analysis. Therefore, with $nk = 0$ the best predictions were obtained. The total number of model parameters is the sum of na and nb, representing the orders of the A and B polynomials respectively.

In terms of the ARX structure, Eqs (7.4) and (7.5) become:

$$A_x(q^{-1},\theta_x)X(t) = B_x(q^{-1},\theta_x)D(t) + N(t) \tag{7.7}$$
$$A_f(q^{-1},\theta_f)F(t) = B_f(q^{-1},\theta_f)D(t) + N(t) \tag{7.8}$$

with

$$A_x(q^{-1},\theta_x) = S(q^{-1})^{-1}H(q^{-1})^{-1} \tag{7.9}$$
$$B_x(q^{-1},\theta_x) = 1 \tag{7.10}$$
$$A_f(q^{-1},\theta_f) = H(q^{-1})^{-1}E(q^{-1})^{-1}S(q^{-1})^{-1} \tag{7.11}$$
$$B_f(q^{-1},\theta_f) = H(q^{-1})^{-1}E(q^{-1})^{-1} \tag{7.12}$$

The one step ahead prediction, $\hat{X}(t)$ and $\hat{F}(t)$ follow from Eqs (7.7) and (7.8):

$$\hat{X}(t|t-\Delta t) = B_x(q^{-1},\hat{\theta}_x)D(t) + (1 - A_x(q^{-1},\hat{\theta}_x))X(t) \tag{7.13}$$
$$\hat{F}(t|t-\Delta t) = B_f(q^{-1},\hat{\theta}_f)D(t) + (1 - A_f(q^{-1},\hat{\theta}_f))F(t) \tag{7.14}$$

The goal is to find parameter vectors that minimize the quadratic criterion functions:

$$V_{x,N}(\hat{\theta}_x, Z_x^N) = \frac{1}{N}\sum_{t=1}^{N}[X(t) - \hat{X}(t|t-1)]^2 \tag{7.15}$$

$$V_{f,N}(\hat{\theta}_f, Z_f^N) = \frac{1}{N}\sum_{t=1}^{N}[F(t) - \hat{F}(t|t-1)]^2 \tag{7.16}$$

with $V_{x,N}$ and $V_{f,N}$ the quadratic functions of prediction errors, N the number of time samples (in this study $N = 2^{10}$), $\hat{\theta}_x$ and $\hat{\theta}_f$ the estimated parameter vectors, $Z_x^N = [D(t)\ X(t)]$ and $Z_f^N = [D(t)\ F(t)]$ the measured data sets.

Since the ARX model structure is linear in its parameters, the solution to this problem is found analytically, which immediately shows the great advantage of ARX models. For the optimal number of parameters of $\hat{\theta}_x$ and $\hat{\theta}_f$, it can be proven that the residual of the prediction error is uncorrelated with the external input, i.e. the force disturbance $D(t)$ in this case (Ljung, 1999).

To prevent overfitting of the model, the smallest number of parameters for $\hat{\theta}_x$ and $\hat{\theta}_f$ should be found. Such a minimal parameter set is determined by trading-off the prediction error with the number of model parameters N_{θ_x} (N_{θ_f}). An effective and commonly used criterion for this purpose is Akaikes Final Prediction Error Criterion (FPE) (Ljung, 1999), which in this case are:

$$FPE_x = \frac{1 + N_{\theta_x}/N}{1 - N_{\theta_x}/N} V_{x,N}(\hat{\theta}_{x,N}, Z_x^N) \tag{7.17}$$

$$FPE_f = \frac{1 + N_{\theta_f}/N}{1 - N_{\theta_f}/N} V_{f,N}(\hat{\theta}_{f,N}, Z_f^N) \tag{7.18}$$

with $V_{x,N}(\hat{\theta}_{x,N}, Z_x^N)$ and $V_{f,N}(\hat{\theta}_{f,N}, Z_f^N)$ the quadratic criterion functions Eqs (7.15) and (7.16) respectively.

Once a minimal model order is found, an accurate estimation of the arm admittance $H(q^{-1})$ is obtained from Eqs (7.9)-(7.12), according to:

$$\begin{aligned} A_x(q^{-1}, \theta_x)^{-1} &= \hat{H}(q^{-1})\hat{S}(q^{-1}) \\ A_f(q^{-1}, \theta_f)^{-1} B_f(q^{-1}, \theta_f) &= \hat{S}(q^{-1})\hat{E}(q^{-1})\hat{H}(q^{-1})\hat{H}(q^{-1})^{-1}\hat{E}(q^{-1})^{-1} = \hat{S}(q^{-1}) \end{aligned}$$

such that

$$A_x(q^{-1}, \theta_x)^{-1}(A_f(q^{-1}, \theta_f)^{-1} B_f(q^{-1}, \theta_f))^{-1} = \hat{H}(q^{-1})\hat{S}(q^{-1})\hat{S}(q^{-1}) = \hat{H}(q^{-1}) \tag{7.19}$$

where $\hat{H}(q^{-1})$ is the estimate of the endpoint admittance.

Parameter estimation

The parameters in the estimate (Eq. 7.19) do not have any physical meaning to underlying neuromuscular properties. Therefore, a physical model of the arm admittance containing all relevant NMS properties is fitted onto the estimated arm admittance $\hat{H}(q^{-1})$. Similarly to the parametric identification, the NMS model parameters have to be estimated by minimization of the quadratic error criterion $W(n\Delta f, p)$ in the frequency domain:

$$W(n\Delta f, p) = \sum_{n=n_1}^{n_2} \frac{1}{(1 + n\Delta f)} \log(|\hat{H}(n\Delta f) - H_{mod}(n\Delta f, p)|)^2 \tag{7.20}$$

where $n\Delta f$ is the discrete frequency in Hz ($\Delta f = \frac{1}{T}$, T the observation period) with $n_1 = 1$ and $n_2 = 327$ (i.e. $n_2\Delta f = 327/16.4 \approx 20$ Hz), $H_{mod}(n\Delta f, p)$ the

frequency response function of the arm model (Eq. E.26 without the environment) and p is the parameter vector of the model. The estimated multivariable frequency response function (MFRF) of the admittance $\hat{H}(q^{-1})$ is obtained by substitution of $q = e^{j2\pi\Delta f}$. Equation 7.20 is solved numerically using a nonlinear least squares algorithm.

A valuable measure for the accuracy of the estimates is the variance of the parameter distribution (Ljung, 1999):

$$\text{Var}\{\hat{p}\} = \mathbf{diag}[(J_p^T J_p)^{-1}]\frac{W(n\Delta f, p)^T W(n\Delta f, p)}{N^3} \tag{7.21}$$

with J_p the Jacobian containing the gradients of the prediction error $W(n\Delta f, p)$, i.e. first derivatives to the parameter vector p. Both J_p and $W(n\Delta f, p)$ are evaluated N times, such that the Jacobians have N rows and as much columns as there are parameters. By taking the diagonal of the first term on the right hand side in Eq. (7.21), only the variances of the parameters are obtained excluding the covariance parts. From Eq. (7.21) it follows that the accuracy of a certain parameter is related to how sensitive the prediction error is with respect to this parameter. Clearly, the more a parameter affects the prediction the easier it will be to determine its value. Generally, parameters that have little contribution to the prediction error will result in correspondingly larger variances.

To obtain an overall validity index for the parametrized models (ARX and arm model), the variance accounted for (VAF) were determined. First, the VAF of the ARX model is obtained by comparison of the predicted and the measured endpoint position, according to:

$$\text{VAF}_{arx} = 1 - \frac{\sum_{n=1}^{N} \left| X_h(t_n) - \hat{X}_{h,arx}(t_n) \right|^2}{\sum_{n=1}^{N} |X_h(t_n)|^2}$$

with $\hat{X}_{h,arx}(t_n)$ the predicted position and $X_h(t_n)$ the measured endpoint position (n indexes the time samples). The predicted position $\hat{X}(t_n)$ is obtained by simulating the ARX model of the total system of arm plus environment $\hat{H}(q^{-1})\hat{S}(q^{-1})$ by simulation of Eq. (7.13) using the corresponding experimental disturbances $D(t)$ as the input signal. The VAF_{arx} value gives an indication of how well the ARX model describes the endpoint position. A value of 100 % means that the model fully describes the measured system response and is equal to the real system. Lower values indicate to either a bad model fit or to the existence of noise. Bad model fits were not likely since the optimal model was selected from a wide range of different model structures. Validation of this assumption was confirmed by the fact that the autospectra of the prediction errors were white noise processes (not shown). Therefore, the VAF_{arx} values are a measure of the linear deterministic part in the recorded signals for which the ARX models gave perfect fits.

VAF values of the arm model (VAF_{arm}) were obtained from the following equa-

tion:

$$\text{VAF}_{arm} = 1 - \frac{\sum_{n=1}^{N} \left| X_{h,arx}(t_n) - \hat{X}_{h,arm}(t_n) \right|^2}{\sum_{n=1}^{N} |X_{h,arx}(t_n)|^2} \tag{7.22}$$

In this expression, the predicted endpoint position $\hat{X}_{h,arm}(t_n)$ of the NMS arm-environment model is compared to that of the linear ARX model. To obtain the hand position $\hat{X}_{h,arm}(t_n)$, the corresponding values of the environmental mass (M_{env}) and damping (B_{env}) were included in the model. The usage of the ARX model prediction instead of the measured position in Eq. (7.22) is logical since the linear arm model is only capable of describing that part in the response that is linearly related to the input, which was just obtained by the ARX model. As the result, VAF_{arm} is a direct indication of the goodness of the parametrized linear arm model. VAF_{arm} values are reduced by inaccurate parameter estimates, that in turn can be the consequence of bad model structures that do not correspond properly to the real system or from inaccuracy of the parameter estimation method of the NMS model.

3-DOF neuromusculoskeletal arm model

To describe the dynamic NMS properties of the human arm, a three-DOF model is developed at the joint level. Muscle properties appear as lumped quantities in joint coordinates. Note that all dynamic joint properties of the human arm are described in a 3×3 matrix structure and that all dynamic properties of the (Cartesian) environment are described in a 2×2 matrix format.

Essential to the model structure is that properties of single- and two-joint muscles are included. For the intrinsic properties this means that visco-elasticity of single-joint muscles of the shoulder, elbow and wrist joints are modelled. For the reflexive part, only autoreflexes (reflex action from the same muscle) are modelled. Both intrinsic and reflexive properties are taken equal for those two-joint muscles that operate in antagonistic pairs.

The model is structured into a state-space form, i.e. implicitly expressed as a function of the complex Laplace operator $s = j2\pi\Delta f$ to facilitate direct evaluation in the frequency domain. Figure 7.4 shows a blockscheme of the NMS arm model. Appendix E gives the matrix and vector structures of all system properties and signals and the derivation of the total input-output transfer function. The subsystems that are used in the model derivation are briefly described below.

The arm inertia I comprises the segmental masses in their configurational relationships. Intrinsic muscle visco-elasticity is represented by the feedback system $H_{int}(s)$:

$$H_{int}(s) = Bs + K \tag{7.23}$$

with B the intrinsic muscle viscosity and K the intrinsic muscle elasticity.

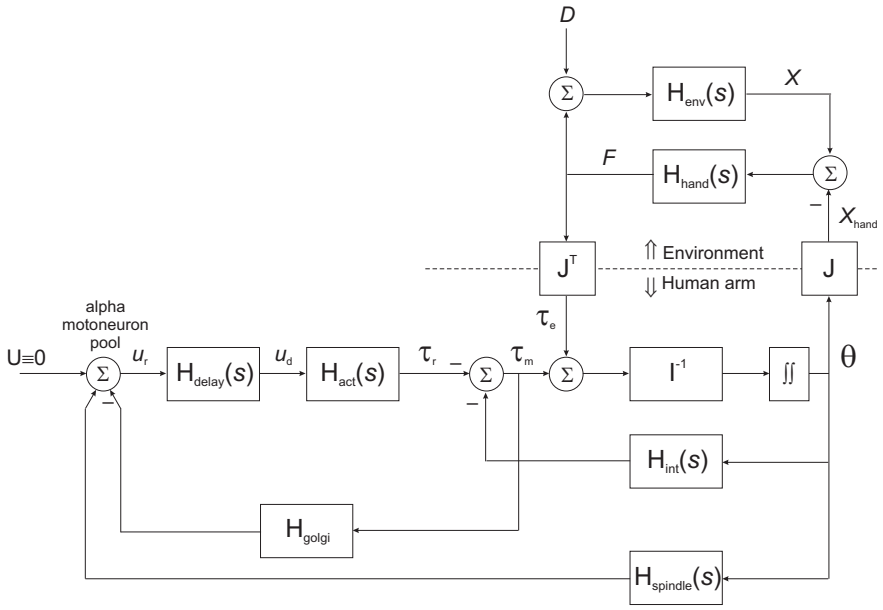

Figure 7.4: *Linear model of the arm admittance in connection with the environment. See Text and Appendix E for explanation of the subsystems. Recorded signals: external force disturbance (D); hand force (F), handle displacement (X) and muscle activation by EMG (A). J is the Jacobian that maps joint coordinates to endpoint coordinates. X_{hand} is the position of the subject's hand and T_{ex} the external joint torque due to the hand force. The leftmost summation point represents the afferent signal processing at the motoneuron pool. During the experiments in this study supraspinal control (U) is not relevant and is modelled as a constant (zero) input, mimicing the task instruction.*

Muscle spindle sensor dynamics are described by position (K_P), velocity (K_V) and acceleration (K_A) feedback gains, according to:

$$H_{spindle}(s) = K_A s^2 + K_V s + K_P \tag{7.24}$$

Golgi tendon organs provide feedback information of muscle force that in contrast to afferent information from the muscle spindles has an inhibitory effect onto the alpha motoneurons. Hence the minus sign at the leftmost summation point (Fig. 7.4). The golgi feedback model equals:

$$H_{golgi} = K_g \tag{7.25}$$

Note that this model includes no dynamics but only a static gain.

The neural delay involved from signal transport from the muscle to the alpha motoneuron and back to the muscle is described by a third order Pade approximation. There are only three time delays included in the model, one for each joint.

This means that the delay of reflex arcs of two-joint muscles are assumed to be equal to their corresponding single-joint reflex arcs. For instance, the reflex delay of the shoulder-to-elbow muscle is the same as that of the single-joint shoulder muscles.

Muscle activation dynamics represent the process from neural excitation to muscle force build-up, which is mainly determined by the calcium in and outflow of the sarcoplasmatic reticulum (Chapter 1). This process is modelled as a critically damped second order (Butterworth) filter having the cut-off frequency as its only parameter. Critically damped second order models were proved to described the activation dynamics accurately (Schouten et al., 2003c).

Movement of the fingers and visco-elasticity of the hand tissues are modelled by the hand dynamics:

$$H_{hand} = B_H s + K_H \tag{7.26}$$

with B_H the viscosity and K_H the elasticity of the handgrip. Due to the hand dynamics, the measured handle displacement X is not identical to the hand displacement X_{hand} (see Fig. 7.4). Because hand stiffness appeared to be very large (see Results), hand displacement is used in the remainder of the text to refer to both handle and hand displacements (i.e. not for the analysis).

Separated by the hand visco-elasticity, the environment acts in parallel to the arm, which is modelled by:

$$H_{env}(s) = M_E s^2 + B_E s + K_E \tag{7.27}$$

where $K_E = 0$ (Nm/rad) and $M_E = 3$ (kg) at all cases (isotropic, i.e. with equal diagonal terms only).

Table 7.3 summarizes all model parameters to be estimated in this study.

The mapping from angular rotations to endpoint displacements is determined by the Jacobian, according to:

$$\partial \mathbf{X} = J \partial \mathbf{\Theta}$$

with J the Jacobian (see Appendix E, Eq. E.23). The Jacobian also transforms forces into joint torques, according to:

$$\tau_e = J^T F$$

where ^{T} denotes the transposed.

7.3 Results

7.3.1 Identification and parameter estimation

Figure 7.5 shows the optimal number of model parameters for both ARX models (Eqs (7.7) and (7.8)) as obtained from the FPE criteria (Eqs (7.17) and (7.18)). The

Table 7.3: *Model parameters to be estimated. The following subscripts refer to the mono- and bi-articular joints: s, from shoulder rotation to shoulder torque; se, from shoulder to elbow; es from elbow to shoulder; e, from elbow to elbow; ew, from elbow to wrist; we, from wrist to elbow and w, from wrist to wrist.*

nr	Parameter	Unit	nr	Parameter	Unit
Segmental Mass			Acceleration feedback (spindles)		
1	m_{hume}	kg	16	ka_s	Nms^2/rad
2	m_{fore}	″	17	$ka_{se}(= ka_{es})$	″
3	m_{hand}	″	18	ka_e	″
Viscosity			19	$ka_{ew}(= ka_{we})$	″
4	b_s	Nms/rad	20	ka_w	″
5	$b_{se}(= b_{es})$	″	Velocity feedback (spindles)		
6	b_e	″	21	kv_s	Nms/rad
7	$b_{ew}(= b_{we})$	″	22	$kv_{se}(= kv_{es})$	″
8	b_w	″	23	kv_e	″
Elasticity			24	$kv_{ew}(= kv_{we})$	″
9	k_s	Nm/rad	25	kv_w	″
10	$k_{se}(= k_{es})$	″	Position feedback (spindles)		
11	k_e	″	26	kp_s	Nm/rad
12	$k_{ew}(= k_{we})$	″	27	$kp_{se}(= kp_{es})$	″
13	k_w	″	28	kp_e	″
Hand Visco-elasticity (2×2 matrices)			29	$kp_{ew}(= kp_{we})$	″
14	B_h	Ns/m	30	kp_w	″
15	K_h	N/m	Force feedback (golgi)		
			31	kf_s	-
			32	$kf_{se}(= kf_{es})$	-
			33	kf_e	-
			34	$kf_{ew}(= kf_{we})$	-
			35	kf_w	-
			Activation cut-off frequency		
			36	f_s	Hz
			37	f_e	″
			38	f_w	″
			Neural time delay		
			39	Td_s	ms
			40	Td_e	″
			41	Td_w	″

number of parameters corresponding to the best fits were na=22 and nb=10 for the ARX model of the system $H(q^{-1})S(q^{-1})$ and na=21 and nb=15 for the ARX model of the system $S(q^{-1})$. The total number of model parameters of the latter system showed a clear convergence to the best one whereas convergence was less pronounced for the former system. There was a clear trend towards the optimal model structures. E.g. the number of parameters $[na, nb]$ of the ten best models varied in the ranges $[22-26, 10-16]$ and $[19-22, 14-17]$ for $H(q^{-1})S(q^{-1})$ and

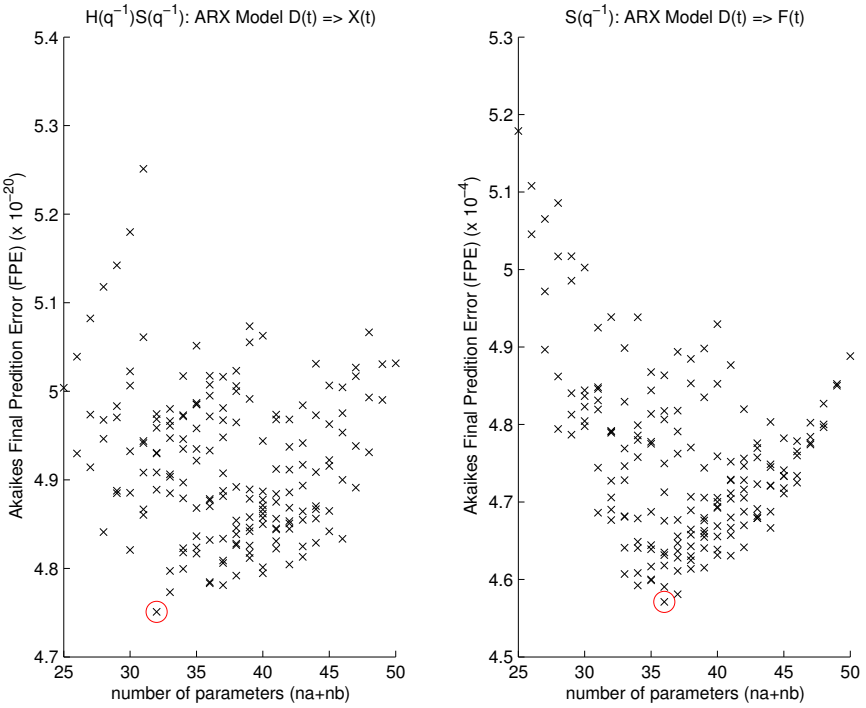

Figure 7.5: *Akaikes Final Prediction Error Criterion (FPE) for a range of different ARX models (Eqs (7.7) and (7.8)). For this trial (Subject 1, displacement 4 mm (RMS), damping 50 Ns/m, repetition (a)) the optimal number of parameters is indicated by circles and equals 32 for* $H(q^{-1})S(q^{-1})$ *and 36 for* $S(q^{-1})$*, with* $[na, nb]$ *is* $[22, 10]$ *and* $[21, 15]$ *respectively.*

$S(q^{-1})$ respectively.

To validate if the estimated admittance indeed gives a good representation of the input-output behavior, the nonparametric estimate is used for comparison (De Vlugt et al., 2003a). Because nonparametric estimators do not separate signals from noise on a structural basis as do ARX models, their estimates contain substantial variance. Comparison is therefore rather crude but gives a direct indication whether the main characteristics are reasonably described by the parametric estimates. Figure 7.6 shows an example of the estimated endpoint MFRFs of the arm admittance (gain and phase characteristics) as obtained by parametric ARX models (black lines) and by nonparametric estimation (gray lines) for a typical condition. The latter is only used for validation of the global frequency characteristics. The nonparametric estimate is traced by the parametric estimate. The parametric estimate is smooth and exhibits subtle changes more pronounced than the nonparametric estimate. At the lowest frequency the admittance is high for all separate

Table 7.4: *Estimated 'invariant' model parameters (mean (SD)) for all subjects: segmental mass ($m_{hume}, m_{fore}, m_{hand}$), handgrip visco-elasticity (b_h, k_h), neural time delay (T_{ds}, T_{de}, T_{dw}) and activation cut-off frequency ($f_{act,s}, f_{act,e}, f_{act,w}$).*

Parameter	Value (mean (SD))				
Subject	1	2	3	4	5
m_{hume} [kg]	1.96 (0.295)	1.88 (0.397)	1.78 (0.262)	1.86 (0.388)	2.17 (0.332)
m_{fore} [kg]	1.13 (0.240)	1.19 (0.154)	1.08 (0.148)	1.27 (0.171)	1.18 (0.202)
m_{hand} [kg]	0.496 (0.0976)	0.363 (0.0628)	0.425 (0.0885)	0.546 (0.0483)	0.384 (0.0883)
b_h [Ns/m]	157 (66.7)	184 (66.1)	194 (101)	167 (74.9)	214 (109)
k_h [kN/m]	7.39 (3.09)	6.46 (2.03)	8.06 (2.53)	13.3 (4.27)	8.28 (4.47)
T_{ds} [ms]	30.4 (2.48)	29.4 (3.17)	28.6 (2.71)	30.7 (2.42)	29.7 (3.51)
T_{de} [ms]	34.2 (3.11)	32.7 (2.89)	34.1 (2.80)	33.4 (2.61)	32.0 (1.80)
T_{dw} [ms]	40.4 (3.00)	37.7 (1.89)	37.6 (1.54)	41.4 (2.13)	39.8 (2.68)
$f_{act,s}$ [Hz]	1.98 (0.0842)	2.11 (0.139)	2.15 (0.164)	1.99 (0.116)	2.08 (0.145)
$f_{act,e}$ [Hz]	2.17 (0.176)	2.30 (0.101)	2.28 (0.107)	2.35 (0.102)	2.26 (0.136)
$f_{act,w}$ [Hz]	2.11 (0.175)	2.21 (0.132)	2.19 (0.140)	2.13 (0.147)	2.09 (0.171)

frequency response functions (FRFs), i.e. all combinations of inputs and outputs. For medium frequencies between 1 and 10 Hz pronounced peaks and troughs were present. The gains decreased clearly with higher frequencies beyond 10 Hz while the phase increased or decreased to approximately 180 or -180 degrees respectively.

A typical result of the NMS model fit onto the estimated parametric ARX model is shown in Figure 7.7. Clear variations of the FRFs from the ARX model (gray lines) were very well approximated by the NMS arm model (black lines) for both phase and gain responses of all four FRFs. Comparable fits were obtained for all other conditions and subjects.

7.3.2 Estimated joint parameters

The parameters that can be regarded as invariant are the segmental mass, the neural delay and the activation cut-off frequency as shown in Table 7.4. Over all subjects and all conditions applied, the estimated values of the mass showed a standard deviation varying from 10-20% of the corresponding mean values. The estimated hand visco-elastic parameters showed the largest variation (30-60%) while the estimated time constants and activation cut-off frequency had the smallest variation (5-8%). As was expected, the mass of the segments decreases with their distance to the shoulder joint. The neural time delay was largest for the wrist joint and smallest for the shoulder joint, as was expected from the increase in nerve fiber length with distality of the joint. The activation cut-off frequency of the elbow joint muscles varied in the range of 2.17-2.35 Hz for all subjects and was 0.15 and 0.3 Hz higher than those of the wrist and shoulder joint respectively. Hand grip visco-elasticity varied substantially over the conditions. These parameters were also shown separately by Table 7.4 because they do not result from direct control of arm muscles, as do the intrinsic and reflexive parameters, but mainly relate to tension of the finger muscles.

The estimated intrinsic and reflexive parameters are shown in Figure 7.8 and

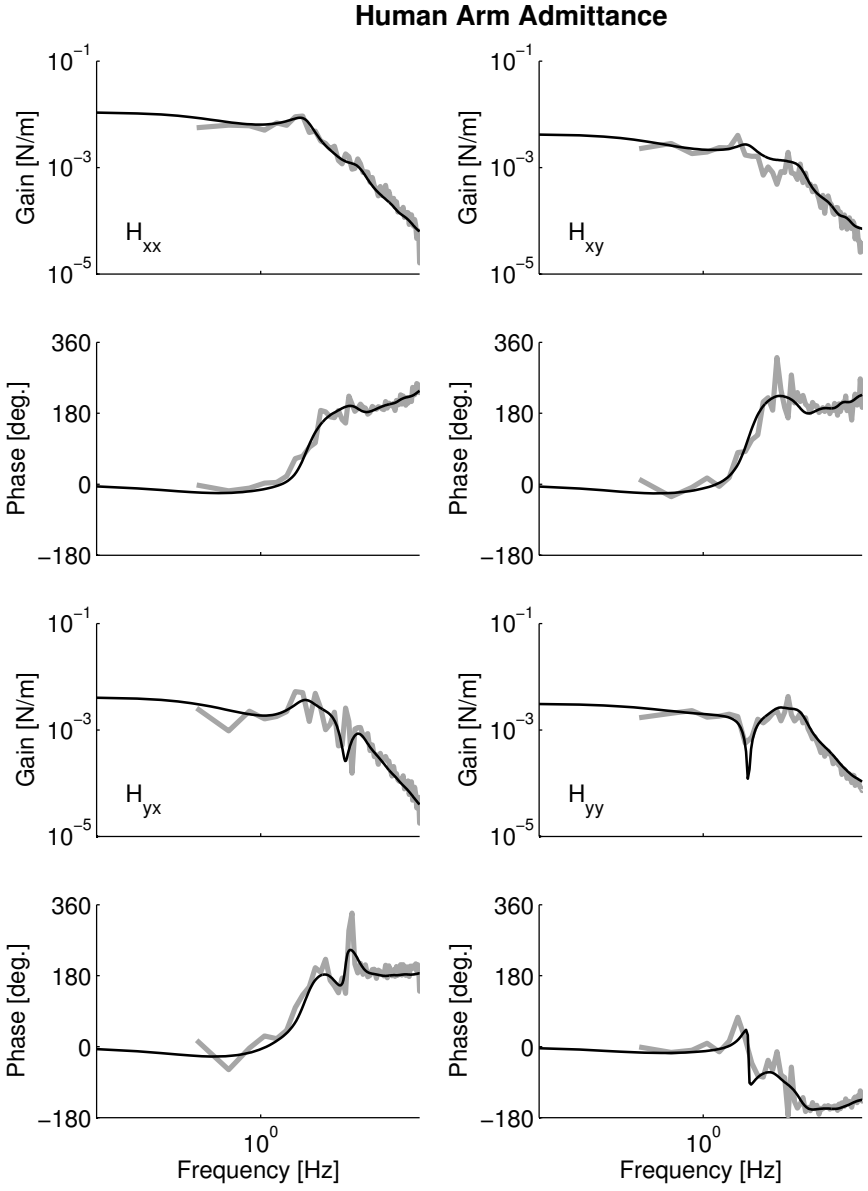

Figure 7.6: *Gain and phase characteristics of the estimated arm admittance obtained from ARX models (black lines) and from nonparametric spectral estimation (grey lines). The latter is used only for global judgement of the ARX model estimate. Subject 2, Left position, B_e=50 Ns/m, X=4 mm (RMS), repetition (a).*

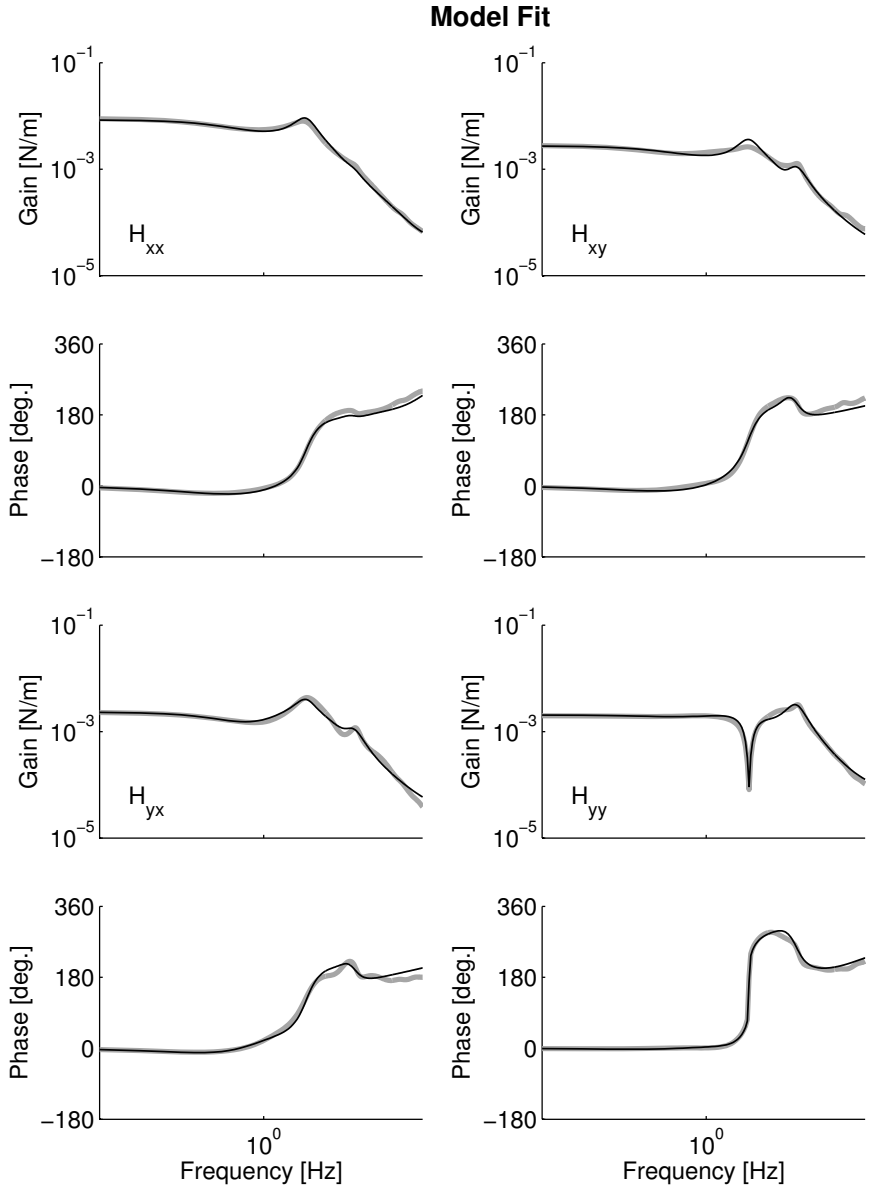

Figure 7.7: *Gain and phase characteristics of the NMS arm model (black lines) after parametrization by fitting onto the corresponding ARX model (grey lines). Subject 2, Central Position, B_e=0 Ns/m, X=5.5 mm (RMS), repetition (a).*

grouped by subject (columns) and hand position (gray scales) for all joint combinations (abscissa). In general, the parameters (intrinsic and reflexive) did not vary consistently with any of the experimental conditions applied, which was rather surprising. Correlation tests (not shown) proved there was no significant relation between parameters and conditions. Also, the estimated MFRFs did not show a clear trend with the conditions applied. There was some increase of the intrinsic parameter values with position from the Left to the Right (upper two rows in Figure 7.8). The velocity feedback gains K_V for the shoulder joint and the shoulder-to-elbow joint (s and se) showed the largest variation with position, especially for Subject 3. These gains were highest in the Left position and lowest in the Right position.

Intrinsic parameters

With respect to the different joints, large difference in the parameters existed. Intrinsic stiffness and damping from the elbow joint was larger (factor 2 or 3) than for the shoulder joint (upper two rows). Elbow joint damping was in the range of 1-2 Nms/rad against 0.5-1 Nms/rad for the shoulder joint, as an average over all subjects. The estimated intrinsic damping and stiffness covaried clearly in all cases. Intrinsic damping and stiffness were smallest for the wrist joint, varying in the range of 0.15-0.25 Nms/rad and 5-15 Nm/rad respectively. Compared to the single joints, two-joint damping and stiffness was generally smaller.

To check if any variation in the intrinsic parameters was due to changes in mean muscle activation levels, the mean and standard deviation of the EMG of each muscle was taken, see Table 7.5. For mutual comparison of the muscles, EMG was normalized to the values corresponding to the Central position. Mean values did not substantially change and also the standard deviation was small (0.06-0.14) for the muscles acting on the elbow and wrist joint. The triceps (longhead), the deltoideus anterior and posterior muscles showed the largest fluctuations of the mean EMG. Correlation tests did not show significant relationship between mean EMG and any estimated parameter (not shown).

Reflexive parameters

The differences of intrinsic parameters between the joints were also found from the reflexive parameters, albeit less pronounced. Acceleration feedback (K_A) showed comparable values between the shoulder and elbow joints. Velocity feedback gains (K_V) exhibited a pronounced decrease from proximal to distal joints. Markedly, velocity feedback exceeded the intrinsic damping by a factor 10 to 15. The ratio between intrinsic damping and reflexive velocity feedback gain was largest for the shoulder joint. For the wrist joint the velocity feedback gains varied between 0.5-2.25, which is 2 to 10 times larger than the corresponding single joint damping. Position feedback (K_P) was largest for the shoulder joint for almost all subjects. In contrast to the acceleration and velocity feedback gains, position feedback gain of the wrist joint was equal to or even higher than the position feedback gain of the elbow joint. The difference between two-joint and single joint position feedback

Table 7.5: *Mean and standard deviation (SD) of normalized EMG (with respect to the values of the Central position) for all muscles. EMG recordings from subjects 1 and 2 were corrupted by large peaks that resulted from cross-talk at the terminals of the analoguous-to-digital computer board. Hence, these recordings were not reliable and were therefore excluded from this study.*

Muscle	EMG (mean (SD))		
Subject	3	4	5
flex.carpi.rad.	0.950 (0.138)	0.956 (0.111)	0.918 (0.117)
ext.carpi.rad.	1.00 (0.0901)	0.918 (0.0625)	0.948 (0.119)
brachio rad.	0.942 (0.168)	0.896 (0.079)	0.932 (0.104)
biceps (short)	1.01 (0.139)	0.994 (0.117)	0.869 (0.142)
triceps lat.	0.933 (0.134)	0.928 (0.107)	0.967 (0.114)
triceps (long)	1.080 (0.229)	1.11 (0.303)	0.895 (0.140)
deltoid.ant.	0.983 (0.270)	0.923 (0.149)	0.950 (0.141)
deltoid.post.	0.929 (0.230)	0.963 (0.108)	1.08 (0.166)

was relatively small for the Left and Central positions compared to the Right position. Force feedback gains (K_G) varied the most with the conditions and therefore showed the largest standard deviation (Fig. 7.8, bottom row). For the shoulder joint the average value over all subjects was approximately 0.15 which is comparable to those for the single- and two-joints of the wrist. The force feedback gains of the elbow had values of about 0.3 and were the largest.

Parameter accuracy

Figure 7.9 shows the standard deviation of the mean estimated parameter values (square root of the variance, Eq. 7.21). The values are averages over all experimental conditions and all subjects (dots). Because large variations existed a logarithmic scale on the ordinate is used. The force feedback gain of the wrist joint ($K_{G,w}$) showed the largest deviation of $10^{-0.7}$, which means that this parameter was obtained with a deviation of approximately 0.2. With respect to its mean values of 0.3 (Fig. 7.8), this parameter was not accurately estimated. The majority of the parameters showed a standard deviation between $10^{-1.5}$ to $10^{-2.5}$ ($\approx$ 0.03 to 0.003). This range of accuracy applied the 'adjustable' intrinsic and reflexive parameters. Markedly, the stiffness and damping of the elbow joint had a relatively small standard deviation compared to the the other joints. The 'invariant' parameters listed in Table 7.4 exhibited the smallest standard deviation. Particularly, the estimates of the time delays and the activation cut-off frequency had standard deviation smaller than 10^{-3}.

The ARX models were able to describe the measured endpoint position rather good, as shown by the VAF$_{arx}$ values which were higher than 70% over the conditions (Figure 7.10, dashed lines). The values used for the external (linear) damping were high compared to those of the human arm at endpoint and therefore had large effect on the overall system behavior. Consequently, the VAF$_{arx}$ values strongly de-

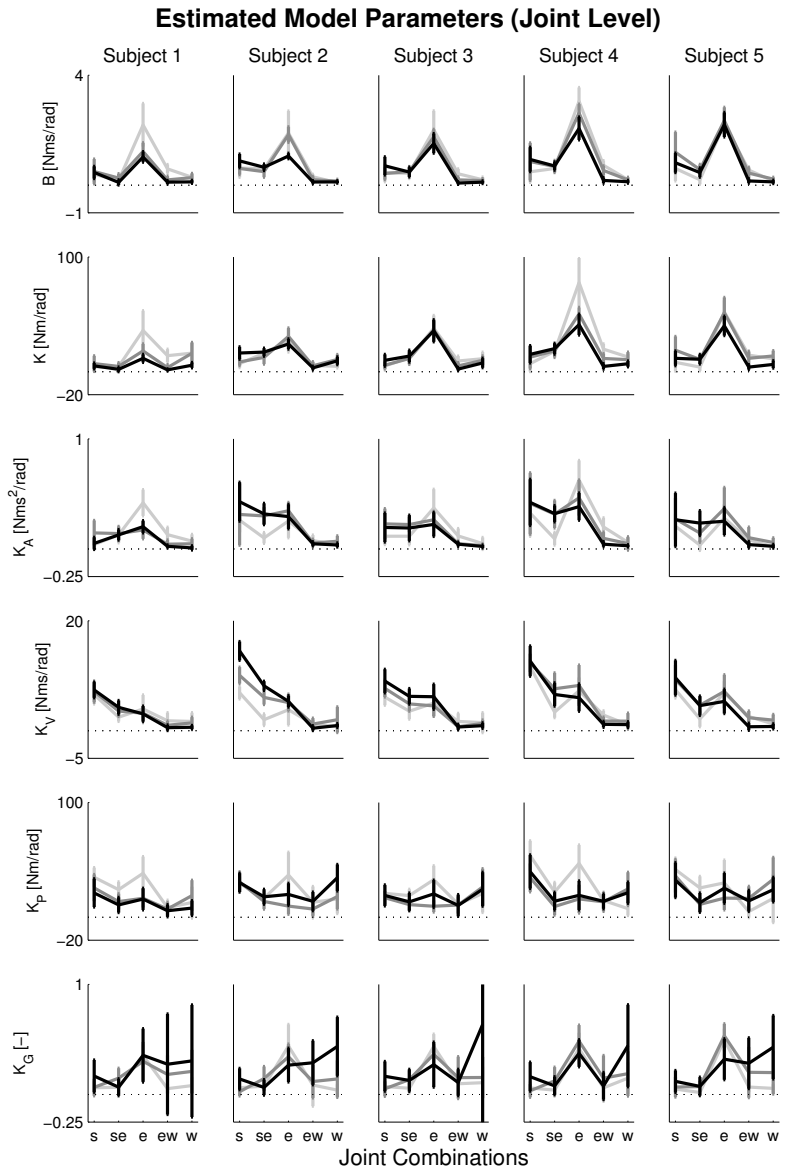

Figure 7.8: *Estimated intrinsic and reflexive model parameters for all joint combinations (abscissae) for all subjects (columns). The vertical bars denote the standard deviation over the applied conditions (external damping values, displacement amplitudes and repetitions). Positions: Left (black lines), Central (dark grey lines) and Right (light grey lines). From top to bottom row: joint damping B (Nms/rad)]; joint stiffness K (Nm/rad); acceleration feedback K_A (Nms^2/rad); velocity feedback K_V (Nms/rad); position feedback K_P (Nm/rad) and force feedback K_G.*

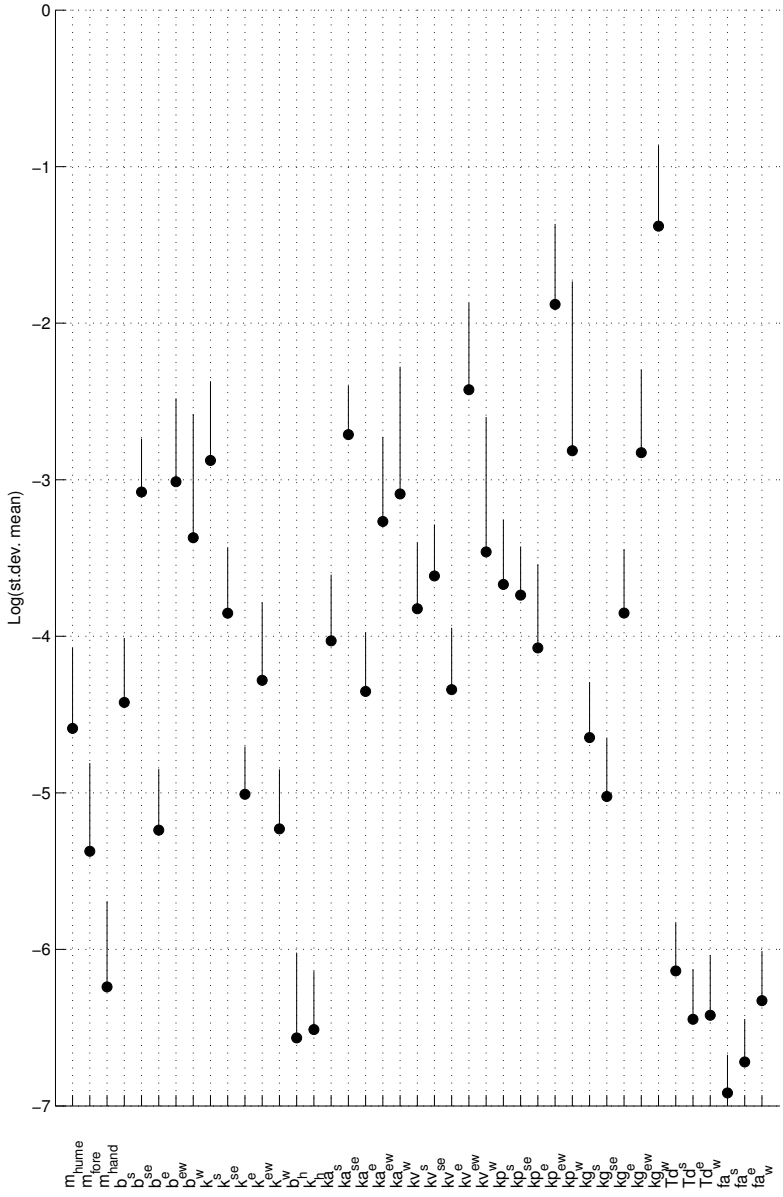

Figure 7.9: *Standard deviation of the mean parameter values (square root of Eq. 7.21) as an indication of the relative contribution of each parameter (abscissa) to the criterion function used (Eq. 7.20). Values are averaged over all trials and all subjects (dots). The vertical lines denote the standard deviation on the logarithmic scale.*

pended on the external damping, which therefore was used on the abscissa. The descriptive ability of the NMS arm-environment model, compared to the ARX model predictions, is shown by the VAF_{arm} values in Figure 7.10 (solid lines). VAF_{arm} values were higher than 60 % in the case the external damping was present. Without external damping, values ranged from nearly 50 % to 70 %, which are slightly lower than the values reported in a comparable 1-DOF study by Schouten et al. (2003c).

7.3.3 Role of single-joint muscles

Intrinsic and reflexive single joint properties are contributed from muscles acting around that joint, i.e. single- and two-joint muscles. In contrast, intrinsic and reflexive two-joint properties are due only to muscles spanning both joints (Hogan, 1985a). To indicate this distinction, reference to joint and joint muscle has been made (see also Appendix E, Eq. (E.1) for the matrix notation). The former refers to joint properties contributed from both single- and two-joint muscles while the latter refers to joint properties contributed by a particular muscle group. E.g. single-joint shoulder stiffness originates from both single-joint shoulder muscles and two-joint shoulder-elbow muscles. And so, single-joint shoulder muscle stiffness only refers to the single-joint shoulder muscles. Using this additive relationship, the joint parameters shown in Figure 7.8 were converted to joint muscle parameters (Fig. 7.11).

Intrinsic muscle stiffness and damping of two-joint shoulder-elbow muscles is generally larger (except for Subject 2) than that of single-joint shoulder muscles and smaller than that of single-joint elbow muscles. This joint related characteristics of intrinsic muscle properties accentuates the characteristics already present on joint level (Figure 7.8). Different characteristics were found from the reflexive muscle properties, particularly of velocity and length feedback. Feedback gains for the single-joint shoulder muscles and two-joint shoulder-elbow muscles were of comparable size and larger than those for the single-joint elbow muscles. Acceleration feedback was mainly due to two-joint shoulder-elbow muscles. Despite their relatively large deviations, force feedback gains were higher for the two-joint elbow wrist and single-joint wrist muscles than for the other shoulder and elbow muscle groups.

7.3.4 Endpoint admittance

A clarifying way of expressing the functionality of the arm admittance at endpoint level is by graphical display of admittance ellipses. In contrast to the often used stiffness ellipse (i.e. at zero frequency of the endpoint impedance), admittance ellipses can be drawn at each (discrete) frequency and visualize the magnitude and direction of endpoint displacements in response to external force disturbances. The major axis of an admittance ellipse denotes the direction along which the endpoint of the arm is least resistant to the external force, while the (orthogonal) minor axis indicates the direction of largest resistance. The endpoint admittance can therefore be characterized by the lengths of the major and minor axis respectively, or singular values, and the orientation ϕ of the major axis. These properties can be obtained by

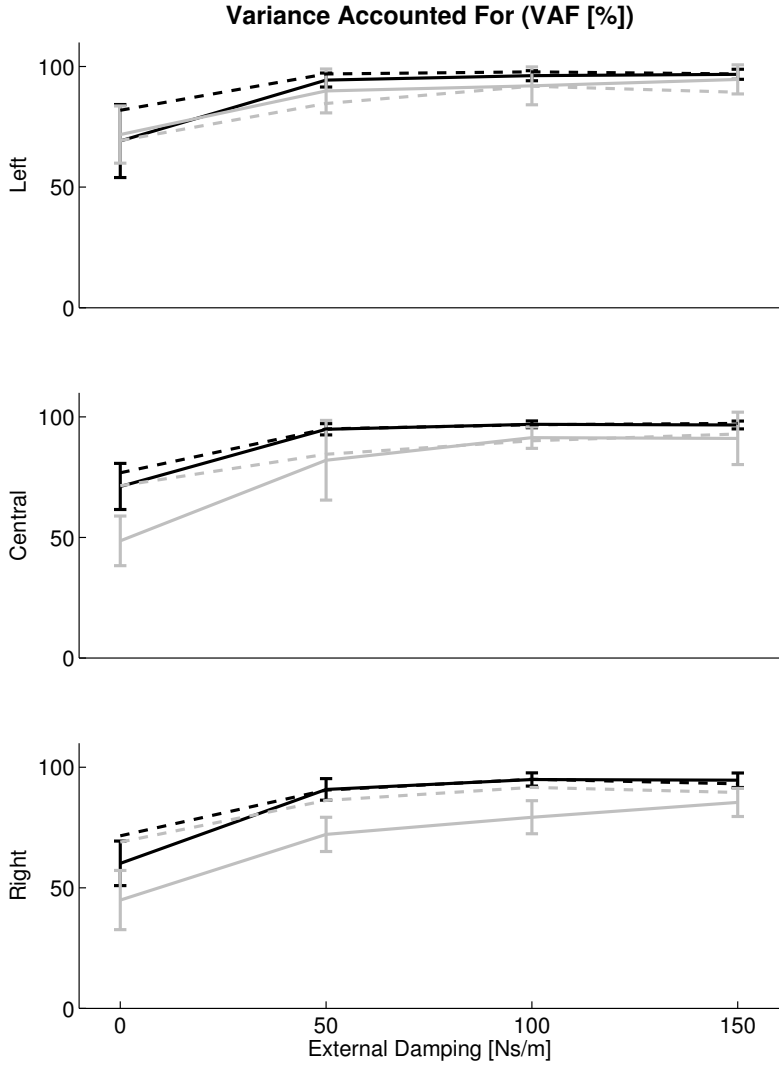

Figure 7.10: *Variance Accounted For (VAF) with external damping for each position (columnwise), averaged over the remaining conditions (disturbance amplitudes, repetitions, subjects). Black: x-direction; grey: y-direction. Solid lines: mean values of the NMS arm-environment model VAF$_{arm}$ and standard deviation over the conditions (vertical bars). Dashed lines: mean values of the ARX models VAF$_{arx}$. Values represent the goodness of the predicted endpoint position of both parametrized models (NMS arm-environment model and ARX model) compared to the predicted endpoint position from the corresponding parametric ARX models (VAF$_{arm}$) and the measured position (VAF$_{arx}$) respectively.*

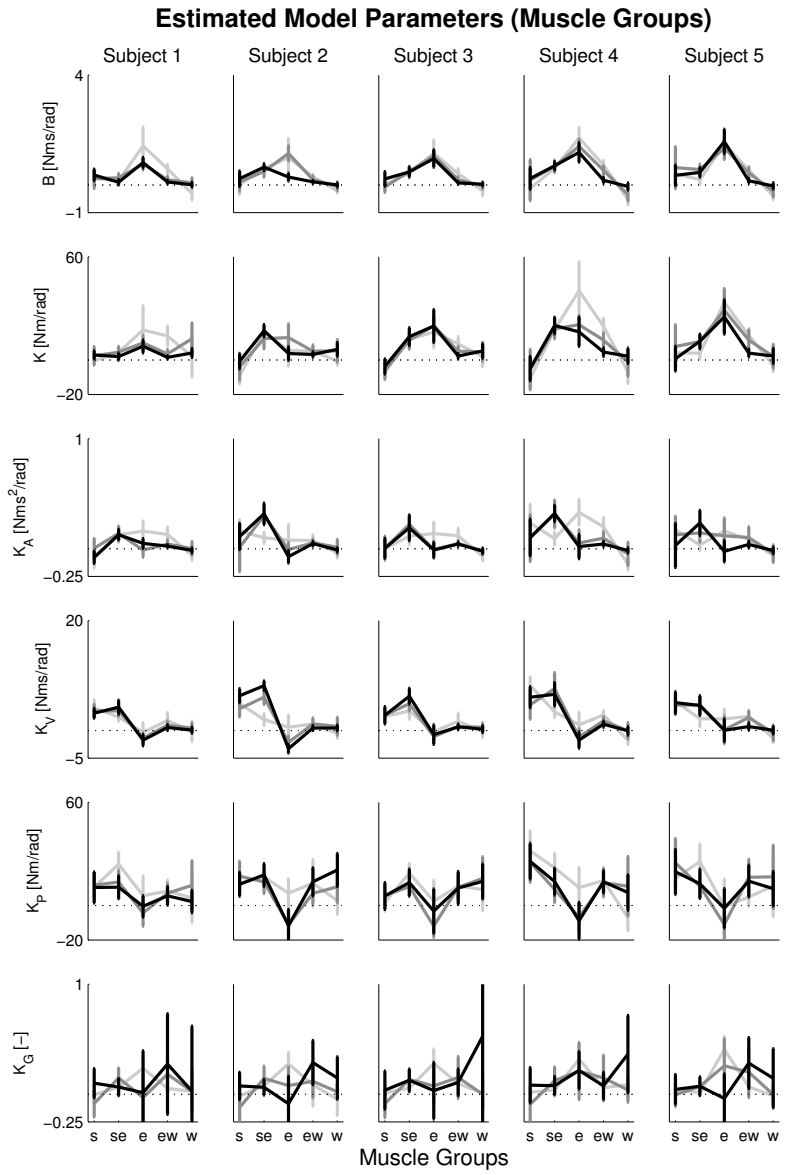

Figure 7.11: *Intrinsic and reflexive joint muscle parameters (abscissae) converted from the estimated joint parameters of Figure 7.8 for all subjects (columns). Positions: Left (black lines), Central (dark gray lines) and Right (light gray lines). From top to bottom row: joint damping B (Ns/rad)]; joint stiffness K (Nm/rad); acceleration feedback K_A (Nms^2/rad); velocity feedback K_V (Nms/rad); position feedback K_P (Nm/rad) and force feedback K_G. Note the scale differences for K and K_P compared to Figure 7.8.*

singular value decomposition of the (complex valued) admittance matrix:

$$\hat{H}(n\Delta f) = U(n\Delta f)\Sigma(n\Delta f)V^T(n\Delta f) \tag{7.28}$$

where $\Sigma(n\Delta f)$ is a diagonal matrix containing the singular values and $U(n\Delta f)$ and $V(n\Delta f)$ are unitary matrices containing the (orthogonal) eigenvectors of both $\hat{H}(n\Delta f)\hat{H}(n\Delta f)^T$ and $\hat{H}(n\Delta f)^T\hat{H}(n\Delta f)$ respectively (Strang, 1998). The orientation of the major axis equals:

$$\phi(n\Delta f) = tan^{-1}\left(\frac{|u_{max,y}(n\Delta f)|}{|u_{max,x}(n\Delta f)|}\right]$$

where

$$U(n\Delta f) = \left[\begin{array}{cc} u_{max,x}(n\Delta f) & u_{min,x}(n\Delta f) \\ u_{max,y}(n\Delta f) & u_{min,y}(n\Delta f) \end{array}\right]$$

Admittance ellipses are displayed as rotating position vectors $[x\ y]^T$ in response to a unit force vector generated by sin and cos functions, according to:

$$\left[\begin{array}{c} x \\ y \end{array}\right] = R(n\Delta f)\Sigma(n\Delta f)\left[\begin{array}{c} \cos\alpha \\ \sin\alpha \end{array}\right] \tag{7.29}$$

for $0 < \alpha < 2\pi$ and $R(n\Delta f)$ a rotation matrix:

$$R(n\Delta f) = \left[\begin{array}{cc} cos(\phi(n\Delta f)) & -sin(\phi(n\Delta f)) \\ sin(\phi(n\Delta f)) & cos(\phi(n\Delta f)) \end{array}\right]$$

Figure 7.12 shows the admittance ellipses for a typical subject at different frequencies, from 0.1 to 5 Hz. The dark-lined ellipses correspond to the NMS arm model using the estimated mean parameters as shown in Figure 7.8. The light gray-lined ellipses correspond to the intrinsic NMS arm model, i.e. the reflexive parameters were set to zero. The shaded area illustrates the additional contribution of the reflexes to the endpoint admittance. Characteristically, at low frequencies to 1.3 Hz the major axis was larger by a factor 5-7 for the intrinsic model. In the orthogonal direction the difference was much smaller. The direction of the ellipses hardly changed due to reflexive feedback. The orientation of the ellipses changed with position of the endpoint. At the Left position, the major axes had mean angles of approximately 20 degrees (anticlockwise with respect to the frontal plane), and was zero and -25 degrees at the Central and Right position respectively. Beyond 1.3 Hz, the effect of reflexes diminished and the responses where mainly due to the inertial properties.

7.4 Discussion

This study examined the intrinsic and reflexive muscle properties that constitute the endpoint admittance of the human arm. Endpoint arm admittance is the dynamic relationship between an external force and the resulting hand displacement.

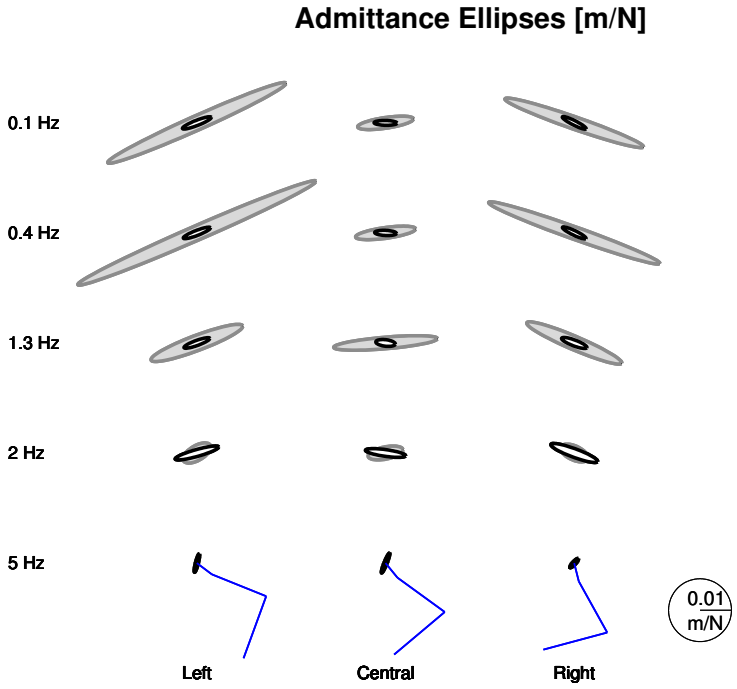

Figure 7.12: *Admittance ellipses (Subject 5) at different frequencies (ordinate, being: 0.1, 0.4, 1.3, 2.0 and 5.0 Hz) for the Left, Central and Right positions (abscissa). Black lines: ellipses for the mean estimated model parameters (Fig. 7.8). Light gray lines: ellipses for the same set of parameters with all reflexive feedback parameters set to zero. The difference (shaded areas) is from reflexive contributions. In nearly all cases reflexes decrease the admittance substantially. Straight lines indicate the arm orientation, with the hand located at the center of the ellipses. The magnitude of the ellipses is given by the radius of the calibration circle at the right bottom corner.*

Thus, it characterizes the sensitivity of the arm to disturbing forces and is a useful property for studying the control properties of the CNS during position maintenance tasks. The admittance can be changed by muscle contraction and adaptation of spinal reflex gains. Both increase the apparent net joint damping and stiffness, i.e. decreasing the admittance. Understanding how the intrinsic and reflexive properties are modulated by the CNS may provide insight into the functioning of human posture control. Intrinsic and reflexive joint properties did not vary with external damping and displacement amplitude. Apart from a moderate change with arm configuration, these findings indicated that intrinsic and reflexive muscle properties were not modulated by the CNS to these external conditions applied.

Intrinsic damping and stiffness were largest for the elbow joint whereas velocity feedback, and to a lesser extent also position feedback, was largest for the shoulder

joint. Average muscle activation levels varied the most for the single-joint shoulder muscles, suggesting that the usage of these muscles had a reduced efficiency compared to the elbow and wrist muscles. The simulated hand displacements in the horizontal plane were predicted accurately, validating the three DOF joint model.

7.4.1 Methodology

A basic requirement to study postural control is the usage of force disturbances. Then, the hand position can be controlled by adjusting the visco-elastic properties of muscles, either intrinsically or reflexively. To estimate the underlying intrinsic and reflexive joint properties, the endpoint admittance was identified followed by fitting of a NMS model onto the identified admittance. Because the force disturbances contained power over a wide bandwidth, a complete dynamic characterization of the endpoint admittance was obtained in a relative short observation time. The small standard deviation of the parameters with respect to their mean values indicates the estimation method was accurate. High VAF values gave further support to the validity of the model structure and the estimated parameters.

The specific usage of ARX models for parametric identification of the arm dynamics has not been used previously. The ARX models were parametrized in the time domain where each time derivative is represented by the shift operator, excluding the need for differentiating (or integrating) the time signals. Furthermore, the discrete ARX model was converted into multivariable frequency response functions that are perfectly suited for fitting the physiological NMS model.

Previous studies of multijoint arm properties have relied on transient (step or pulse) perturbations that measured the state just before the onset of the perturbation (Mussa-Ivaldi et al., 1985; Dolan et al., 1993; Tsuji et al., 1995; Gomi and Osu, 1998). A recent multijoint study by Perreault et al. (2001) used continuous position perturbations while requiring subjects to maintain a constant force in different directions. The results of that study showed that endpoint stiffness was primarily due to single-joint muscles spanning the shoulder and elbow. Then, the question arises what the functionality of endpoint stiffness is during the performance of a force maintenance task? Just like the majority of the previously referred studies, the results were not interpreted from a functional relationship between the disturbance type and the instructed task. Position perturbations require the performance of force tasks which hardly give insight into the stabilizing or disturbance properties of the arm during natural posture maintenance tasks. For posture control, a position task is evident which subsequently determines the requirement of force disturbances. Visco-elastic properties do have direct effect on the task performance and it is to investigate how these properties are controlled and what determines the range of adaptation by the CNS. Furthermore, no attempt has been made previously to separate intrinsic from reflexive muscle properties for the multijoint case. This study even reaches further by separating these properties for the multijoint redundant case, reflecting natural arm functioning.

7.4.2 Redundancy

Dynamic properties of the arm were studied in the horizontal plane as the result of the shoulder, elbow and wrist joint dynamics such that kinematic redundancy existed. Since the parameters were found consistently and with reasonable accuracy, redundancy was not an obstruction to the estimation procedure. This indicates that the NMS arm model was realistic and that the task execution was repeatable. Initial parameter values have been varied randomly by 50 % which had no effect on the final solutions. Larger variations of the initial values often resulted in larger values of the criterion functions, indicating to suboptimal local minima.

7.4.3 Intrinsic and reflexive joint parameters

High cocontraction levels were also reported in a comparable one DOF study by Schouten et al. (2003c) yielding large intrinsic damping and stiffness at the hand of 32 Ns/m and 380 N/m respectively. In that study, the hand moved in anterior-posterior directions with the elbow at 90 degrees flexion (zero degrees elevation of the humerus) such that only single-joint shoulder muscles contributed to the endpoint admittance. Accounting for a mean humeral length of 0.3 m, these values correspond to a damping from the single-joint shoulder muscles of $32 \times 0.3^2 \approx 3$ Nms/rad and a stiffness of $380 \times 0.3^2 \approx 34$ Nm/rad, since joint stiffness and damping scale with the square of the moment arm. In the current study, mean estimated values (over all subjects) of 0.4 Nms/rad and 2 Nm/rad were found for respectively the single-joint damping and stiffness from the shoulder muscles (Fig. 7.11). These values are a factor 10 to 15 smaller than those found by Schouten et al. (2003c).

An explanation for these differences might be the difference in moment arms of shoulder muscles acting around the gleno-humeral joint. With respect to the arm configuration as used in the study by Schouten et al. (2003c) (moments in the sagittal plane), the moment arms in this study (moments in the horizontal plane) of the posterior muscles were smaller by a factor 2-4 (Van der Helm, 1994) depending on the hand position (Left, Central, Right). On the contrary, the moment arms of the anterior muscles were larger by a factor 1-1.5. This implicates that the mean muscle activation of the anterior muscles must be reduced by a factor $2 \times 1 = 2$ to $4 \times 1.5 = 6$ for static moment balance. Since joint stiffness scales with the square of the muscle moment arm and approximately linearly with muscle force, this means that the contribution to the shoulder joint stiffness from the anterior muscles is reduced by a factor $\frac{1}{6} \times 1.5^2 \approx 0.37$ at most. The total joint stiffness (from anterior plus posterior muscles) was $1 + 1 = 2$ and reduces to $0.37 + \frac{1}{4^2} = 0.44$, which a reduction by a factor 4.5. This comparison is worst case which is only $30\% - 50\%$ of the difference with the 1-DOF study. Perhaps, the efficiency of the shoulder muscles might also play a role in the control of muscle force. Because the moment arm of the shoulder with respect to the hand was larger in the current study, the increase in endpoint stiffness from an increase in shoulder joint stiffness is relatively smaller. If performance is traded-off against metabolic energy, a possible reduction in the activation of shoulder muscles also explains part of the difference in intrinsic shoulder

visco-elasticity.

Overlapping conditions (force disturbances, external damping) were also used to study rotational dynamics of the wrist joint by Schouten et al. (2003d). In that study the estimated mechanical wrist properties originated from both single-joint wrist and two-joint elbow-wrist muscles and therefore correspond to the single-joint wrist parameters in this study (and not to the single-joint wrist muscle parameters). Mean damping and stiffness were 0.1 Nms/rad and 10 Nm/rad for the wrist joint which are nearly the same as found in this study, being 0.15 Nm/rad and 11 Nm/rad respectively. The values found by Schouten et al. (2003d) were obtained for high cocontraction levels, suggesting maximal values of the intrinsic wrist parameters in the present study.

In previous studies, elbow stiffness was found to range between 0-100 Nm/rad (Perreault et al., 2001; Gomi and Osu, 1998), obtained from unilateral contractions during a force maintenance task and without distinguishing between intrinsic and reflexive contributions. The total elbow joint stiffness (intrinsic plus reflexive) found here ranged from 35 Nm/rad to 70 Nm/rad, which is significantly lower even while the elbow muscles in this study operated in cocontraction. Most likely, position tasks exhibit contraction levels that are the result from weighting muscular effort ($\sim$ force) to performance ($\sim$ position) in an efficient way comparing to force tasks. Force tasks induce higher unilateral contraction levels that likely are not weighted against effort since effort is similar to performance (i.e. the force task). Large differences in mean EMG levels between position and force tasks were also found by Abbink (2002).

Muscle spindles are known to increase their sensitivity to stretch with decreasing stretch amplitude, as measured during imposed position perturbations (Stein and Kearney, 1995; Cathers et al., 1999). The range of displacement amplitudes used here overlapped to those used in previous multijoint studies (Tsuji et al., 1995; Gomi and Osu, 1998; Perreault et al., 2001). Nonlinear effects due to displacement amplitude were not observed in this study.

The reflex gains estimated were accompanied by neural time delays that correspond to the monosynaptic Ia afferents (from muscle spindles) and disynaptic Ib afferents (from golgi tendon organs). No significant differences were found between the estimated neural time delays with those from previous studies. For the shoulder joint muscles the average time delay was 29 ms, where Schouten et al. (2003c) found a mean value of 28 ms. The time delay of the wrist joint was 39 ms which is comparable to the previously found value of 41 ms (Schouten et al., 2003d).

Acceleration feedback has not been identified in vivo before. Chen and Poppele (1978) have found that muscle spindles in the anaesthetized cat exhibited an increased responsiveness to increasing frequency of displacement. Their findings correspond to an acceleration term in the transfer function of the spindle dynamics similar to the gain included in the present spindle model. Acceleration feedback was substantially present for the two-joint shoulder-elbow muscles and consequently for the corresponding single-joints. Acceleration feedback was assumed here to describe the nonlinear effects from the unidirectional sensitivity of the mus-

cle spindles. Kukreja et al. (2003) showed that linearization of an unidirectional velocity sensitivity results in higher order terms including a pronounced acceleration term. In a recent one DOF model study, the endpoint dynamics were estimated from a nonlinear NMS model including unidirectional velocity sensitivity (Stienen et al., 2003). An acceleration term was needed to describe the estimated behavior, suggesting that acceleration feedback is an artifact of muscle spindle unidirectionality rather than a distinct sensory function. Assuming nonlinear spindle behavior is indeed the cause of an acceleration feedback term, then slower rotational movements of the shoulder joint compared to the elbow joint might as well be the reason for the observed differences. The effect of acceleration feedback becomes important at relatively high frequencies above $\pm$ 3 Hz where inertial effects also begin to dominate. Therefore, acceleration feedback has less effect to the task performance than velocity and position feedback.

The functionality of golgi tendon organs has been studied very scarcely. In fact, the only known property is that golgi tendon organs provide feedback of the muscle force with a rather linear characteristic (Houk and Henneman, 1966). Its contribution is counterproductive to the mechanical joint resistance since it has an inhibitory effect on motoneurons and thereby decreasing muscular activation. Force feedback gains were found for the two-joint and single-joint wrist muscles. Rozendaal (1997) showed by model simulations that force feedback increases the bandwidth of the activation process such that the muscle responds faster to motoneuron excitation. A possible role of Golgi tendon organs is to regulate hand contact forces during force tasks. In that case, wide bandwidth force control is useful while the admittance does not have to be minimal but sufficient only to preserve contact (grip), which is mainly performed by the distal joints.

The cut-off frequency of the shoulder muscles was 2.07 Hz, which is 0.1 Hz lower than found by Schouten et al. (2003c). Bobet and Norman (1990) identified the activation cut-off frequency of the elbow flexor and extensor muscles and found values of 1.9-2.8 Hz against an average of 2.27 Hz found here. Notice the small standard deviations in these parameters as well as for the neural time delays, indicating the accuracy of the parameter estimation.

7.4.4 Role of single-joint and two-joint muscles

Muscles need to be controlled to obtain the desired joint behavior taking into account that two-joint muscles operate on two different joints. Intrinsic stiffness and damping from single-joint shoulder muscles was almost zero implicating that the single-joint stiffness of the shoulder was contributed mainly from the two-joint shoulder-elbow muscles. Apparently, the required position task did not appeal to efficient usage of the shoulder muscles that is most likely because of the relatively large moment arm from the gleno-humeral joint to the hand, as also noted in the previous section. Apparently, large intrinsic muscle stiffness and damping (that is directly related to metabolic effort) has a relatively smaller effect on endpoint performance compared to the elbow and the wrist. Markedly, single-joint shoulder position and velocity reflexes were substantial and compensate for the lack of in-

trinsic shoulder stiffness and damping in an efficient way, since muscles are only activated when stretched. For the two-joint shoulder-elbow and single-joint elbow muscles, the ratios of intrinsic and reflexive properties were clearly different. Taking notice of these highly varying ratios, it appeared that the CNS adapted reflexive feedback gains independently of the amount of mean muscle activation.

Two joint shoulder-elbow muscles also increase the elbow stiffness and damping, which were high already due to the single-joint elbow muscles themselves. Compared to the single-joint shoulder muscles and two-joint shoulder-elbow muscles the reflex gains of the single-joint elbow muscles were minimal.

On the joint level, the ratio of intrinsic stiffness to reflexive position feedback was found to increase with distality of the joint. For the single-joint shoulder stiffness and position feedback gain, mean values (all averaged over the subjects) were 12 and 28 Nm/rad respectively. For the two-joint elbow these values were 12 and 18 Nm/rad, and for the single-joint elbow these values were 32 and 23 Nm/rad respectively. The total stiffness is thus 40, 30 and 55 Nm/rad for the single joint shoulder, the two-joint shoulder-elbow and the single-joint elbow respectively. Apparently, two joint stiffness has a significant role during arm posture tasks. This result is in contrast to the previous findings during force regulating tasks where two-joint stiffness was minimal with respect to the corresponding single-joint shoulder and elbow stiffness (Gomi and Osu, 1998; Perreault et al., 2001). An increased force production (from EMG and motorunit activity) of two-joint arm muscles was found during movement tasks compared to force tasks, for one sided contractions (Tax et al., 1990; Van Bolhuis and Gielen, 1997; Van Groeningen and Erkelens, 1994). These results indicate that two-joint muscles play a substantial role during posture maintenance. Rozendaal (1997) showed by model simulations that two-joint shoulder-elbow muscles have large effect on the the size and orientation of the endpoint stiffness ellipse. Because the two-joint biceps and triceps muscles also generate joint torque around the elbow, these two-joint muscles play an important role to suppress external force disturbances acting upon the hand under the present conditions.

7.4.5 Endpoint admittance

The task instruction given to the subjects was to minimize their hand displacements. A small endpoint admittance in both directions was therefore desired to suppress the effect of the force disturbances. The results showed that the endpoint admittance was elliptic with its largest gain in the direction that was approximately perpendicular to the line connecting the shoulder joint with the hand. In previous studies that measured the endpoint stiffness, the major axis was always directed towards the shoulder (Mussa-Ivaldi et al., 1985; Gomi and Osu, 1998; Perreault et al., 2001). This agrees with the admittance ellipses (for the lowest frequency) from this study since stiffness is the static part of the impedance which on its turn is the inverse of the admittance. The main reason for the characteristic elliptic shape of the endpoint admittance is the configuration of the arm. Since the admittance increases with the square of the moment arm (from joint center to hand), the admittance of

the shoulder joint has the largest effect on the endpoint.

In the previous single-joint studies by Schouten et al. (2003c) and De Vlugt et al. (2002), external damping was used from the hypothesis that increased stability margins of the combined arm-environment system at endpoint level facilitates the usage of reflex gains to improve the task at lower frequencies. This hypothesis was proven by their results, showing a clear decrease of endpoint admittance from increasing position feedback gains. Such a phenomenon was not found in this study. A possible explanation is that for the single-joint case the displacement of the endpoint was the direct result of single-joint shoulder muscles only. This is different from the present redundant multiple-joint case where several muscle groups act on three different joints that control the planar endpoint admittance. Probably, if the number of joints involved in controlling the endpoint behavior increases, minimizing the effort (mean muscle activation) is more emphasized in the trade-off against performance. The high single-joint shoulder reflexes might already be optimal such that any further increase due to additional damping at endpoint did not further improve efficiency. Another possible explanation for the absence of reflex modulation with external damping is related to the existence of redundancy. Because the joints can freely rotate irrespective the viscosity of the endpoint, a change in the endpoint admittance from varying external properties does not directly change the dynamic properties of the individual joints. Therefore, it was verified if there was a combined effect on endpoint level due to additional external damping. It was found that endpoint admittance did not change consistently with external damping.

In conclusion, the results from this study indicate that during multijoint posture maintenance reflexive properties are adjusted to control the mechanical properties on the joint level and not on the endpoint level.

Chapter 8

General discussion

Erwin de Vlugt

8.1 Quantification of spinal reflexes during posture maintenance

This thesis developed and applied identification techniques to quantify the properties of the human reflex system and analyzed its role to the control of posture maintenance. As such, these techniques contribute to the understanding of fundamental issues in human movement control and can be applied for medical diagnosis to explain movement disorders in terms of affected feedback functioning. There is an increasing number of studies (Lee and Tatton, 1975; Schouten et al., 2003a; Smith et al., 2000) that direct to malfunctioning of neural transmission at brain and segmental levels in the CNS that could explain abnormal movement behavior. Relevant diseases to which the technique can be applied are Parkinson's Disease (PD), Reflexive Sympathetic Dystrophy (RSD), Repetitive Strain Injury (RSI), Spasticity and Huntington's' Disease (Schouten, 2004).

Posture maintenance is a steady state act of the human body, aiming to keep the joints in a certain configuration. It is important that the joints are mechanically robust. That is, resistant to external disturbing forces and sufficiently stable. It is also favorable to minimize energy consumption in order to maintain posture for a longer period. The CNS needs to find an optimum weighting between these conflicting requirements by adjusting the intrinsic and reflexive muscle properties.

Intrinsic muscle visco-elasticity is effective but continuous co-activation costs a large amount of metabolic energy. On the contrary, reflexive control is energy efficient but is constrained by the inherent neural time delays. Excessive reflex gains induce mechanical oscillation.

In all experiments, the co-activation levels were high and constant for all conditions. This indicates that the subjects performed the task using high intrinsic viscoelasticity. Since modulation of the intrinsic properties was not found, energy efficiency was most likely not taken into account to adjust the reflexive system.

8.1.1 Spinal reflexes

The modulation of the reflex gains was found to be determined from weighting performance against control effort and stability demands (Chapter 2, De Vlugt et al. 2001, Van der Helm et al. 2001). And, such gain modulations obviously took place within seconds. The short latency of approximately 30-40 ms that was found suggests that the reflexive contribution was from monosynaptic pathways. Possibly, these adaptations are accomplished by specific controlled presynaptic depolarization of afferent terminals that reduces feedback sensitivity of the motoneuron (Rudomin 1999).

In the case the damping of the environment was increased, the estimated reflexive position feedback gain also increased. These results correspond to those of Milner et al. (1993) who found experimental evidence that monosynaptic reflexes are

adapted to different external dynamics. Their results are comparable in the sense that they found the same effects in the opposite direction, namely that feedback gain decreased with increasing (positive) velocity feedback of the manipulator. The results from this study support these findings in a more specific way by stating that humans act like optimal controllers to optimize the combined dynamics of limb and environment together. Under the current experimental conditions, i.e. continuous unpredictable force perturbation while maintaining a reference position, short latency reflex gain adjustment appear to be quite effective in performing such optimizations.

Control effort weighting had a great impact on the reflex gains. This simply meant that when performance improvement was small with a modest increase in feedback gains, control effort weighting highly suppressed reflexive activation. The results from the model optimizations in Chapter 2 suggested that humans optimize performance with limited control effort. Zero weighting would result in the best performance but excessively high gains. It is unclear which mechanisms contribute to the weighting or limitation of afferent control effort and a single parameter is likely too simple to describe the underlying mechanism. However, the predicted position reflex gains showed strong resemblance with the estimated gains, in the case the velocity feedback was omitted from the optimization. These results indicate the presence of some kind of restricting mechanism between afferent position and velocity information.

8.1.2 Task and perturbation dependency

The existence of reflex gain modulation is doubted by previous studies which suggested that any gain adaptation may not be a usual mechanism by which the stretch reflex is controlled (Crago et al. 1976; Jaeger et al. 1982; Lee and Tatton 1975). From those studies the effect of different tasks on reflex action of the human elbow muscles was investigated and considerable changes in the short latency stretch reflex were not found. However, they neither changed the properties of the force perturbation nor varied the external dynamics to assess reflex gain adjustment. Just like the majority of studies aiming to reveal the function of reflexive feedback, these researchers applied transient perturbations that did not allow sufficient time for the human controller to adapt to the mechanical environment, let alone to optimize some sort of a performance measure in the presence of perturbations (Carter et al. 1993; Houk 1978; Stein and Kearney 1995; Toft et al. 1991). In fact, those experiments aimed to measure the state of the subject at the time just before onset of the perturbation rather than the performance of the reaction. Furthermore, the subjects knew in advance that they would be perturbed so that the measured response reflected anticipatory behavior. Actually, a naive person can only be perturbed once. In accordance with Smeets et al. (1991) we believe that transient like perturbations are somewhat poor test signals to elicit short latency gain modulation. Because short latency length reflexes varied substantially during our experiments, continuous random force perturbations have been proved better suited to

investigate reflex control (Agarwal and Gottlieb 1977b; Dufresne et al. 1978). The random character of the perturbations prevented anticipatory behavior such that the measured response was completely determined by subconscious control.

Agarwal and Gottlieb (1977a) perturbed the ankle joint with a random $0-50$ Hz force perturbation while the subjects were instructed to counteract various bias torques (a force task) such that foot movement was symmetrical with respect to a reference angle. The mechanical environment was formed only by the inertia of the footplate which was slightly larger than that of the foot. They neither did find a distinct resonance peak and their corresponding FRF of the ankle admittance was quite similar with the responses from this study where reflexive feedback was absent. At least the argument of Agarwal and Gottlieb, as were reflexive feedback not functional during random perturbations per se, is strongly contradicted by the results of our study. Their conclusion is misleading and can be attributed to the fact that both task instruction and perturbation were force based. This results in unnatural adjustments of the limb, i.e. the only way to maintain a mean force level while the limb is being perturbed is to move in the same directions as the force perturbation, which for random signals is impossible. Therefore, the limb stiffness had to be kept small as to approximate such (unnatural) behavior. Most likely, reflexive gain control during force perturbations is not suited to force tasks but highly suited to position tasks.

The functional importance of task instruction has not been fully recognized in literature when interpreting human motion control. Most studies chose position perturbations (whether continuous or transient), and formulated a force task, without mentioning the effect of such experimental conditions on reflexive and intrinsic feedback mechanisms. Current results showed that the endpoint admittance changed with the task instruction and that muscle spindle feedback was more pronounced during position tasks compared to force tasks. In general, the endpoint admittance was high for force tasks and small for position tasks (Chapter 4).

8.1.3 Other feedback mechanisms

The neural time delay of spinal reflexes is approximately 30-40 ms for arm muscles. Other control systems that are relevant to posture maintenance are the medium and long latency reflexes, the visual and vestibular system. Compared to spinal reflexes, the neural time delays associated with these systems are much longer because higher brain centra are involved in processing information from these sensors. The neural delay for medium and long latency reflexes for arm muscles are approximately 60 ms and 120 ms respectively (Jaeger et al., 1982; Lee and Tatton, 1975) and 200 ms for the visual system (McRuer and Jex, 1967). These latencies reduce the effectiveness for posture control to relatively low frequency perturbations. To exclude the contributions from these additional control systems, random perturbations were applied. The results proved that the measured behavior above 1 Hz to these perturbations were almost completely determined from spinal reflexes (Chapters 2, 3 and 7).

8.1.4 Nonlinearities

Despite the highly non-linear nature of the NMS, the mechanical behavior at endpoint was well described by a linear model for all experimental conditions applied. High VAF values proved that linear models adequately described the mechanical response of the arm at endpoint level. On a muscle level, most relevant nonlinearities are the unidirectional (stretch amplitude and velocity) sensitivity of the muscle spindles (e.g. Stein and Kearney 1995), different calcium activation-deactivation rates, and mechanical properties like the force-length and force-velocity characteristics. In multiple muscle systems these nonlinearities apparently cancel out at endpoint level under specific experimental conditions. The demonstrated linear behavior can be explained by the following arguments: 1) the application of small amplitude disturbances does not excite nonlinearities; 2) unidirectionality in sensor sensitivity and muscle force generation presumably turns into bi-directional behavior in the case of muscles acting as antagonistic pairs and 3) from a functional anatomical point of view, different muscles are likely to act at different lengths hence distributing their characteristics over a wider range of motion which smooths out the nonlinearities. Furthermore, nonlinearities from inertial properties (configurational, centripetal, Coriolis) can be considered negligible for the perturbations used because the angular excursions were small.

The application of a linear model is further supported by a phenomenon found by Kirsch et al. (1994). They demonstrated that stochastic perturbations tends to linearize the intrinsic muscle response, probably because of changed dynamics of the cross-bridge turn over. In particular, stiffness properties were found to remain constant and not exhibit a dependence on displacement amplitude, even for movements which significantly exceeded the yield length revealed by step stretches.

8.1.5 Force feedback from Golgi tendon organs

The studies in Chapters 2 and 3 attributed observed reflexive activity to muscle spindle feedback while force feedback from Golgi tendon organs was ignored. The reason why force feedback was not included in the analyses is because its contribution was considered not functional for disturbance rejection during posture maintenance. However, the results shown in Chapter 4 showed a local increase in the gain of the endpoint admittance for several subjects (Group A) which could only be explained by force feedback. Since force feedback decreases the effect of intrinsic visco-elasticity, larger reflex gains would be required to describe the same endpoint admittance. Consequently, the estimated parameter values in Chapter 2 might be a little underestimated. Actually, this was already demonstrated by the inclusion of the acceleration term (which has similar effect to force feedback) in Chapter 3, showing slightly larger values of the length and velocity feedback gains.

Other studies that used position tasks in combination with force perturbations (e.g. Jaeger et al. 1982; Doemges and Rack 1992ab and this thesis) found high resistance to movement (small endpoint admittance) which was attributed to high levels of co-contraction and substantial feedback from muscle spindles. However,

force feedback may very well be present, which changes the relative contributions from intrinsic and reflexive feedback from muscle spindles. Conclusions about the precise magnitude of muscle spindle activity are to be reviewed, but the characteristics of the spindle gains are expected to remain valid in general.

Force feedback improves the bandwidth of the activation dynamics (Rozendaal, 1997). On the contrary, force feedback increases the endpoint admittance which is counterproductive for posture tasks such used in this thesis. The magnitude of this latter negative effect was shown to be dependent on intrinsic visco-elasticity and muscle spindle feedback gains (Appendix B). In the case the endpoint behavior was comparable to that of a second order system, the effect of force feedback on endpoint admittance was even canceled completely by a certain combination of position and velocity feedback gains. From the experimental findings, strong indications were found that force feedback was present during force tasks as well as position tasks for a subpopulation of the subjects (Group A). For another population of subjects (Group B), the admittance exhibited a second order behavior. Apparently, Group A subjects did not compensate for force feedback while Group B subjects did. Force feedback could even be absent for Group B subjects. Intrasubjective variation of force feedback was not observed, which presumably means that force feedback was not modulated with the applied conditions. Experimental conditions should be developed in the future which are more appealing to the usage of force feedback (see Section 8.2.2).

8.1.6 Improvement of the parameter estimation

The usage of the reflexive impedance based on EMG measurements included direct information of the reflexive system into the identification procedure. The parameters of a more detailed model were quantified, such as the neural time delay and an acceleration feedback term (Chapters 3 and 7). Application of EMG for estimating FRFs is not a trivial case due to bad signal to noise ratio (SNR) of raw EMG signals. Therefore, the SNR needed to be improved by conditioning the external force disturbance before application (frequency clustering, cresting) and by conditioning the raw EMG signals (whitening, filtering). The resulting coherence was high ($>$ 0.8) and is significantly better than was found before by Cathers et al. (1999) who did not applied signal conditioning methods before estimation of the FRFs.

Parametric ARX models were used providing more accurate descriptions of the mechanical endpoint admittance compared to the nonparametric estimators. Parametric estimators use a predefined model structure, including a noise filter, and a limited set of parameters. For comparison, nonparametric estimators do not require any apriori model structure and produce a large number of parameters, i.e. as much as there are time samples. The results of Chapter 7 showed that the parametric estimates described even the most subtle variations in the endpoint admittance that were sometimes hardly visible in the nonparametric estimations. The conversion of the ARX model to the frequency domain is a new and highly valuable for the cur-

rent applications of parameter estimation. Based on the improved FRFs of the parametric models, a detailed multiple DOF NMS arm model could be parametrized. Parametric system identification is therefore the future tool for parameter estimation of physiological models.

The main conclusions of this thesis are:

- Force perturbations facilitate natural posture tasks and are the key requirements for the analysis of human movement control in vivo.
- Force controlled haptic manipulators are necessary devices to apply force disturbances. The constructional demands of such devices are high, requiring lightweight but stiff materials and powerful direct-drive actuators to avoid mechanical resonance.
- The mechanical endpoint admittance, as a measure for the sensitivity of the arm to external forces, is the best description to analyze underlying intrinsic and reflexive muscle properties because it preserves causality (force input, position output). Admittance is identified from measurements of hand position and reaction forces that are relatively easy to obtain.
- Spinal reflexes from muscle spindles (Ia-afferents) have significant contribution to the endpoint admittance that can be of the same magnitude or even larger than the contribution from intrinsic muscle visco-elasticity.
- Mechanical properties of the environment and the frequency content of the force perturbation have both large effect on the reflex gains. For increased bandwidth of the force perturbation signal, reflex gains decreased to avoid oscillation near the eigenfrequency of the arm. In the case the environment supplied sufficient damping, reflex gains were likely determined from trading-off performance (reducing endpoint admittance) against control effort.
- Intrinsic visco-elasticity of the shoulder was smaller compared to the elbow and wrist during multiple DOF posture maintenance in the horizontal plane. A compensatory effect was found by reflexive control gains, showing the largest gains for the shoulder joint and smallest for the wrist joint. These results indicated that reflexive feedback of the shoulder joint was controlled independently of its intrinsic visco-elasticity.

8.2 Future directions

8.2.1 Reflexes at muscle level

The studies described in this thesis measured the mechanical endpoint behavior and quantified mechanical properties at the joint level. The mechanical properties of a joint are the result of many muscles that operate as synergists or antagonists.

Quantitative measures of reflexive feedback on the muscle level would be highly informative to study the functional control of different muscle groups. However, EMG measurements off all the muscles involved for producing arm movements are not possible. To obtain the contribution of different muscles, model optimizations of a detailed NMS model should be carried out (Rozendaal, 1997). The optimized activation patterns can then be compared for those (few) muscles that are measurable by EMG.

8.2.2 Submaximal tasks

The task instruction given to the subjects was "minimize the displacements of the hand", yielding to high co-contraction levels. Furthermore, these levels remained almost constant for all conditions applied. As the result, intrinsic visco-elasticity was constant. Maximal co-contraction was apparently part of the best control strategy.

It is interesting to reveal the control strategy in the case co-contraction levels are used at smaller levels during submaximal posture tasks like 'maintain position deviations within certain bounds'. Energy efficiency likely becomes more important to the optimal solution since maximal co-contraction levels are no longer required. Consequently, the energy efficient reflexive feedback from muscle spindles will presumably be more pronounced. In such a scenario, the improvement of the activation bandwidth by force feedback is beneficial. Forthcoming results can elucidate the functioning of Golgi tendon organs of which the role is still rather vague.

8.2.3 Identification of reflexes during movement

Compared to posture maintenance, control of the CNS is substantially more difficult during movement because the mechanical properties of the arm continuously change over time (muscle lengths and forces, inertial configuration). How is optimal performance achieved to what metabolic costs? How does the CNS controls such a time variant system? Is the stability of movement preserved? And how is performance (speed, accuracy) reflected by the control system?

Until now, there exist no technique to quantify the properties of feedback and forward control during movement. Forward refers to voluntary control from higher brain centra. Previous methods are severely limited by measuring only the spring-like properties of the human arm to sudden transient perturbations during the movement (Gomi and Kawato, 1996, 1997). These methods cannot reveal underlying controller properties of the CNS as the consequence of improperness of the used identification techniques and limited performance of manipulators.

To understand how human movement is controlled, a technique should be developed that quantifies the properties of both the feedback and forward controller during human arm motion. With this technique, stability and performance of movements can be addressed in terms of controller properties of the CNS. These expected results are a tremendous step ahead in the field of human movement control and

will be very helpful in explaining movement irregularities originating from neurological disorders.

Forward control is based on the assumption of an Internal Model (IM) in the brain that directly sends motor commands down to the motoneurons in the spinal cord (Fig. 8.1). Motoneurons activate the muscles that accelerate the limb to follow the reference trajectory. It is assumed that the IM comprises knowledge of the dynamical properties of the muscles and the skeleton. Imperfections in the IM can be compensated for by feedback control (proportional and differential) of the muscle lengths and of the muscle forces. At novel situations like unknown objects, unexpected disturbances or high motion accurateness requirements, feedback is necessary. It is also believed that sensory signals during novel conditions are used to train the IM. Since it takes some time (about 30-40 msec for arm muscles) for the neural feedback signals to travel from the sensors to the spinal cord and back to the muscle, the feedback loop is only able to apply corrections for slow movements (up to 3 Hz). During fast movements (up to 6-7 Hz), the activation of muscles is likely to be only under forward control, while feedback is minimal to prevent interference with the high-speed motions. Feedback is used towards the (slower) end of the movement phase to achieve high targeting precision. Figure 8.2 illustrates the hypothesized shift between feedback and forward control with movement speed, as culminated into the known IM-hypothesis (Gerdes and Happee, 1994).

The IM cannot be identified directly because the reference trajectory is a brain act (as is the IM itself), generated as a certain coded neural activation pattern that cannot be measured by a representative physical quantity. More downwards to the spinal cord, the central brain commands are decoded into measurable signals like muscle activation (via electromyography), limb reaction force and position (via the manipulator) and the joint angles (e.g. via optical camera systems).

The main challenge for the future is to identify the properties of the feedback controller from these peripheral variables during movement. Once these properties are revealed, the contributions of the forward controller might then be derived. The method should be intended to be used as a non-invasive in-vivo technique. Quantification of the feedback and forward control mechanisms will definitely prove if the IM-hypothesis is valid, which will be of crucial importance to the broad field of human movement science.

A major problem is that the time-variant properties of the moving limb make it difficult to identify the system properties (position, velocity and force feedback gains, neural delays, muscle visco-elasticity) because it is not known if a variation is the result of the perturbation or of a varying property. Furthermore, biological systems are non-linear by nature such that at other speeds or other properties of the force perturbation signal (amplitude, frequency) the response can be completely different. An integral identification strategy is to use a neuromusculoskeletal (NMS) model including non-linear system properties from a priori knowledge. Such an approach can be successful if the chosen model structure is close to that of the real system. The parameters are found by optimization techniques that min-

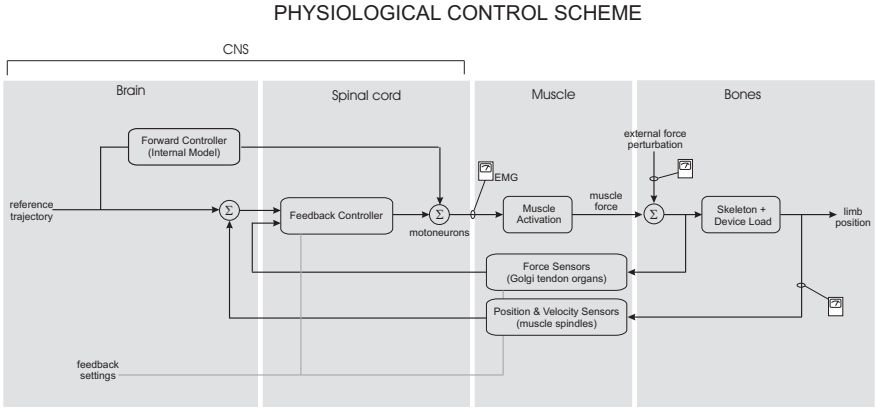

Figure 8.1: *Schematic representation of the different parts of the human movement control system. The overal function is to control the limb position to follow a reference trajectory. Corresponding motor commands are generated from an internal model (IM) in the brain (forward controller) and send to the motoneurons in the spinal cord that activate the muscles. Muscle forces move the skeleton plus any additional load from the perturbing device that is needed for identification. Deviations from the intended path and commanded muscle forces are corrected by position and velocity feedback from the muscle spindles and by feedback of the muscle force from Golgi tendon organs. Available variables from measurements are illustrated by analogue indicators.*

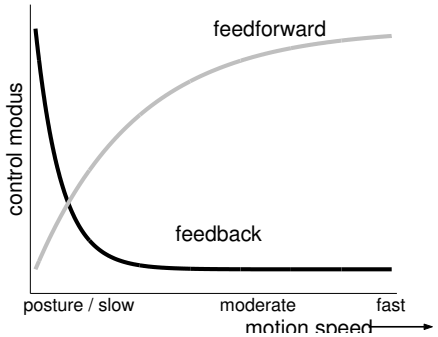

Figure 8.2: *Illustration of the IM-hypothesis, showing the interchange between feedback and forward control modi with speed of movement. For posture maintenance and slow movements, limb motion is mainly under feedback control. Due to the limited bandwidth of the feedback loops, forward control takes over at higher speed of movement. The exact contributions are to be determined by the future identification technique.*

imize the difference between the model prediction and the real system response, similar to the criterion functions used in this thesis.

An alternative approach is to divide the movement into quasi-linear subsystems sequenced in time and apply standard linear techniques to each linearized subsystem. For each property there are as much values as there are subsystems. The advantage of linear techniques is that nonparametric models without a priori knowledge can be used initially. These two approaches span the range of possible identification techniques (Kearney and Hunter, 1990). Development of the most suited technique will be a question of the stage at which a priori system knowledge has to be implemented in the analysis.

The existing ARMANDA manipulator provides a unique opportunity for the development of such identification techniques as it is yet the only compliant manipulator that is able to apply wide bandwidth force perturbations during motion.

It is expected that crucial research questions that have been put forward from the fields of human motion control can be addressed if the feedback and forward controller can be identified during movement. These questions are:

- Modulation of feedback during movement generation. Does feedback indeed decrease during movement according to the IM-hypothesis? Previous measurements showed that the spring-like property of the human arm at endpoint (hand) decreased during movement (Gomi and Kawato, 1996). Can this be explained from a reduced feedback gain of muscle spindles?

- Learning new movements by feedback error learning (Karniel and Mussa-Ivaldi, 2002). Is feedback enhanced during learning new movements or during interaction with new environments? And if so, does feedback reduces over learning time and how fast do feedback settings change?

- Dynamic stability and disturbance analyses. How optimal is the human controller and what is optimized during movement? Model optimizations can be performed and compared to the measured behavior.

Appendix A

Dynamic model of arm, hand and environment

In this study only the endpoint dynamics are identified, representing the lumped effect of joint dynamics at hand level. It consists of four parts: (1) the intrinsic arm mass, damping and stiffness; (2) the (intrinsic) hand damping and stiffness; (3) the reflexive length and velocity feedback including muscle activation and (4), the external mass, damping and stiffness of the environment. Figure A.1 shows the compound blockscheme of all different parts.

The model is expressed in the frequency domain where the higher derivatives are given as powers of the Laplace operator s $(= \lambda + j2\pi f)$.

A.1 Intrinsic part

For small displacements the visco-elastic properties of muscles can be described well by a linear spring-damper system. Together with the arm mass the intrinsic properties are modelled as:

$$H_i(s) = \frac{X_a(s)}{F_{int}(s)} = \frac{1}{m_a s^2 + (b_a s + k_a)u_0} \tag{A.1}$$

Any stiffness and viscosity from passive tissues surrounding muscles and joints are also included in the model. The amount of cocontraction is represented by u_0 and scales intrinsic stiffness and damping, which seems to be justified (Agarwal and Gottlieb 1977a). In case of silent reflexes, i.e. when the intrinsic model is estimated, u_0 is set to one as a reference.

The spring-damper system k_h and b_h acts in series with the arm dynamics, representing the interaction of the hand with the handle. The position of the handle x_h in the model is different from the position of the arm x_a (Fig. A.1) and represents movement of the wrist, skin displacement and movement of the fingers:

$$H_h(s) = \frac{F_h(s)}{X_h(s) - X_a(s)} = b_h s + k_h \tag{A.2}$$

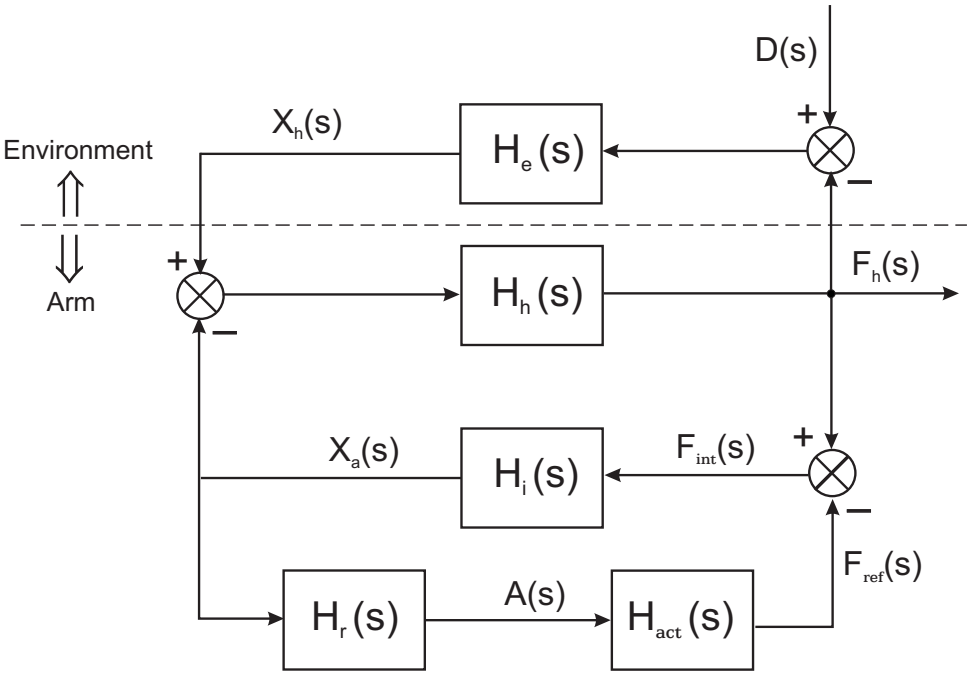

Figure A.1: *Blockscheme of combined arm-hand-environment model expressed in the frequency domain. Arm dynamics (indicated below the dashed border line) consisting of H_r: reflexive length and velocity feedback, H_{act}: activation dynamics, H_i: intrinsic arm dynamics and H_h: hand dynamics. H_e represents the dynamics of the environment (above the dashed line). $X_a(s)$ is the position of the arm, $X_h(s)$ the (measured) position of the hand, $F_h(s)$ the (measured) interaction force applied by the hand, $F_{int}(s)$ the intrinsic force, $F_{ref}(s)$ the reflexive force, $A(s)$ is the reflexive activation, and $D(s)$ is the applied external force perturbation.*

The intrinsic arm model becomes ($F_{int}(s) = F_h(s)$):

$$\frac{X_h(s)}{F_h(s)} = \frac{1 + H_h(s)H_i(s)}{H_h(s)} = H_h^{-1}(s) + H_i(s) \tag{A.3}$$

The intrinsic parameters to be estimated are: m_a, b_a, k_a, b_h and k_h ($u_0 = 1$).

A.2 Reflexive part

Spindle dynamics are described by a first order transfer function $H_r(s)$, relating arm position $X_a(s)$ to the afferent neural signal $A(s)$ (Fig. A.1) according to:

$$H_r(s) = \frac{A(s)}{X_a(s)} = (k_v s + k_p)e^{-T_d s} \tag{A.4}$$

Linear approximation of the spindle dynamics seems to be justified during the small stationary periodic perturbations as used in this study (Soechting and Dufresne 1980, Zahalak and Pramod 1985). The reflex gains k_p and k_v represent the reflexive position and velocity feedback gains respectively. Transmission delay and processing time in the spinal cord are described by a time-delay $T_d = 25$ ms (Smeets and Erkelens 1991).

Activation and deactivation processes of the muscle are approximated by a first order system with time constant $\tau_a = 30$ ms (Winters and Stark, 1985):

$$H_{act}(s) = \frac{F_{ref}(s)}{A(s)} = \frac{1}{\tau_a s + 1} \tag{A.5}$$

Intrinsic arm (without hand dynamics) and reflexive feedback can now be formulated as:

$$H_a(s) = \frac{X_a(s)}{F_h(s)} = \frac{H_i(s)}{1 + H_i(s)H_r(s)H_{act}(s)} \tag{A.6}$$

which forms the feedback path to the hand dynamics $H_h(s)$, resulting in the arm dynamics (including the hand) $H_{arm}(s)$:

$$H_{arm}(s) = \frac{X_h(s)}{F_h(s)} = H_h^{-1}(s) + H_a(s) \tag{A.7}$$

A.3 Combined model: arm plus environment

The environment acts in parallel to the arm and hand, where the sum of the reaction force at the hand and the external force perturbation forms the input (Fig. A.1). The second order dynamics of the environment equals:

$$H_e(s) = \frac{X_h(s)}{D(s) - F_h(s)} = \frac{1}{m_e s^2 + b_e s + k_e} \tag{A.8}$$

with m_e the mass, b_e the viscosity and k_e the stiffness of the environment. The complete model including the environment becomes:

$$H_{DX}(s) = \frac{X_h(s)}{D(s)} = \frac{H_e(s)}{1 + H_e(s)H_{arm}^{-1}(s)} \tag{A.9}$$

As part of the optimization $H_{DX}(s)$ is used for calculating the cost function J_x and the poles for system's stability.

For calculating the control effort cost function J_a, the closed loop function $H_{DA}(s)$ is used. Therefore, the afferent reflexive signal $A(s)$ (Fig. A.1) is first expressed as:

$$A(s) = H_r(s)X_a(s) \tag{A.10}$$

substituting (A.6), (A.7) and (A.9) in (A.10) gives:

$$H_{DA}(s) = \frac{A(s)}{D(s)} = H_r(s)H_a(s)H_{arm}(s)H_{DX}(s) \tag{A.11}$$

A.4 Frequency form of J_x

The task instruction *'minimize the displacements'* is represented mathematically in the form of a cost function to be minimized. Having a linear, noise-free system with stationary stochastic inputs, the cost function J of the displacement $x(t)$ is:

$$J_x = E\left\{x^2(t)\right\}$$

where $E\{\cdot\}$ is the expectation operator. When $E\{x(t)\} = 0$, J_x is the variance σ_x^2 of $x(t)$. By using the following relations:

$$J_x = \sigma_x^2 = \int_{-\infty}^{\infty} S_{xx}(f)df = 2 \cdot \int_{0^+}^{\infty} S_{xx}(f)df$$

and,

$$\begin{aligned} S_{xx}(f) &= E\{X(f) \cdot X(-f)\} \\ X(f) &= H_{DX}(f) \cdot D(f) \end{aligned}$$

J_x can be rewritten in the frequency domain:

$$J_x = 2 \cdot \int_{0^+}^{\infty} |H_{DX}(f)|^2 S_{dd}(f)df$$

$S_{dd}(f)$ is the power spectrum of the input signal. The system inputs have rectangular power spectra:

$$S_{dd}(f) = c \quad \forall \ f_l \leq f \leq f_h$$

and zero elsewhere, so that J_x can be written as:

$$J_x = c \cdot \int_{f_l}^{f_h} |H_{DX}(f)|^2 df \tag{A.12}$$

with c is set to one.

Appendix B

Interplay between reflexive and intrinsic parameters

It was investigated to what extent a model expressing substantial reflexive activity (Eq. 4.10) can resemble a simple intrinsic MBK system H_{mbk} (hand dynamics cancel out). For identical endpoint behavior:

$$\begin{aligned} H_{arm}(s) &= H_{mbk}(s) \\ \frac{1}{m_a\, s^2 + B\, s + K} &= \frac{1}{m\, s^2 + b\, s + k} \end{aligned}$$

where b and k denote the viscosity and stiffness of the MBK model respectively. It can be readily seen that m_a always equals m. Furthermore:

$$B = \frac{b_a + k_v H_{act}\, e^{-\tau_{ms}}}{1 + k_f H_{act}\, e^{-\tau_{gto}}} = b \tag{B.1}$$

$$K = \frac{k_a + k_p H_{act}\, e^{-\tau_{ms}}}{1 + k_f H_{act}\, e^{-\tau_{gto}}} = k \tag{B.2}$$

It is assumed that $\tau_{gto} = \tau_{ms}$, since the diameter of nerves from Ib-afferents from Golgi tendon organs (GTO) are approximately equal to those from the Ia-afferents from muscle spindles. The stiffness and damping of H_{arm} are determined by a combination of reflexive and intrinsic parameters. For the following linear combinations Eqs B.1-B.2 hold:

$$b_a = \frac{k_v}{k_f} \quad , \quad k_a = \frac{k_p}{k_f}$$

It follows that $B = b = b_a$ and $K = k = k_a$. In other words: all dynamics of muscle spindles can be *totally* compensated for by GTO force feedback, as if there was no reflexive activity at all.

Appendix C

State space model of arm, hand and environment

The complete model is described by three equations (see Fig. 5.4).

The arm model:

$$\mathbf{F}(s) + \mathbf{N}(s) = M_a\ddot{\mathbf{Y}}(s) + B_a\dot{\mathbf{Y}}(s) + K_a\mathbf{Y}(s) \tag{C.1}$$

The hand model:

$$\mathbf{F}(s) = B_h(\dot{\mathbf{X}}(s) - \dot{\mathbf{Y}}(s)) + K_h(\mathbf{X}(s) - \mathbf{Y}(s)) \tag{C.2}$$

The environmental model:

$$\mathbf{D}(s) - \mathbf{F}(s) = M_e(s)\ddot{\mathbf{X}}(s) + B_e\dot{\mathbf{X}}(s) + K_e\mathbf{X}(s) \tag{C.3}$$

where s is the Laplace operator. Eliminating $\mathbf{F}(s)$ by substituting Eq. (C.2) into Eqs (C.1) and (C.3), results in the following two system equations:

$$\begin{aligned}
\ddot{\mathbf{X}} &= M_e^{-1}\left[-(B_e + B_h)\dot{\mathbf{X}} - (K_e + K_h)\mathbf{X} + B_h\dot{\mathbf{Y}} + K_h\mathbf{Y} + \mathbf{D}\right] \\
\ddot{\mathbf{Y}} &= M_a^{-1}\left[B_h\dot{\mathbf{X}} + K_h\mathbf{X} - (B_h + B_a)\dot{\mathbf{Y}} - (K_h + K_a)\mathbf{Y} + \mathbf{N}\right]
\end{aligned}$$

where the Laplace operator is omitted for readability. The state space model equals:

$$\begin{aligned}
\dot{\mathbf{\Psi}} &= \mathrm{A}\mathbf{\Psi} + \mathrm{B}\mathbf{U} \\
\mathbf{\Phi} &= \mathrm{C}\mathbf{\Psi} + \mathrm{D}\mathbf{U}
\end{aligned}$$

with A the 8×8 system matrix, B the 8×4 input matrix, C the 4×8 output matrix

and D the 4×4 throughput matrix:

$$\mathrm{A} = \begin{bmatrix} -M_e^{-1}(B_e + B_h) & -M_e^{-1}(K_e + K_h) & M_e^{-1}B_h & M_e^{-1}K_h \\ I & O & O & O \\ M_a^{-1}B_h & M_a^{-1}K_h & -M_a^{-1}(B_h + B_a) & -M_a^{-1}(K_h + K_a) \\ O & O & I & O \end{bmatrix}$$

$$\mathrm{B} = \begin{bmatrix} M_e^{-1} & O \\ O & O \\ O & M_a^{-1} \\ O & O \end{bmatrix}$$

$$\mathrm{C} = \begin{bmatrix} O & I & O & O \\ B_h & K_h & -B_h & -K_h \end{bmatrix}$$

$$\mathrm{D} = \begin{bmatrix} O & O \\ O & O \end{bmatrix}$$

I is the 2×2 identity matrix and **O** the 2×2 nulmatrix.
The state vector **X** equals:

$$\mathbf{\Psi} = \begin{bmatrix} \dot{\mathbf{X}} \\ \mathbf{X} \\ \dot{\mathbf{Y}} \\ \mathbf{Y} \end{bmatrix}$$

with $\mathbf{X} = [X_x X_y]^T$ and $\mathbf{Y} = [Y_x Y_y]^T$. The input and output vectors equal:

$$\mathbf{U} = \begin{bmatrix} \mathbf{D} \\ \mathbf{N} \end{bmatrix}$$

with $\mathbf{D} = [D_x D_y]^T$, $\mathbf{N} = [N_x N_y]^T$ and

$$\mathbf{\Phi} = \begin{bmatrix} \mathbf{X} \\ \mathbf{F} \end{bmatrix}$$

with $\mathbf{F} = [F_x F_y]^T$

Appendix D

Spatial derivation of the true stiffness field

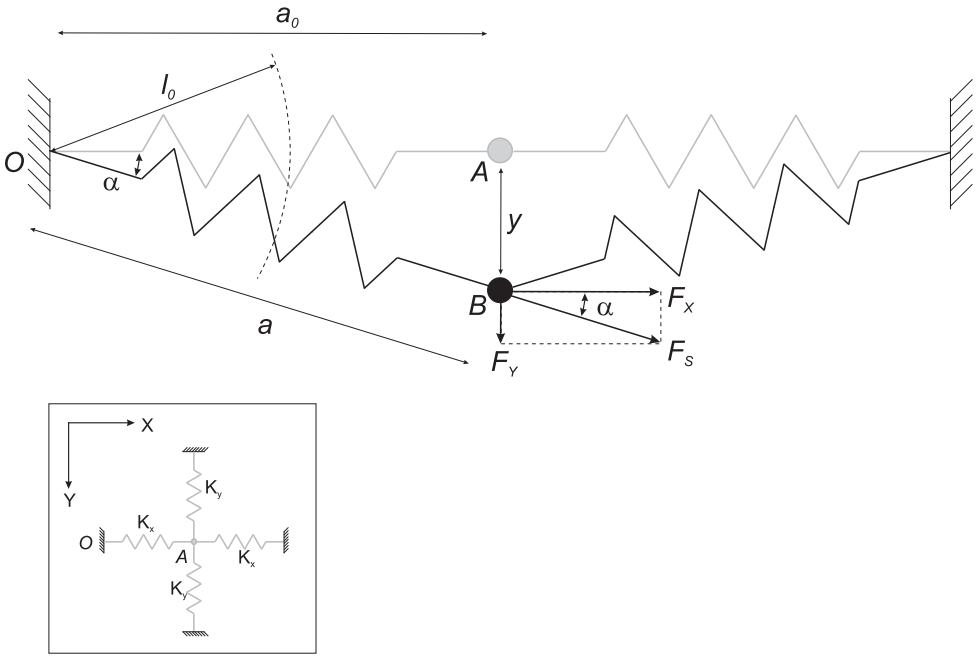

Figure D.1: *Technical spring system used for calibration, consisting of four linear springs at* 90° *angles (see inset) constituting a static equilibrium (point* A*).* K_x*: stiffness of springs in* x *direction;* K_y*: stiffness of springs in* y *direction. The stiffness in one direction (either* x *or* y*) consists of a longitudinal (linear) and a tangential part. A small movement in the* y *direction is vizualized to elaborate on the stiffness contribution in the* x *direction. See Text for further explanation and derivation of the resulting stiffness field.*

The total stiffness field of the applied technical spring system at the interconnection point A (Fig. D.1, inset) equals:

$$K = \begin{bmatrix} K_{xx} & K_{xy} \\ K_{yx} & K_{yy} \end{bmatrix} \tag{D.1}$$

Since the configuration is taken to be symmetrical, no force in y direction emerges when moving in the x direction and vice versa, i.e. $K_{xy} = K_{yx} = 0$. The stiffness field is therefore only determined by the diagonal terms being:

$$\begin{aligned} K_{xx} &= \frac{\partial F_x}{\partial x} \\ K_{yy} &= \frac{\partial F_y}{\partial y} \end{aligned}$$

E.g. the stiffness K_{yy} is derived from a movement of the interconnection point in the y direction (from A to B, Fig. D.1; springs in the y direction are omitted for clarity). Similar derivation holds for the stiffness K_{xx}.

At initial lengths a_0 ($O - A$, *gray springs*)) the force exerted by one spring in the x direction (x spring) F_{s_0} equals:

$$F_{s_0} = K_x(a_0 - l_0)$$

with K_x the stiffness of the x springs and l_0 the length at zero spring force. In the case where the connection point is moved from A to B, the x spring forces increase to:

$$\begin{aligned} F_s &= F_{s_0} + K_x(a - a_0) \\ &= K_x(a_0 - l_0) + K_x(a - a_0) \\ &= K_x(a - l_0) \end{aligned} \tag{D.2}$$

with a the the x spring length ($O - B$). In point B, the force in the y direction F_y equals:

$$F_y = 2K_y y + F_s \sin\alpha \tag{D.3}$$

with K_y the stiffness of the y springs. Substituting Eq. D.2 (for both x springs) into Eq. D.3 gives:

$$F_y = 2K_y y + 2K_x(a - l_0)\sin\alpha \tag{D.4}$$

Expressing a and $\sin\alpha$ into the initial length a_0 and the displacement y:

$$\begin{aligned} a &= \sqrt{a_0^2 + y^2} \\ \sin\alpha &= \frac{y}{a} = \frac{y}{\sqrt{a_0^2 + y^2}} \end{aligned}$$

and substituting into Eq. D.4 gives:

$$\begin{aligned} F_y &= 2K_y y + 2K_x(\sqrt{a_0^2+y^2} - l_0)\frac{y}{\sqrt{a_0^2+y^2}} \\ &= 2\left[K_y y + K_x y - K_x l_0 \frac{y}{\sqrt{a_0^2+y^2}}\right] \end{aligned} \tag{D.5}$$

Partial derivation of Eq. D.5 around $y = 0$ results in the stiffness K_{yy}:

$$\begin{aligned} \left.\frac{\partial F_y}{\partial y}\right|_{y=0} &= 2\frac{\partial}{\partial y}\left[K_y y + K_x y - K_x l_0 \frac{y}{\sqrt{a_0^2+y^2}}\right] \\ &= 2\left[K_y + K_x - K_x l_0 \frac{1}{\sqrt{a_0^2+y^2}} - K_x l_0 y \frac{\partial}{\partial y}\left(\frac{1}{\sqrt{a_0^2+y^2}}\right)\right] \\ &= 2\left[K_y + K_x - K_x l_0 \frac{1}{\sqrt{a_0^2+y^2}} + K_x l_0 y^2 \left(\frac{1}{\sqrt{a_0^2+y^2}}\right)^3\right] \\ &= 2\left[K_y + K_x\left(1 - \frac{l_0}{a_0}\right)\right] \end{aligned} \tag{D.6}$$

In the case where the springs have zero initial force ($F_{s_0} = 0$) such that it is possible to let a_0 be equal to l_0, the additional stiffness of the x-springs is zero, i.e. $K_{yy} = 2K_y$. Normally, springs do have an initial force at rest length (pre-tension) such that $a_0 > l_0$ and so the x springs increase the net stiffness in the y direction.

In summary, for small displacements around the initial equilibrium position y, the stiffness field is diagonal and equal to:

$$\begin{aligned} K_{xx} &= 2\left[K_x + K_y\left(1 - \frac{l_0}{a_0}\right)\right] \\ K_{yy} &= 2\left[K_y + K_x\left(1 - \frac{l_0}{a_0}\right)\right] \end{aligned}$$

Appendix E

Three DOF Joint Model

The model describes the dynamic relation from the hand reaction force (input) to the handle position (output) in state space format. The resulting transferfunction is expressed in a 2-DOF extracorporal cartesian coordinate frame. The model part describing the NMS system is expressed in 3-DOF joint coordinates ($[\theta_s\ \theta_e\ \theta_w]$), where the subscripts s, e, and w denote the shoulder, elbow and wrist joint respectively. The following variables are used for model development (see also the blockscheme of Figure 7.4 for reference).

θ	$=$	$[\theta_s\ \theta_e\ \theta_w]^T$	joint angle
τ_e	$=$	$[\tau_{e,s}\ \tau_{e,e}\ \tau_{e,w}]^T$	joint torque (from external force)
τ_r	$=$	$[\tau_{r,s}\ \tau_{r,e}\ \tau_{r,w}]^T$	joint torque (from reflexive muscle force)
τ_m	$=$	$[\tau_{m,s}\ \tau_{m,e}\ \tau_{m,w}]^T$	joint torque (from nett muscle force)
x	$=$	$[x_x\ x_y]^T$	endpoint (handle) coordinate
f	$=$	$[f_x\ f_y]^T$	endpoint (hand) reaction
a	$=$	$[a_s\ a_e\ a_w]^T$	muscle activation (active state)
r	$=$	$[r_s\ r_e\ r_w]^T$	output Pade filter
u_r	$=$	$[u_{r,s}\ u_{r,e}\ u_{r,w}]^T$	reflexive excitation
u_d	$=$	$[u_{d,s}\ u_{d,e}\ u_{d,w}]^T$	delayed reflexive excitation
d	$=$	$[d_x\ d_y]^T$	endpoint force disturbance

where ^{T} denotes the transpose. All model parameters are structured in matrix notation, being:

$$B_h = \begin{bmatrix} b_h & 0 \\ 0 & b_h \end{bmatrix} \quad \text{hand grip viscosity}$$

$$K_h = \begin{bmatrix} k_h & 0 \\ 0 & k_h \end{bmatrix} \quad \text{hand grip elasticity}$$

$$B = \begin{bmatrix} b_s & b_{se} & 0 \\ b_{se} & b_e & b_{ew} \\ 0 & b_{ew} & b_w \end{bmatrix} \quad \text{intrinsic joint damping}$$

$$K = \begin{bmatrix} k_s & k_{se} & 0 \\ k_{se} & k_e & k_{ew} \\ 0 & k_{ew} & k_w \end{bmatrix} \quad \text{intrinsic joint stiffness}$$

$$K_a = \begin{bmatrix} ka_s & ka_{se} & 0 \\ ka_{se} & ka_e & ka_{ew} \\ 0 & ka_{ew} & ka_w \end{bmatrix} \quad \text{acceleration feedback gain}$$

$$K_v = \begin{bmatrix} kv_s & kv_{se} & 0 \\ kv_{se} & kv_e & kv_{ew} \\ 0 & kv_{ew} & kv_w \end{bmatrix} \quad \text{velocity feedback gain}$$

$$K_p = \begin{bmatrix} kp_s & kp_{se} & 0 \\ kp_{se} & kp_e & kp_{ew} \\ 0 & kp_{ew} & kp_w \end{bmatrix} \quad \text{position feedback gain}$$

$$K_g = \begin{bmatrix} kg_s & kg_{se} & 0 \\ kg_{se} & kg_e & kg_{ew} \\ 0 & kg_{ew} & kg_w \end{bmatrix} \quad \text{force feedback gain}$$

The above matrices describe properties on the joint level. The corresponding matrix notation (only given for the stiffness) for the joint muscle properties (contributed by muscle groups) equals (Hogan, 1985a):

$$K = \begin{bmatrix} k_s^* + k_{se} & k_{se} & 0 \\ k_{se} & k_e^* + k_{se} + k_{ew} & k_{ew} \\ 0 & k_{ew} & k_w^* + k_{ew} \end{bmatrix} \tag{E.1}$$

where the star (*) denotes the single-joint muscle stiffness. Single-joint muscle properties follow from the estimated single-joint and two-joint properties: $k_s^* = k_s - k_{se}$, $k_e^* = k_e - k_{se} - k_{ew}$ and $k_w^* = k_w - k_{ew}$.

The model consists of four connected subsystems, being: intrinsic, activation, neural delay and the environment.

Intrinsic musculoskeleton

The explicit equation of motion of the three-joint system of the arm in state space is:

$$\begin{bmatrix} \ddot{\theta} \\ \dot{\theta} \end{bmatrix} = A_i \begin{bmatrix} \dot{\theta} \\ \theta \end{bmatrix} + B_i(\tau_e - \tau_r) \tag{E.2}$$

with A_i the system matrix containing the rotational joint dynamics including the stiffness, damping and inertial properties and B_i the input matrix. The inputs τ_e and τ_r are the joint torque due to external forces from the hand and the reflexive forces respectively. The derivation of the equations of motion is elaborated in the following.

The joint inertia is derived by transformation of the motion of mass from the cartesian frame to the joint frame using the transformation matrix from joint to cartesian space and described in the following.

Lets define the following distances of the centre of mass (COM) of the segments with respect to the joint positions:

$$\begin{aligned} l_{m,1} &= l_{hume}/2 \\ l_{m,2} &= l_{fore}/2 \\ l_{m,3} &= l_{hand}/1.25 \end{aligned}$$

with l_{hume}, l_{fore} and l_{hand} the segment length of humerus, forcearm and hand respectively. The following rotation matrices are used. Rotation of the humerus with respect to the frontal plane, R1:

$$R1 = \begin{bmatrix} \cos\theta_s & -\sin\theta_s \\ \sin\theta_s & \cos\theta_s \end{bmatrix} \tag{E.3}$$

Rotation of the forearm with respect to the humerus, R2:

$$R2 = \begin{bmatrix} \cos\theta_e & -\sin\theta_e \\ \sin\theta_e & \cos\theta_e \end{bmatrix} \tag{E.4}$$

Rotation of the hand with respect to the forearm, R3:

$$R3 = \begin{bmatrix} \cos\theta_w & -\sin\theta_w \\ \sin\theta_w & \cos\theta_w \end{bmatrix} \tag{E.5}$$

with θ_s, θ_e and θ_w the angle of the shoulder, elbow and wrist joint respectively. Then, the position of the COM of all segments becomes:

$$\begin{aligned} x_{m,1} &= x_s + R1 \begin{bmatrix} l_{m,1} \\ 0 \end{bmatrix} \\ x_{m,2} &= x_e + R1 * R2 \begin{bmatrix} l_{m,2} \\ 0 \end{bmatrix} \\ x_{m,3} &= x_w + R1 * R2 * R3 \begin{bmatrix} l_{m,3} \\ 0 \end{bmatrix} \end{aligned}$$

with x_s, x_e and x_w the position of the shoulder joint, elbow joint and wrist joint respectively, being:

$$\begin{aligned} x_s &= \begin{bmatrix} 0 \\ 0 \end{bmatrix} \\ x_e &= R1 \begin{bmatrix} l_{hume} \\ 0 \end{bmatrix} \\ x_w &= l_e + R1R2 \begin{bmatrix} l_{fore} \\ 0 \end{bmatrix} \end{aligned}$$

Take a vector T containing the COM of all segments:

$$T = \begin{bmatrix} x_{m,1} \\ x_{m,2} \\ x_{m,3} \end{bmatrix} \tag{E.6}$$

The velocity vector of the COMs, $\dot{x}_m$, equals:

$$\dot{x}_m = \dot{T}(q) = \frac{\partial T(q)}{\partial q}\dot{q} \tag{E.7}$$

with

$$\dot{x}_m = \begin{bmatrix} \dot{x}_{m,1} \\ \dot{x}_{m,2} \\ \dot{x}_{m,3} \end{bmatrix}$$

the vector of COM velocities and

$$q = \begin{bmatrix} \theta_s \\ \theta_e \\ \theta_w \end{bmatrix} \tag{E.8}$$

the vector of joint angles. Eq. (E.7) relates motions of mass from the cartesian frame to the joint frame. Differentiating once more gives:

$$\ddot{x}_m = \frac{\partial \partial T(q)}{\partial q \partial q}\dot{q}\dot{q} + \frac{\partial T(q)}{\partial q}\ddot{q} \tag{E.9}$$

Now take the Newton-Euler equation of motion, applied to the segmental masses of each linkage:

$$\sum_{k=1}^{k=3} F_k - M_x \ddot{x}_m = 0 \tag{E.10}$$

with F_k the force acting at the COM of segment k and M the (diagonal) mass matrix:

$$M = \begin{bmatrix} m_{hume} & 0 & 0 & 0 & 0 & 0 \\ 0 & m_{hume} & 0 & 0 & 0 & 0 \\ 0 & 0 & m_{fore} & 0 & 0 & 0 \\ 0 & 0 & 0 & m_{fore} & 0 & 0 \\ 0 & 0 & 0 & 0 & m_{hand} & 0 \\ 0 & 0 & 0 & 0 & 0 & m_{hand} \end{bmatrix}$$

where m_{hume}, m_{fore} and m_{hand} the mass of the humerus, forearm and hand respectively. Substitution of $\ddot{x}_m$ (Eq. E.9) into Eq. (E.10) gives:

$$\sum_{k=1}^{k=3} F_k - M_x \left(\frac{\partial T_q}{\partial q} \dot{q}\dot{q} + T_q \ddot{q} \right) = 0 \tag{E.11}$$

with $T_q = \frac{\partial T(q)}{\partial q}$. Premultiplication of Eq. (E.11) by T_q^T and rearranging gives:

$$T_q^T M_x T_q \ddot{q} = T_q^T \sum_{k=1}^{k=3} F_k - T_q^T M_x \frac{\partial T_q}{\partial q} \dot{q}\dot{q} \tag{E.12}$$

Since only small variations around a fixed working point were studied, the non-linear velocity terms (centrifugal and Coriolis) were neglected. Additionally, the mapping of the angular velocities to the endpoint velocities T_q was taken constant, corresponding to the mean joint angles. Finally, the intrinsic stiffness and damping properties are included leading to the final linear intrinsic model:

$$\ddot{q} = \left(T_q^T M_x T_q \right)^{-1} T_q^T \sum_{k=1}^{k=3} F_k - \left(T_q^T M_x T_q \right)^{-1} \left(B\dot{q} + Kq \right) \tag{E.13}$$

The first term on the right-hand side of Eq.(E.13) contains the input from which the (6×1) input matrix B_i follows, where $T_q^T \sum_{k=1}^{k=3} F_k = \tau_e - \tau_r$. The second term on the right-hand side contains the system dynamics from which the (6×6) system matrix A_i is obtained.

Activation dynamics

$$\begin{aligned} \begin{bmatrix} \ddot{a} \\ \dot{a} \end{bmatrix} &= A_{act} \begin{bmatrix} \dot{a} \\ a \end{bmatrix} + B_{act} u_d \\ \tau_r &= C_{act} \begin{bmatrix} \dot{a} \\ a \end{bmatrix} \end{aligned} \tag{E.14}$$

and similar filters for the elbow and wrist.

The activation dynamics were modelled as a second order Butterworth filter for each joint. E.g. for the shoulder joint the filter was:

$$\frac{a_s(s)}{\tau_s(s)} = \frac{1}{\frac{1}{\omega_0^2}s^2 + \frac{2\beta}{\omega_0}s + 1}$$

where $\omega_0 = 2\pi f_{act,s}$ is the cutt-off frequency and $\beta = \frac{1}{2}\sqrt{2}$ the relative damping. The state-space model matrices are:

$$\begin{aligned} A_{acts,s} &= \begin{bmatrix} -2\beta\omega_0 & -\omega_0^2 \\ 1 & 0 \end{bmatrix} \\ B_{acts,s} &= \begin{bmatrix} \omega_0^2 \\ 0 \end{bmatrix} \\ C_{acts,s} &= \begin{bmatrix} 0 & 1 \end{bmatrix} \\ D_{acts,s} &= 0 \end{aligned} \tag{E.15}$$

Corresponding state-space matrices were obtained for the other joints and taken together separately as partitions of one state space model (Eq. E.14). The input of the activation model u_d is the output of the model of the neural time delays.

Neural delay

Neural time delays are modelled by third order Pade approximations.

$$\begin{bmatrix} \dddot{r} \\ \ddot{r} \\ \dot{r} \end{bmatrix} = A_{del} \begin{bmatrix} \ddot{r} \\ \dot{r} \\ r \end{bmatrix} + B_{del} u_r \tag{E.16}$$

$$u_d = C_{del} \begin{bmatrix} \ddot{r} \\ \dot{r} \\ r \end{bmatrix} + D_{del} u_r \tag{E.17}$$

where the input u_r is the 'reflexive joint torque' representing the output of the muscle spindles and Golgi tendon organs:

$$u_r = [K_a \; K_v \; K_p] \begin{bmatrix} \ddot{\theta} \\ \dot{\theta} \\ \theta \end{bmatrix} - K_g \tau_m$$

with

$$\begin{aligned} \tau_m &= -\tau_r - \tau_i \\ &= -C_{act} \begin{bmatrix} \dot{a} \\ a \end{bmatrix} - [B \; K] \begin{bmatrix} \dot{\theta} \\ \theta \end{bmatrix} \end{aligned} \tag{E.18}$$

The three Pade filters are taken together as separate partitions of the state space model (Eq. E.17).

Environment

$$\begin{bmatrix} \ddot{x} \\ \dot{x} \end{bmatrix} = A_{env} \begin{bmatrix} \dot{x} \\ x \end{bmatrix} + B_{env}(d - f) \tag{E.19}$$

with

$$\begin{aligned} A_{env} &= \begin{bmatrix} -B_e M_e^{-1} & -K_e M_e^{-1} \\ I & O \end{bmatrix} \\ B_{env} &= \begin{bmatrix} M_e^{-1} \\ O \end{bmatrix} \\ C_{env} &= \begin{bmatrix} O & I \end{bmatrix} \\ D_{env} &= O \end{aligned}$$

where

$$\begin{aligned} I &= \begin{bmatrix} 1 & 0 \\ 0 & 1 \end{bmatrix} \\ O &= \begin{bmatrix} 0 & 0 \\ 0 & 0 \end{bmatrix} \end{aligned} \tag{E.20}$$

Algebraic equations used to link the intrinsic arm model to the environment:

$$\tau_e = J^T f \tag{E.21}$$

$$\begin{aligned} f &= B_h(\dot{x} - J\dot{q}) + K_h(x - Jq) \\ &= [-B_h J \; -K_h J] \begin{bmatrix} \dot{q} \\ q \end{bmatrix} + [B_h \; K_h] \begin{bmatrix} \dot{x} \\ x \end{bmatrix} \end{aligned} \tag{E.22}$$

J is the Jacobian:

$$J = \begin{bmatrix} -l_h s_s - l_f s_{se} - l_w s_{sew} & -l_f s_{se} - l_w s_{sew} & -l_w s_{sew} \\ l_h c_s + l_e c_{se} + l_w c_{sew} & l_e c_{se} + l_w c_{sew} & l_w c_{sew} \end{bmatrix} \tag{E.23}$$

with

$$\begin{aligned} s_s &= \sin\bar{\theta}_s \\ s_{se} &= \sin(\bar{\theta}_s + \bar{\theta}_e) \\ s_{sew} &= \sin(\bar{\theta}_s + \bar{\theta}_e + \bar{\theta}_w) \\ c_s &= \cos\bar{\theta}_s \\ c_{se} &= \cos(\bar{\theta}_s + \bar{\theta}_e) \\ c_{sew} &= \cos(\bar{\theta}_s + \bar{\theta}_e) + \bar{\theta}_w \end{aligned}$$

and $\bar{\theta}_s$, $\bar{\theta}_e$ and $\bar{\theta}_w$ the mean shoulder, elbow and wrist angle respectively.

The final arm-environment model has the structure of:

$$\begin{aligned} \dot{z} &= Az + Bd \\ x &= Cz + Df \end{aligned} \tag{E.24}$$

with A (25×25) the system matrix, B (25×2) the input matrix, C (2×25) the output matrix and D (2×2 null matrix) the throughput matrix. These matrices follow after elaboration on Eqs (E.2)-(E.23). The state vector z (25×1) equals:

$$z = [\dot{\theta}\ \theta\ \dot{a}\ a\ \ddot{p}\ \dot{p}\ p\ \dot{x}\ x]^T \tag{E.25}$$

The multivariable transfer function (MTF) of the combined arm-environment model is:

$$H(s)_{tot} = C[sI - A]B + D \tag{E.26}$$

The MTF of the arm only is obtained by adjusting the values of the external dynamics (A_{env} and B_{env}), by setting M_e at a small value and B_e and K_e to zero.

References

Abbink D. The effect of different tasks and perturbation signals on human arm posture control. Report nr. S-965, Literature Survey, Delft University of Technology, 2001

Abbink D. The effect of position and force tasks on human arm admittance. Report nr. A-965, Master Thesis, Delft University of Technology, 2002

Acosta AM, Kirsch RF, Perreault EJ. A robotic manipulator for the characterization of two-dimensional dynamic stiffness using stochastic displacement disturbances. J Neurosci Methods 2000; 102: 177-186

Adams RJ, Hannaford B. Stable haptic interaction with virtual environments. IEEE Trans Robot Automat 1999; 15: 465:74

Agarwal GC, Gottlieb CL. Compliance of the human ankle joint. J Biomech Eng 1977; 99: 166-170

Agarwal GC, Gottlieb CL. Oscillation of the human ankle joint in response to applied sinusoidal torque on the foot. J Physiol (Lond) 1977; 268: 151-176

Akazawa K, Milner TE, Stein RB. Modulation of reflex EMG and stiffness in response to stretch of human finger muscle. J Neurophysiol 1983; 49: 16-27

Bendat JS, Piersol AG. Random data: analysis and measurement procedures, second ed. Wiley: New York, 1986

Bennett DJ, Gorassini M, Prochazka A. Catching a ball: contributions of intrinsic muscle stiffness, reflexes, and higher order responses. Can J Physiol Pharmacol 1993; 72: 525-534

Bobet J, Norman RW. Least-squares identification of the dynamic relation between the electromyogram and joint moment. J Biomech 1990; 23: 1275-1276

Brouwn GG. Posture control of the human arm. PhD thesis, Delft University of Technology, The Netherlands, 2000

Burleigh A, Horak F. Influence of instruction, prediction, and afferent sensory information on the postural organization of step initiation. J Neurophysiol 1996; 75: 1619-1628

Carter RR, Crago PE, Keith MW. Stiffness regulation by reflex action in the normal human hand. J Neurophysiol 1990; 64: 105-118

Carter RR, Crago PE, Gorman PH. Nonlinear stretch reflex interaction during cocontraction. J Neurophysiol 1993; 69: 943-952

Cathers I, O'Dwyer N, Neilson P. Dependence of stretch reflexes on amplitude and bandwidth of stretch in human wrist muscle. Exp Brain Res 1999; 129: 278-287

Crago PE, Houk JC, Hasan Z. Regulatory actions of human stretch reflex. J Neurophysiol 1976; 39: 925-935

Carignan CR, Cleary KR. Closed-loop force control for haptic simulation of virtual environments. Haptic-e 2000; 1:1-14 (http://www.haptics-e.org)

Small-signal analyses of response of mammalian muscle spindles with fusimotor stimulation and a comparison with large-signal responses. J Neurophysiol 1978; 41: 15-27

Clancy EA, Morin EL, Merletti R. Sampling, noise-reduction and amplitude estimation issues in surface electromyography. J Electromyogr Kinesiol 2002; 12: 1-16

Colgate JE. The control of dynamically interacting systems. PhD thesis, MIT Department of Mechanical Engineering, USA, August 1988

Craig JJ. Introduction to robotics, mechanics and control, second ed., Reading: Addison-Wesley, 1989

De Vlugt E. Mechanisms underlying intrinsic muscle stiffness. Report nr. S-922, Literature Survey, Delft University of Technology, 1998a

De Vlugt E. Force enhancement after stretch of actively contracting skeletal muscle fibres: a model approach based on cross-bridge dynamics, Report nr. A-922, Master Thesis Delft University of Technology, 1998b

De Vlugt E, Van der Helm FCT, Schouten AC, Brouwn GG. Analysis of the reflexive feedback control loop during posture maintenance. Biol Cybern 2001; 84: 133-141

De Vlugt E, Schouten AC, Van der Helm FCT. Adaptation of reflexive feedback during arm posture to different environments. Biol Cybern 2002; 87: 10-26 (Chapter 2)

De Vlugt E, Van der Helm FCT, Schouten AC. Closed-loop multivariable system identification for the characterization of the dynamic arm compliance using continuous force disturbances: a model study. J Neurosci Methods 2003a; 122: 123-40 (Chapter 5)

De Vlugt E, Schouten AC, Van der Helm FCT, Teerhuis PC, Brouwn GG. A force-controlled planar haptic device for movement control analysis of the human arm. J Neurosci Methods 2003b; 129: 151-168 (Chapter 6)

De Vlugt E, Van der Helm FCT. Quantification of intrinsic and reflexive muscle properties of the multi-degree-of-freedom human arm. To be submitted

Doemges F, Rack PMH. Changes in the stretch reflex of the human first dorsal interosseous muscle during different tasks. J Physiol 1992a; 447: 563-573

Doemges F, Rack PMH. Task-dependent changes in the response of human wrist joints to mechanical disturbance. J Physiol 1992b; 447: 575-585

Dolan JM, Friedman MB, Nagurka ML. Dynamic and loaded impedance components in the maintenance of human arm posture. IEEE Trans Syst Man Cybern 1993; 23: 698-709

Dufresne JR, Soechting JF, Terzuolo CA Electromyographic response to pseudo-random torque disturbances of human forearm position. Neuroscience 1978; 3: 1213-1226

Duysens J, Clarac F, Cruse H Load-regulating mechanisms in gait and posture: comparative aspects. Physiol Rev 2000; 80: 83-133

Feldman AG, Orlovsky GN. The influence of different descending systems on the tonic stretch reflex in the cat. Exp. Neurol. 1972; 37: 481-494

Gerdes VG, Happee R. The use of internal representation in fast gold-directed movements:

a modeling approach. Biol Cybern 1994; 70: 513-524

Gomi H, Kawato M. Equilibrium-point control hypothesis examined by measured arm stiffness during multijoint movement. Science 1996; 272: 117-120

Gomi H, Kawato M Human arm stiffness and equilibrium-point trajectory during multi-joint movement. Biol Cybern 1997; 76: 163-171

Gomi H, Osu R. Task-dependence viscoelasticity of human multijoint arm and its spatial characteristics for interaction with environments. J Neurosc 1998; 18: 8965-8978

Hannaford B, Jee-Hwan Ryu. Time-domain passivity control of haptic interfaces. IEEE Trans Robot Automat 2002; 18: 1-10

Hill AV. The heat of shortening and the dynamic constants of muscle. Proc R Soc Lond B Biol Sci 126: 136-195

Heintze J, Peters RM, Van der Weiden AJJ. Cascade Δp and sliding mode for hydraulic actuators. In Proceedings of the 3rd European Control Conference, Roma, Italy, 1995; 1471-77

Hoffer JA, Andreassen S. Regulation of soleus muscle stiffness in premammillary cats: intrinsic and reflex components. J Neurophysiol 1981; 45: 267-285

Hogan N. The mechanics of multi-joint posture and movement control. Biol Cybern 1985a; 52: 315-331

Hogan N. Impedance control: an approach to manipulation: Part I-Theory. J Dyn Sys Meas Con 1985b; 107(1): 1-7

Hogan N, Bizzi E, Mussa-Ivaldi FA, Flash T Controlling multijoint behavior. Exerc Sport Sci Rev 1987; 15: 153-190

Hogan N, Colgate E. Stability problems in contact tasks. In The Robotics Review, O Khatib, JJ Craig and T Lozano-Perez (Eds). Cambridge, MA: MIT Press, 1989; 339-48

Houk JC, Henneman E Responses of golgi tendon organs to active contractions of the soleus muscle of the cat. J Neurophysiol 1966; 30: 466-481

Houk JC. Participation of reflex mechanisms and reaction-time processes in the compensatory adjustments to mechanical disturbances. Cerebral Motor Control in Man: Long Loop Mechanisms. Prog clin Neurophysiol Ed. Desmedt JE 1978; 4: 193-215

Jaeger RJ, Gottlieb GL, Agarwal GC. Myoelectric responses at flexors and extensors of human wrist to step torque perturbations. J Neurophysiol 1982; 48: 388-402

Jankowska E. Interneurol relay in spinal pathways from proprioceptors. Prog Neurobiol 1992; 38: 335-378

Jenkins GM, Watts DG. Spectral analysis and its applications. Holden Day: San Francisco, 1968

Kandel ER, Schwartz JH, Jessell TM. Principles of neural science. Fourth edition McGraw-Hill, 2000

Kanosue K, Akazawa K, Fujii K. Modulation of reflex activity of motor units in response to stretch of a human finger muscle. Jpn J Physiol 1983; 33: 995-1009

Karniel A and Mussa-Ivaldi FA Does the motor control system use multiple models and

contact switching to cope with a variable environment. Exp Brain Res 2002; 143: 520-524

Kearney RE, Hunter IW. System identification of human joint dynamics. CRC Crit Rev Biomed Eng 1990; 18: 55-87

Kearney RE, Stein RB, Parameswaran L. Identification of intrinsic and reflex contributions to human ankle stiffness dynamics. IEEE Trans Biomed Eng 1997; 44: 493-504

Kessel RG, Kardon RH Tissues and organs, a text-atlas of scanning electron microscopy. WH Freeman, New York 1979

Kirsch RF, Kearney RE, MacNeil JB. Identification of time-varying dynamics of the human triceps surae stretch reflex. Exp Brain Res 1993; 97: 115-127

Kirsch FK, Boskov D, Rymer WZ. Muscle stiffness during transient and continuous movements of cat muscle: disturbance characteristics and physiological relevance. IEEE Trans Biomed Eng 1994; 41: 758-770

Kukreja SL, Galiana HL, Kearney RE. NARMAX representation and identification of ankle dynamics. IEEE Trans Biomed Eng 2003; 50: 70-81

Lacquaniti F, Licata F, Soechting, JF. The mechanical behavior of the human forearm in response to transient perturbations. Biol Cybern 1982; 44: 67-77

Lacquaniti F, Soechting JF. Simulation studies on the control of posture and movement in a multi-jointed limb. Biol Cybern 1986; 54: 367-378

Lee RG, Tatton WG. Motor responses to sudden limb displacements in primates with specific CNS lesions and in human patients with motor system disorders. Can J Neurol Sci 1975; 2: 285-293

Ljung L. System Identification - Theory For the User, second ed. PTR Prentice Hall: Upper Saddle River, N.J., 1999

Van Lunteren T. Identification of human operator describing function models with one or two inputs in closed loop systems. PhD thesis, Delft University of Technology, The Netherlands, 1979

Maciejowski JJ. Multivariable feedback design. Harlow: Addison-Wesley, 1989

Matthews PBC. Evolving views on the internal operation and functional role of the muscle spindle. J Physiol (London) 1981; 320: 1-30

Mathews PBC. Observations on the automatic compensation of reflex gain on varying the pre-existing level of motor discharge in man. J Physiol (Lond) 1986; 374: 73-90

McIntyre J, Mussa-Ivaldi FA, Bizzi E. The control of stable posture in the multijoint arm. Exp Brain Res 1996; 110: 248-64

McRuer DT, Jex HR. A review of quasi-linear pilot models. IEEE Trans Human Factors Electr 1967; 8: 231-249

Milner TE, Cloutier C. Compensation for mechanically unstable loading in voluntary wrist movement. Exp Brain Res 1993; 94: 522-532

Mirbagheri MM, Barbeau H, Kearney RE Intrinsic and reflex contributions to human ankle stiffness: variation with activation level and position. Exp Brain Res 2000; 135: 423-436

Mirbagheri MM, Barbeau H, Ladouceur M, Kearney RE. Intrinsic and reflex stiffness in normal and spastic, spinal cord injured subjects. Exp Brain Res 2001; 141: 446-459

Mussa-Ivaldi FA, Hogan N, Bizzi E. Neural, mechanical, and geometric factors subserving arm posture in humans. J Neurosci 1985; 5: 2732-2743

Nichols TR, Houk JC. Improvement in linearity and regulation of stiffness that results from actions of stretch reflex. J Neurophysiol 1976; 39: 119-142

Olney SJ, Winter DA. Predictions of knee and ankle moments of force in walking from EMG and kinematic data. J Biomech 1985; 18: 9-20

Peeters F, Pintelon R, Schoukens J, Rolain Y. Identification of rotor-bearing systems in the frequency domain, Part I: Estimation of frequency response functions. Mech Syst Signal Pr 2001; 15(4): 759-773

Perreault EJ, Kirsch RF, Acosta AM. Multiple-input multiple-output system identification for characterization of limb stiffness dymanics. Biol Cybern 1999; 80: 327-337

Perreault EJ, Crago PE, Kirsch RF. Estimation of intrinsic and reflex contributions to muscle dynamics: a modeling studyness dymanics. IEEE Trans Biomed Eng 2000; 47: 1413-1421

Perreault EJ, Kirsch RF, Crago PE. Effects of voluntary force generation on the elastic components of endpoint stiffness. Exp Brain Res 2001; 141: 312-323

Perreault EJ, Kirsch RF, Crago PE. Voluntary control of static endpoint stiffness during force regulation tasks. J Neurophysiol 2002; 87: 2808-16

Pintelon R, Guillaume P, Rolain Y, Schoukens J, and Van Hamme H. Parametric identification of transfer functions in the frequency domain - A survey. IEEE Trans Autom Contr 1994; 39: 2245-2260

Pintelon R, Schoukens J. System identification: a frequency domain approach. 2001 IEEE Press, New York

Poppele RE. An analysis of muscle spindle behavior using randomly applied stretches. Neuroscience 1981; 6: 1157-1165

Potvin JR, Norman RW, McGill SM. Mechanically corrected EMG for the continuous estimation of erector spinae muscle loading during repetitive lifting. Eur J Appl Physiol 1996; 74: 119-132

Rozendaal LA. Stability of the shoulder. PhD thesis, Delft University of Technology, The Netherlands, 1997

Rudomin P. Presynaptic selection of afferent inflow in the spinal cord. J Physiol (Paris) 1999; 93: 329-347

Schaafsma A, Otten E, Van Willigen J. D. A muscle spindle model for primary afferent firing based on a simulation of intrafusal mechanical events. J Neurophysiol 1991; 65: 1297-1312

Schoukens J, Guillaume P, Pintelon R. Design of broadband excitation signals. In Godfrey K, editor. Perturbation Signals for System Identification. Prentice-Hall: Englewood Cliffs, NJ, 1993; 126-159

Schouten AC, De Vlugt E, Van der Helm FCT, Brouwn GG. Optimal posture control of a musculo-skeletal arm model. Biol Cybern 2001; 84: 143-152

Schouten AC, Van de Beek WJT, Van Hilten JJ, Van der Helm FCT. Proprioceptive reflexes in patients with Reflex Sympathetic Dystrophy. Exp Brain Res 2003a; 151: 1-8

Schouten AC, De Vlugt E, Van der Helm FCT. Design of perturbation signals to improve the signal-to-noise ratio in electromyography during human postural control. To be submitted

Schouten AC, De Vlugt E, Van Hilten JJ, Van der Helm FCT. Quantifying reflexes with mechanical admittance and reflexive impedance. To be submitted, (Chapter 3)

Schouten AC, Zwaan BCP, Van der Helm FCT Quantifying proprioceptive reflexes in the human wrist joint. To be submitted

Schouten AC. Proprioceptive reflexes and neurological disorders. PhD thesis, Delft University of Technology, The Netherlands, 2004

Shadmehr R, Arbib M A. A mathematical analysis of the force-stiffness characteristics of muscles in control of a single joint system. Biol Cybern 1992; 66: 463-477

Shadmehr R, Brashers-Krug T. Functional stages in the formation of human long-term motor memory. J Neorosci 1997; 17: 409-19

Smeets JB, Erkelens CJ. Dependence of autogenic and heterogenic stretch reflexes on pre-load activity in the human arm. J Physiol (Lond) 1991; 440: 455-65

Smith MA, Brandt J, Shadmehr R. Motor disorder in Huntington's disease begins as a dysfunction in error feedback control. Nature 2000; 403: 544-549

Soechting JF, Dufresne JR. An evaluation of nonlinearities in the motor output response to applied torque perturbations in man. Biol Cybern 1980; 36: 63-71

Stein RB, Capaday C (1988) The modulation of human reflexes during functional motor tasks. Trend Neurosci 11: 328-332

Stein RB, Kearney RE. Nonlinear behavior of muscle reflexes at the human ankle joint. J Neurophysiol 1995; 73: 65-72

Stienen AHA, Schouten AC, Van der Helm FCT. Integrating a biological neural network into a musculoskeletal model to analyse postural control reflex modulation. Submitted to Biological Cybernetics

Strang G. Introduction to linear algebra. Wellesley-Cambridge Press, Wellesley 1998

Stroeve S. Impedance characteristics of a neuromusculoskeletal model of the human arm I. Posture control. Biol Cybern 1999 81: 475-494

Tax AA, Denier van der Gon JJ, Erkelens CJ. Differences in coordination of elbow flexor muscles in force tasks and in movement tasks. Exp Brain Res 1990; 81 :567-572

Toft E, Sinkjær T, Andreassen S, Larsen K. Mechanical and electromyographic responses to stretch of the human ankle extensors. J Neurophysiol 1991; 65: 1402-1410

Toft E, Sinkjaer T. H-reflex changes during contractions of the ankle extensors in spastic patients. Acta Neurol Scand 1993; 88: 327-333

Tsuji T, Morasso PG, Goto K, Ito K. Hand impedance characteristics during maintained posture. Biol Cybern 1995; 72: 475-485

Van Bolhuis BM, Gielen CC. The relative activation of elbow-flexor muscles in isometric

flexion and in flexion/extension movements. J Biomech 1997; 30: 803-811

Van der Helm FCT, Veeger HE, Pronk GMV, Van der Woude LH, Rozendal RH. Geometry parameters for musculoskeletal modelling of the shoulder system. J Biomech 1992; 25: 129-44

Van der Helm FCT. A finite element musculoskeletal model of the shoulder mechanism. J Biomech 1994; 27: 551-569

Van der Helm FCT, Schouten AC, De Vlugt E, Brouwn GG. Identification of intrinsic and reflexive components of human arm dynamics during postural control. J Neurosci Methods 2002; 119: 1-14

Van der Kooij H, Jacobs R, Koopman B, Grootenboer H A multisensory integration model of human stance control. Biol Cybern 1999; 80: 299-308

Van der Linden GW. High performance robust manipulator motion control. PhD thesis, Delft University of Technology, The Netherlands, 1997

Van Groeningen CJ, Erkelens CJ. Task-dependent differences between mono- and bi-articular heads of the triceps brachii muscle. Exp Brain Res 1994; 100: 345-352

Welch PD. The use of fast fourier transform for the estimation of power spectra: a method based on time averaging over short, modified periodograms. IEEE Trans Audio Electroacoustics 1967; 15: 70-73

Winters JM, Stark L. Analysis of fundamental human movement patterns through the use of in-depth antagonistic muscle models. IEEE Trans Biomed Eng 1985; 32: 826-839

Winters J, Stark L, Seif-Naraghi A. An analysis of musculoskeletal system impedance. J Biomech 1988; 21: 1011-1025

Won J, Hogan N. Stability properties of human reaching movements. Exp Brain Res 1995; 107: 125-36

Zhang LQ, Rymer WZ. Simultaneous and nonlinear identification of mechanical and reflex properties of human elbow joint muscles. IEEE Trans Biomed Eng 1997; 44: 1192-1209.

Zahalak GI, Pramod R. Myoelectric response of the human triceps brachii to displacement-controlled oscillations of the forearm. Exp Brain Res 1985; 58: 305-317

Summary

In this thesis, experimental and analytical techniques are developed to quantify the properties of spinal reflexes that are part of the human neuromuscular (NMS) system. Spinal reflexes are important for the maintenance of postures by sending information of the stretch and stretch rate of the muscles to the central nervous system (CNS). From a control theoretical point of view it is shown that reflexes are effective in suppressing undesired displacements that result from external force disturbances. By obtaining quantitative measures of the reflexive system, new fundamental knowledge is obtained about the functioning of the human motion control system. These measures are very helpful in explaining movement irregularities originating from neurological disorders.

Research was embedded in the Man Machine Systems group at the Delft University of Technology. This research group has an established reputation in biomechanics of the upper extremities, from fundamental issues to clinical applications. This was the reason why technique development was focused to the reflex system of the human arm. The techniques are not restricted to the arm and can be applied to any (bio)mechanical system.

Spinal reflexes were quantified in vivo from measurements of the hand force and hand position. For this purpose, continuous random force perturbations were applied to the hand by haptic manipulators while the subject had to minimize the hand displacements that resulted from these perturbations. The dynamic relation between the hand force and hand position, called the endpoint admittance, was identified as a frequency response function (FRF) comprising the contributions from intrinsic and reflexive properties. These properties were obtained as the parameters of a NMS model that was fitted onto the endpoint admittance.

The innovation of this methodology is that spinal reflexes can be studied from in vivo experiments while the subject performs a natural motion task. Spinal reflex control gains can be explained functionally by analyzing their effect onto the task performance, i.e. the endpoint admittance.

Humans continuously interact with the environment by means of hand contact. Objects are grasped, moved and hold into different positions for many purposes. Task performance and mechanical stability are properties that are crucial to posture control and are determined by the dynamics of both the arm and the object. Therefore, it was investigated if the reflex system adapts to mechanical properties of the environment it interacts with. High reflex gains tend to destabilize the joint

due to time delays from neural signal transport. Therefore, an external damper was simulated by the haptic device to determine if the CNS takes advantage of the increased stability margins by increasing the strength of the reflex system. Force perturbations were applied to the hand in one direction resulting in small one degree-of-freedom (DOF) rotations of the shoulder. It was found that the reflexive length feedback gain increased strongly with external damping. Model optimizations suggested that the length feedback gain was optimal as to maximize performance at minimum reflexive control effort.

In the next study, electromyography (EMG) was used as an additional measurement to identify the reflexive impedance, being the dynamic relationship between hand position and EMG. The advantage of using the reflexive impedance was that intrinsic and reflexive properties could be quantified without the need for an a priori assumption to separate them. In the previous studies, such an assumption was necessary. Furthermore, the NMS model was extended by an acceleration feedback term.

An important result was that position and velocity feedback gains were larger when the force disturbance contained only low frequencies below the eigenfrequency (2-3 Hz) compared to wide bandwidth perturbation signals (0-20 Hz). Acceleration feedback decreased with external damping. It was concluded that the CNS modifies the reflexive gains to maximize the mechanical resistance while preserving sufficient stability margins of the whole arm.

To investigate if the previous findings were specific to the experimental conditions, different combinations of disturbance types and task instructions were used and their effect on the reflex system was explained. In comparison to force tasks, position tasks entailed considerably lower admittances mainly due to higher levels of muscle co-contraction. Force feedback from Golgi tendon organs was most likely present in some subjects irrespective which of the two tasks was performed. Muscle spindle feedback appeared to be reduced during force tasks and therefore seemed not functional to control endpoint force.

Studying motion control of the single (shoulder) joint was attractive because of practical simplicity. The previous single joint studies described in the first part of this thesis together with numerous others, have contributed to the fundamental understanding of neuromuscular functioning. However, single joint motions are rare under physiological conditions and do not provide the opportunity to study the complex interactions between joints that are typical of normal motor functioning. Multiple degree-of-freedom (DOF) movements are more natural and provide a richer field of study. The additional property of multiple DOF movement control is that the endpoint admittance has a spatial direction. This is beneficial when resistance in one specific direction is required.

To study multiple DOF posture control, a nonparametric identification technique was developed to estimate the multivariable endpoint admittance. Its appli-

cation and performance were tested and validated by a case study. Nonparametric estimates do not require apriori system knowledge, are fast to obtain and useful in the early stage of system identification.

To apply force disturbances in two directions, a new 2-DOF force controlled device has been build, called the ARMANDA manipulator. A general problem of force-controlled haptic devices is the occurrence of contact instability, especially when a small virtual mass is required. This negative effect was reduced by the use of a lightweight but stiff construction and a robust servo-based controller. The application of the manipulator was evaluated by an experiment with a subject performing a position maintenance task. With this device it is possible to study the adaptability of the neuromuscular system to a variety of environments, enabling a new and functional approach to the research of multiple DOF human motion control.

In the last study, a multiple DOF posture experiment was performed to quantify the intrinsic and reflexive properties of single-joint and two-joint muscles acting around the shoulder, elbow and the wrist joints during posture maintenance in the horizontal plane. A large scale NMS model was fitted onto the endpoint admittance. The latter was estimated by a parametric identification algorithm using ARX models.

Compared to the previous single joint studies (zero degrees humeral elevation), intrinsic visco-elasticity of the shoulder joint was substantially smaller during posture maintenance in the horizontal plane (90 degrees humeral elevation). This was explained from reduced moment arms of shoulder muscles acting around the gleno-humeral joint. Markedly, shoulder reflex gains were comparable to the previous single DOF studies. Apparently, reflexes compensate for the reduction of intrinsic visco-elasticity due to a reduction of muscle moment arms.

The main conclusions of this thesis are:

- Force perturbations facilitate natural posture tasks and are the key requirements for the analysis of human movement control in vivo.
- Force controlled haptic manipulators are necessary devices to apply force disturbances. The technical demands of such devices are high, requiring lightweight but stiff material and powerful actuators to avoid contact instability.
- The mechanical endpoint admittance, as a measure for the sensitivity of the arm to external forces, is the best description of underlying intrinsic and reflexive muscle properties and is identified from measurements of hand position and reaction forces that are relatively easy to obtain
- Spinal reflexes from muscle spindles (Ia-afferents) have significant contribution to the endpoint admittance that can be of the same magnitude or even larger than the contribution from intrinsic muscle visco-elasticity

- Mechanical properties of the environment and the frequency content of the force perturbation have both large effect on the reflex gains. For increasing bandwidth of the force perturbation signal, reflex gains decreased to avoid oscillation near the eigenfrequency of the arm. In the case the environment supplied sufficient damping, reflex gains were likely determined from trading-off performance (reducing endpoint admittance) against control effort (minimizing afferent control).

- Intrinsic visco-elasticity of the shoulder was smaller compared to the elbow and wrist during multiple DOF posture maintenance in the horizontal plane. A compensatory effect was found by reflexive control gains, showing the largest gains for the shoulder joint and smallest for the wrist joint. These results indicated that reflexive feedback of the shoulder joint was controlled independently of its intrinsic visco-elasticity.

The techniques developed in this thesis have been approved to reveal important functionality of the human reflex system during posture maintenance of the human arm. To attain reflex functionality over a wider range of physiological operation, interesting future research would be to identify the reflexive system during submaximal tasks.

A completely new research line for the future is the identification of reflexes during goal directed movements. The application of force perturbations with the aid of the ARMANDA manipulator facilitate the development of new identification techniques that should be able to identify the time variant properties of the NMS during movement.

Samenvatting

In dit proefschrift worden experimentele en analytische technieken ontwikkeld om de eigenschappen van spinale afferente terugkoppelbanen te kwantificeren welke deel uitmaken van het menselijke neuromusculaire systeem (NMS). Spinale terugkoppelbanen, ofwel spinale reflexen, zijn belangrijk voor o.a. houdingstaken waarbij informatie over de verlenging van skeletspieren naar het centrale zenuwstelsel (CZS) wordt gestuurd. Vanuit een regeltechnisch standpunt kan worden aangetoond dat reflexen effectief zijn voor het onderdrukken van ongewenste bewegingen ten gevolge van externe krachtverstoringen. Door het verkrijgen van een kwantitatieve maat van het reflexieve systeem zijn nieuwe fundamentele inzichten verkregen van de functie van het menselijke bewegingssysteem. Deze kennis is zeer waardevol voor het verklaren van bewegingsstoornissen welke de oorzaak zijn van neurale aandoeningen.

Het onderzoek zoals beschreven in dit proefschrift is uitgevoerd bij de sectie Mens Machine Systemen van de faculteit Werktuigbouwkunde aan de Technische Universiteit Delft. Deze onderzoeksgroep heeft een goede reputatie in o.a. de biomechanica van de schouder, reikend van fundamentele aspecten tot klinische toepassingen. Dit was de reden waarom het reflexieve systeem van de schouder en later ook die van de elleboog en de pols zijn onderzocht. De beschreven technieken zijn niet gebonden aan de arm en toepasbaar voor elk (biomechanisch) systeem.

Spinale reflexen zijn gekwantificeerd in vivo uit metingen van de hand positie en de hand reactiekracht. Hiertoe werden continue onvoorspelbare krachtverstoringen aangebracht op de hand met behulp van haptische manipulatoren terwijl de proefpersoon als taak had de verplaatsingen van de hand te minimaliseren. De dynamische relatie tussen de hand reactiekracht en de hand positie, aangeduid als de eindpunt admittantie, is geïdentificeerd en uitgedrukt als een overdrachtsfunctie in het frequentie domein. Deze overdrachtsfunctie omvat bijdragen van intrinsieke spier visco-elasticiteit en van reflexen. Kwantificatie van deze bijdragen geschiedde door het schatten van de corresponderende parameters van een model van het NMS. De schatting volgde uit de minimalisatie van het verschil tussen de werkelijke en de gemodelleerde overdrachtsfuncties. De gebruikte modellen waren in alle gevallen lineair.

Het innovatieve van deze methode is dat de functionaliteit van de reflexen kan worden bestudeerd gedurende de uitvoering van een natuurlijke houdingstaak. De bijdrage van spinale reflexen kan worden beoordeeld door analyse van het effect op de prestatie van de taakuitvoering: de eindpunt admittantie.

Mensen interacteren continu met hun omgeving door middel van hand contact. Objecten worden vastgepakt, bewogen en op een plaats gehouden voor verschillende doeleinden. Hierbij zijn de prestatie van de bewegingstaak en de mechanische stabiliteit belangrijke aspecten welke worden bepaald door de dynamische eigenschappen van zowel de menselijke arm als die van het object, ofwel de omgeving. In een eerste studie was onderzocht in hoeverre de reflexieve eigenschappen adapteren aan een veranderende omgeving. Een sterke reflexieve terugkoppeling kan de eindpunt admittantie verlagen (prestatie verbeteren) maar eveneens leiden tot mechanische instabiliteit als gevolg van de gepaard gaande tijdvertragingen door neuraal signaaltransport. Ter voorkoming van mechanische instabiliteit is de omgeving uitgevoerd als een mechanische demper. Hiermee kon worden vastgesteld of, en in hoeverre, het CZS voordeel haalt uit de toegenomen stabiliteitsmarges door gebruik van een hogere reflexieve terugkoppeling. Krachtverstoringen werden opgelegd in één richting zodanig dat kleine rotaties van het glenohumerale gewricht optraden. Het resultaat was dat de reflexieve lengte terugkoppeling sterk toenam met de omgevingsdemping. Model optimalisaties suggereerden dat de lengte terugkoppeling optimaal is waarbij de prestatie wordt afgewogen tegen de grootte van de reflexieve activiteit.

In een volgende studie is electromyografie (EMG) toegepast waarmee de reflexieve impedantie is geïdentificeerd als zijnde de dynamische overdracht tussen hand positie en het EMG van verschillende schouderspieren. Het voordeel van het gebruik van de reflexieve impedantie was dat de intrinsieke en reflexieve eigenschappen direct konden worden gekwantificeerd zonder a priori aannamen. In de vorige studie was een dergelijke aanname nodig. Verder was het NMS model uitgebreid met een term voor versnellingsterugkoppeling. Een belangrijk resultaat was dat de positie- en snelheidsterugkoppelingen sterker waren in het geval de krachtverstoringen alleen uit lage frequenties bestond, lager dan de eigenfrequentie van de arm (2-3 Hz), in vergelijking met breedbandige verstoringen (0-20 Hz). Versnellingsterugkoppeling nam af met externe demping. In overeenstemming met de vorige studie is geconcludeerd dat het CZS de grootte van de reflexieve terugkoppeling maximaliseerd om een maximale weerstand tegen externe verstoringen te bieden terwijl de mechanische stabiliteitsmarges van de arm worden behouden.

Om vast te stellen of de vorige bevindingen specifiek waren voor de toegepaste experimentele condities moesten de proefpersonen in de volgende studie zowel een kracht- als een positietaak uitvoeren, en werden naast kracht- ook positieverstoringen opgelegd. Vergeleken met de krachttaak (houdt de kracht zo goed mogelijk constant) was de admittantie significant lager voor de positietaak. Dit was vooral het gevolg van een hoger gemiddeld cocontractie niveau. De modellen in deze studie waren uitgebreid met krachtterugkoppeling welke de functie van de Golgi peesorgaantjes beschrijft. Door deze uitbreiding was een eenduidige kwantificatie van de intrinsieke en reflexieve parameters niet meer mogelijk. Modelsimulaties

suggereerden dat krachtterugkoppeling aanwezig was voor een aantal proefpersonen, ongeacht de taak. Lengte en snelheidsterugkoppeling waren zeer waarschijnlijk gering gedurende het uitvoeren van de krachttaak waaruit geconcludeerd kan worden dat spierspoeltjes niet erg functioneel zijn om kracht te regelen.

Het bestuderen van de menselijke bewegingssturing van één (schouder) gewricht was aantrekkelijk vanwege de praktische eenvoud. De vorige studies, zoals beschreven in dit proefschrift, hebben samen met andere bijgedragen aan het begrip van de functionaliteit van het reflexieve systeem. Echter, beweging is zelden het resultaat van één gewricht en dergelijke studies geven niet de mogelijkheid om complexere bewegingen door meerdere gewrichten te analyseren. Meervoudige graad-van-vrijheid bewegingen zijn natuurlijker en verschaffen een rijker veld van studie. Een belangrijke eigenschap van meervoudige graad-van-vrijheid bewegingen is dat de eindpunt admittantie een spatiële afhankelijkheid heeft. Dit is voordelig indien in de éne richting een grotere mechanische weerstand is gewenst dan in de andere. Om meervoudige graad-van-vrijheid bewegingen (tijdens houding) te bestuderen is een niet-parametrische identificatietechniek ontwikkeld op basis van bestaande kennis waarmee de multi-ingang multi-uitgang admittantie kan worden geïdentificeerd. De toepassing en nauwkeurigheid van de techniek is getest en gevalideerd.

Om krachtverstoringen toe te passen in twee verschillende richtingen is een nieuwe twee graden-van-vrijheid krachtgestuurde manipulator ontwikkeld, de zogenoemde ARMANDA manipulator. Een algemeen bekend probleem van krachtgestuurde manipulatoren is het optreden van contact instabiliteit wanneer de eindeffector (het handvat) stevig wordt beetgepakt. Met name wanneer de manipulator een kleine virtuele belasting dient te zijn, wat in dit geval gewenst is, is het gevaar voor instabiliteit het grootst. Dit negatieve effect is verkleind door gebruik van direct aangedreven hydraulische motoren, een sterke lichtgewicht constructie en een robuuste servoregelaar. Met de ARMANDA manipulator is het mogelijk om de functionaliteit van het NMS tijdens complexere houdingstaken te bestuderen.

In de laatste studie is een drie graden-van-vrijheid houdingsexperiment uitgevoerd waarmee de intrinsieke en reflexieve eigenschappen van mono- en bi-articulaire spieren rond het schouder-, elleboog- en polsgewricht zijn gekwantificeerd. De bewegingen van de arm waren gelimiteerd in een horizontaal vlak. De eindpunt admittantie was geïdentificeerd in het tijd-domein met behulp van ARX modellen. Een large-scale NMS model was gebruikt waarvan de parameters zijn gekwantificeerd.

In vergelijking met de één graad-van-vrijheid studies (nul graden elevatie van de humerus) was de intrinsieke visco-elasticiteit van de schouder substantieel kleiner tijdens de drie graden-van-vrijheid houdingstaak in het horizontale vlak (90 graden elevatie). Dit is verklaard door de reductie van momentarmen van een aantal schouderspieren rond het gleno-humerale gewricht. Opvallend was dat de reflexieve parameters vergelijkbaar waren met die uit de één graad-van-vrijheid stu-

dies. Blijkbaar compenseren reflexen de reductie in intrinsieke bijdrage als gevolg van geometrische variaties.

De belangrijkste conclusies van dit proefschrift zijn:

- Krachtverstoringen maken het mogelijk om de mechanische eigenschappen van het NMS te kwantificeren tijdens natuurlijke houdingstaken en zijn cruciaal voor de studie naar de functie van de menselijke beweginsturing in vivo.
- Krachtgestuurde haptische manipulatoren zijn noodzakelijk om krachtverstoringen op te leggen. De technische eisen van dergelijke apparaten zijn hoog om de kans op contactinstabiliteit te minimaliseren.
- De mechanische eindpunt admittantie is een maat voor de gevoeligheid van de arm voor externe krachtverstoringen en wordt gezien als de beste beschrijving van het NMS tijdens houdingstaken. De admittantie kan worden geïdentificeerd uit de hand positie en hand reactiekracht welke relatief makkelijk zijn te meten.
- Spinale reflexen van spierspoeltjes (Ia-afferenten) dragen substantieel bij aan de admittantie van de arm en kunnen van dezelfde orde of zelfs groter zijn als de intrinsieke bijdrage.
- Mechanische eigenschappen van de omgeving en de frequentie-inhoud van de krachtverstoring hebben een groot effect op de reflexieve eigenschappen. Met toenemende bandbreedte van de krachtverstoring neemt de grootte van de reflexieve terugkoppeling af om oscillatie rond de eigenfrequentie te voorkomen. In het geval dat de omgeving mechanische demping verschaft lijkt de reflexieve terugkoppeling bepaald te worden door een afweging van prestatie (het reduceren van de admittantie) en neurale regelaarinspanning (minimaliseren van het afferente signaal).
- Intrinsieke visco-elasticiteit van de schouder is relatief kleiner dan die van de elleboog en de pols gedurende houding in het horizontale vlak, in vergelijking tot de één graad-van-vrijheid houdingstaken. Een reflexief compenserend effect lijkt te bestaan, waarbij de grootste reflexieve terugkoppeling is gevonden voor de schouder. De resultaten wijzen er temeer op dat de reflexieve terugkoppeling onafhankelijk wordt geregeld van de intrinsieke visco-elasticiteit.

De ontwikkelde technieken in dit proefschrift hebben in hun toepassing bewezen belangrijke functionaliteit van het reflexieve systeem in kaart te brengen. Om de reflexieve sturing gedurende een breder fysiologisch gebied te bestuderen zal in de toekomst ook gekeken moeten worden naar de mogelijkheden voor identificatie van het NMS tijdens doelgerichte bewegingen. De toepassing van krachtverstoringen en de inzet van de ARMANDA manipulator is essentieel voor dergelijk vernieuwend onderzoek.

Dankwoord

Mijn onderzoek is met hulp van velen tot stand gekomen welke ik hier wil bedanken.

De belangrijkste bijdrage voor de wetenschappelijke kwaliteit van mijn promotie onderzoek is geleverd door mijn promotor Frans van der Helm. De bravoure waarmee je nieuwe ideeën op een overtuigende manier wist te brengen en de flexibiliteit waarmee je ze ook weer terzijde kon schuiven voor nog betere, hebben mijn enthousiasme voor het onderzoek steeds op een gezond peil gehouden. Er was aldoor een aangename spanning alsof we de wereld binnenkort zouden laten schudden met een topontdekking. Gelukkig blijven we voorlopig nog samenwerking om dit waar te maken. Verder heb je tal van mijn grillige uitspraken, afzwaaiende ideeën en sommige ondoorgrondelijke bedoelingen moeten doorstaan. Door geduldig en gericht door te vragen kwam de kern altijd boven tafel. Heel veel dank voor je bijdrage.

Vijf jaar lang met Alfred in een klein kamertje, dat schepte een band. Het schouderonderzoek heeft ons in een compleet nieuwe wereld geworpen. Uitgerust met zelf ontwikkelde experimentele en analytische technieken wisten we steeds meer van het menselijke bewegingssysteem te ontrafelen. Zowel voor praktische als ook theoretische problemen had je altijd een oplossing. Verder heb ik jouw, aan een obsessie grenzende, neiging tot afwijken altijd met veel genoegen aangezien. Afwijken is vooruitgaan, en zo heb ik de samenwerking met jou zeker ervaren. Het duurde soms even, maar dan had je wat.

Tijdens het eerste halfjaar van mijn aanstelling als promovendus heeft Guido Brouwn me veel geholpen met het opstarten van mijn onderzoek. Door zijn onderzoek is het gebruik van krachtverstoringen ingeburgerd en heeft hij de ARMANDA manipulator grotendeels ontwikkeld. Een inhoudelijke bijdrage aan dit proefschrift is eveneens geleverd door David Abbink (H4). Veel dank voor je “Golgi-bobbel” en natuurlijk je doorgewinterde drum adviezen. Henk Stassen heeft vanwege zijn onorthodoxe verschijning en overenthousiasme voor het vak Mens Machine Systemen mijn aandacht getrokken en ben ik mede door hem bij het schouderonderzoek terecht gekomen.

Ad en John hebben ervoor gezorgd dat alle apparatuur in het schouderlab altijd in orde was. Met name de ondersteuning voor de hydrauliek was onontbeerlijk. Bedankt voor jullie adviezen, geduld en precisie. Leo heeft de regeling en de beveiliging van ARMANDA ontworpen en gerealiseerd. Ik heb bewondering voor je passie voor alles wat met elektronica te maken heeft. Ondanks dat onze samenwer-

king te veel tijd gekost heeft ben ik je dankbaar voor je bijdrage. En verder bedank ik natuurlijk Piet voor de kleppen, Kees voor het vele bijklussen, Peter Valk voor de open-end software oplossingen, Fred voor de pomprimpel, Dineke voor de goede afloop en de (im)materïele zorg, Peter Wieringa voor de mens-machine interactie, Paul Breedveld voor een avondwandeling, Tjeerd voor de spoedservice en laptops, Jenny voor uitleg van de fax, Ed Chadwick voor controle van de spelling en grammatica van mijn manuscripten en Sippe Douma voor de waardevolle tips. En verder iedereen die de technische wetenschap vrolijk vooruit duwt, te weten Martijn, Göran, Richard, Erik, Jan, Daan, Dennis, Marit, Dimitra, Dirk-Jan, Michel Verhaegen, Paul van den Hof, Evelien, Machteld, Joanne, Just, Dick, Sybert, Herman, Bart, Arjan en Stepan. Niet te vergeten zijn alle K-studenten en studenten van de Haagse Hogeschool die hun opdracht hebben gedaan binnen het schouderonderzoek en veel goede ideeën hebben uitgewerkt. Zonder proefpersonen was het onderzoek naar de rol van reflexen niet veel meer dan een handjevol hypothesen gebleven. Iedereen die voor een geringe vergoeding vaak een hele middag op een stoel heeft gezeten en naar een beeldscherm heeft moeten staren; alle proefpersonen hartelijk bedankt.

Pap, mam, bedankt voor jullie altijd gemoedelijke steun, vitaminen en mijn aangeboren afwijkingen. Als laatste, en belangrijkste van alles, ben ik veel dank verschuldigd aan Tecla en later ook aan Luka. Mijn beide meiden hebben lang een geheimschrift inkloppend verschijnsel achter een beeldscherm zien zitten. Tecla, ik verheug me op de tijden die ik meer bij jouw en ook bij Luka zal zijn.

Erwin
April 2004, Heemskerk

Curriculum vitea

8 April 1968	Geboren te Heemskerk
1980 - 1986	HAVO, Bonnhoeffer College te Castricum
1986 - 1991	Studie HTS Elektrotechniek te Alkmaar Afstudeervariant: Meet- en Regeltechniek Afstudeeropdracht: Ontwerp en bouw van een volautomatische regeling voor gelijkstroommotoren met energie teruglevering.
1991 - 1992	Post HTO opleiding Meet- en Regeltechniek HTS te Arnhem
1992 - 1996	Assistent projectleider ingenieursbureau Witteveen en Bos te Deventer Ontwerpen van regelsystemen voor Drink- en Rioolwaterzuiveringsinstallaties
1996 - 1998	Studie Werktuigbouwkunde Technische Universiteit Delft Afstudeervariant: Mens-Machine-Systemen Afstudeeronderzoek: Analyse van krachtvermeerdering na verlenging van spieren middels cross-bridge modellen
1998 - 2004	Promovendus aan de Technische Universiteit Delft. Onderzoek naar de menselijke reflexieve sturing van de armspieren
2004 -	Aanstelling als post-doc in het TREND project aan de Technische Universiteit Delft. Verbetering en vernieuwing van identificatie technieken voor quantificatie van reflexen.